Development of Passive RFID Sensors Dedicated to the Monitoring of Power Plant Generators

Konstantinos Zannas

Communauté
UNIVERSITÉ Grenoble Alpes

THÈSE

Pour obtenir le grade de

DOCTEUR DE L'UNIVERSITÉ GRENOBLE ALPES

Spécialité : **Optique et Radiofréquence**

Arrêté ministériel : 25 mai 2016

Présentée par

Konstantinos ZANNAS

Thèse dirigée par **Smail TEDJINI, Professeur, Université de Grenoble-Alpes**
et co-dirigée par **Yvan DUROC, Professeur, Université Claude Bernard Lyon 1**

préparée au sein du **Laboratoire de Conception et d'Intégration des Systèmes (LCIS)**

dans **l' École Doctorale Électronique, Électrotechnique, Automatique, Traitement du Signal (EEATS)**

Développement de capteurs RFID passifs dédiés au monitoring des groupes alternateurs

Thèse soutenue publiquement le **8 Octobre 2019**,
devant le jury composé de :

Mme. Alessandra COSTANZO
Professeur à l'Université de Bologne, Italie, Rapporteur

M. Omar ELMAZRIA
Professeur à l'Université de Lorraine, France, Rapporteur

M. Dominique BAILLARGEAT
Professeur à l'Université de Limoges, France, Examinateur

M. Robert STARAJ
Professeur à l'Université de Nice-Sophia Antipolis, France, Président du jury

M. Ville VIIKARI
Professeur associé à l'Université de Aalto, Finlande, Examinateur

M. Yvan DUROC
Professeur à l'Université Claude Bernard Lyon 1, France, Co-Directeur de thèse

M. Smail TEDJINI
Professeur à l'Université de Grenoble-Alpes, France, Directeur de thèse

Σὰ βγεῖς στὸν πηγαιμὸ γιὰ τὴν Ἰθάκη, νὰ εὔχεσαι νᾶναι μακρὺς ὁ δρόμος, γεμάτος περιπέτειες, γεμάτος γνώσεις. Τοὺς Λαιστρυγόνας καὶ τοὺς Κύκλωπας, τὸν θυμωμένο Ποσειδῶνα μὴ φοβᾶσαι, τέτοια στὸν δρόμο σου ποτέ σου δὲν θὰ βρεῖς, ἂν μέν᾽ ἡ σκέψις σου ὑψηλή, ἂν ἐκλεκτὴ συγκίνησις τὸ πνεῦμα καὶ τὸ σῶμα σου ἀγγίζει. Τοὺς Λαιστρυγόνας καὶ τοὺς Κύκλωπας, τὸν ἄγριο Ποσειδώνα δὲν θὰ συναντήσεις, ἂν δὲν τοὺς κουβανεῖς μὲς στὴν ψυχή σου,ἂν ἡ ψυχή σου δὲν τοὺς στήνει ἐμπρός σου.

Κωνσταντίνος Π. Καβάφης

Quand tu partiras pour Ithaque, souhaite que le chemin soit long, riche en péripéties et en expériences. Ne crains ni les Lestrygons, ni les Cyclopes, ni la colère de Neptune. Tu ne verras rien de pareil sur ta route si tes pensées restent hautes, si ton corps et ton âme ne se laissent effleurer que par des émotions sans bassesse. Tu ne rencontreras ni les Lestrygons, ni les Cyclopes, ni le farouche Neptune, si tu ne les portes pas en toi-même, si ton cœur ne les dresse pas devant toi.

Constantin P. Cavafy

As you set out for Ithaka hope your road is a long one, full of adventure, full of discovery. Laistrygonians, Cyclops, angry Poseidon—don't be afraid of them: you'll never find things like that on your way as long as you keep your thoughts raised high, as long as a rare excitement stirs your spirit and your body. Laistrygonians, Cyclops, wild Poseidon—you won't encounter them unless you bring them along inside your soul, unless your soul sets them up in front of you.

C. P. Cavafy

ACKNOWLEDGEMENTS

I would like to thank my supervisors, Professor Smail Tedjini and Professor Yvan Duroc, for their excellent advice and collaboration throughout this doctoral thesis. I will always have pleasant memories from this period. In addition, I would like to express my gratitude to Prof. Alessandra Costanzo, Prof. Omar Elmazria, Prof. Dominique Baillargeat, Prof. Robert Staraj and Prof. Ville Viikari for accepting to serve as members of the jury at my PhD defense and for their comments and observations regarding the presented work. Moreover, warm thanks to Mr. André Petit for serving as an invited jury member and also for his cooperation and discussions during the past 3 years in the context of my PhD thesis main project, the Innov'Hydro project.

Also I would like to thank several members of the LCIS laboratory, PhD students, post-doctoral researchers and professors for their positive attitude, our daily friendly interactions and their important contribution to the excellent working environment. Namely I would like to thank Dr. Hatem El Matbouly, Dr. Zeshan Ali, Dr. Mushir Ahmed, Dr. Abanob Abdelnour, Dr. Yoann Hervagault, Dr. Raphael Tavares de Alencar, Dr. Imbolatiana Rakotomalala, Dr. Athanasios Papadimitriou, Dr. Igisso Zafeiratou, Dr. Marco Garbati, Prof. David Hely, Prof. Nicola Barbot, Prof. Ionela Prodan, Prof. Vincent Beroulle, Mrs. Carole Seyvet, Mrs. Jennyfer Duberville, Mrs. Caroline Palisse, Mr. Romain Doleux and Mr. Cedric Carlotti.

Of course I would like to express my gratitude to my family, my parents Nikoletta and Grigoris and my two brothers Zisis and Alexandros for their continuous support. Also my thanks to my good friend Pavlos Georgas for his support.

Last but not least my biggest gratitude to my other half, Vasiliki Gavriilidou for her courage to bare with me during this period (and in general).

TABLE OF CONTENTS

Acknowledgments i

List of Tables vii

List of Figures ix

Introduction 1

0.1 The evolution of radio frequency identification technology: From identification to sensing . . 1

0.2 Thesis scope and contributions 2

Chapter 1: RFID technology and sensing 5

1.1 Introduction 5

1.2 RFID technology in a nutshell 5

1.2.1 RFID technology in general 6

1.2.2 UHF RFID technology 9

1.2.3 Internet of Things (IoT) and RFID 11

1.3 RFID communication chain 14

1.3.1 RFID sensor tag 14

1.3.2 RFID data capture level 15

1.3.3 RFID tag process level 16

1.3.4 RFID communication channel 17

1.3.5 RFID reader process level & RFID reader 18

1.4 RFID sensor tags: Examples from literature and commercially available products 20
1.5 Comparison of different types of RFID temperature sensors 27
1.6 Conclusion 29

Chapter 2: Environment of operation 31
2.1 Introduction 31
2.2 Effects of metal on the antennas 32
2.2.1 Effects of metal on the radiation of antennas 32
2.2.2 Numerical model and representation of the radiation pattern 35
2.2.3 Effects of metal on the impedance of antennas 40
2.2.4 Numerical model and representation of the antenna impedance 42
2.3 Multipath effects on RFID communication 46
2.4 Numerical model of a complex metallic environment 47
2.5 Time constraints of RFID communication 48
2.5.1 Real time RFID communication 49
2.5.2 Exploration on the causes of time delay 50
2.5.3 Analysis of time delay in rotating RFID sensing system 52
2.6 Effects of high magnetic field on the RFID sensor-tags and RFID communication 55
2.7 Effects of high electric field on the RFID sensor-tags and the RFID communication 56
2.8 Conclusion 57

Chapter 3: Design of UHF RFID sensor-tags with enhanced RFID chips 58
3.1 Introduction 58
3.2 Specifications 58
3.3 Measurement and characterization of the SL900A RFID chip 60

3.4 Designs of UHF RFID antenna-tags for sensing applications in metallic environment 64
3.4.1 Circular UHF RFID tag-antenna 65
3.4.2 Rectangular UHF RFID tag-antenna corresponding to $\lambda/2$ length 70
3.4.3 Rectangular UHF RFID tag-antenna corresponding to λ/4 length 74
3.5 Conclusion 87

Chapter 4: Twin RFID sensor tags 89
4.1 Introduction 89
4.2 Twin RFID sensor tag 89
4.2.1 Twin RFID tag antenna design 90
4.3 Antenna designs for the RFID reader 104
4.3.1 Specifications of the antennas of the RFID reader 105
4.3.2 Design of RFID reader antenna with lumped component 105
4.3.3 Design of RFID reader antenna with the inset technique 108
4.4 Conclusion 112

Chapter 5: Temperature and strain measurements in the lab 114
5.1 Introduction 114
5.2 Considerations on thermal conductivity issues 114
5.3 Sensing capabilities of the SL900A RFID chip 117
5.3.1 Temperature measurements with the integrated sensor 117
5.3.2 Stress measurements using an external strain sensor 122
5.4 Temperature measurements with the twin RFID sensor tag 125
5.5 Conclusion 131

Chapter 6: Different approaches on RFID sensing 132

6.1 Introduction . . . 132
6.2 Self-tuning RFID chips . . . 132
6.3 Self-tuning circuit for sensing operation . . . 133
6.3.1 Selection of substrate . . . 135
6.3.2 Simulation of the proposed RFID sensor tag . . . 136
6.3.3 Fabrication and measurements of the self-tuning RFID sensor tag . . . 138
6.3.4 Application on temperature sensing . . . 143
6.3.5 90° Hybrid coupler concept for insensitive to power received self-tuning RFID sensor tag . . . 147
6.4 Chipless RFID sensing approaches . . . 150
6.4.1 Threshold temperature sensing chipless RFID tag . . . 151
6.4.2 Dual chipless RFID threshold sensor for temperature and humidity . . . 152
6.4.3 Rotational motion sensing . . . 154
6.4.4 Chipless sensor reader architecture and operation principle . . . 156
6.4.5 SDR chipless RFID reader . . . 158
6.5 Conclusion . . . 163

Chapter 7: Installations and measurements in industrial sites . . . 164

7.1 Introduction . . . 164
7.2 Visits in different industrial sites . . . 164
7.2.1 Visit in the hydroelectric power-plant of *Châteauneuf-sur-Isère* . . . 165
7.2.2 Visit in the hydroelectric power-plant of *Prévenchères* . . . 167
7.2.3 Visit in the hydroelectric power-plant of Beauvoir . . . 169
7.2.4 Visit in the hydroelectric power plant of Saint-Chamas . . . 172
7.2.5 Visit in the hydroelectric power-plant of Grand'Maison . . . 174

7.2.6 Visit in the hydroelectric power-plant of Super-Bissorte . . . 183
7.2.7 Visit in the hydroelectric power-plant of Aussois . . . 185
7.3 Conclusion . . . 189

Chapter 8: Conclusion . . . 191
8.1 General conclusion . . . 191
8.2 Future research lines . . . 193
8.3 List of publications . . . 194

Appendix A: AMS SL900A RFID chip . . . 198

Appendix B: AMS Femto AS3993 RFID reader . . . 201

References . . . 213

Summary . . . 214

LIST OF TABLES

1.1 Overview of RFID systems 8

1.2 UHF RFID chip sensitivity and read range for ETSI regulation during the past 20 years . . . 13

1.3 RFID ICs with extra functionalities 17

1.4 Summary of RFID sensor types 20

1.5 Comparison of Examples from Literature 27

1.6 Comparison of temperature sensing examples 28

2.1 Resonance frequency of dipole antenna as function of distance h 45

3.1 Specifications of the RFID sensor-tag 59

3.2 Eigen-Mode simulation results 80

3.3 Component values of the equivalent circuit of the RFID tag in a free space scenario 81

3.4 Values of the components of the RFID antenna equivalent model for different distances . . . 83

3.5 Summary of the proposed UHF RFID sensor tags 88

5.1 Values of the temperature probes for each case study 116

5.2 SL900A ADC reference voltages 117

5.3 SL900A theoretical lower temperature limit 118

5.4 SL900A reference voltage difference, resolution and measuring range 118

6.1 Capacitance values of auto-tune circuit of Monza R6 133

6.2 Properties of common used substrate materials 135

6.3 Complex impedance of the 3 RFID chips as function of temperature 141

6.4 Comparison between simulated and measured impedance of the RFID tag antenna 143

6.5 Self-tune value versus temperature 145

7.1 Phase 1 181

7.2 Phase 2 182

7.3 Phase 3 182

A.1 SL900A RFID chip main characteristics 198

B.1 Femto AS3993 RFID reader main characteristics 202

LIST OF FIGURES

1.1 Typical near field HF RFID tag [3] 7

1.2 Typical far-field UHF RFID tags [8] 7

1.3 Typical chipless RFID tag [12] 8

1.4 Standard UHF RFID system 9

1.5 RFID frequency bands over the globe 10

1.6 Increase and projected revenues of the RFID market 12

1.7 Description of the classification format. Each Latin number represents a part of communication between the RFID reader and the RFID sensor tag 14

1.8 Example of the internal/external RFID sensor concept 15

1.9 Typical RFID reader architecture 19

1.10 Orientation sensing with RFID tags [45] 21

1.11 Motion and temperature sensing RFID sensor tag [46] 21

1.12 RFID temperature sensor (a) (external type) 22

1.13 RFID temperature sensor (b) (internal type) 23

1.14 Pressure sensing RFID sensor[25] 23

1.15 Chipless gas sensor 24

1.16 Light sensing RFID sensor tag 24

1.17 Threshold temperature RFID sensor tag 25

1.18 Meat quality sensing RFID tags 25

1.19 Temperature sensor from RFMicron 26

1.20 Temperature and pressure sensing RFID tag from Farsens 27

2.1 Example of horizontal dipole parallel to an infinite large PEC [54] 33

2.2 Far-field observation of the horizontal dipole [54] 34

2.3 Model of horizontal dipole close to infinite large PEC 35

2.4 Radiation pattern for distance $h = \lambda/8$ 36

2.5 Radiation pattern for distance $h = \lambda/4$ 36

2.6 Radiation pattern for distance $h = \lambda/2$ 37

2.7 Radiation pattern for distance $h = 3\lambda/4$ 37

2.8 Radiation pattern for distance $h = \lambda$ 38

2.9 Radiation pattern for distance $h = 2\lambda$ 38

2.10 Directivity of dipole for different values of h at 900MHz 39

2.11 (a) two port network (b) T-network equivalent representing the mutual coupling between antenna and image antenna as a two port network 40

2.12 Resistance of dipole for different values of h 43

2.13 Reactance of dipole for different values of h 43

2.14 Complex impedance of dipole as function of distance h at 900 MHz 44

2.15 Complex impedance of dipole as function of distance h (small values) at 900 MHz 44

2.16 Numerical model of a real sized generator with RFID antennas in the interior 47

2.17 Radiation pattern of the 4 RFID antennas in the interior of the generator model 48

2.18 RFID wireless sensor communication link with sources of time delays constrains 49

2.19 The measurement setup for reader-sensor tag rotational motion 53

2.20 RSSI values recorded by the interrogator software 54

2.21 Time responses for different Tari values of the RFID tag to the rotational motion 55

2.22 Measurement setup in high magnetic field 56

3.1 SL900A RFID chip soldered on the RF connector 61

3.2 Reflection coefficient of RFID chip in a power sweep mode for the frequency of 915 MHz . 62

3.3 Real and imaginary values of impedance for different values of power 62

3.4 Impedance of RFID chip for different values of power in Smith chart 63

3.5 Variation of impedance for different tested RFID chips 63

3.6 Comparison of identical RFID tags to demonstrate the low yield of the RFID chip 64

3.7 Circular RFID tag-antenna: (a) RFID tag-antenna profile, (b) RFID tag-antenna top and bottom view, (c) RFID tag-antenna dimension, (d) position of via, (e) dimension of each layer 65

3.8 Real and imaginary part of the impedance of the circular RFID tag-antenna versus the radius of the circular feed 66

3.9 Radiation pattern of the circular RFID tag-antenna 67

3.10 (a) Fabrucated prototype of the circular RFID sensor tag (b) Measurement of the read range in the anechoic chamber 68

3.11 Measured theoretical read range and calculated read range from simulation results 69

3.12 S11 parameters for different RFID chip input impedance values 69

3.13 Rectangular RFID tag-antenna corresponding to $\lambda/2$ length. (a) the dimension of the feeding area (b) bottom view (c) top view 70

3.14 Gain of RFID tag-antenna 71

3.15 Directivity of RFID tag-antenna 72

3.16 S11 of RFID tag-antenna 72

3.17 Gain and radiation efficiency of RFID tag-antenna 73

3.18 Fabricated $\lambda/2$ UHF RFID sensor tag 73

3.19 Read range of the RFID tag 74

3.20 UHF RFID antenna-tag corresponding to $\lambda/4$ 75

3.21 λ/4 UHF RFID antenna tag on a metallic plane (a) with the top side closer to the metallic plane (b) with the bottom side closer to the metallic plane 76

3.22 Simulated input impedance of the UHF RFID tag for scenario (a) 77

3.23 Simulated input impedance of the UHF RFID tag for scenario (b) 78

3.24 Radiation pattern for each scenario 79

3.25 Equivalent circuit of the RFID tag in free space 81

3.26 Comparison of simulated and equivalent model impedance and Q factor of the RFID tag in free space 82

3.27 Equivalent circuit of the RFID antenna with the effects of the metallic plate as a parallel RLC circuit 82

3.28 Comparison of the real and imaginary values of impedance and Q factor of the simulated RFID antenna and the equivalent circuit for scenario (a) for different values of distance between RFID antenna and metallic plate 84

3.29 Comparison of the real and imaginary values of impedance and Q factor of the simulated RFID antenna and the equivalent circuit for scenario (b) for different values of distance between RFID antenna and metallic plate 85

3.30 Fabricated UHF RFID tag 85

3.31 Measured and simulated results of the RFID antenna in a free space scenario 86

3.32 Measured read range of the RFID tag in scenario (a), scenario (b) and free space scenario . . 87

4.1 Twin RFID tag antenna based on the rectangular λ/2 design 90

4.2 S-parameters of the λ/2 twin RFID tag antenna design 91

4.3 Distribution of surface current at 868 MHz for excitation only at the one sub-RFID antenna . 92

4.4 Distribution of surface current at 868 MHz at the RFID chip 1 92

4.5 Distribution of surface current at 868 MHz at the RFID chip 2 93

4.6 Variation of the real and imaginary part of the impedance of the λ/2 twin RFID tag 93

4.7 Radiation efficiency for different values of the gap for the λ/2 twin RFID tag 94

4.8 Simulated gain of the λ/2 twin RFID tag 95

4.9 Electric field distribution for phase values 0°, 90°, 180° and 270° at 868 MHz 95

4.10 Fabricated λ/2 twin RFID tag with the trimmed areas marked 96

4.11 Read range comparison of the λ/2 twin RFID tag 96

4.12 Twin RFID tag antenna based on the rectangular λ/4 design 98

4.13 S-parameters of the λ/4 twin RFID tag antenna design 99

4.14 Variation of the real and imaginary part of the impedance of the λ/4 twin RFID tag 99

4.15 Radiation efficiency for different values of the gap for the λ/4 twin RFID tag 100

4.16 Distribution of surface current at 868 MHz for excitation only at the one λ/4 sub-RFID antenna 101

4.17 Distribution of surface current at 868 MHz at the input of the RFID chip 1 (with the excitation applied) 101

4.18 Distribution of surface current at 868 MHz at the input of the RFID chip 2 102

4.19 Electric field distribution for excitation signal phase values 0°, 90°, 180° and 270° at 868 MHz 102

4.20 Simulated gain of the λ/4 twin RFID tag 103

4.21 Fabricated λ/4 twin RFID tag with the trimmed areas 103

4.22 Read range comparison of λ/4 twin RFID tag 104

4.23 RFID reader antenna with lumped component 105

4.24 S11 parameters for the RFID reader antenna with lumped component 106

4.25 Realized gain of the RFID reader antenna with lumped component at 868 MHz 106

4.26 Radiation efficiency of the RFID reader antenna with lumped component 107

4.27 Fabricated prototype of the RFID reader antenna with lumped component 107

4.28 Comparison of input reflection coefficient between simulated and measured results 108

4.29 Inset RFID reader antenna 109

4.30 Input reflection coefficient of inset RFID reader antenna 110

4.31 Realized gain of the inset RFID reader antenna at 868 MHz 110

4.32 Radiation efficiency of inset RFID reader antenna 111

4.33 Fabricated prototype of the RFID reader antenna with lumped component 111

4.34 Comparison of input reflection coefficient 112

5.1 Mockup of generator with the RFID sensor tag 115

5.2 Temperature distribution with the RFID chip on bottom of the RFID sensor tag 115

5.3 Temperature distribution with the RFID chip on top of the RFID sensor tag 116

5.4 Temperature measurement setup 120

5.5 Case 1: output code and absolute error using the 5.1 and 2-point calibration 120

5.6 Case 2: output code and absolute error using the 5.1 and 2-point calibration 121

5.7 Strain gauge from Micro Measurements company [109] 122

5.8 Strain versus ΔR for the used strain gauge 123

5.9 Strain measurement setup 124

5.10 Resistance versus ADC output and normalized strain measured by the RFID sensor tag . . . 124

5.11 Twin and single RFID sensor tags settings 126

5.12 Experimental setup for temperature measurement 127

5.13 Details of measurement setup(a) Trimmed twin RFID sensor tag (b) RTD probe in the hole of the copper block 128

5.14 RTD probe in the hole of the copper block 128

5.15 The absolute error of the temperature measurement for the twin RFID sensor tag 129

5.16 The ADC output of the single RFID sensor-tag versus the measured temperature 130

5.17 Absolute temperature error of the single RFID sensor-tag 130

6.1 Self-tuning effect on the read range of an RFID tag 133

6.2 Operating principle of the auto-tune circuit 134

6.3 Dependency of thermal coefficient of relative permittivity versus the temperature for the RT 6010.2LM substrate . . . 136

6.4 Layout of the proposed RFID sensor tag . . . 137

6.5 Complete simulation setup including the RFID tag, the SMA connector, the coaxial cable and the copper block . . . 137

6.6 Simulated complex impedance of the antenna as function of temperature and span of real and imaginary values of the impedance at 868 MHz . . . 138

6.7 Fabricated self-tuning RFID sensor tag . . . 139

6.8 The RFID chips on the copper block on the hot plate . . . 140

6.9 Real and imaginary part of the impedance of the RFID chips versus the temperature . . . 140

6.10 Measurement setup of the RFID antenna tag . . . 142

6.11 Measured complex impedance of the antenna as function of temperature and span of real and imaginary values of the impedance at 864 MHz . . . 142

6.12 Change of resonance frequency due to temperature change and different power extracted level 144

6.13 Measured read range for different temperature values . . . 145

6.14 Self-tune value vs reader power vs temperature. (* In the black area there was no response from the tag) . . . 146

6.15 3-dB 90° Hybrid coupler for equal impedance terminations . . . 148

6.16 3-dB 90° Hybrid coupler system with the addition of a circulator . . . 149

6.17 Fabricated system with the circulator, 3-dB 90° hybrid coupler and the RFID chips with the matching circuits . . . 149

6.18 Self-tuning value versus transmitted power . . . 150

6.19 Temperature threshold chipless RFID tag(a) The chipless RFID sensor tag structure (b) operation for different temperature values . . . 151

6.20 Measurement of the shift of the resonance peak inside (a-top) ETSI band (b-down) ISM band 152

6.21 The dual chipless threshold sensor structure . . . 152

6.22 Measurement of the dual chipless RFID threshold sensor . . . 153

6.23 Measurement results (a) temperature threshold sensor (b) humidity threshold sensor . . . 154

6.24 Rotational motion sensing chipless RFID sensor 155

6.25 Measurement setup for the rotational motion sensor 155

6.26 Measurement and simulated results of the rotational motion sensor 156

6.27 Generic block diagram of the proposed chipless sensors reader 157

6.28 The Fourier transform of the signal with bandwidth B (a) transmitted and (b) received backscattered signals from the proposed chipless sensor, (c) is the output calculated signal in frequency domain after processing by the arithmetic operation 157

6.29 Modulating the 10 MHz base band signal using VCO to generate the ISM 2.45 GHz band by USRP 2900 159

6.30 TX/RX output of the USRP 2900 for the 100 MHz ISM 2.45 GHz band 159

6.31 Schematic diagram of the experimental setup for the sensing system 160

6.32 (up) Illustration of the resonance frequency shift due to heating (down) The measurement results for the chipless temperature threshold sensor in the ETSI band 161

6.33 The measurement results for the chipless rotational motion sensor in the ETSI band by the USRP. The time interval between two minima represents one cycle 162

7.1 Outer view of the generator at the power-plant of *Châteauneuf-sur-Isère* 165

7.2 Inside view of the generator at the power-plant of *Châteauneuf-sur-Isère* 166

7.3 Interpolar connection at the hydroelectric power-plant of *Châteauneuf-sur-Isère* 166

7.4 Outer view of the generator at power-plant of *Prévenchères* 167

7.5 Position 1 of the RFID sensor tag 168

7.6 Position 2 of the RFID sensor tag 168

7.7 Generator geometry in hydroelectric power-plant of Beauvoir 169

7.8 Example position of the RFID sensor tag and reader's antenna inside the generator 170

7.9 Example position of the RFID sensor tag and reader's antenna inside the generator 170

7.10 Position of the antenna of spectrum analyzer (SA) 171

7.11 Received power during the rotation of the generator 172

7.12 Generator at Saint-Chamas power-plant . . . 173

7.13 Interpolar connections in Saint-Chamas power-plant . . . 173

7.14 Transformers in hydroelectric power-plant of Grand'Maison . . . 175

7.15 Fabricated RFID sensor tag (a) bottom view (b) top view (c) placement with the glue . . . 175

7.16 Transformer with RFID sensor tags in various installation positions . . . 176

7.17 Installation positions of the RFID sensor tags in each transformer connection (seven positions overall) . . . 176

7.18 Developed interface for acquiring the output value of the integrated temperature sensor of the SL900A RFID chip . . . 178

7.19 Shielded measurement setup . . . 179

7.20 Tested positions of the antenna . . . 180

7.21 Measurement of the RFID sensor tags from position A . . . 181

7.22 Stator of the generator at the hydroelectric power-plant of Super-Bissorte . . . 183

7.23 Rotor of the generator and the interpolar connections at the hydroelectric power-plant of Super-Bissorte . . . 184

7.24 Attached RFID sensor tags on the interpolar connection of the rotor at the hydroelectric power-plant of Super-Bissorte . . . 185

7.25 Rotor of the generator at the hydroelectric power-plant of Aussois . . . 186

7.26 (a) Interpolar connection of the rotor with the installed RFID sensor tags at the hydroelectric power-plant of Aussois (b) Interpolar connection after the application of the protective tape . 186

7.27 (a) The stator at the hydroelectric power-plant of Aussois (b) The air ducts with the RF cable (c) The installed antenna of the RFID reader . . . 187

7.28 RF cable ending behind the stator . . . 188

A.1 Impedance of the SL900A RFID chip from the equivalent RC circuit . . . 199

A.2 Block diagram of the SL900A RFID chip [31] . . . 200

B.1 Femto AS3993 RFID reader . . . 201

INTRODUCTION

0.1 The evolution of radio frequency identification technology: From identification to sensing

The origin of the Radio Frequency Identification (RFID) technology can be tracked down back during the middle of the 20th century and in the period before and after the World War II. The radar has already been invented by Sir Robert Alexander Watson-Watts in 1935 and was used by both opposing sides to turn the tides of the ongoing war. It was this time that this great invention faced a main problem: the radar could detect an airplane but it could not identify it. Nobody could tell if the incoming blinking dot in the radar screen was an ally or a hostile airplane. This problem was partially solved by the Germans who discovered that if their returning airplanes performed rolling maneuvers, the reflected signal received by their radars would be alternating and they could identify their own airplanes. This rolling maneuvers can be considered as a backscatter modulation of the radar signal and a very first implementation of an RFID system.

Some years later and during the birth of the cold war, a wooden plaque of the U.S. Great Seal was given as a gift from the Soviets to the U.S. ambassador in Moscow and it turned out to be something more than a nice gesture. Inside the structure of the plaque, there was one cavity with a metallic membrane and a monopole antenna, designed in such a way that could act as a backscatter modulator of sound waves when a proper RF beam was pointed at the location of the plaque. Due to this device, known later as “The Thing”, the Soviets would intercept conversations from the office of the U.S ambassador.

Since, these early “RFID” systems and their value in espionage and air-combat, a lot of progress has been made. The RFID technology has been commercialized and standardized and is being used since the late 80’s - early 90’s initially for applications such as access control in public transportations and later on for applications concerning supply chain control.

In the dawn of the 21st century, the RFID technology is being redefined targeting sensing applications due to the Internet of Things (IoT). The IoT is a concept, which aims to introduce, develop and establish the smart management and lead the fourth industrial evolution. According to IoT everything will be connected with everything, monitoring the environment and sending continuously information and data regarding the operating conditions. To achieve the monitoring functions, the IoT concept is required to have somewhere in the physical layer a number of wireless sensor networks (WSNs). These WSN’s are required to be able

to send information regarding temperature, pressure, proximity, strain, displacement, illumination, humidity; to name just a few of the countless parameters which need to be monitored. This is where the RFID technology comes handy, demonstrating numerous advantages to fulfill the required sensing and monitoring part.

0.2 Thesis scope and contributions

The main goal of this thesis was to explore the capability of the RFID technology to offer sensing solutions in the harsh industrial environment of hydroelectric power plants and especially in the interior of the generators. The bulky generators of power plants are susceptible to break downs due to the oxidation of high current conducting parts. One solution to avoid such break downs is to monitor the temperature or the deformation in the interior of the generators and especially of the vulnerable parts. In order to monitor these parts, the small size, the high accuracy and a potential passive operation of the sensors are critical attributes of the sensing solution. In addition to these constrains regarding the sensors, the interior of the generators is consisted by a big fast rotating metallic rotor with high electric and magnetic fields, which can result in major perturbation of the wireless communications. The recent developments of the RFID technology and especially in the UHF band towards the concept of sensor-tag can offer solution to this complex and challenging problem. The UHF RFID technology offers many promising options while exhibiting the inherent advantages of this technology: unitary identification, small size, low-cost and remote supply which allows power autonomy and maintenance-free operation for years.

The first step of the thesis was to study the environment of an operating generator to identify disruptive parameters of performance and radio communication, determining the most favorable areas and conditions of operation. Initially, the effects of the heavy metallic environment on the sensor tag as well as on the RFID communication were studied. By this study more robust and efficient sensor-tags could be designed in order to achieve their communication and sensing functionality. The following step was to analyze and assess the time delay of a UHF RFID system, aiming to identify the capability of the RFID system to operate within fast rotating setups. This study focused on the minimum time required for the RFID system, including the respective RFID protocol and processing hardware, to perform the appropriate steps for establishing a communication link. Furthermore, experiments were conducted in environment with high magnetic field to identify any disruptive effects on the RFID communication link.

The second step was to define the RFID sensor specifications by considering the following two ap-

proaches: (a) traditional integrated sensor to the RFID sensor-tags (including the associated challenge of energy autonomy) and (b) RFID sensor-tags integrating the sensor functionality via their antenna or their chip used as a transducer (sensitive to the parameter to measure). In this step, it was necessary to compare the performance of commercially available RFID chips and quantify their potential to enable sensor functions for the specific application. This established detailed specifications based on the state of the art and the specifications required by the particular application as they were defined in the first step. The final required specifications excluded the possibility of utilizing RFID sensor-tags with their functionality based on the approach (b). However, several original RFID sensor-tag concepts based on such approach were proposed and developed.

The third step of the thesis involved the design, fabrication of the final RFID sensor-tags. They were developed by appropriate simulation in electromagnetic tools and they were validated by fabricating a number of prototypes. In parallel, the associated reading protocol and its integration into an RFID reader was also developed. The reading protocol was based on the EPC Gen2 protocol of the RFID UHF technology. In addition, antennas for the RFID reader were also designed, simulated and fabricated in order to conform to the appropriate specifications of the application.

The fourth and final step of the thesis was the selection of the qualified designed UHF RFID sensor-tags and their laboratory validation. Also, the fabricated RFID reader antennas were experimentally validated to ensure their operation with the total RFID system. In addition, these RFID sensor-tags were tested and validated in real conditions.

The work which was conducted in the context of this thesis is organized as follows:

- **Chapter 1:** A short introduction in RFID technology is initially presented followed by a presentation of the state of the art of the RFID technology for sensing applications. Following, a generalized classification of the RFID sensing systems is proposed, aiming to set the distinguishing parameters of the different techniques. Finally, a detailed analysis of the different approaches found in the literature is illustrated, with examples and comparison between them, focusing in applications in the UHF band.

- **Chapter 2:** The impact of the harsh environment on antennas in general and on RFID tags specifically is discussed. This chapter includes among other, theoretical discussion and simulations of case studies regarding the impact of metal on antenna structures. In addition, the impact of high electric and magnetic fields on the RFID communication is discussed. Finally, an exploration on the time

constraints which govern the RFID communication is presented.

- **Chapter 3:** A variety of novel RFID sensor tag antenna designs are presented, aiming to evaluate their performance according to imposed specifications. The design process with simulations, fabrication and measurement details is illustrated. Additionally, a property of one of the designs is further exploited to offer a multiband operation in the specific RFID sensor tag.

- **Chapter 4:** A developed RFID sensor tag structure is the main subject of this chapter. This structure, named as twin RFID sensor, offers a solution towards a higher quality temperature measurement. Also, in this chapter the design and validation of some antenna structures for operation as RFID reader antennas are presented and discussed

- **Chapter 5:** In this chapter, measurements of temperature and stress in the laboratory environment are presented. In order to perform these measurements, the previously designed RFID sensor tags were used. In addition, the capability of the twin RFID sensor tag is accessed.

- **Chapter 6:** Some different approaches on RFID sensing are presented in this chapter. A novel technique utilizing a self-tuning feature of some RFID chips is exploited in order to transform an off-the-shelf chip to a temperature sensor. In addition, a series of chipless RFID sensor tags are presented and discussed, while a type of chipless RFID reader is proposed.

- **Chapter 7:** In this chapter, the developed RFID sensor tags will be installed and tested in hydroelectric power-plants and in particular on the interior of large-scale generators as well as on high voltage transformers. The discussion will include also a variety of other information regarding the different types and the geometries of the generators, the advantageous characteristics which can be utilized to better exploit the RFID communication and the different issues faced during the visits in the different industrial sites.

- **Chapter 8:** In the final chapter of this thesis, the general conclusion of this work is summarized while future work regarding various concepts is proposed.

CHAPTER 1
RFID TECHNOLOGY AND SENSING

1.1 Introduction

The Radio-Frequency Identification (RFID) technology is currently one of the most promising technologies as far as identification is concerned. It has been developed and exploited for the past few decades offering more and more solutions in a variety of applications, such as traceability, access, security, and payments, to name a few. Due to the versatility and the advantages that it offers, the RFID technology has been in the center of a lot of research activity in order to find even more usages in areas where other technologies have been traditionally used. Such usages included sensing applications, where the inherited passive operation of the RFID technology, as well as the low cost and size of RFID devices, could offer great advantages. Last but not least, the worldwide regulation of RFID is a decisive characteristic that favors its implementation in a real environment.

In this chapter, a comprehensive description of the RFID systems is presented, discussing the various RFID subcategories, focusing mainly on the Ultra High Frequency (UHF) RFID category. Following, the evolution of the RFID technology into a sensing solution in the context of the Internet of Things (IoT) is discussed and analyzed, presenting the different techniques which are implemented in the literature. This implementation, concerning the RFID transformation into a sensing solution, is divided into multiple stages, focusing each time in a different part of the RFID operational chain (i.e. RFID tags, radio interface, RFID reader). Based on the different techniques and implementations, a general classification of the RFID sensors is proposed, aiming to clarify the logic behind the main RFID sensing adaptations. This state of the art discussion is also accompanied with different examples found not only in the literature but also in commercially available solutions, in order to offer a clear view of the differences of each technique and implementation. Also, another objective of this chapter is to highlight the advantages and disadvantage of each case as well as their performance by considering and comparing some examples of temperature sensing solutions.

1.2 RFID technology in a nutshell

A good way to start a chapter about RFID technology and sensing is to display and cite the principles of the RFID technology. The goal is to set the basic lines of understanding and keep everyone on the same

page during this chapter and this thesis overall. Presenting the RFID technology in many details is out of the scope of this work, so the RFID technology will be presented in general lines. For more information on the principles and the RFID technology in general, numerous articles and books can be referred such as [1, 2, 3, 4, 5, 6, 7, 8].

1.2.1 RFID technology in general

In general, the main components of an RFID system are the RFID reader, the antenna of the RFID reader and the RFID tags. The RFID technology has quite numerous different implementations, protocols, operating frequencies, and applications, making a classification of the different types of RFID systems a not so easy task. One of the simplest ways to categorize the RFID systems could start by a separation between active and passive RFID systems. In the first category, the active RFID tags, a power source is being used to support their operation. This feature allows a wider range of communication and the ability to use more complex and energy consuming functions, but at the expense of a higher cost. The passive RFID tags do not have a conventional power source and they rely on the electromagnetic energy transmitted by the RFID reader to power up their functions and communicate. The passive RFID tags exhibit less communication range than the active RFID tags but they allow a lower cost, they are maintenance-free and they are easily disposable.

Another categorization feature for the RFID systems is the separation between near field and far field RFID systems. This classification is based on the difference of coupling between the RFID reader and the RFID tags. In the near field RFID systems, the nature of coupling is mainly inductive [3] and the data transmission is performed through load modulation. The near field RFID systems are divided between two major categories, the Low Frequency (LF) and the High Frequency (HF) depending on their frequency of operation. The range of communication for near field RFID systems is between some centimeters to less than a meter due to the fact that the near field coupling drops off at a fast rate relative to $\sim \frac{1}{r^3}$, where r is the distance between tag and reader antenna. Moreover, the maximum range which inductive coupling can be used is relative to the factor $\sim \frac{C}{2\pi f}$, where c the light speed and f the frequency, resulting in the need for low frequency in order to operate with sufficient range. This low frequency imposes constraints relative to the data transmission rates due to the limited available bandwidth. In Fig. 1.1 typical HF RFID tags are presented.

The far field RFID systems can operate with much higher communication range and with higher data transmission rates. The most used frequency band for far field RFID systems is the UHF 860-960 MHz

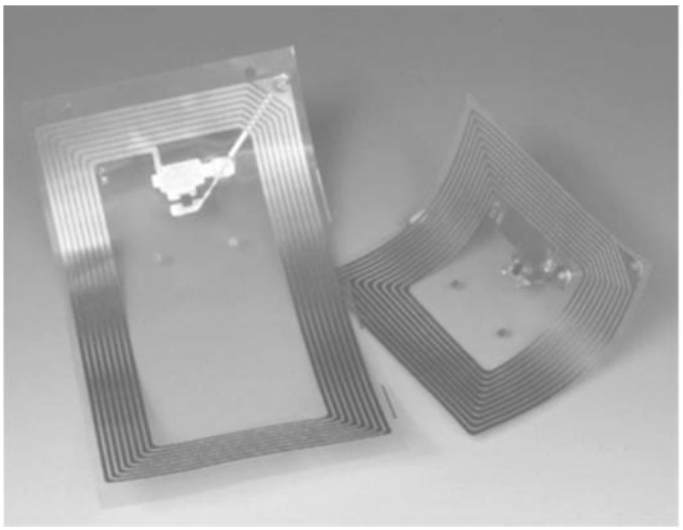

Figure 1.1: Typical near field HF RFID tag [3]

Industrial Scientific Medical (ISM) frequency band. Other frequency bands are also used, such as the 433 MHz band and the 2.45-5.8 GHz band but with limited usage. A closer look at the operation of the far field RFID systems will follow in the next subsection. In Fig. 1.2 some typical UHF RFID tags are illustrated.

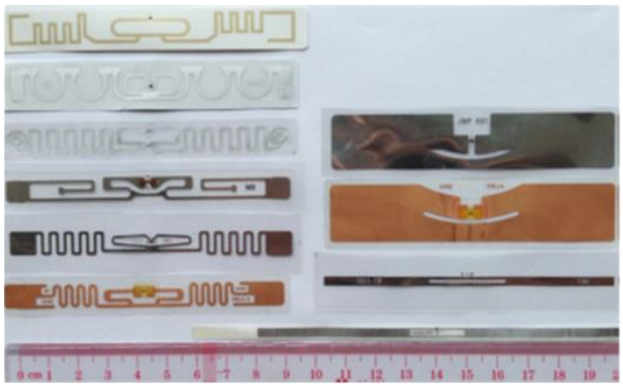

Figure 1.2: Typical far-field UHF RFID tags [8]

Finally, it is worth mentioning the category of chipless RFID tags. In comparison to the traditional RFID tags, there is no switching device (RFID chip), as their name suggests, and thus the communication is not based on load or backscatter modulation. The chip-less RFID tags are actually a set of resonators with different sizes or shapes and electromagnetic signatures (EMS). In order to model this EMS, the radar cross section (RCS) feature is being used. For every resonator of the chip-less RFID tag, the RCS feature is calculated and their combination is the identifier of the specific chip-less RFID tag. In order to achieve

high capacity and readability, the chipless RFID tags require to operate in Ultra Wide Band frequency (UWB) from 3.1 GHz to 10.6 GHz. More information regarding chipless RFID systems can be found in [9],[10],[11]. In Fig. 1.3 a typical chipless RFID tag is presented.

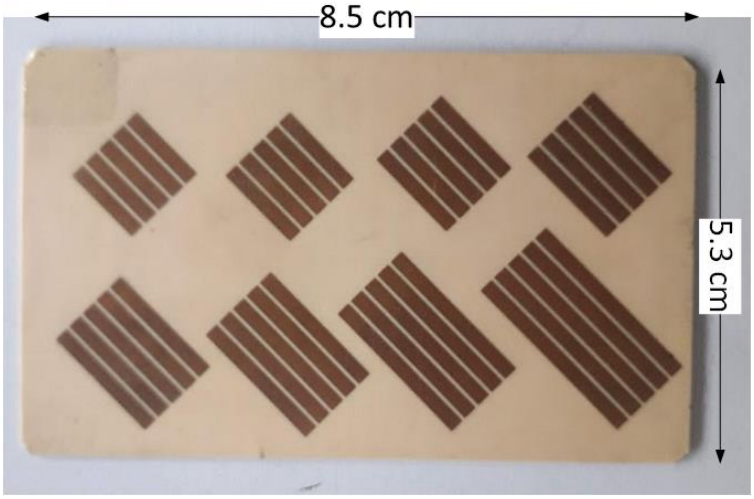

Figure 1.3: Typical chipless RFID tag [12]

In Table 1.1 is presented an overview of the RFID technology with information regarding near and far field RFID systems.

Table 1.1: Overview of RFID systems

Type	*Near Field*		*Far Field*
	LF	*HF*	*UHF/Microwave*
Frequency	*120-150 kHz*	*13.56 MHz*	*433 MHz, 860-960 MHz, 2.45-5.8 GHz*
Read Range	*∼few centimeters*	*<1m*	*<20m*
Protocols of communication	*ISO 14223/ 18000-2*	*ISO 14443/15693/ 18000-3*	*ISO 18000-6/ 18000-4*
Regulation	*Regulated power and frequency*	*ISM band*	*ISM band*
RFID tags	*Passive*	*Passive*	*Passive/Active*
Memory of tags	*Low*	*Up to 8 Kbytes*	*Up to 8 Kbytes*
Data rate	*Low*	*Moderate*	*High*
Common applications	*Animal identification*	*Access, payments*	*Identification, asset tracking*

1.2.2 UHF RFID technology

In this thesis, the focus is the UHF RFID case and specifically for RFID tags with passive operation. The main parts of a standard UHF RFID system are the RFID reader and the RFID tags. Such a system is presented in Fig. 1.4.

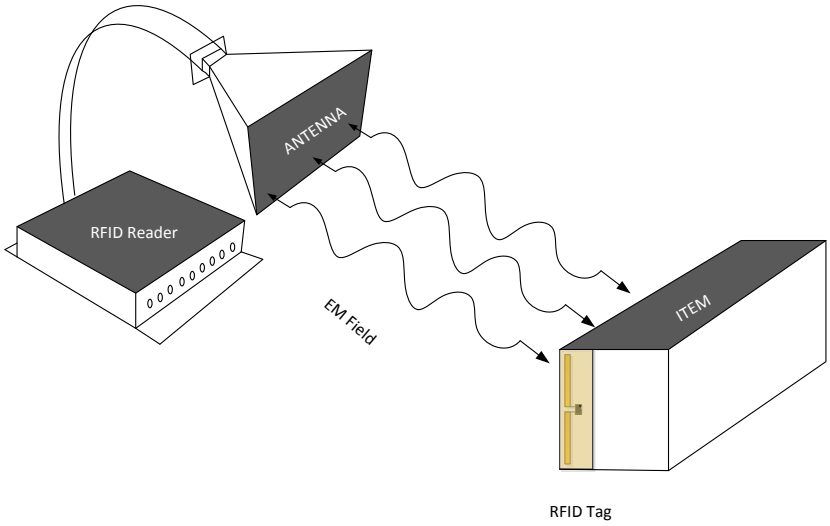

Figure 1.4: Standard UHF RFID system

The RFID reader is responsible for multiple operations. First of all, it contains all the appropriate software in order to store and correctly encode the transmitting baseband signal, according to specific protocols (e.g. ISO 18000-6). Secondary, it contains the RF front end where the baseband signal is up-converted to higher frequency according to the appropriate frequency band depending on the region of operation (e.g. Europe, North America). The difference for each geographical region is associated to the regulatory institution which supervises the operation of wireless communications (see Fig. 1.5). Besides the frequency, the transmitted power is also regulated, depending on the operating region, and it is limited either by the figure of the effective isotropic radiated power (EIRP) or the effective radiated power (ERP, EIRP=ERP+2.15 dBi). For instance, in Europe according to the European Telecommunication Standards Institute (ETSI) the limit is 2 W or 33dBm of ERP, while in North America, according to the Federal Communication Commission (FCC) the limit is 4 W or 36 dBm of EIRP.

The RFID reader is connected to an antenna which is the mean for transmitting the interrogating signal to the environment and eventually to the RFID tags. The antenna used can differ, according to the desired

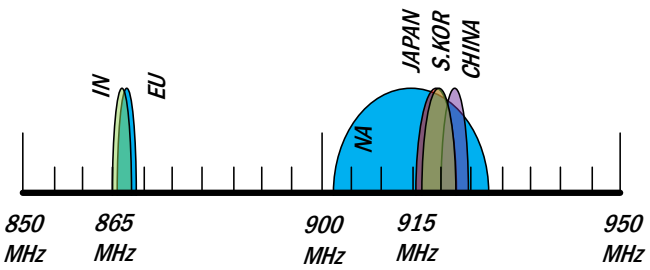

North America	902 to 928 MHz
Europe	865.6 to 867.6 MHz
China	920.5 to 924.5 MHz
Japan	916.7 to 923.5 MHz
S. Korea	917 to 923.5 MHz
India	865 to 867 MHz

Figure 1.5: RFID frequency bands over the globe

application, but the typical choice for the UHF RFID operation is a circular polarized antenna with 6 dBi of gain. This choice is usually made because the standard RFID readers have an output of around 30 dBm and by adding the gain of this antenna results to 36 dBm of EIRP which is the maximum allowed power, according to FCC. Also the choice of the circular polarization is made in order to avoid problems related to miss-polarization due to the fact that the RFID tags are usually linear polarized.

The RFID tags are the most unique part of the RFID system, since so far the RFID reader and the antenna are pretty much similar to other wireless communication systems. The RFID tags consist of two parts: the antenna and the application specific integrated circuit (ASIC) which will be referred from now on as the RFID chip. The main parts of the RFID chip include a digital processing unit, a non-volatile memory and an RF power harvesting circuit. In the memory of the RFID chip appropriate information regarding the protocol of operation are stored, while the digital processing unit among others, is responsible for different functions such as the switching the input impedance of the RFID chip between two impedance states. The energy harvesting circuit is responsible for powering up the RFID chip using the ambient electromagnetic energy transmitted from the RFID reader. Without the existence of an RFID reader, the RFID tags cannot be powered up and they do not operate. In order for this power to be maximized, it is important for the used antenna to operate as efficient as possible, meaning that the RFID chip and the antenna of the RFID tag should be carefully conjugated matched in as wide frequency band as possible. By this condition the RFID tag can more easily power on its circuitry and operate. When powered, the RFID chip is switching

between the two aforementioned impedance states, resulting to switching the RCS of the RFID tag between two different values. This operation is leading in the modulation of the backscatter signal, enabling the exchange of the information sent by the RFID chip according to the chosen protocol of communication. This function that the RFID tag performs is known as backscatter modulation. The antenna of the RFID tag can be chosen from a variety of different designs, based on the intended application, but the typical selection is usually a meandered, for size reduction, dipole (see Fig. 1.2).

1.2.3 Internet of Things (IoT) and RFID

The concept of Internet-of-Things (IoT) is getting into everyone's life more and more as the time progresses. A universal network, interconnecting multiple devices and integrating multiple functionalities will be the backbone towards the realization of various "smart" environments (smart cities, smart houses, smart agriculture, smart industries). With the IoT concept, the users will have access and will be able to monitor and control many devices remotely through their smart phones, tablets or laptops. Many domains, such as health care, smart grids, environment monitoring, traffic control, etc. can take advantage of the IoT, enabling a vast amount of information to be distributed and shared among the end users. The IoT has the potential to become a key service for automating small, daily tasks such as controlling the heating system in a smart house but also automating more complex functions such as controlling smart cars in highways. In addition, the IoT can have a great impact on industrial environments by better monitoring and controlling the production process. This could eventually result in a higher productivity, less industrial accidents and a more effective usage of energy [13]. Furthermore, the IoT concept becomes even more appealing when it is connected with the upcoming 5G technology [14]. The parameters of 5G cellular networks are expected to be flexible and able to target specific applications and services with IoT being one of the top priorities [15]. Considering this flexibility of 5G technology it will be very advantageous for the implementation of Wireless Sensor Networks (WSN) which are the backbone of the physical layer of IoT.

In order to realize such WSN's effectively, several attributes are very substantial. The IoT WSN's should be robust and reliable, especially when sensitive and impactful processes should be controlled and monitored (for instance in healthcare or industry); secure and resilient to malicious interactions; sustain their functionality with low power requirements; offer good accuracy; and present a low cost in order to be easily adopted. All these attributes have created the need of cheap, easy deployed sensors and actuators, which are capable of operating autonomous with very low energy consumption. These, so needed sensors, will be able

to transmit the sensed information from the environment, as well as, interact with it. A very good candidate for realizing the sensing functionalities for such an ambitious plan is the RFID technology [16]. The RFID technology is a well-established identification technology which has become popular during the past two decades and is still expanding. It offers reliable wireless identification solutions for many applications. This is also indicated by the current trend of the RFID market which is expected to grow in revenues in the near future (see Fig. 1.6 and [17]).

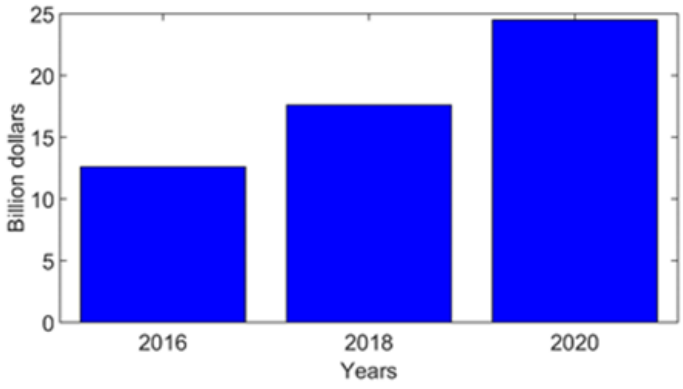

Figure 1.6: Increase and projected revenues of the RFID market

Due to the mass production printing techniques and the advances in fabrication of Integrated Circuits (ICs) the cost of an RFID tag can be very low, less than 0.10 for passive tags intended for general use [18]. However, there are also RFID tags with more capabilities and complexity that can cost more than 100. These tags are usually active tags with very long read range (more than 100 m) and more than just identification capabilities [19]. The RFID tags can work without energy source, in a passive mode, acquiring theoretically lifelong autonomous operation.

The advances in IC technology in the last decade allowed the development of very sensitive RFID chips, which offer a very sufficient read range that enables several new applications and can lead the implementation of the last few meters of the IoT. Table 1.2 presents the evolution of passive UHF RFID chip sensitivity and its impact on the read range. Moreover, recent advances in RFID chips enabled them to be designed for sensing a variety of physical parameters, such as temperature, pressure, acceleration, humidity, light, inclination, strain and location to name a few, with adjustable characteristics, such as sensitivity, read range and accuracy.

Table 1.2: UHF RFID chip sensitivity and read range for ETSI regulation during the past 20 years

Year	**Sensitivity (dBm)**	**Read Range (m)**
1997	*-8*	*5.07*
1999	*-10*	*6.38*
2005	*-12*	*8.03*
2007	*-13*	*9.01*
2008	*-15*	*11.34*
2010	*-18*	*16.02*
2011	*-20*	*20.16*
2014	*-22*	*25.38*

Note: Estimated theoretical read range considering operating frequency $868\ MHz$, reader power $2W$ ERP, reader antenna with gain 2 dBi, tag antenna ideal dipole and perfect match between RFID chip-tag antenna

Furthermore, the RFID technology, especially when operating in the Ultra-High Frequency (UHF) band is very promising. It offers connectivity to a widely used frequency band (860-960 MHz) according to the local regulations (mainly the European Telecommunication Standards Institute (ETSI) or the Federal Communication Commission (FCC)) with well-defined protocols of operation (ISO, EPCglobal), achieving reading ranges in some cases up to 20 meters for passive tags. Moreover, the RFID has a unique characteristic in comparison with other technologies used for establishing WSN: The RFID sensor is actually a "fusion" between a communication protocol and a sensor, while in the other technologies there is an actual sensor connected to a communication module, in order to transmit the information. Also the RFID technology allows WSN to consist of vast number of sensors due to the 32-bit EPC code used for identification, whereas in other technologies this number is considerably lower. Because of this particularity of RFID technology, any new features should be capable to be implemented in the communication protocol. In addition, the RFID technology is mainly operating passively lowering substantially the cost of the devices, prolonging their lifetime, while reducing the carbon footprint [20]. All these aspects are presenting a clear view of why during the last years much effort has been given in designing and developing efficient UHF RFID sensors for a wide range of applications. Several classification attempts have been made in the past regarding the integration of RFID sensor systems in WSN [21]-[22]. Also proposals about RFID sensor classification, either in terms of "transducer" type RFID tags have proposed in [23] and [24] or in more general context concerning RFID tags including circuits and chips with processing capabilities have been proposed in [25]-[26] and [27]. In [28] there is a classification between analog and digital sensor and in [29] is presented an

RFID classification specialized in food industry.

1.3 RFID communication chain

In Fig. 1.7, a general and synthetic diagram describes every block of the UHF RFID sensor communication chain (integrating identification and sensing functionalities) with ultimate goal of underlining the properties of each block. This diagram serves also as a summary of all the met cases and highlights the different links in each step of radio communication, including the transmission of sensing data and identification (ID). The communication chain between RFID sensor tag and RFID reader is presented in six levels: the RFID sensor tag, the RFID data capture level, the RFID tag process level, the RFID communication channel, the RFID reader process level and the RFID reader.

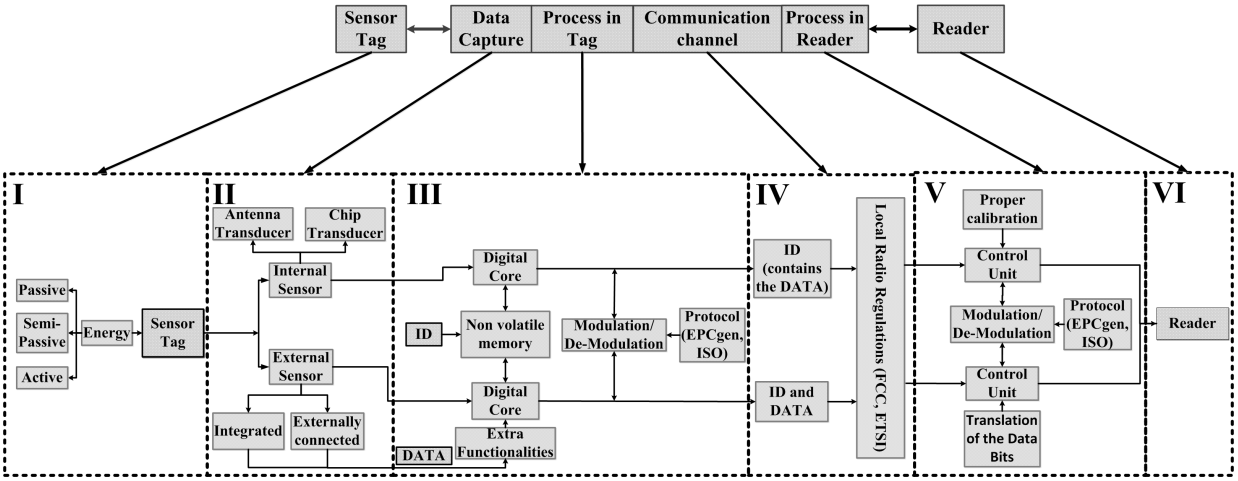

Figure 1.7: Description of the classification format. Each Latin number represents a part of communication between the RFID reader and the RFID sensor tag

1.3.1 RFID sensor tag

The RFID sensor tag exceeds the usual RFID tag functionality by offering sensing capabilities on top of the identification functionality. This is why these types of RFID tags are also known as augmented RFID sensor tags [30]. One important parameter that must be taken into account is the energy requirements of the RFID sensor tag, Fig. 1.7 level I. The optimum design should be capable to sustain its functionality without any additional external power source (passive mode), using only the rectifying capabilities of the RFID chip. However, in many situations this is not feasible, thus the RFID tag should have a complementary external power source (semi-passive mode) or it is powered exclusively by an external power source (active

mode). For instance, in many cases additional power source is required either to power up sensors or an extra micro-controller, while the communication with the reader is supported by the rectified RF power. In any case the energy requirement is an application oriented characteristic and it is dependent on the operating environment and the desired read range.

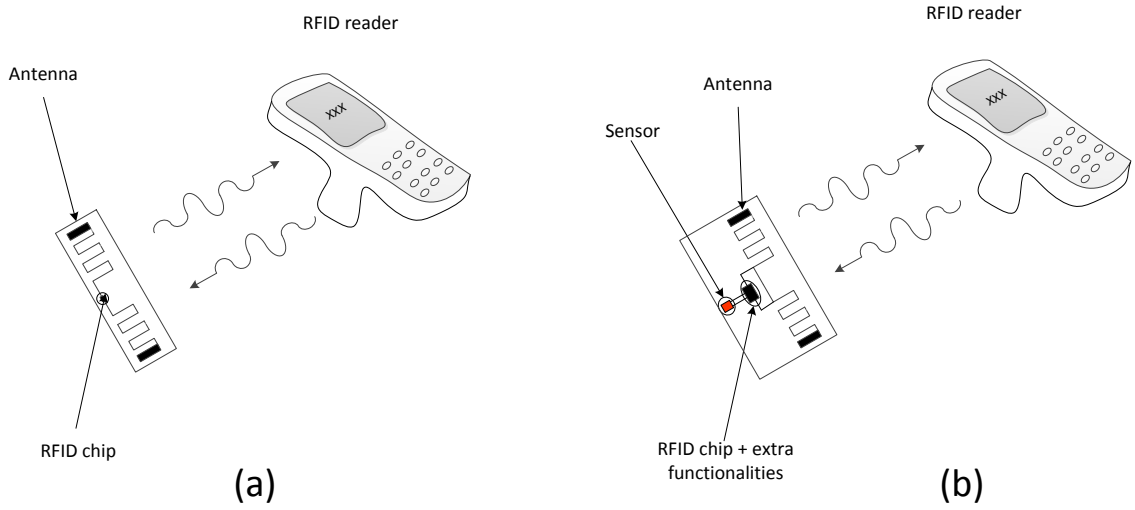

Figure 1.8: Example of the internal/external RFID sensor concept

1.3.2 RFID data capture level

Initially, the state of the sensor must be clarified in terms of how the sensing procedure is being performed at the sensor tag. The desired physical parameter can be sensed either using an internal sensor (Fig. 1.8a.) or an external sensor (Fig. 1.8b.). The concept of internal sensor refers to designs using partially or even the whole RFID tag structure to perform the physical parameter detection. The associated technique consists of either frequency shifts due to the effective permittivity changes or the polarization conditions (i.e., where the antenna is used as a transducer) or matching condition alterations due to changes to the input impedance of the chip (i.e., where the chip is used as a transducer). Sensor tags without a chip (so called chipless RFID tags) can also be classified in this category. These sensing capabilities can be detected in the reader as backscattered signal alterations: power variations, shifts of frequency or phase variations. On the other hand, external sensor is referred to RFID sensor tags that use sensors to enhance the sensing mechanism. These sensors are connected to the RFID chip either with an external port through a microcontroller or they are integrated within. There is a variety of sensors that can be used in such cases depending on the application.

Usually the types of sensors used in these cases are resistive, capacitive or even voltage sources. Besides the characteristics of each sensor type, regarding the RFID communication chain, there are some more considerations that should be taken into account. The number of sensors that each type of RFID sensor tag can accommodate is one interesting parameter. For instance, for the internal type sensor, the simultaneous measurement of different physical parameters is a challenge, since the behavior of different parameters is very difficult to be separated and recognized. On the other hand, for the external type sensor RFID tag, the existence of external ports can allow the simultaneous usage of sensors for different physical parameters. The limitation of the number of sensors for the external type sensor tag is due to the energy requirements since each sensor consumes more power in order to be operational. In addition, the range, resolution and accuracy of the measured parameter is an important factor, where the internal type sensor tag usually relies heavily on the capability of the RFID reader to detect the corresponding changes, while in the external type sensor these attributes depend on the used sensor and the resolution of the Analog to Digital Converter (ADC) used for the measurement. A graphical representation of this level can be seen in the Fig. 1.7 level II.

1.3.3 RFID tag process level

The processing capability of the ICs used in RFID sensor tags is a very important feature for their overall operation. The ICs used in RFID sensor tags can be divided into two categories: common off-the-shelf ICs with their functionality limited to identification and ICs with upgraded functionalities including microprocessors, ADCs, serial peripheral interface (SPI) ports or Inter-Integrated Circuit I2C) ports for more processing capabilities and extra functionalities. Currently there are a series of RFID IC's with these kinds of capabilities from different manufacturers and with different specifications as presented in Table 1.3. This separation is related to the internal/external sensor concept. Internal type sensor tags can be realized with any types of ICs. On the other hand, in order to realize a sensor tag with an external type sensor, the usage of an IC or a circuitry with additional processing capabilities either with an integrated sensor or external ports which can accommodate various sensors is mandatory. However, the RFID chips with additional capabilities usually have a low sensitivity which reflects to limited read range, while the off-the-shelf RFID chips have higher sensitivity and thus superior read ranges.

For the internal type sensor tag, the physical parameter can be evaluated when the RFID reader receives the interrogation response and according to the received power level or frequency or phase, the state of the

Table 1.3: RFID ICs with extra functionalities

Functionality	**RFID ICs**						
	SL 900A [31]	*Rocky 100* [32]	*Andy 100* [33]	*RFM 405 Xerxes-I* [34]	*Magnus S-3* [35]	*EM 4325* [36]	*Monza X-8K* [37]
Power-on sensitivity in passive mode (dBm)	*-6.9*	*-13*	*-2*	*-18.6*	*-16.6*	*-8.3*	*-21.6 (dual-antennas)*
Analog to digital converter	*Yes*	*No*	*No*	*Yes*	*No*	*No*	*No*
SPI or I^2C	*SPI*	*SPI*	*SPI*	*-*	*-*	*SPI*	*I^2C*
Integrated temperature sensor	*Yes*	*No*	*No*	*Yes*	*Yes*	*Yes*	*No*
Temperature accuracy	*$\pm 1\ ^\circ C$*	*-*	*-*	*$\pm 0.5^\circ C$*	*$\pm 1^\circ C$*	*$\pm 0.5^\circ C$*	*-*
Temperature range	*-40 to 125°C*	*-*	*-*	*-40 to 85°C*	*-40 to 85°C*	*-40 to 64°C*	*-*

physical parameter can be determined according to preliminary calibration curves. In this case the RFID sensor tag transmits the unique ID code which is stored in the non-volatile memory of chip and the useful information is acquired by the reader prior to decoding process of the received signal. For the external type sensor tag, a portion of the generated data from the sensor is digitalized and processed in the tag (since the RFID tag in this case has extra functionalities) and embedded in the binary signal transmitted to the reader. A great example for the case of the external type RFID sensor tag can be seen in [38]. In this case the information about the physical parameter is acquired after the decoding process of the received signal. The graphical representation of these processes can be seen in Fig. 1.7 level III.

1.3.4 RFID communication channel

The concept of internal/external sensor is closely related to the communication channel (Fig. 1.7 level IV) and to its role at the sensing procedure. In the case of internal sensor concept, the communication channel is being altered in connection to the sensed physical parameter. These alterations include the back-scattered signal power level, the center frequency and the phase. In this way, the variations of physical parameters are linked to measurable quantities in the reader by calibration curves which correspond to the status of the sensor to the measured physical parameter. Moreover, the most advanced off-the-shelf RFID chips include ”auto-tuning” capabilities. In this case the RFID chips are capable of changing their input

impedance according to environmental de-tuning effects. These changes can then be detected by the RFID reader by simply acquiring the value of the ”auto-tune” parameter from the memory bank of the chip. If these changes can be related to certain effects linked to a physical parameter, then the RFID tag can work as an internal type sensor communicating digitally [39].

In the case of the external sensor concept, the communication channel for an RFID tag sensor in a fixed position is independent from the status of the physical parameter measured. The sensing information is being processed in the RFID chip and it is enhanced in the bit stream received by the reader. The signal contains all the information about the status of the sensor in binary form acquired by the reader after the decoding process of the received signal.

Another consideration is the read range for each type of RFID sensor, especially in a passive mode case. The internal type sensor depends on phase/frequency shift and impedance mismatches to transmit information. This fact has an immediate impact on the read range, due to the condition of maximum power transfer to the RFID IC, since the perfect match condition cannot be maintained continuously in most of the cases. This issue is discussed in [40] where a different approach is suggested. For the external type RFID sensor, an initial clarification to the meaning of read range should be made. When the desired information is included in the binary stream a separation between the “power on” and “read” range should be included. The fact that the RFID tag can be identified by the reader and there is a received power indication does not ensure that the sensor tag can transmit the necessary power so that the bit steam with the information of the sensor to be read. Thus, in this case the “read” range corresponds to the actual read range.

From this prospective there can also be a distinction of internal/external sensor to a distinction between analog/digital information transmissions over the communication link.

1.3.5 RFID reader process level & RFID reader

In the RFID technology the main processing load is carried out by the RFID reader. A typical RFID reader architecture can be seen in Fig. 1.9. The main parts of a typical RFID reader are the high frequency (HF) interface and the control unit, responsible for the radio communication and the data processing respectively [3]. The reader according to the RFID sensor tag should have different attributes. In the case of the internal sensor type tags, the reader should be first calibrated with appropriate curves in order to translate correctly the backscattered power, frequency shift or phase alterations received, to match them to the correct physical parameter status. In this part it is very important to take into consideration the regulations, since for ETSI

the available bandwidth is 2 MHz and for the FCC is 26 MHz. Furthermore, if the polarization of the signal is used as an indicator parameter, the reader's antenna should be carefully selected to match the criteria.

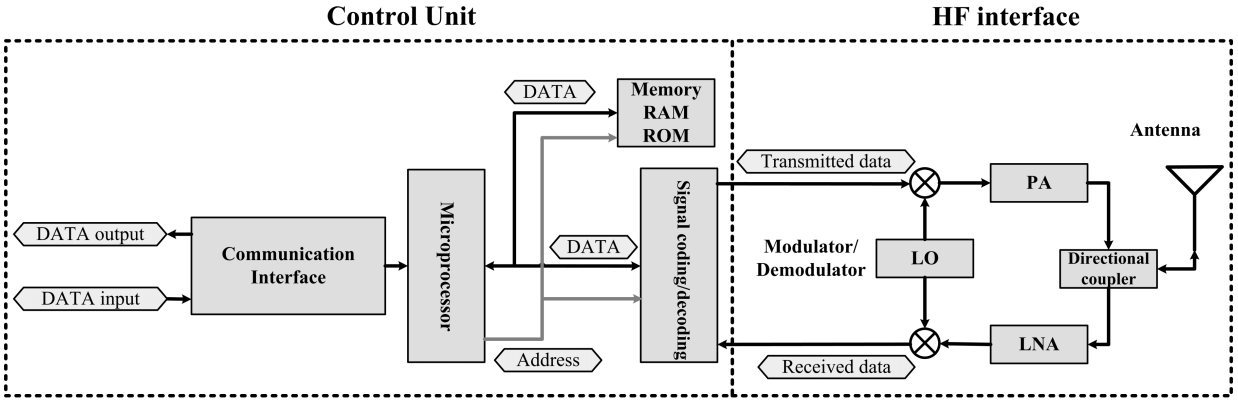

Figure 1.9: Typical RFID reader architecture

In the case of external type sensors, since the communication channel, for a fixed position RFID tag sensor, remains relatively stable, the reader has to be programmed to match the binary code, which is included to the received bit stream, to the appropriate physical parameter magnitude. In the case of external sensor type the antenna polarization is not as significant factor as in the case of internal type sensor. The RFID reader and RFID reader process block corresponds to Fig. 1.7 level V and VI.

Furthermore, a very important attribute is the existence of the same protocol in both sensor types. For the RFID tag sensor to be identified by the majority of commercial readers, the existence of a communication protocol is crucial. In the literature, designs without the existence of protocol can be found, which mainly focus to the proof of a certain concept. On the other hand, since there are globally used predefined protocols like EPCglobal and ISO 18000-6, the majority of designs in the literature are compatible with either of these protocols.

Finally, another characteristic which applies to both categories is the local regulations of the RFID communication. The regulations used for the RFID communication, as it was already mentioned, can be distinguished mainly between the regulations in USA (FCC) and the regulations in Europe (ETSI). The main differences can be found at the frequency bands that are being used for each territory (865-868 MHz for ETSI band and 902-928 MHz for FCC band), at the transceiver technique (4 channel plan for ETSI and Frequency Hopping Spread Spectrum (FHSS) for FCC) as well as the maximum allowed transmitted power from the reader, using the effective isotropic radiated power (EIRP) indication (3.2 W for ETSI and 4 W for

FCC). Finally, it is worth noting that a new UHF spectrum, in addition to the 865-868 MHz band, is planned to be available in Europe (around 917 MHz) demonstrating the dynamic of UHF RFID evolution [41]. In Table 1.4 a summary of the attributes of each RFID sensor type are presented.

Table 1.4: Summary of RFID sensor types

Types of sensors		
Level	*Internal*	*External*
Data capture	*Via tag structure*	*Via dedicated sensors*
Tag processes	*Basic RFID functionalities*	*Advanced functionalities*
Communication channel	*Varying/stable*	*Stable*
Reader processes	*Predefined calibration/memory bank*	*Programmed with respective commands*

1.4 RFID sensor tags: Examples from literature and commercially available products

Significant examples of prototypes of UHF RFID sensors proposed in the literature are presented according to the sensed parameter(s) and described according to the general diagram proposed in Fig.1.7. In Table 1.5 the literature examples, as well as some commercially available UHF RFID sensors are summarized, highlighting their characteristics according to the introduced classification. Finally based on RFID temperature sensing which is one of the most researched areas regarding RFID sensors (e.g. [42], [43] and [44]), an example of illustrative comparison is made for sensors of both types aiming to underline the performance in terms of read range, accuracy, resolution and temperature range.

1. **Orientation sensing**: In [45] the orientation of an object is determined by the usage of two passive UHF RFID tags attached on an object. These two tags have a known angle difference between them. The communication channel is varying according to the orientation and the status of the orientation parameter is calculated by a statistical estimator based on the Received Signal Strength (RSS) variation, which is being caused by the polarization angle between the tags and the antenna of the reader. This is an example of an RFID tag with an internal type sensor, since the sensing data capture is due

to antenna's characteristics. The chip used in this case is an off-the-self chip (ALN-9740) with basic identification capabilities.

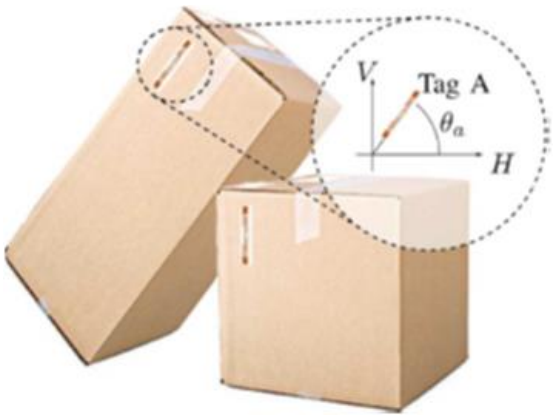

Figure 1.10: Orientation sensing with RFID tags [45]

2. **Motion and temperature sensing**: In [46] (see Fig. 1.11), a both motion and temperature semi-passive UHF RFID sensor tag is presented. The communication channel in this case is independent of the physical parameters which are being sensed and an appropriate programmed reader is needed to evaluate the status of these parameters. According to the inclination of the object towards the earth's magnetic field, the sensor can monitor and log the motion of the object and at the same time it can monitor the temperature of the object as well.

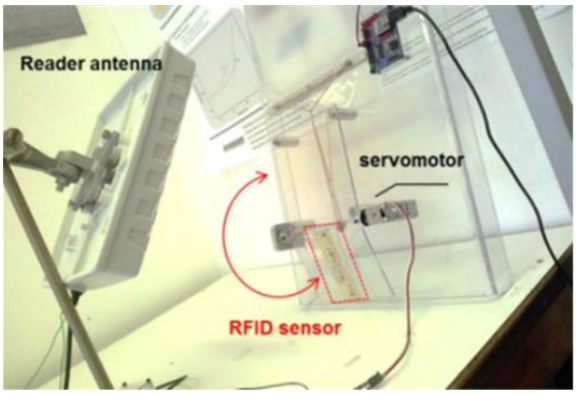

Figure 1.11: Motion and temperature sensing RFID sensor tag [46]

This is an external type RFID sensor able to detect the motion and the temperature of an object, using a

chip with processing capabilities (AMS SL-900A), accommodating an integrated temperature sensor and an externally connected anisotropic magneto-resistive sensor.

3. **Temperature sensing**: In the example of [47], two temperature passive UHF RFID sensors are presented, one external type (example a) in Fig. 1.12 and one internal type (example b) in Fig. 1.13. For the external type sensor, an RFID chip (EM Microelectronic- EM 4325) with an integrated temperature sensor and extra functionalities is being used. The communication channel is independent of the physical parameter sensed and the reader must be programmed to make the temperature readout. In this case a double folded patch antenna is used. For the internal type RFID sensor, a meander dipole antenna is used with a thermistor connected in parallel to the chip. According to the ambient temperature the resistance of thermistor changes which affects the reflecting impedance of the RFID chip. The chip used is an off-the-shelf chip (Impinj Monza-R6), the communication channel is varying according to the physical parameter and a reader will be able to make the measurement of the temperature using calibration curves.

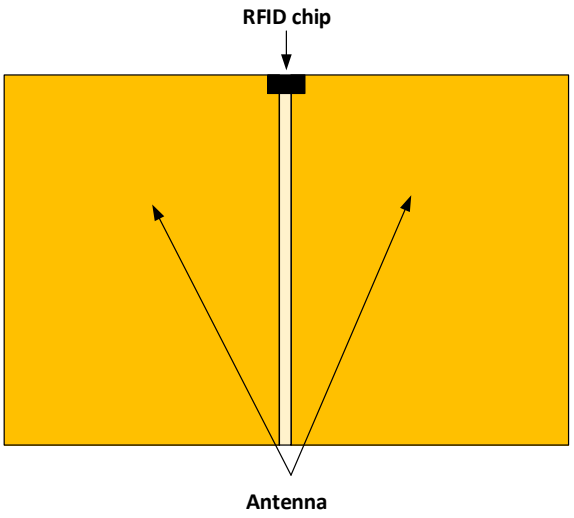

Figure 1.12: RFID temperature sensor (a) (external type)

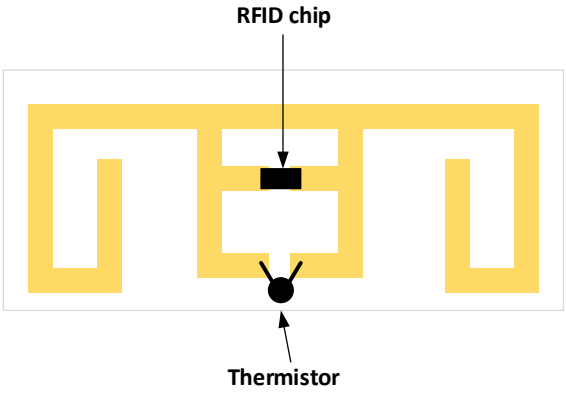

Figure 1.13: RFID temperature sensor (b) (internal type)

4. **Pressure sensing**: In the example of Fig. 1.14, [25] a passive RFID external sensor is presented. The pressure sensor is externally connected to the RFID tag and a chip with processing capabilities is used (AMS SL900A), connected with a micro controller in SPI mode. The communication channel is independent from the physical parameter and the reader must be programmed in order to have the readout of the pressure. A dipole antenna is used in this case.

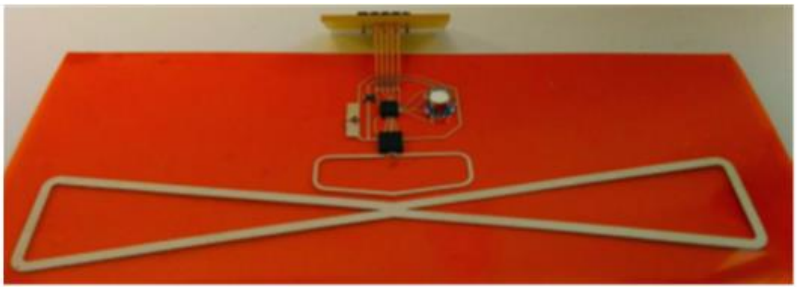

Figure 1.14: Pressure sensing RFID sensor[25]

5. **Gas sensing**: In the example of Fig. 1.15, [48], a passive internal RFID sensor for gas sensing (ammonia), is designed utilizing carbon nanotubes (CNT). The CNT drop is connected with a meander dipole antenna. The existence of ammonia in the vicinity of the CNT is causing an impedance change and this change affects the back-scattered power. This is an example of internal RFID sensor. Even though this example is chip-less it can be classified as an internal type passive RFID sensor with the sensing mechanism operating due to matching alterations caused by the physical parameter sensed.

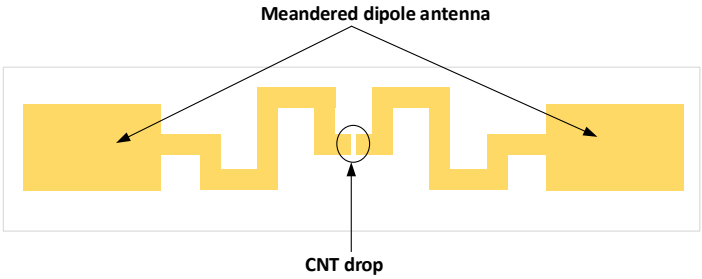

Figure 1.15: Chipless gas sensor

The communication channel changes according to the physical parameter and a reader with calibration curves should be used in order to measure the quantity of ammonia.

6. **Light sensing**: In the example of Fig. 1.16 [25], an external type passive UHF RFID light sensor is being realized using a chip with processing capabilities (AMS-SL900A). The communication channel is independent of the physical parameter variations and the reader must be programmed to translate the data bits. Since this chip includes an integrated temperature sensor, it is capable of sensing temperature and luminosity at the same time.

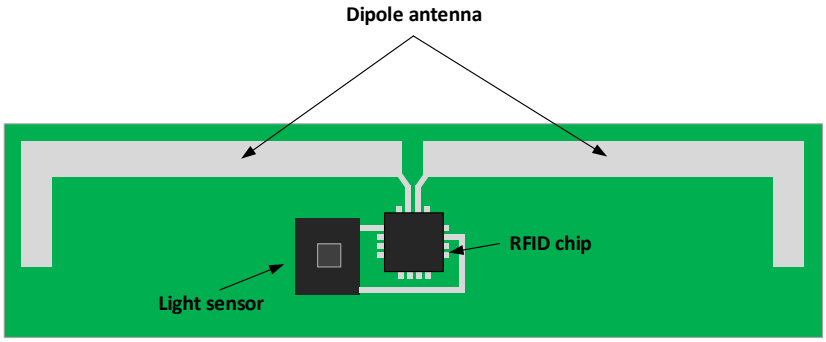

Figure 1.16: Light sensing RFID sensor tag

7. **Threshold temperature sensing**: The internal type RFID sensors can be also used as threshold sensors. In the example of Fig. 1.17, [49] a passive UHF RFID sensor with an internal type temperature sensor, realized on appropriate paraffin substrate, can sense the temperature rise over a certain threshold. An off-the-shelf chip is used (Alien Higgs 2) and the communication channel is varying along with the temperature. From the reader's part calibration curves should exist. When the temperature exceeds a certain threshold the RFID sensor changes its proprieties permanently.

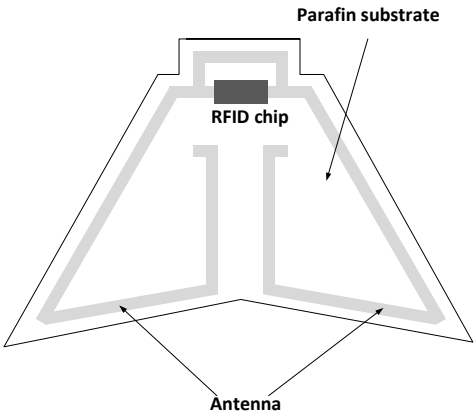

Figure 1.17: Threshold temperature RFID sensor tag

8. **Meat quality sensing**: Another method of sensing is to exploit the permittivity variations of the substrate. It is well known that foods, like meat, contain a large percentage of water (more than 60%) that will decrease over time due to the evaporation process. Exploiting this feature can be used to measure the freshness of meat. This process has been exploited in [50] to design an RFID sensor of meat quality that provides back-scattered signal linked to the freshness of the meat. The communication channel is varying in this case and a reader with predefined curves should be used in order to evaluate the condition of the meat.

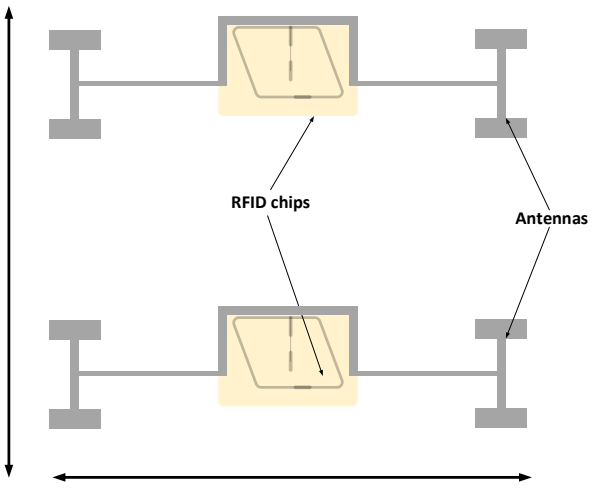

Figure 1.18: Meat quality sensing RFID tags

9. **Commercial temperature sensing**: A commercially available UHF RFID sensor in the RFM3240 of RF Micron [51] is presented in Fig. 1.19. It is a passive temperature sensor dedicated for on-metal applications with a temperature range from -40 °C to +85°C. This sensor utilizes the Magnus S3 RFID chip which has the ability to change its internal impedance to de-tuning effects. It can be classified to internal sensors but in this case the communication channel is not varying since the information is in digital form. Based on the value of the variable input impedance of the chip this sensor can be calibrated to transmit information about the temperature which is a detuning factor. The accuracy of this sensor is less than $\pm$ 2 °C.

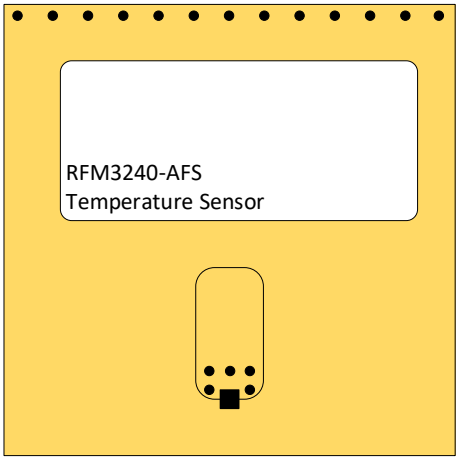

Figure 1.19: Temperature sensor from RFMicron

10. **Commercial pressure and temperature sensing**: Another commercially available UHF RFID sensor is the CYCLON-14BA from the company Farsens [52], Fig. 1.20. This is a passive pressure and temperature sensor utilizing a circuit with an ANDY100 RFID chip, a microcontroller, a pressure and a temperature sensor. It has a pressure range from 0 to 14 bars with an accuracy of $\pm$ 140 mbar and resolution of 14 mbar. The temperature range is from -30 °C to +85 °C, with an accuracy of $\pm$ 1 °C and resolution 0.1 °C. This is an external type RFID sensor.

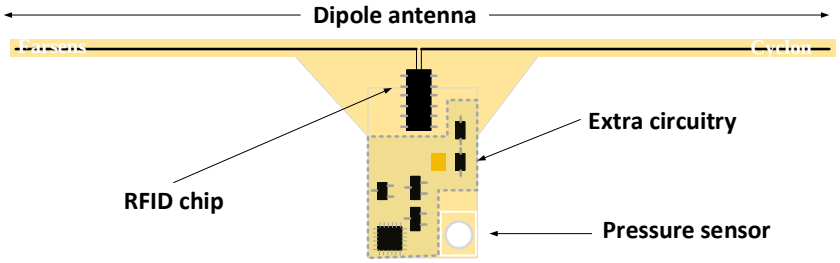

Figure 1.20: Temperature and pressure sensing RFID tag from Farsens

Table 1.5: Comparison of Examples from Literature

Example	1	2	3*a*	3*b*	4	5	6	7	8	9	10
Energy (Level I)	*Passive*	*Semi-passive*	*Passive*	*Passive*	*Semi-passive*	*Passive*	*Passive*	*Passive*	*Passive*	*Passive*	*Passive*
Physical parameter	*Orientation*	*Motion temperature*	*Temperature*	*Temperature*	*Pressure*	*Gas*	*Light & temperature*	*Temperature*	*Permittivity of meat*	*Temperature*	*Temperature & pressure*
Number of sensors	*1*	*2*	*1*	*1*	*1*	*1*	*2*	*1*	*1*	*1*	*2*
Data capture (level II)	*Internal via antenna*	*External*	*External*	*Internal via chip*	*External*	*Internal via chip*	*External*	*Internal via chip*	*Internal via antenna*	*Internal via antenna*	*External*
Tag Process (level III)	*ALN 9640*	*SL-900A*	*EM-4325*	*Monza R6*	*SL-900A*	*Chip-less*	*SL-900A*	*Alien-H2*	*AK3-Tagsys*	*Magnus-S3*	*ANDY-100*
Chip Sensitivity (passive mode)	*-20 dBm*	*-6.9 dBm*	*-8.3 dBm*	*-21 dBm*	*-6.9 dBm*	*-*	*-6.9 dBm*	*-14 dBm*	*-15 dBm*	*-16.6 dBm*	*-2 dBm*
Communication channel (level IV)	*Varying*	*Stable*	*Stable*	*Varying*	*Stable*	*Varying*	*Stable*	*Varying*	*Varying*	*Stable*	*Stable*
Reader process (level V)	*Calibration curves*	*Programmed*	*Programmed*	*Calibration curves*	*Programmed*	*Calibration curves*	*Programmed*	*Calibration curves*	*Calibration curves*	*Through memory bank*	*Programmed*
Maximum read range	*2 m*	*7 m*	*1.5 m*	*1.3 m*	*1.5 m*	*-*	*1.6 m*	*7 m*	*1.4 m*	*19 m*	*1.5 m*
Protocol	*EPC Gen2/ISO*	*EPC Gen 2*	*EPC Gen2/ISO*	*EPC Gen2/ISO*	*EPC Gen 2*	*No Protocol*	*EPC Gen 2*	*EPC Gen2/ISO*	*EPC Gen2*	*EPC Gen2/ISO*	*EPC Gen2*
Regulations	*ETSI/FCC*	*ETSI/FCC*	*ETSI/FCC*	*ETSI/FCC*	*ETSI/FCC*	*ETSI*	*ETSI/FCC*	*ETSI/FCC*	$ETSI$	*ETSI/FCC*	*ETSI/FCC*
Dimensions (mm^3)	–	$102 \times 22 \times NaN$	$52 \times 74 \times 3$	$80 \times 34 \times NaN$	$135.7 \times 22.2 \times 2$	$120 \times 30 \times 0.2$	$79 \times 5.5 \times 1.5$	$44 \times 30 \times 1$	$63 \times 67 \times 0.2$	$50 \times 52.5 \times 3.55$	$76 \times 34 \times 4$

1.5 Comparison of different types of RFID temperature sensors

In this part some of the RFID sensor tags capable to measure the temperature are selected from Table 1.5. Based on the previous discussion, the type of RFID sensor tag (internal/external) is expected to have an important role to the performance of the temperature RFID sensor tag.

In the case of the internal RFID temperature sensor tag type, the sensing mechanism is realized through

the variation of the reflection impedance and thus, the read range is expected to be affected due to miss match between antenna and RFID IC. The other attributes, such as resolution, accuracy and temperature range are mostly results from the designing process, the interacting method with temperature and the calibration curves used in the reader to quantify the measured parameter.

In the case of the external RFID temperature sensor tag, the actual sensor used for the measurement of the temperature presents a specific resolution, accuracy and temperature range. When an integrated temperature sensor is used in a chip with processing capabilities the aforementioned attributes are fixed according to its initial characteristics. When the temperature sensor such as a thermistor or a thermocouple is interconnected externally through a microcontroller, the resolution, accuracy and temperature range are solely dependable on the sensor used. Finally, the fact that the communication channel is independent from the measured physical parameter makes the reading range dependent upon the chip sensitivity, the polarization miss match, the antenna design, the operating environment and the power of the RFID reader. In general, the comparison of the examples of RFID temperature sensor tags, can lead to remarks concerning in general the RFID sensor tags. In both types, internal and external, pros and cons can be observed, (see Table 1.6).

Table 1.6: Comparison of temperature sensing examples

Example # attributes	*# 3a*	*# 3b*	*# 4*
Sensor Type	*External*	*Internal*	*External*
RFID chip	*EM 4325*	*Monza R6*	*SL900A*
EIRP of RFID reader	*0.47 W*	*0.13 W*	*0.4 W*
RFID chip sensitivity	*-8 dBm*	*-22 dBm*	*-15 dBm (semi-passive)*
Read Range	*1.5 m*	*1.3 m*	*1.5 m*
Temperature resolution	$0.25°C$	$0.5°C$ *to* $3°C$	$0.15°C$
Temperature accuracy	$\pm 0.5°C$	$\pm 1°C$	$\pm 1°C$
Temperature range	-40 *to* $64°C$	28 *to* $200°C$	-40 *to* $125°C$

For the case of external type RFID temperature sensors, the usage of RFID ICs with low sensitivity results in limited read range and also the processing functions of the chip are adding a time delay which is important, especially when there are involved in real time sensing applications [53]. On the other hand the connectivity option of these chips with a variety of sensors using even the Serial Peripheral Interface (SPI) mode offers great advantages in terms of design flexibility, ease of realization and reliability in the communication.

For the case of internal type RFID sensor tags the usage of chips with high sensitivity, leads to higher read ranges even though the techniques used involve impedance miss-matching conditions which affect partially the performance of the sensor tag. The physical phenomena detected by such sensor tags can be seen to the reader faster, without additional delay due to processing functionalities at the side of the tag. The internal type RFID sensor lacks the ease of realization and usually requires high expertise in antenna design, since in every case the tags should be carefully designed and matched to the sensing structure or mechanism. Also effects in the communication channel can lead to ambiguous results. The fact that calibration curves should pre-exists makes these type of tag sensors highly customized according to the operating environment and application.

1.6 Conclusion

The main target of this chapter was to present the state of art in RFID sensing. Initially, a short introduction on the RFID technology has been attempted and hopefully it will be able to offer a basic understanding on the operation of the RFID systems in general.

In addition, the connection between the RFID sensing and the IoT is illustrated, pinpointing the important role of the RFID technology in the 4th industrial revolution which is upon us. Enabling smart cities, industries, agriculture is a step towards the future and the qualities that the RFID technology is offering in the field of sensing is something which is difficult to be denied.

Following up, the RFID sensing concepts have been introduced through a review and a comprehensive classification. The main differences in each part of the RFID communication chain have been highlighted while the different techniques of realizing RFID sensors are listed. From this part, someone can affiliate the different approaches for designing and realizing RFID sensors based on specific requirements. Different design approaches offer different advantages and disadvantages related to read range, quality of sensing, cost, processing requirements and ease of fabrication. Furthermore, a plethora of UHF RFID sensor designs

are discussed, explained and compared. This part holds a high interest as it can illustrate the potential of the RFID sensing technology which is quite versatile, since the sensing function can be implemented with different materials, transducers and communication style (i.e. phase shift, frequency shifts). Moreover, in this conclusion section it is quite important to mention and underline the unique features of the RFID technology as far as it concerns the formation of Wireless Sensing Networks (WSN). The RFID technology has the privilege to be à priori passive, a feature that other technologies are not designed for and this attribute has the potential to enable a vast amount of RFID sensor to be deployed in the environment of interest. This potential scenario of numerous RFID sensors in the same environment can be linked to another feature of the RFID technology: the EPC code used in the RFID tags is a 32-bit number which results to around 4 billion of unique EPCs. This feature results in a practical unlimited number of RFID sensing tags in a single node of a WSN. Finally, the well-established protocols and regulations which govern the RFID communication is another facilitating element towards the vision of the future WSNs. Concluding, the 5G and IOT implementation and the current and future research on RFID sensing worldwide is very likely to enable new and unprecedented applications. These milestones can be the breakthrough to move a step closer to the realization of the IoT of the future and all these reasons are making the RFID sensing technology without any doubt a cornerstone of WSN and IoT.

CHAPTER 2
ENVIRONMENT OF OPERATION

2.1 Introduction

A very important part of the thesis has been the efforts to study and understand the impact of the very unhospitable environment of the interior of a big scale generator and generally of the industrial environment. The interior of a generator has some, very specific properties, which can pose great limitations on the propagation of electromagnetic waves, while dramatically impacts the operation of the RFID tags, in particular at UHF bands.

The interior of a large scale generator is entirely made from different kind of metallic parts (iron, copper, steel, silicon steel). The presence of metal has a very detrimental effect on the antenna structures, as well as on the RFID communication due to multipath phenomena. Moreover, the impact of the high electric and magnetic field which are present in the interior of the generator has to be explored to fix any complication on the performance of either the RFID sensor-tags or of the RFID communication. The important and nonnegotiable feature is to be compliant with RF ad RFID regulations that impose the frequency band, the maximum power and communication protocol.

In addition, the fast rotation of the generator can contribute to these potential limitations and more specifically disturb the RFID communication. The overall system (RFID tags-RFID reader) is in a dynamic state in such a rotating scenario where their relative positions are quickly and periodically varying. This behavior can introduce small time windows were the RFID communication is possible, with limitations depending on the rotational speed and the delays due to the processing capabilities of the individual subsystems and the communication protocols.

In this chapter, the described points of interest are discussed and explored through a theoretical background study and through testing the RFID communication and the performance of the RFID sensor-tags in such conditions. Initially, the effects of metal on antennas in general are discussed and analyzed. Furthermore, the radiation properties of antennas in the interior of a large generator is studied by constructing numerical models of the generator and of the RFID antennas and simulating their co-existence in appropriate electromagnetic tools. An exploration on the time constrains of the RFID communication is following,

presented through theoretical and experimental results. The last part presents test and measurements in environments where high magnetic field is present.

2.2 Effects of metal on the antennas

In general, the presence of conductive materials in close proximity to an antenna, affects its performance and mainly its radiation pattern and impedance and therefore its effective efficiency.

2.2.1 Effects of metal on the radiation of antennas

In this section the effects of a conductive surface in close proximity to a dipole antenna will be examined, aiming to evaluate the impact on the radiation pattern. Initially the case where the dipole is positioned near to an infinite large conductive plane will be examined. The conductive plane will be considered to exhibit infinite conductivity, which is a good approximation of real cases where good conductors are used, such as copper or aluminum surfaces. Finally, the conductive plane will be considered as infinite with regard to the operating wavelength, which can be considered accurate when antennas with high enough frequencies are studied.

The radiation pattern and the effects of a metallic surface on a random antenna can be analyzed by the image theory [54]. The analysis of the effects on the radiation of a dipole antenna near a conductive surface with the image theory is mainly done by considering either the case of a horizontal or vertical dipole antenna over the conductive plane. The RFID antennas are usually positioned in parallel to a surface, since they need to maintain a low profile. Hence, an analysis of a horizontal dipole over a perfect electric conductive surface will be used to demonstrate the effects of the metallic surface on the farfield of the antenna.

Let's consider for simplification an infinite large electrically conductive surface with infinite conductivity $\sigma \rightarrow \infty$ (perfect electric conductor denoted as PEC hereinafter), as depicted in Fig. 2.1 and Fig. 2.2. The dipole is positioned in a distance h from the conductive surface and the generated reflections can be modeled with an imaginary dipole at a distance h below the surface.

The direct component of the electric field at the point P_1 will be (2.1):

$$E_{\psi}^{d} = j\eta \frac{kI_0 l e^{-jkr_2}}{4\pi r_1} sin\psi \tag{2.1}$$

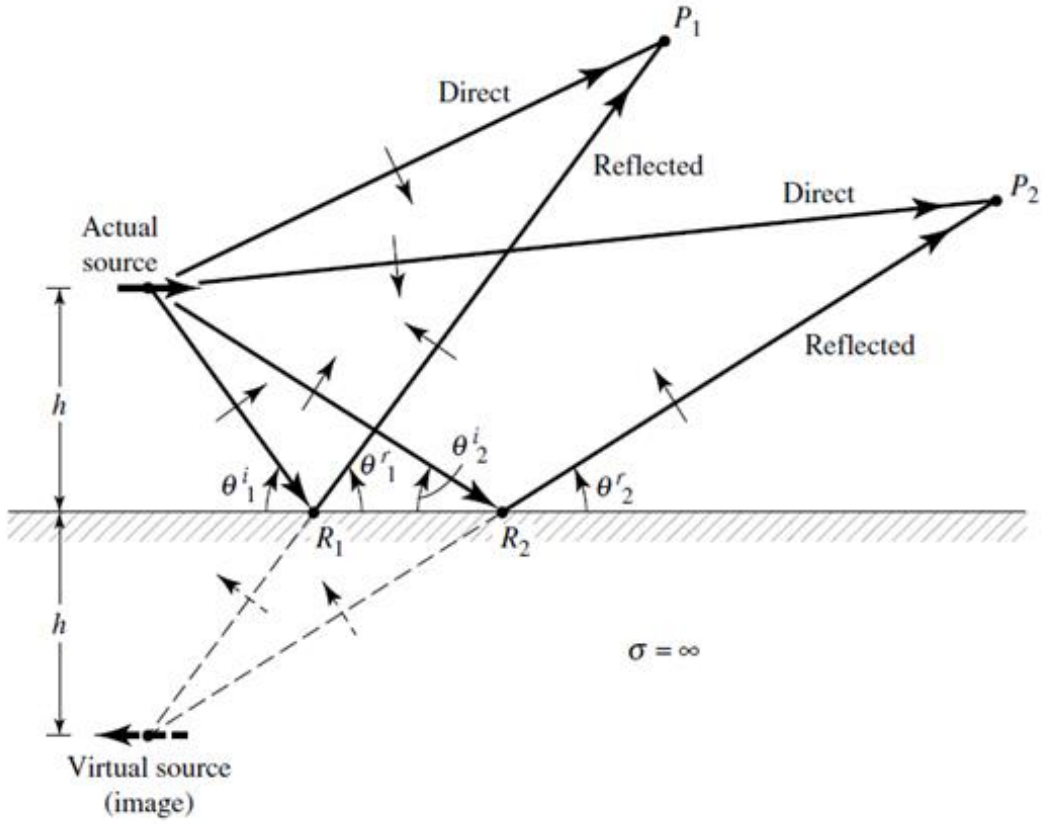

Figure 2.1: Example of horizontal dipole parallel to an infinite large PEC [54]

And the reflected component will be (2.2):

$$E^r_\psi = jR_h\eta\frac{kI_0le^{-jkr_2}}{4\pi r_2}sin\psi = -j\eta\frac{kI_0le^{-jkr_2}}{4\pi r_2}sin\psi \tag{2.2}$$

where η the intrinsic impedance of the medium, k the wavenumber, I_0 the magnitude of current at the feeding port of dipole, l the length of dipole in meters, r_1 and r_2 the distance in meters of P_1 from the source and source image respectively and $R_h = -1$ the reflection coefficient.

Where the $sin\psi$ will be (2.3):

$$sin\psi = \sqrt{1 - sin^2\theta sin^2\phi} \tag{2.3}$$

In addition, for the farfield where the distances r_1 and r_2 are much greater than h the following approx-

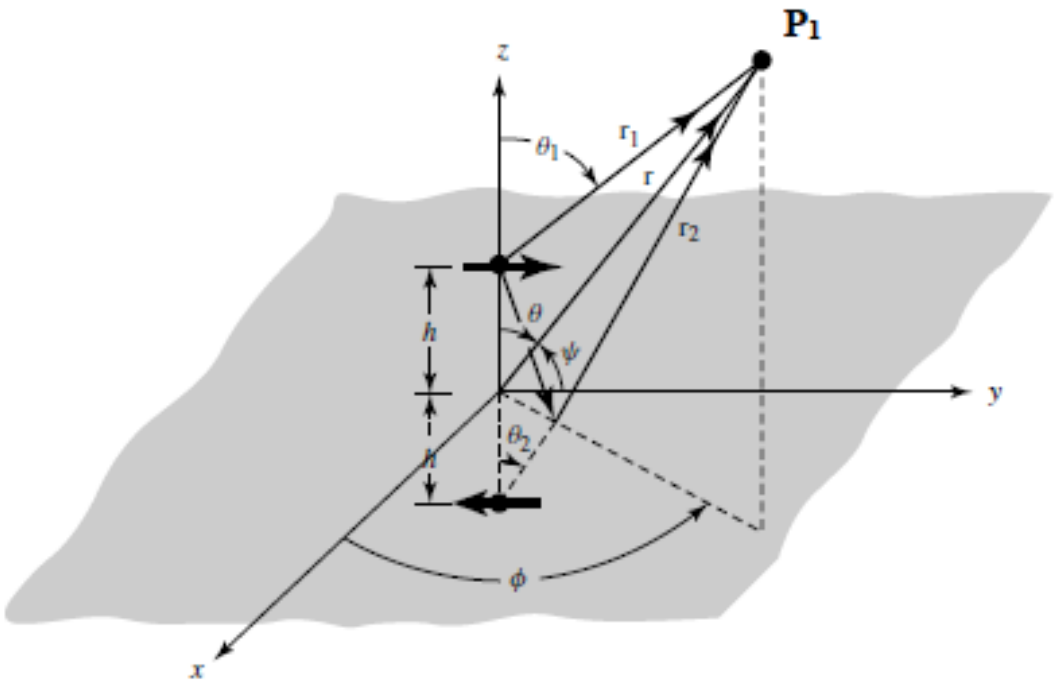

Figure 2.2: Far-field observation of the horizontal dipole [54]

imations are used(2.4),(2.5):

$$\text{for phase variations: } \begin{cases} r_1 & \approx r - hcos\theta \\ r_2 & = r + h\cos\theta \end{cases} \tag{2.4}$$

$$\text{and for amplitude variations : } r_1 \approx r_2 \approx r \tag{2.5}$$

Hence, the total electric field at the point P_1 will be:

$$E_\psi = E_\psi^d + E_\psi^r \Rightarrow E_\psi = j\eta\frac{kI_0le^{-jkr}}{4\pi r}\sqrt{1 - sin^2\theta sin^2\phi}[\,j\ 2sin(kh\ cos(\theta))] \tag{2.6}$$

The expression 2.6 will be valid only above the infinite large conductive surface, when the point of observation P_1 will satisfy the conditions of : $z \geq h, 0 \leq \theta \leq \frac{\pi}{2}$ and $0 \leq \phi \leq 2\pi$. Based on the behavior of the electric field at the farfield, the radiation pattern will be affected by the distance h and the angles θ and ϕ of the observation point.

2.2.2 Numerical model and representation of the radiation pattern

The impact of the conductive plane on the antenna which was described in the above section can be more intuitive if the results are demonstrated in a more straightforward way. For this reason, a simple numerical model of an ideal, center-fed dipole antenna in parallel with an infinite sized metallic plane was used in Matlab [55]. The dipole and the infinite large conductive plane were simulated for different distances ($\lambda/8, \lambda/4, \lambda/2, 3\lambda/4, \lambda$ and 2λ where λ the wavelength for frequency 900 MHz). In Fig. 2.3 the corresponding setup in graphic interface of Matlab is presented:

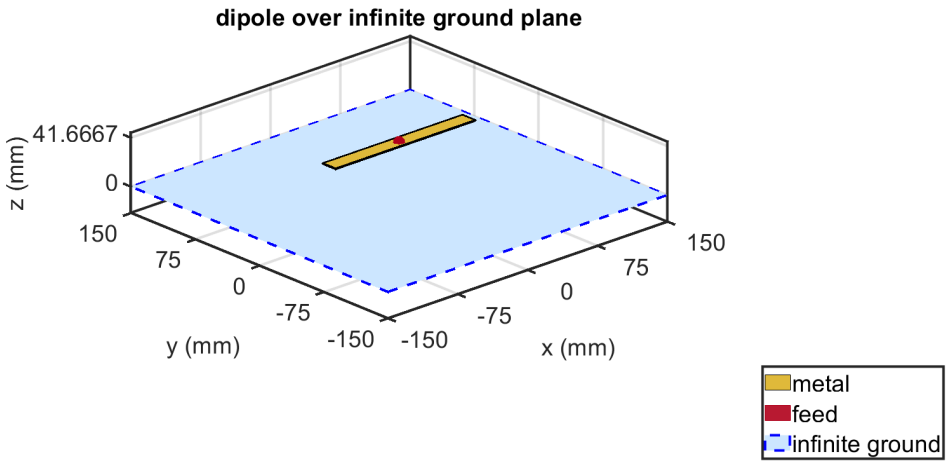

Figure 2.3: Model of horizontal dipole close to infinite large PEC

The corresponding radiation pattern of the dipole for variable distance h is depicted in Fig. 2.4 through Fig. 2.9.

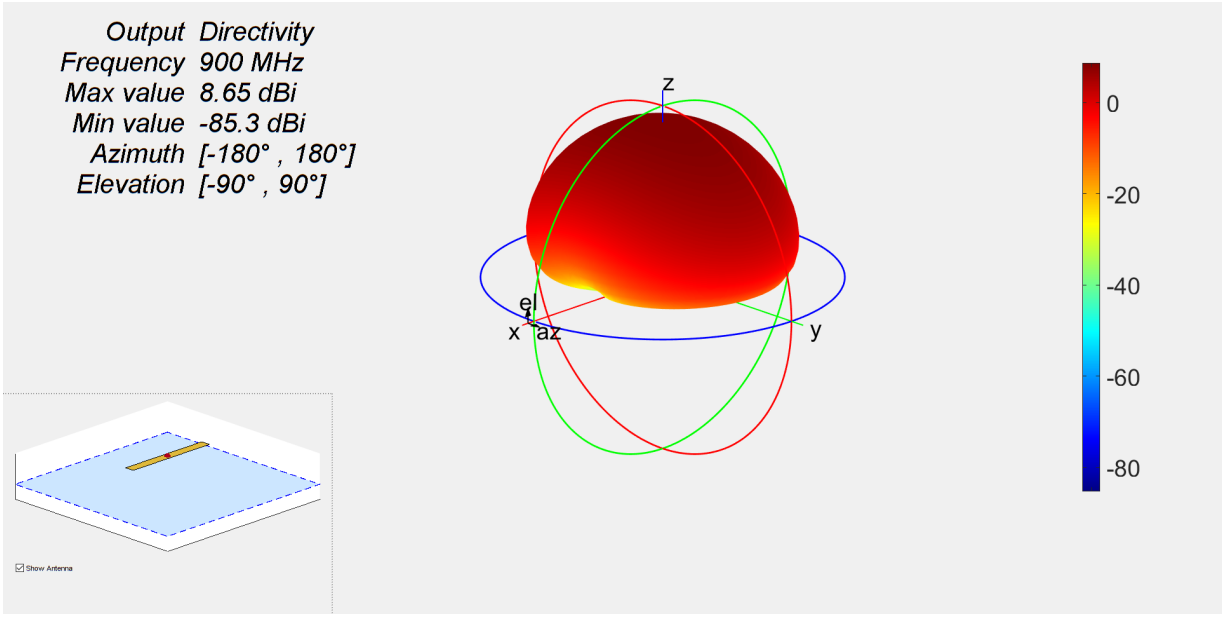

Figure 2.4: Radiation pattern for distance $h = \lambda/8$

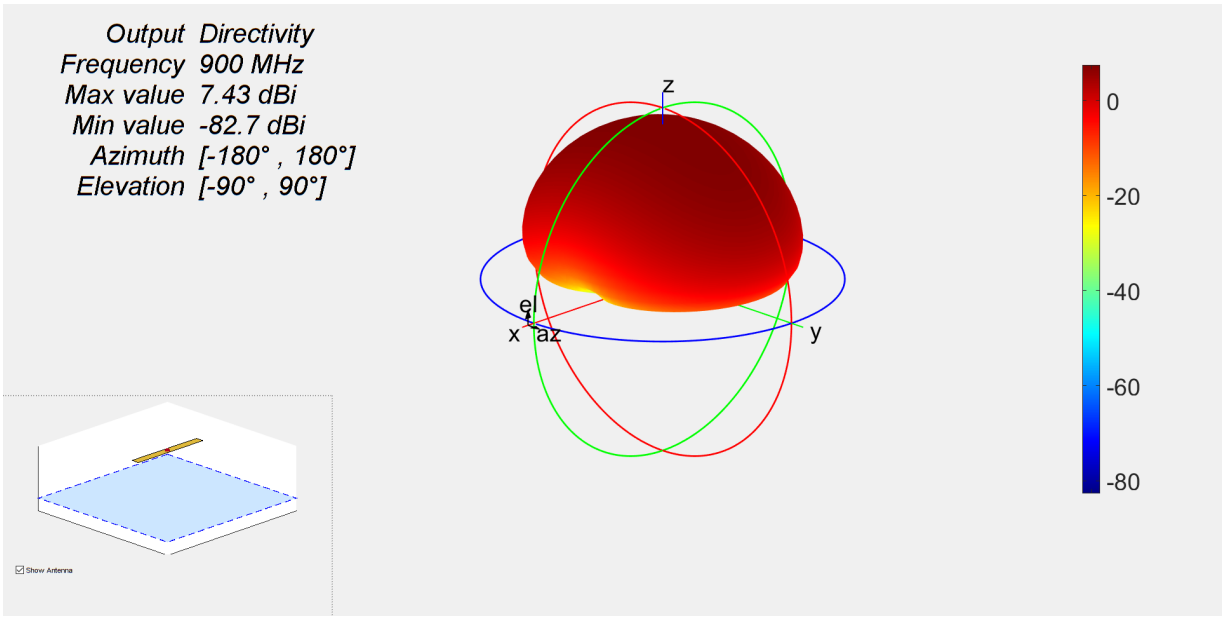

Figure 2.5: Radiation pattern for distance $h = \lambda/4$

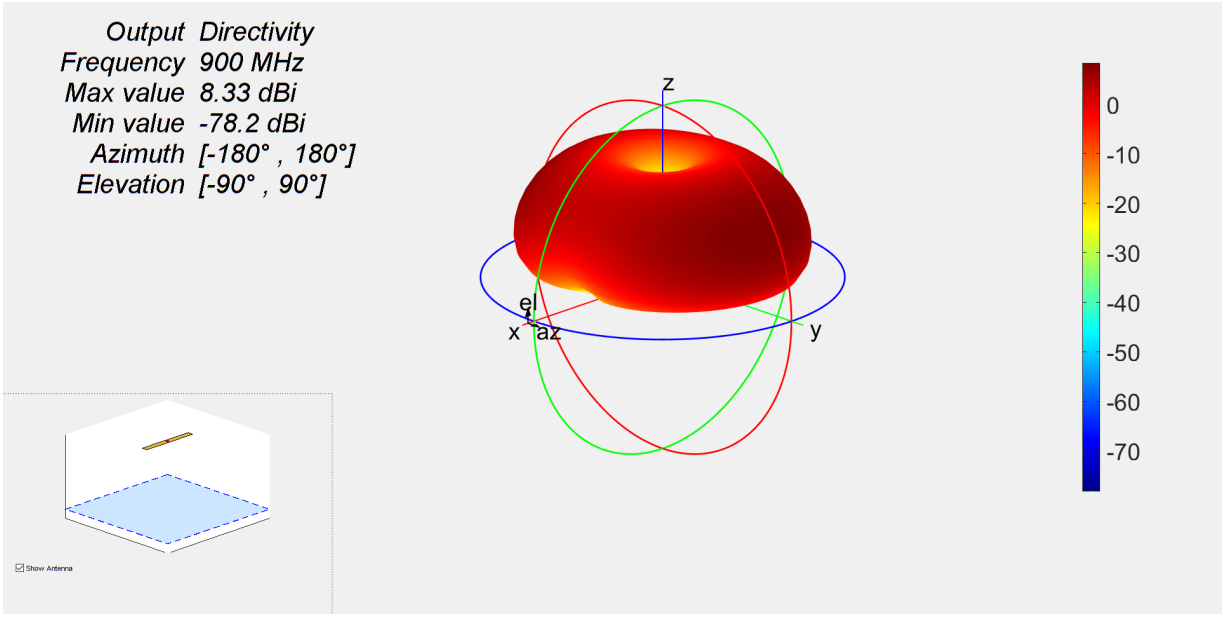

Figure 2.6: Radiation pattern for distance $h = \lambda/2$

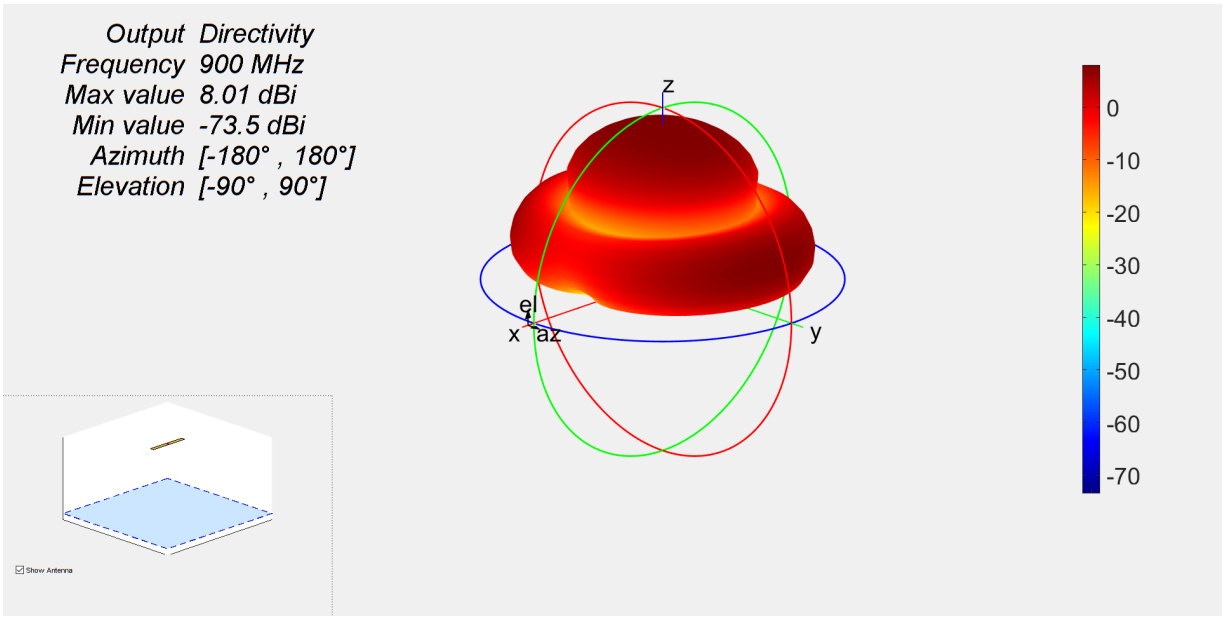

Figure 2.7: Radiation pattern for distance $h = 3\lambda/4$

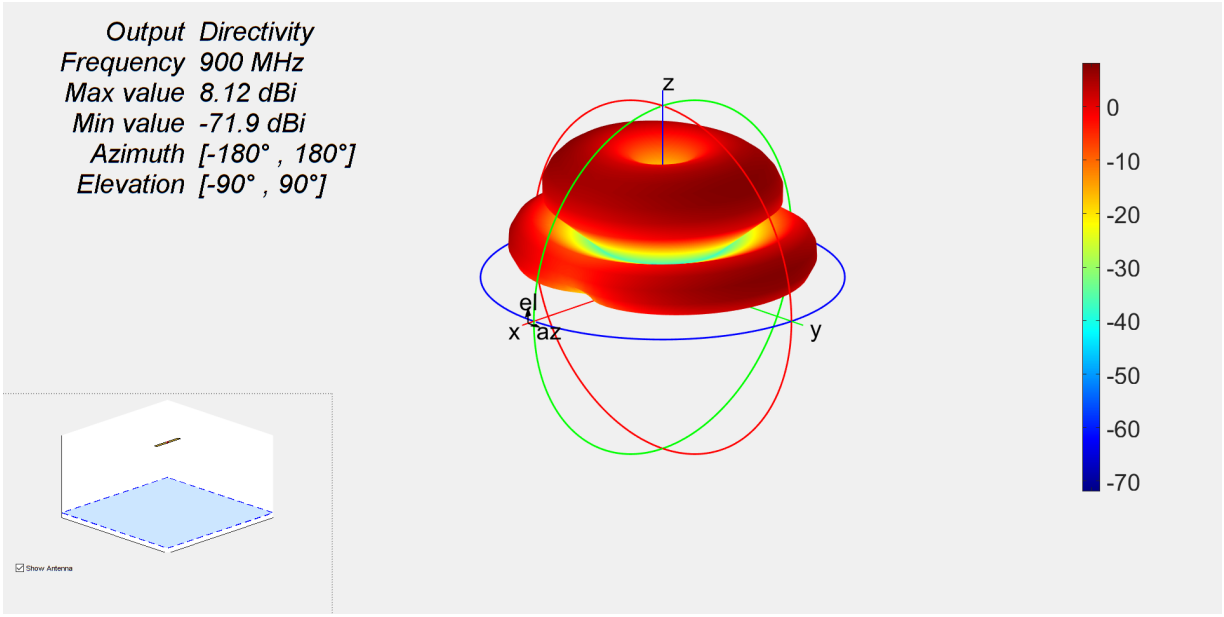

Figure 2.8: Radiation pattern for distance $h = \lambda$

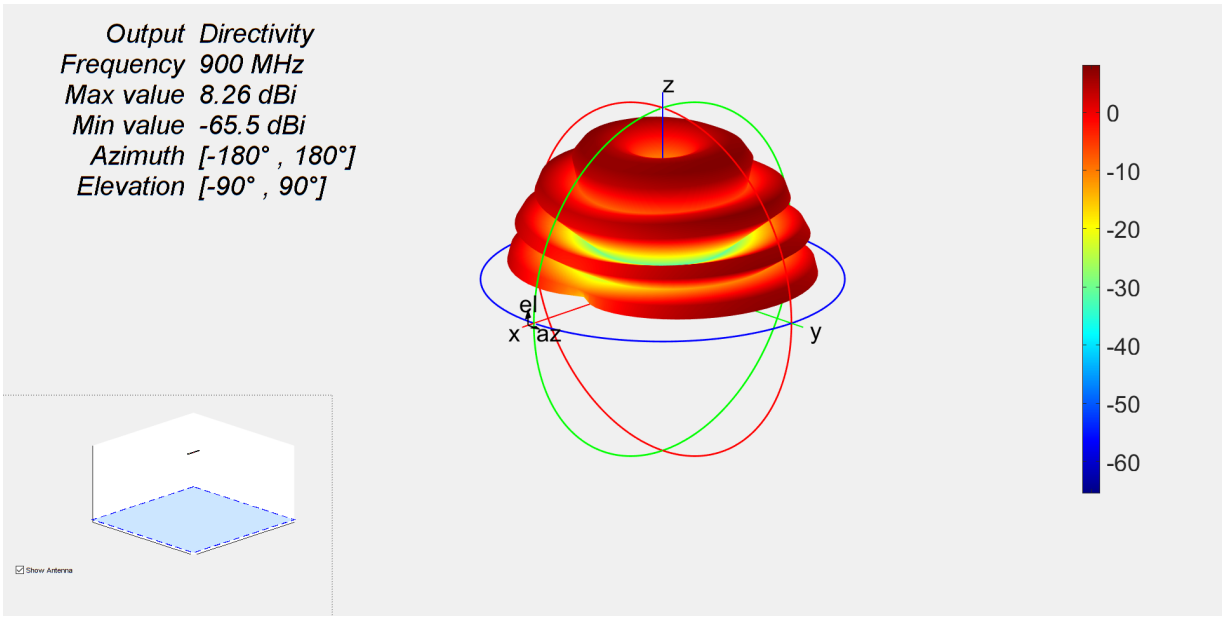

Figure 2.9: Radiation pattern for distance $h = 2\lambda$

As the dipole is placed at greater distance from the conductive surface, additional lobes are appearing with their number being dictated by the relation in 2.7:

$$1 \leq N \approx 2\frac{h}{\lambda} \tag{2.7}$$

where N $\in$ Z is the number of lobes.

The directivity of the antenna, as presented in [54] varies according to the distance h at 900 MHz, as demonstrated in Fig. 2.10.

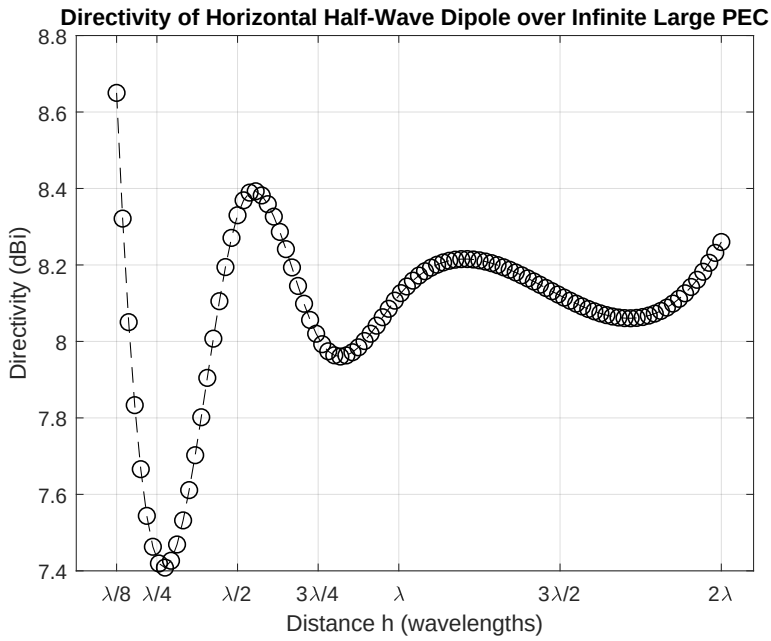

Figure 2.10: Directivity of dipole for different values of h at 900MHz

For distances $h < \frac{\lambda}{2}$ the directivity is varies rapidly and significantly When the distance increases to values $h > \frac{\lambda}{2}$ the variation of directivity becomes smaller. The expression of the directivity is governed by (2.8):

$$D = \begin{cases} \frac{4sin^2(kh)}{R(kh)} & , kh \leq \frac{\pi}{2} (h \leq \frac{\lambda}{4}) \\ \frac{4}{R(kh)} & , kh > \frac{\pi}{2} (h > \frac{\lambda}{4}) \end{cases} \tag{2.8}$$

where R is the radiation resistance which will be defined later on and depends on the intrinsic impedance of the medium n, the wavelength λ, the length of the antenna l and the distance h.

2.2.3 Effects of metal on the impedance of antennas

The effects of conductive materials on the radiation properties of the antennas are not the only disturbing factors. Also, the impedance of the antenna varies and is closely related to the distance between the metallic surface and the antenna. One way to demonstrate such an effect is to consider the mutual coupling between the antenna and the image antenna as presented in the previous section. The system of two identical antennas can be described by the following two ports network, presented in Fig. 2.11 [56],[57]:

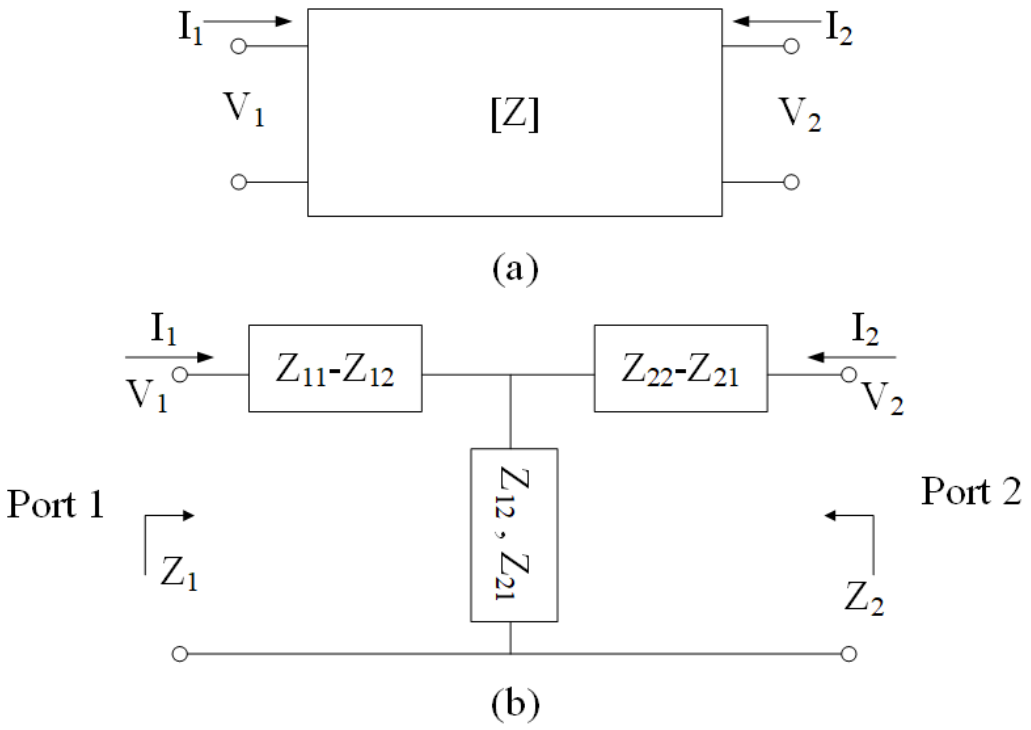

Figure 2.11: (a) two port network (b) T-network equivalent representing the mutual coupling between antenna and image antenna as a two port network

The Z_{11}, Z_{21}, Z_{12} and Z_{22} are defined by the voltage-current relations [54](2.9),(2.10) :

$$\begin{aligned} V_1 &= Z_{11}I_1 + Z_{12}I_2 \\ V_2 &= Z_{21}I_1 + Z_{22}I_2 \end{aligned} \tag{2.9}$$

and

$$\begin{aligned} Z_{11} &= \frac{V_1}{I_1}\Big|_{I_2=0} \\ Z_{12} &= \frac{V_1}{I_2}\Big|_{I_1=0} \\ Z_{21} &= \frac{V_2}{I_1}\Big|_{I_2=0} \\ Z_{22} &= \frac{V_2}{I_2}\Big|_{I_1=0} \end{aligned} \tag{2.10}$$

The Z_{11} is the input impedance at port 1 when port 2 is open circuited, the Z_{21} is the mutual impedance at port 1 due to the current at port 2 (when port 1 is open circuited), Z_{12} is the mutual impedance at port 2 due to the current at port 1 (when port 2 is open circuited) and Z_{22} is the input impedance at port 2 due to the current when port 1 is open circuited. The distance between the two antennas will be $2h$, (see Fig. 2.1). For a single isolated antenna, where $Z_{22} = 0$ and $h \to \infty$, the mutual coupling would be $Z_{12} \to 0$ and $Z_1 = Z_{11}$. In general, where there are two identical real antennas in proximity the procedure to find the mutual coupling would follow the below steps [56]:

- Open circuit antenna 2 and measure the open circuit impedance $Z_{OC} = Z_{11}$ at the terminals to antenna 1.
- Open circuit antenna 1 and measure the open circuit impedance $Z_{OC} = Z_{22}$ at the terminals to antenna 2.
- Short circuit antenna 2 and measure the short circuit impedance Z_{SC} at the terminals to antenna 1.
- Compute Z_{12} with (2.11)

$$Z_{12} = \sqrt{Z_{OC}(Z_{OC} - Z_{SC})} \tag{2.11}$$

The input impedance at the feeding point for each dipole will be (2.12), (2.13):

$$Z_1 = Z_{11} + Z_{12}\frac{I_2}{I_1} \tag{2.12}$$

$$Z_2 = Z_{22} + Z_{21}\frac{I_1}{I_2} \tag{2.13}$$

For reciprocal network $Z_{12} = Z_{21}$ and for identical dipoles $I_1 = I_2 = I_0$ resulting for the examined case in (2.14)

$$Z = Z_{11} + Z_{12} \tag{2.14}$$

,where $Z_{11} = Z_{22}$ and Z_{12} according to (2.15)

$$Z_{12} = \frac{V_{12}}{I_0} = -\frac{1}{2I_0}\int_{-\frac{l}{2}}^{\frac{l}{2}} E_{z12}(z)I_0(z)dz \tag{2.15}$$

Such a procedure is used mainly in array antennas, where there are a lot of identical antenna elements in close proximity. In the case examined here, this kind of method is impossible to be applied since the real and image antennas cannot be treated with different configurations (open/short circuit one at a time). However, this kind of procedure is useful to demonstrate how the effects of conductive surface can be treated. In practice, the required currents and voltages can be computed with other numerical procedures such as Method of Moments (MoM) [58].

The general trend, as far as the mutual coupling is concerned, can be summarized as follows [56]:

- The distance h between the antennas (real and image) is impacting the mutual impedance.
- The radiation pattern in far field, as shown previously, is indicating coupling effects. In (2.6) this interaction is presented by the terms in the bracket (array factor).
- The orientation of the electric fields of each antenna can lead to greater disturbance and the coupling effect is maximized when they are parallel in contrast when they are vertical. For the studied case the two antennas (real and image) will always have parallel electric field lines

2.2.4 Numerical model and representation of the antenna impedance

The variation of the impedance of the antenna can be demonstrated by the same way used in §2.2.2. Using the numerical model of a half wave, center-fed, dipole over an infinite large PEC for different values of distance h ($\lambda/8, \lambda/4, \lambda/2, 3\lambda/4, \lambda$ and 2λ where λ is the wavelength for frequency 900 MHz) the resistance and reactance of the dipole antenna can be computed and it is presented in Fig. 2.12 and Fig. 2.13, respectively.

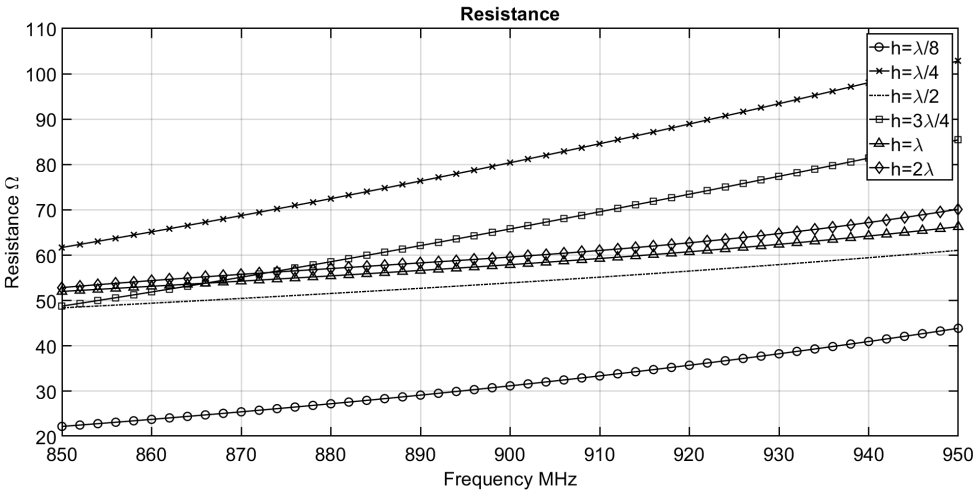

Figure 2.12: Resistance of dipole for different values of h

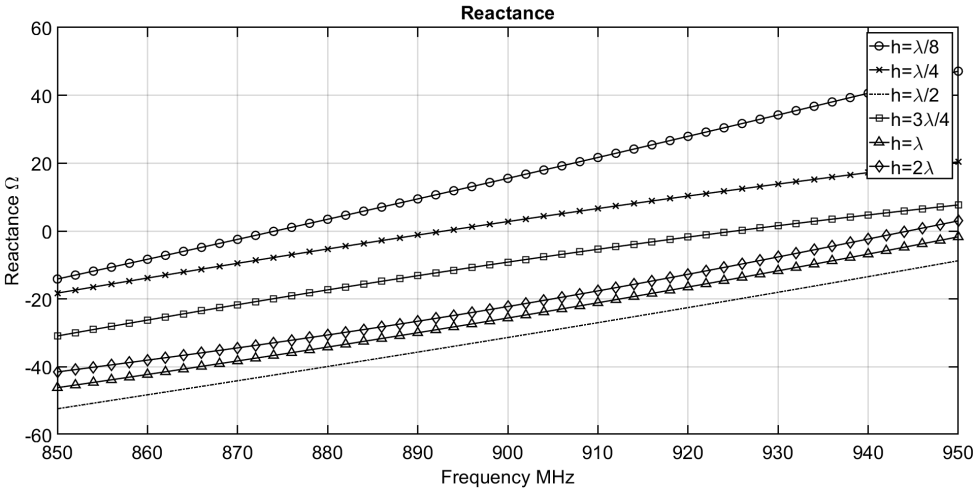

Figure 2.13: Reactance of dipole for different values of h

The variation of the complex impedance for the half-way, centre-fed, dipole at the frequency of 900 MHz as function of distance h is presented in Fig. 2.14.

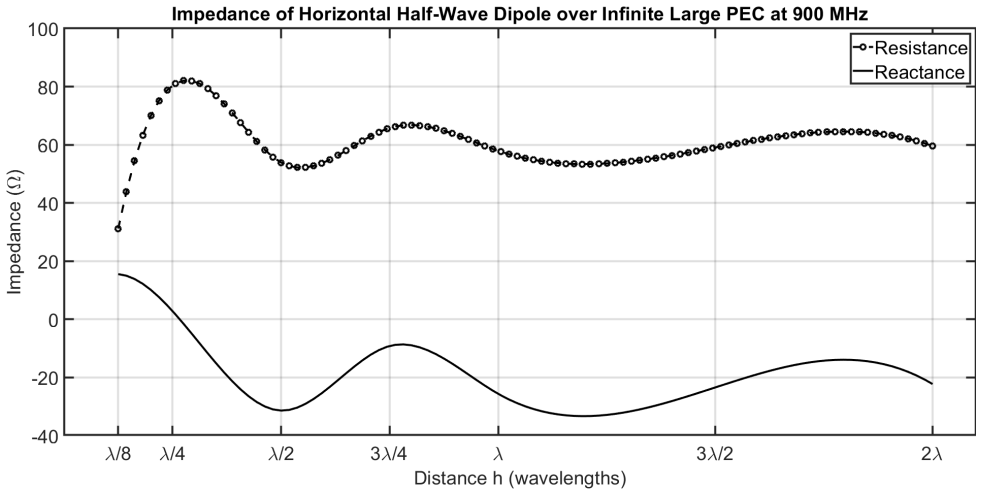

Figure 2.14: Complex impedance of dipole as function of distance h at 900 MHz

The complex impedance varies in similar way as the directivity presented in Fig. 2.10. It exhibits strong variation for smaller values of h and it acquires more stable values as the distance h becomes greater and the effect of mutual coupling between the antenna and its image weakens. For the case of RFID antennas, where they are required to be attached on metal, it could be more interesting to follow the impedance changes for very small values of h, as it is demonstrated in Fig. 2.15.

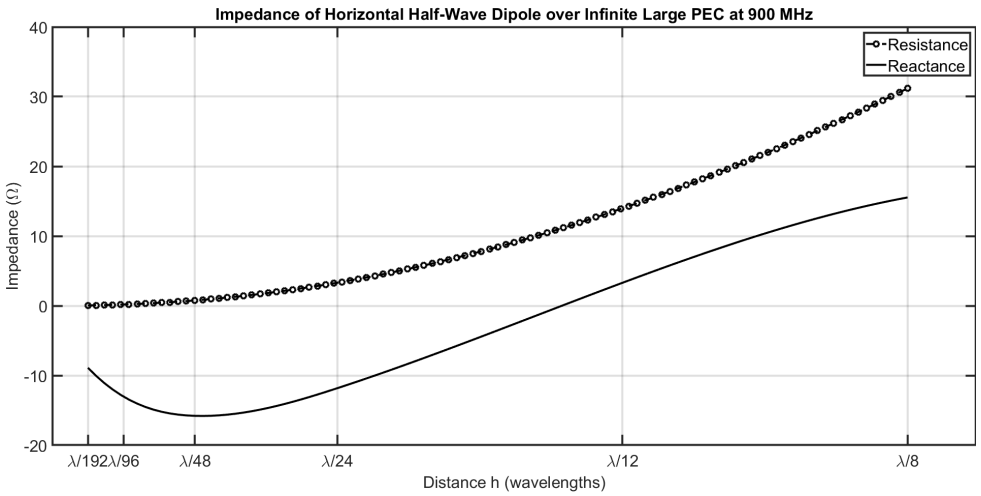

Figure 2.15: Complex impedance of dipole as function of distance h (small values) at 900 MHz

The resistance part of the impedance is very close to zero and since the examined case is for an ideal

lossless dipole, this value will be only dependant on the radiation resistance (2.16), (2.17):

$$R_r = \eta\pi(\frac{l}{\lambda})^2[\,\frac{2}{3} - \frac{\sin(2kh)}{2kh} - \frac{\cos(2kh)}{(2kh)^2} + \frac{\sin(2kh)}{(2kh)^2}] \tag{2.16}$$

And for values $kh \to 0$:

$$R_r^{kh\to 0} = \eta\pi(\frac{l}{\lambda})^2[\,\frac{2}{3} - \frac{2}{3} - \frac{8}{15}(\frac{2\pi h}{\lambda})^2] = \eta\frac{32\pi^3}{15}(\frac{l}{\lambda})^2(\frac{h}{\lambda})^2 \tag{2.17}$$

The reactance of the antenna also varies rapidly as function of distance h, which results in the shift of the resonance frequency of the dipole antenna. From the Fig. 2.13 the resonance frequency will vary according to Table 2.1:

Table 2.1: Resonance frequency of dipole antenna as function of distance h

Distance h (wavelengths)	**Resonance frequency (MHz)**
$\lambda/8$	*874*
$\lambda/4$	*890*
$\lambda/2$	*960*
$3\lambda/4$	*930*
λ	*954*
2λ	*945*

The reactance variation has a great impact on antennas, especially when the antenna is connected to another device with a specific input impedance. According to the distance of the antenna with the metallic surface the matching between antenna and device will also vary and result in an increase of the insertion loss. Moreover, when the antenna has to operate in a limited frequency bandwidth, such variation poses even a greater problem since small variation of distance could lead the system to operate out of the designated frequency band.

2.3 Multipath effects on RFID communication

When the communication channel between two antennas is considered, usually the analysis is based on a line of sight (LOS) scenario in free space propagation. In such a system, the communication is assumed to be carried out by a single path, connecting directly the two antennas. In reality though, beside the considered main single path, there is a number of paths, mainly due to reflections and diffractions, which are forming the communication channel [59]. Each of the additional paths will result in a signal at the destination antenna with different amplitude and phase characteristics from the direct path. The phase difference between the direct signal and all the additional signals will result in a constructive or a destructive interference causing either higher or lower signal strength in the receiving position of the antenna. Such multipath scenario is very dependent on the geometry and the materials forming the environment of propagation between the two antennas. For instance, in an environment with absorbing materials the reflections and diffractions will be minimized (case anechoic chamber), while in an environment with metallic objects, like an industrial environment, the effect of multipath will be stronger [60].

The single path transfer function takes the form (2.18):

$$H(\omega) = \alpha e^{-i\omega t} \tag{2.18}$$

,where t is the propagation delay and α is the path attenuation.

For multipath communication the transfer function will be (2.19):

$$H(\omega) = \sum_{k=1}^{N} \alpha_k e^{-p\tau_k}, p = \sigma + i\omega \tag{2.19}$$

,where τ_k is the delay of the k^{th} reflection, α_k the k^{th} path attenuation and N is the number of reflections [7-8].

The multipath phenomena should be taken into consideration for the RFID communication, especially in an environment with multiple metallic surfaces and objects [61]. For a given RFID system, where RFID reader's antenna and RFID tags have fixed positions, a proper placement of each component can be achieved by finding the positions where there will be a constructive interference. This proper selection will enhance the read range of the RFID tags. In a moving system, where the antenna of the RFID reader is fixed but the RFID tags are moving, the multipath phenomena will be quite difficult to predict since the system is

time variant. In such case, a more practical and straightforward approach is by conducting real tests in the intended environment.

2.4 Numerical model of a complex metallic environment

In the previous section an ideal case of an antenna near a PEC surface was studied. In a real environment with higher complexity, such analytical representation of the phenomena would be very difficult to be calculated. Imagine an antenna in the interior of a complex metallic structure. For every metallic surface in the vicinity of the antenna there would be an image antenna and in order to compute for instance the impedance of the antenna, the mutual coupling between numerous antennas should be calculated. Likely computational algorithms, such as the Method of Moments (MoM) [58], Finite Difference Time Domain (FD-TD) [62] and Finite Elements Method (FEM) [63], can solve this kind of problems as far as numerical models of the antennas and the environment of operation can be constructed in appropriate electromagnetic tools, such as CST Microwave [64] and HFSS [65].

In order to explore the radiation characteristics of an RFID antenna in a complex metallic environment, a numerical model of a real sized generator with four RFID antennas in the interior was constructed and simulated. The materials which were used for designing the generator were copper, iron and steel with a plexiglas material at the exterior. The design of the generator model was inspired by a real generator. In Fig. 2.16 the designed generator is presented.

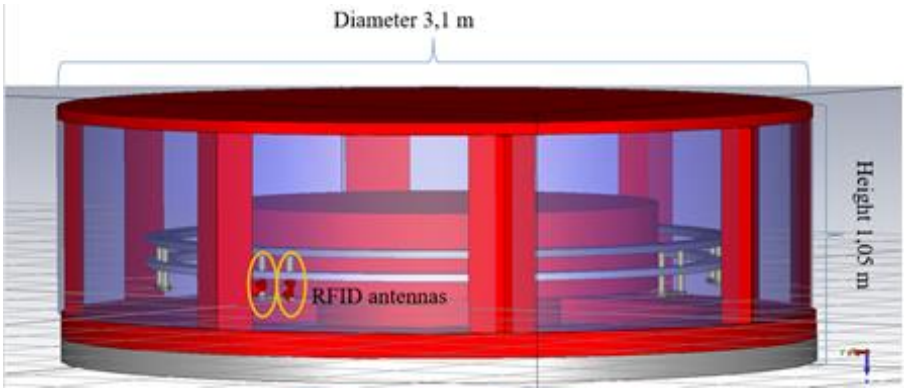

Figure 2.16: Numerical model of a real sized generator with RFID antennas in the interior

The numerical model was simulated, aiming to point out the radiation pattern of the four RFID antennas.

Due to the size of the simulated structure and the frequency of the desired operation (868 MHz), the time of simulation was quite considerable (more than two weeks for an Intel i7 processor with 52 GB of RAM) and the amount of generated mesh cells was in the order of a million. The radiation pattern of the simulation is presented in Fig. 2.17.

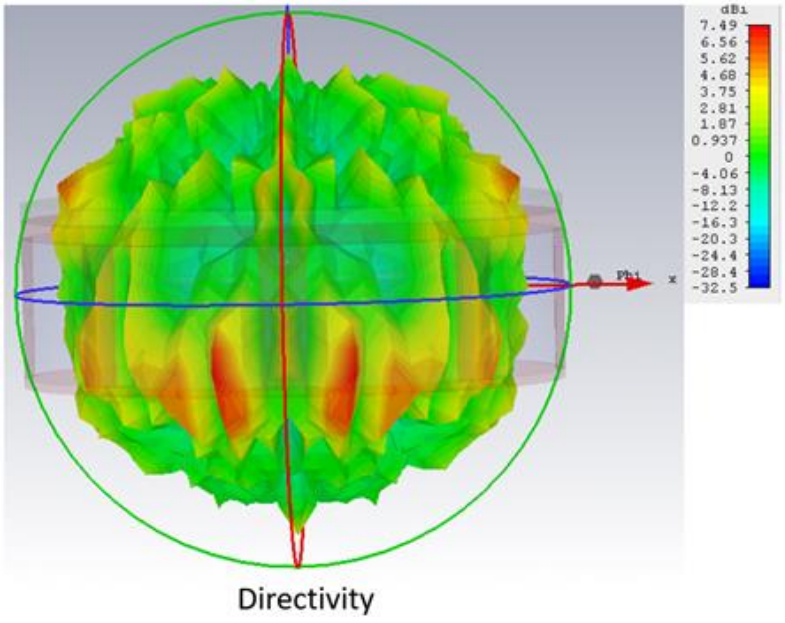

Figure 2.17: Radiation pattern of the 4 RFID antennas in the interior of the generator model

From the radiation pattern it can be seen that due to multipath phenomena the directivity is presenting peaks and valleys in multiple positions, enhancing the radiation in some directions, while degrading it in other directions. This simulation cannot account for the case where the generator is rotating, but it provides some useful information regarding the expected performance.

2.5 Time constraints of RFID communication

In typical RFID identification systems, parameters such as sensitivity, backscatter signal strength and read range or read rate are considered the most important performance parameters [66]. However, the assessment of time delay in the RFID system is also important since it is a significant factor that must be taken into consideration when using RFID tags in real time sensing applications [67]. Tracking motion [68, 69, 70] and phase based positioning identification [71] are significant examples of application that are based on real

time events, in which time delays play a crucial role. In addition, timing will play an important role when the tagged objects are under motion such as when parts of the rotor of a generator are required to be monitored.

2.5.1 Real time RFID communication

When implementing RFID sensor-tag in real-time systems, some new challenges arise. These challenges are due to the fact that in real time the control process requires continuous monitoring through different sensor-tags that collect the required data for the controller for decisions making. This means that the system control information must flow in a time frame faster than the physical flow; so there will be no data loss. This issue is critical for real time sensing in which the RFID sensor-tag and reader response and/or recovery times are important parameters [72]. In Fig. 2.18, the schematic diagram representing the RFID wireless sensors communication link is shown.

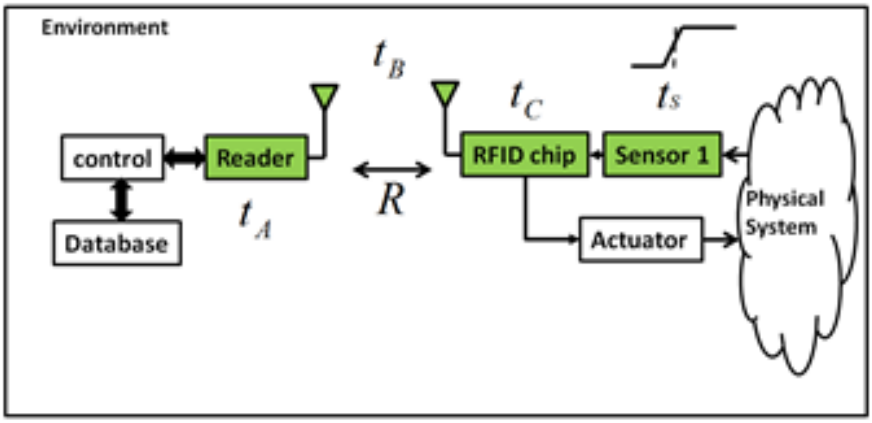

Figure 2.18: RFID wireless sensor communication link with sources of time delays constrains

RFID sensors are used to send the data together with identification in order for the RFID reader to distinguish multiple sensors in the network. The communicated data can be stored in a network database for later time manipulations or comparisons. The notion of environment in Fig. 2.18 represents the surrounding conditions in which the RFID sensors network operates. The RFID sensor-tag component imposes several time-delay constrains that play a crucial role on the entire system. In order to accurately analyze these constraints, Fig. 2.18 focuses on RFID sensor-tag part and introduces the time delays associated with each component in addition to the time delay due to the radio link. The time delays in RFID sensor-tag arise from

two sources: first the delays that are due to sensor component and the extra functionalities associated with it such as analog to digital conversion and digital control; second, the delays that need to be respected as a timing requirement following the specifications of the standardized RFID protocols.

Any sensor requires a sensing time ts. This time depends on the physical phenomena to be sensed as well as the sensor principle of operation [73]. It is usually divided into two times: the response time t_{90} which is the time required to reach 90% of its sensing signal and a recovery time t_{10} which is the time to reach 10 % of its reading and being ready for next measure [74].

The second delay arises from the RFID chip t_C which is due to either RFID tag read time delay or RFID data processing time delay resulting from the chip microelectronic components. In some cases, where the RFID chip has embedded sensor, t_C comprises the sensing time t_S and extra commands are added to the standard protocol to access the sensed values [75, 76, 77]. The network communication time delay t_B is due to the propagation of the electromagnetic wave in the medium. t_A is the reader response time which comprises protocol and processing delays.

Since this work concentrates on the RFID communication link, other delays such as decision-making time delay by the controller, local or remote databases query response time delay and actuator decision execution time delay are not going to be considered in this analysis.

2.5.2 Exploration on the causes of time delay

As depicted in Fig. 2.18, the overall time delay in an RFID sensing system can be estimated by taking into consideration all the possible delays in all the components of the system (sensor, RFID tag, communication channel, RFID reader).

Sensing time t_S

The sensing time tS can vary based on the sensor type (chemical, pressure, temperature, gas concentration, humidity, etc.). Since each of these physical parameters requires particular transducing phenomena, the sensing time will be different for different transduction principles. For instance, measuring temperature using thermocouple a transducer will have a delay based on the time constant of the thermocouple. This time delay depends on the material from which the thermocouple is made. Otherwise, for sensing gas concentration or humidity the transduction process is done by chemical interaction between the gas and the sensor material. Hence, the sensing time will depend on the kinetics of the reaction. Typical values of

responses for sensors are 10-20 seconds for thermocouple sensors, 4-8 seconds for humidity sensors and 3-15 seconds for gas sensors. So sensor timing can be estimated in the order of seconds or longer [78, 79, 80].

RFID chip delay t_C

The RFID chip delay t_C is due to the processing control unit which is limited to certain data rate. Typical values can be in the range of 160 to 640 kbit/s. This RFID chip data rate can be used to estimate the delay time based on the number of communicated bits. For instance, to process 32 bits the RFID integrated circuit will need between 0.05 to 0.2 milliseconds. It is important to note that this delay is due to digital processing unit. However, RFID chip with a built in sensor can have extra delay for processing the sensed values by its internal sensor.

Propagation delay t_B

The communication delay tB is caused by the medium (i.e., the propagation channel). It occurs due to two mechanisms, single or multi path delay. In the single path propagation, the delay t_B is equal to $\tau = \frac{R}{v}$, where v is the speed of the electromagnetic wave in the medium and R the distance traveled. For UHF band t_B can be estimated in the order of 3 nanoseconds for 1-meter direct free space link. In the case of multi path, t_B will depend on the number of reflections having a delay τ_k.(see (2.19)) In case of multi path, the delay has been measured and analyzed statistically in [81] to be up to 400 nanoseconds in operational factory with metal and concrete environment.

Reader delay t_A

The reader delay t_A comprises the latency in interrogation in one part from the EPC protocol and in other part from the processing time of the reader. Since the protocol requires certain interrogation sequences from the moment the communication is established between the reader and the tag till the reception of the sensor value from the tag, this sequence will enter as a timing factor in real time sensing and will be crucial when the RFID tag is interrogated for sensed values [82]. These sequences are treated by the reader based on its processing capability. These processing capabilities are controlled by a microcontroller unit (MCU) with typical bit rate of 5 Mbps. For processing 32 bits of information this requires 6.4 μs Another factor that increases the reader processing delay is the implementation of the anti-collision mechanism [83,

84, 85], as this increases the interrogation bits' sequence and hence, the reader processing time. Even though the anti-collision mechanism is used for a population of tags, it can be implemented by default for single tag communication. It is important to note that even if the reader processing rate is high (in order of microseconds) the reader delay is limited by the implementation of the EPC protocol requirements. These requirements set the time constraints that define the rate of interrogation and waiting time between commands. Their values are calculated based on the 'Tari' values which define the pulse width of the interrogation bit sequences (see EPC Gen2 standard [86]).

2.5.3 Analysis of time delay in rotating RFID sensing system

The time constraints of an RFID sensing system were additionally studied in a rotating measurement setup.

Motion detection using polarization mismatch

Since the interest here is to analyze time delay, a method to measure the response time due to rotation speed is introduced here. The idea is to use the polarization mismatch for motion detection is based on measuring the backscattered power from the tag with linearly polarized antenna. The backscattered power is given by [23]

$$P_{reader \leftarrow tag} = \frac{1}{4\pi}(\frac{\lambda}{4\pi R^2})^2 P_{th}\, G^2_{reader}(\theta, \phi)\eta_p^2\, RCS_{tag} \tag{2.20}$$

where η_p is the polarization mismatch, G_{reader} is the reader antenna gain, RCS_{tag} is the tag radar cross section, λ is the wavelength of the signal, R is the distance between the reader and the tag, ϕ, θ are the spherical coordinates and P_{in} the input power to the reader.

During the interrogation, if the RFID tag is set into rotation the polarization mismatch η_p will change based on the rotated angle. Given that all other parameters in (2.20) are held constant the backscattered power level $P_{reader \leftarrow tag}$ measured by the reader will change. For rotational motion, the polarization mismatch will oscillate between minimum to maximum as a function of time as the tag rotates which in turn induces a time variation in the backscattered power level. This time varying power level can be used as indicator for the rotation motion and from which the rotational motion delay can be deduced.

Motion detection measurement setup

The experimental setup used to measure the backscattered signal from an RFID tag during rotation motion is depicted in Fig. 2.19. The tag under test is mounted vertically on a rotating platform with rotation speed of 3.5 rpm. The interrogation distance was fixed to be 30 cm and the backscattered signal power level was recorded by the reader. The EPC code is recorded by the reader software in each communication round and at the same time the reader shows the received signal strength indicator (RSSI) value. The RSSI value will change according to the angle of rotation of the tag.

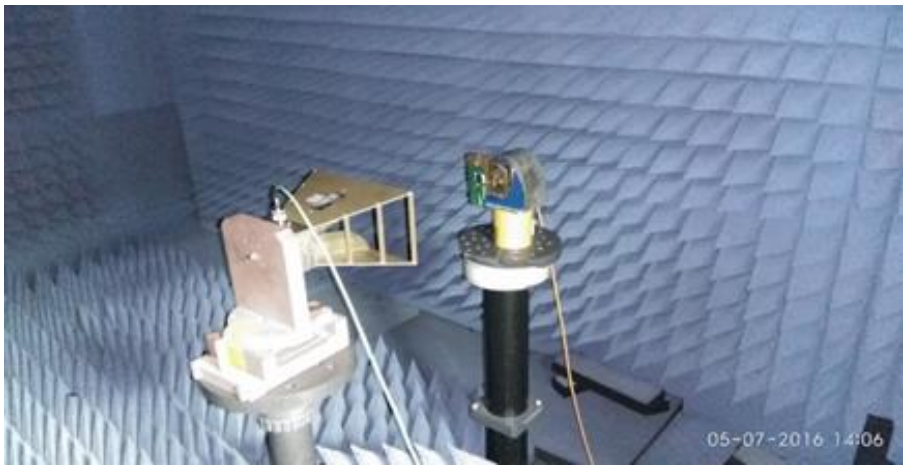

Figure 2.19: The measurement setup for reader-sensor tag rotational motion

In this case study, one tag using the AMS SL900A RFID chip (see Appendix) was chosen as a test sample for time delay measurement.

Motion detection results

The effect of protocol and tag processing delays can be investigated from the rotational response of the RFID tag as a motion sensor. The RSSI values recorded by the reader during one rotation of the RFID tag are shown in Fig. 2.20. In this test, the Tari has been chosen to be 25 μs for both tag samples for response time comparison. Without loss of generality, the RSSI values recorded by the Femto reader (see Appendix) are left in their binary code form since the transition time from maximum to minimum backscattered power is the main parameter to be measured in this study. By analyzing Fig. 2.20 for the RFID tag, the response time to the variation of polarization from vertical to horizontal is 17.4 ms and 27.8 ms from horizontal to

vertical variation.

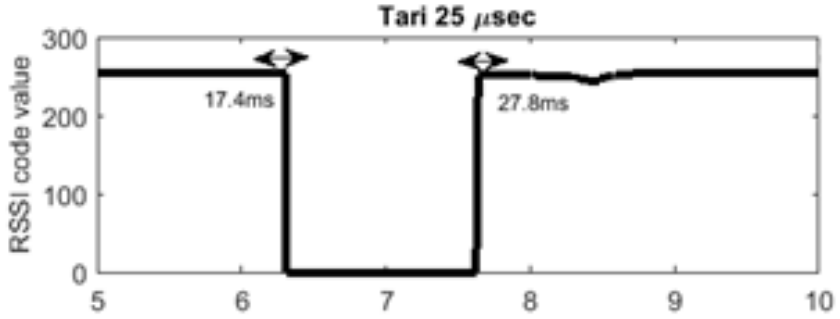

Figure 2.20: RSSI values recorded by the interrogator software

Tari effect on the response to the rotational motion

The same measurement has been conducted as described in the previous section using different Tari values in the interrogation. The transmitted power and the sensitivity of the reader are kept at 20 dBm and -83 dBm respectively at 865.7 MHz and 30 cm separation between the reader and tag antennas. The response time has been measured for the three Tari values (6.25 μs, 12.5 μs and 25 μs for the SL900A RFID tag. The results are shown in Fig. 2.21. The response times comprise the delays due to protocol and processing t_A and t_C. However, from §2.5.2, one can see that the channel propagation delay t_B is negligible (order of ns) compared to the other delays and can be omitted from the response time analysis. The results show that an increase in the response time as the Tari value increases. This is due to the fact that the choice of the Tari affects the EPC protocol timing which affects the separation time between interrogation in one communication round between the reader and the RFID tag. From the results of Fig. 2.21 and with the suitable values of Tari, an RFID sensor-tag with the chip SL900A could operate in a system with rotational frequency of around 100 Hz.

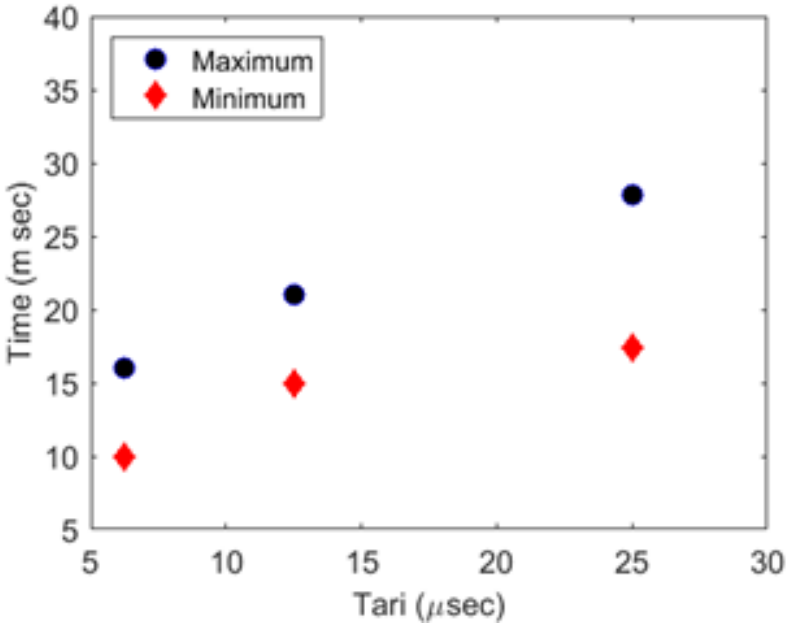

Figure 2.21: Time responses for different Tari values of the RFID tag to the rotational motion

2.6 Effects of high magnetic field on the RFID sensor-tags and RFID communication

Another point of interest of this thesis was to assess the impact of high magnetic field on the RFID communication as well as on the RFID tag's operation. The magnetic field in the interior of generators can be as high as 1.5 Tesla with amplitude of oscillations of 100 mTesla with a frequency dependent on the rotational speed. To explore experimentally the impact of high magnetic field on the RFID communication and on RFID sensor-tags, measurement in an environment with high magnetic field of the order of 4.7 Tesla in the CREATIS/ Platform PILoT of Lyon INSA University.

The measurement setup is presented in Fig. 2.22 where and RFID sensor-tag operating with SL900A RFID chip was inserted in the middle of a Magnetic Resonance Imaging (MRI) scanner. The RFID sensor-tag was positioned very close to the entrance of the 100mm diameter tube, in order to avoid rapid downgrading of the transmitted signal due to the transmission in the narrow tube of the MRI scanner. The antenna of the RFID reader was positioned 30 cm away from the MRI scanner and the RFID communication was tested, as well as the integrity of the transmitted backscattered data to the RFID reader.

The measurement results did not yield any worth noting effect, since the communication and the oper-

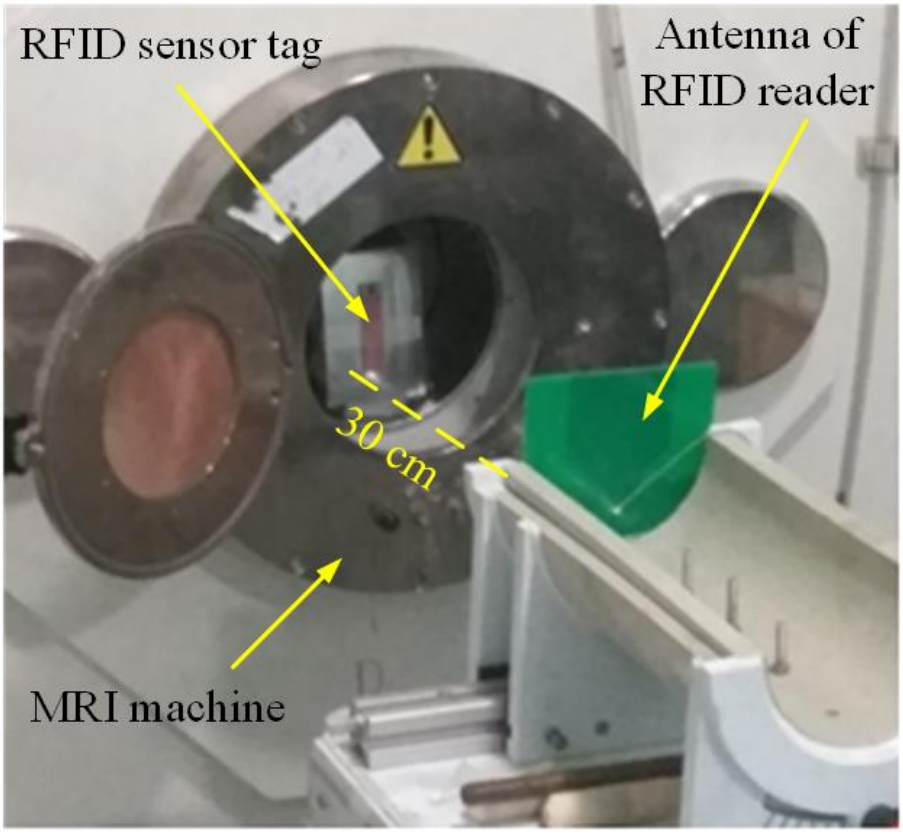

Figure 2.22: Measurement setup in high magnetic field

ation of the RFID sensor-tag, remained unaffected by the high magnetic field. All the backscattered data, including the temperature value detected by the integrated temperature sensor of the RFID chip were able to be received by the RFID reader. Similar results were extracted by additional tests conducted in the presence of small (100mTesla) alternating magnetic field.

This measurement setup was not the perfect mock up for a real operating generator and its magnetic field, due to the absence of high magnitude alternating.

2.7 Effects of high electric field on the RFID sensor-tags and the RFID communication

Another consideration in this thesis was the impact of high electric field on the RFID sensor-tags and the RFID communication overall. The electric field produced in the interior of generators can be very high due to the very high potential of the generator's connection which can be as high as 12 kV at a frequency of 50 Hz. Regarding the effects of the electric field on an RFID sensor-tag some information for a small generator

can be found in [87] where the electromagnetic noise was found to be high in low frequencies (below 100 MHz), but quite insignificant in higher frequencies including the UHF band of RFID, 860-960 MHz. At the author's knowledge, for high electric field there were no more information in the literature.

In addition, creating a setup with such high values of electric field would be quite difficult to be realized and also quite dangerous. Thus, the effects of high electric field were decided to be tested at a later stage of the thesis, when measurements from areas with high electric field would be available.

2.8 Conclusion

In this chapter, a study and exploration of the impact of harsh industrial environment of generators on the RFID communication and RFID antennas/RFID sensor-tags was presented. The conclusion of this part was utilized in next stages of the thesis, mainly by guiding the formulation and the design procedure of proper RFID sensor tags and their positioning in the intended places to be monitored.

The analysis on the impact of metallic surfaces/items in the vicinity of the antennas was one of the most important conclusions, since it guided the characteristics which one RFID sensor-tag antenna should possess to operate successfully in such environment. Furthermore, even though, the multipath phenomena cannot be predicted, by appropriate positioning of the RFID sensor-tags some constructive interferences could be utilized to enhance their operation. In addition, a time delay study, confirmed the potential of the RFID technology to monitor real time rotating systems and indicated a threshold on the maximum frequency of movement that could be potentially monitored. Finally, the exploration on the impact of high magnetic field cleared any doubts regarding the feasibility of the RFID technology operating in such environment.

CHAPTER 3
DESIGN OF UHF RFID SENSOR-TAGS WITH ENHANCED RFID CHIPS

3.1 Introduction

The design of the RFID sensor tags is a non-trivial task, due to the fact that it is depending on the nature of the intended application. For instance, when the application would require the RFID sensor tag to operate on non-conductive materials, the constraints imposed on the design of the RFID antenna are very few and a variety of different antenna configurations can be selected without impacting greatly the performance of the RFID antenna. On the contrary, when the RFID sensor-tag is oriented in operation in a metallic environment then the design specifications become much stricter and every small touch can impact, positively or negatively, the performance. One common practice to overcome the impact of the effects of conductive items to the UHF RFID tags is to take advantage of metallic surfaces and adopt different antenna tag designs such as Inverted-F or patch based antennas [88, 89, 90, 91, 92] with the appropriate miniaturization techniques applied [93].

In addition to constraints due to the environment of operation, there can be additional constraints due to the required position of the RFID sensor-tag. More specifically, if a small metallic part is required to be monitored, constraints on the size or weight of the RFID sensor-tag can arise. This is the case in this thesis and chapter where several specifications needed to be taken into account.

In this chapter, a series of different designs of UHF RFID sensor tags are presented. Initially, an exploration on the performance of the UHF RFID chip SL900A [31] (see also Appendix) is performed in order to extract as many information as possible regarding its operation and its RF behavior. In addition, a series of UHF RFID sensor tags were realized following the same consecutive steps: design, simulation, fabrication and measurements. Finally, in this chapter, an RFID tag-antenna with dual band operation is presented by utilizing a unique approach.

3.2 Specifications

As pointed out in the introduction, the main goal of the thesis was to monitor the temperature of the inter-polar connections of large generators. Different designs and geometries of generators are used in various power-plants, with each one presenting different configuration with different size. Due to this fact, and in

order to monitor small areas, the RFID sensor-tag should maintain a small size and a low profile. Moreover, every generator has multiple interpolar connections and the weight of each RFID sensor-tag has to be low especially since the generator is rotating with high speed, presenting acceleration up to 1000 G. Due to this acceleration the actual weight of each RFID tag-sensor can be considerably higher and if multiple RFID tag-sensor are installed the overall weight needs to be accounted. Furthermore, this development should include the sensor characteristics which are required for the intended application, such as temperature range, temperature precision, and temperature accuracy. For each application, different temperature requirements apply. For instance, for temperature monitoring in the food industry, temperatures up to 40 °C are sufficient. On the other hand, monitoring a generator is required to measure temperatures more than 100 °C. Simultaneously, the expected variation of temperature is important if small variations can result in warning incidents. Based on this, the accuracy and precision of the measured temperature are important. Finally, one more important consideration for the design of the RFID sensor tags was the need to avoid closed loop structures. The very high magnetic field in the interior of the generators can result to the creation of very high currents and thus designs which would not result in closed loops should be selected. According to all these considerations, a specification list of the characteristics of the RFID sensor-tag was formed initially to guide the design of the RFID sensor-tag-antenna as well as the selection of the RFID chip, see Table 3.1.

Table 3.1: Specifications of the RFID sensor-tag

Characteristics	**Values**
Length (mm)	< 60
Width (mm)	< 15
Thickness (mm)	< 4
Weight $(grammars)$	< 10
Temperature range (°C)	*20-125*
Temperature accuracy (°C)	$< \pm 1$

From the discussion in chapter 1 and the sensing enhanced RFID chips, the most prominent candidate to be utilized was the RFID chip of AMS, SL900A. It was the only RFID chip which according to the datasheet at the period of selection, could sense temperatures up to 125 °C.

3.3 Measurement and characterization of the SL900A RFID chip

The general target when designing an RFID tag-antenna is to maximize the power driven into the input of the RFID chip, in order to maximize the performance of the RFID tag mainly regarding the read range. This is usually achieved by conjugate matching the RFID antenna with the RFID chip [94], [95].

Assuming that the power delivered to the RFID chip is P_c:

$$P_c = P_\alpha \cdot \tau = S \cdot A_{eff} \cdot \tau = S \cdot \frac{\lambda^2 G}{4\pi} \cdot \frac{4 \cdot Re\{Z_{antenna} Z_{chip}\}}{|Z_{chip} + Z_{antenna}|^2} \tag{3.1}$$

where P_a is the maximum available power from the antenna, τ is the power transmission coefficient, S is the poynting vector, A_{eff} the antenna effective area, G the gain of the antenna, λ the wavelength and $Z_{chip} = R_{chip} + j \cdot X_{chip}$ and $Z_{antenna} = R_{antenna} + j \cdot X_{antenna}$ the complex impedances of the RFID chip and RFID antenna respectively. For maximum power transfer from the RFID antenna to the RFID chip, the coefficient τ, should acquire a value of 1. This is valid when:

$$\begin{aligned} Z_{antenna} &= Z_{chip}* \\ R_{antenna} &= R_{chip} \\ X_{antenna} &= -X_{chip} \end{aligned} \tag{3.2}$$

According to (3.2), for maximum power transfer, the RFID antenna should present a conjugate impedance. For this reason, it is very important to know as accurately as possible the impedance of the RFID chip. In addition, since the input impedance of the RFID chips present a non-linear behavior due to the diodes which are operating in their inputs, the input impedance of the RFID chip will depend on the specific operating frequency and the input power. Having in mind the above-mentioned characteristics the input impedance of the RFID chip SL900A was measured by connecting it to an RF connector, as presented in Fig. 3.1.

The RFID chip was then measured with a Vector Network Analyzer (VNA), Keysight (Agilent) PNA-X series, N5242A. The VNA was calibrated with the mechanical standard of the calibration kit of Agilent 85052D and then using the port extension option to take into account the delay of the signal due to the length of the RF connector. Initially, a power sweep was performed to find the minimum power required in order the RFID chip to be activated. When the RFID chip is being activated, then a rapid change in the reflection coefficient can be observed marking the initiation of the operation. This procedure is demonstrated in Fig. 3.2, where the RFID chip starts to operate for an input power of 5.3 dBm. This power value will be

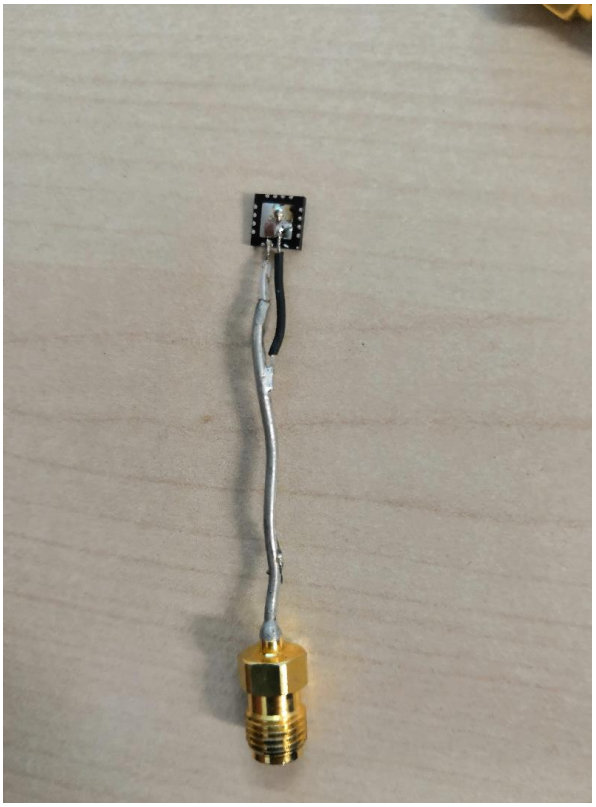

Figure 3.1: SL900A RFID chip soldered on the RF connector

different than the reported value of -6.9 dBm which is provided at the RFID chip's datasheet, since there is no matching between RFID chip and RF connector and thus more power is required to activate the RFID chip due to impedance mismatch.

In Fig. 3.3 the values of the real and imaginary part of impedance measured for different power levels are provided. In contradiction to Fig. 3.2 it can be seen that at the activation power (5.3 dBm) the input impedance of the RFID chip at 915 MHz is $29.35 - j273.5\ \Omega$. This value is close to the value of input impedance which was provided with an earlier version of the datasheet of the SL900A RFID chip ($32 - j323\ \Omega$) (version 1.5). The latest version of the RFID chip datasheet is indicating an impedance value of $123 - j303\ \Omega$ (version 1.12).

As the power is increasing the value of impedance will be changing and for the value of 9 dBm, the input impedance will be $80.81 - j243\ \Omega$.

Fig. 3.4 presents the input impedance of the SL900A RFID chip for the different values of input power in a Smith chart. For the design of all the RFID tag-antennas which will be presented later on, the impedance

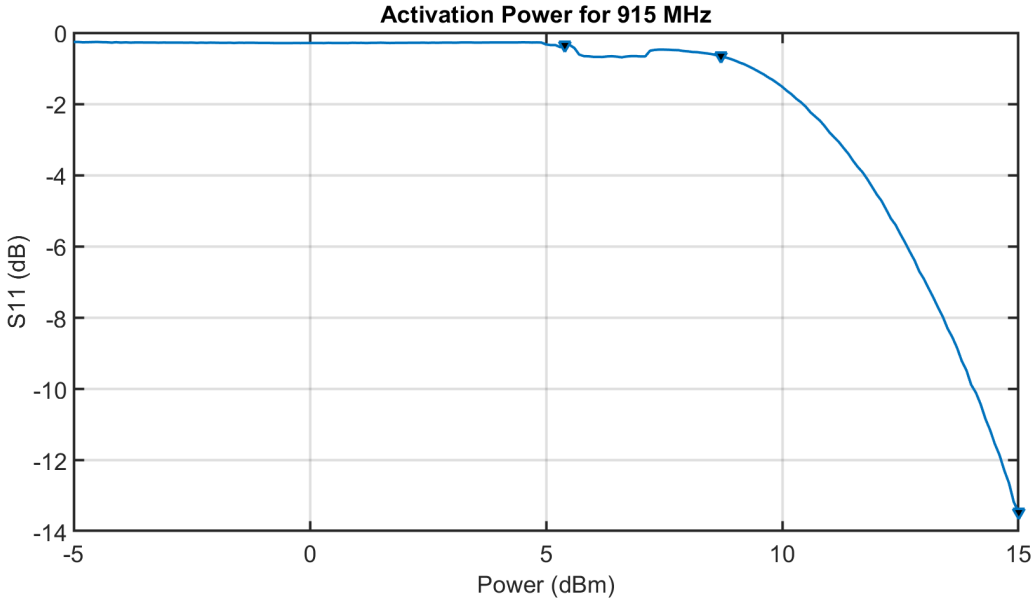

Figure 3.2: Reflection coefficient of RFID chip in a power sweep mode for the frequency of 915 MHz

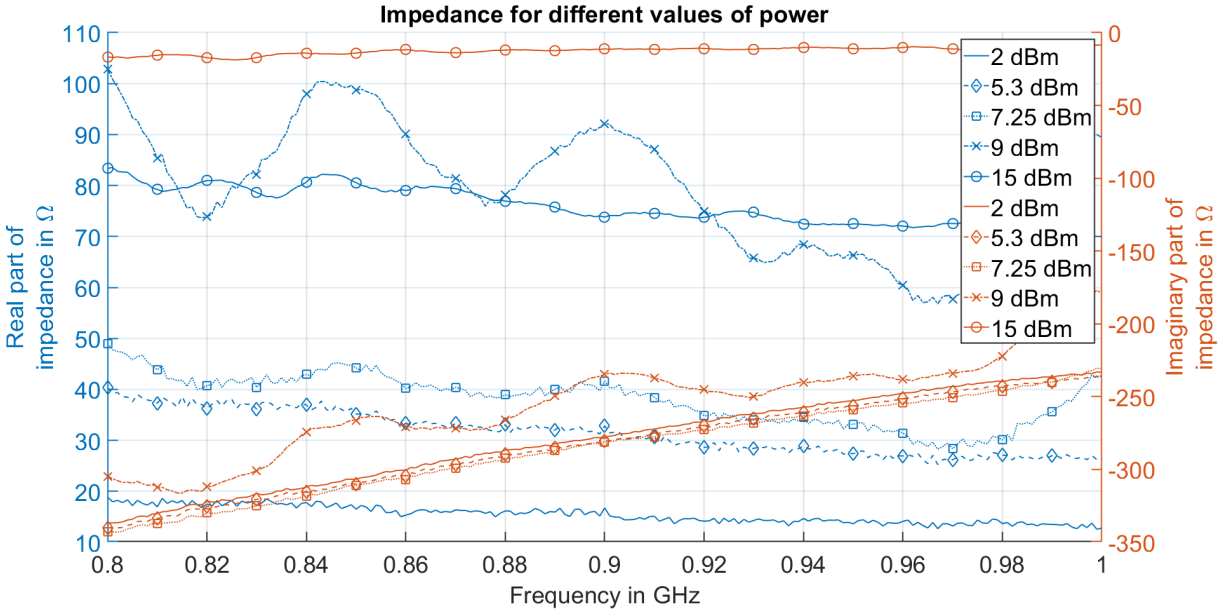

Figure 3.3: Real and imaginary values of impedance for different values of power

used was the one provided in the latest version of the data sheet $123 - j303\ \Omega$ except from the first design (circular UHF RFID tag-antenna) where the former value of impedance was used ($32 - j323\ \Omega$) since the newer version of the datasheet was not published at the time. More information regarding the SL900A RFID chip are available in the Appendix.

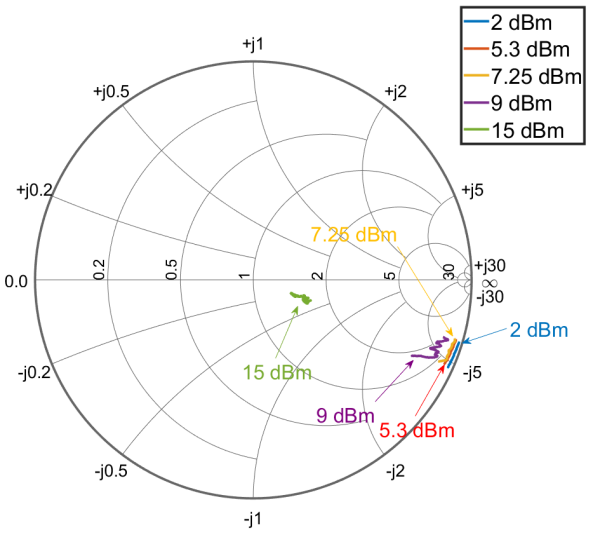

Figure 3.4: Impedance of RFID chip for different values of power in Smith chart

Another important point was that the impedance of the RFID chips would differ from chip to chip. This can be observed in Fig. 3.5 where for three different SL900A RFID chips at 915 MHz and for 9dBm input power the impedance values differ substantially. This low yield is widely due to the soldering temperature and technique (hand soldered).

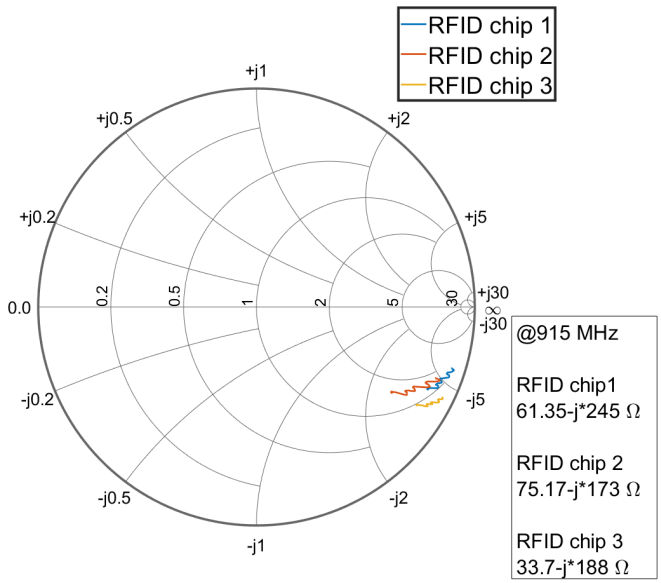

Figure 3.5: Variation of impedance for different tested RFID chips

This inconsistency of the particular chip was also observed in the fabricated prototypes. To demonstrate this inconsistency, 4 prototypes which were realized by a PCB fabrication company and soldered by a pick and place soldering machine, were measured in order to assess their performance regarding their resonance frequency and read range, see Fig. 3.6. The resonance frequency of the prototypes differs in a span of 8 MHz (854-862 MHz) and the read range is between 3.1 and 3.3 meters.

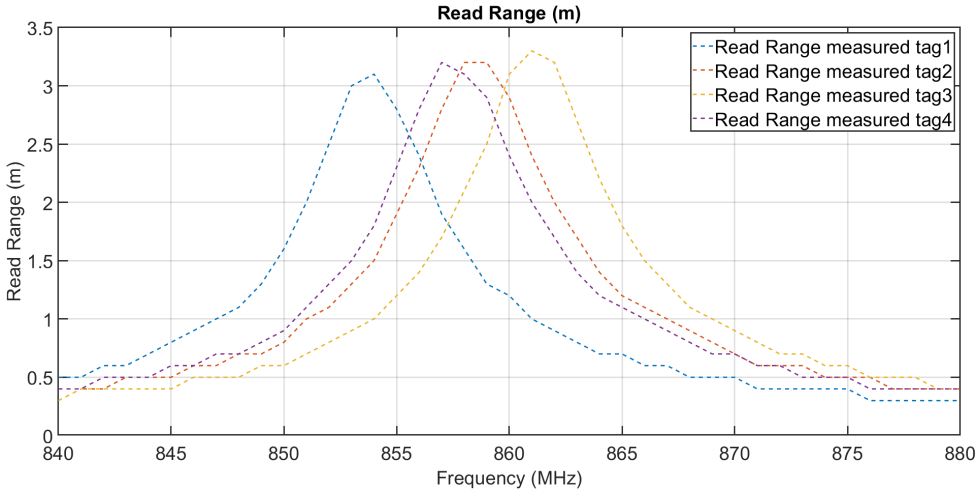

Figure 3.6: Comparison of identical RFID tags to demonstrate the low yield of the RFID chip

3.4 Designs of UHF RFID antenna-tags for sensing applications in metallic environment

One task of the thesis has been the conception, design, fabrication, and validation of different RFID tag-antennas. In general, since the RFID sensor tags are intended to be operating in proximity to metallic surfaces, all the designed RFID tag-antennas followed some specific design lines:

- The designed RFID tag-antennas include a ground plane, aiming to confine the electric field between at least two metallic layers. With this technique the RFID tag-antenna is less susceptible to the metallic environment. Typical antenna structures with this characteristic used as inspiration are the patch antennas and the Inverted-F antennas.

- The used substrate has a high value of permittivity, for miniaturization purposes, and with low losses for read range maximization.

In the next section, different RFID tag-antennas based on the above design lines will be presented and discussed.

3.4.1 Circular UHF RFID tag-antenna

One of the developed designs was a three layers circular RFID tag-antenna with a capacitive feed in the middle layer, as presented in Fig. 3.7. This design was inspired by [96].

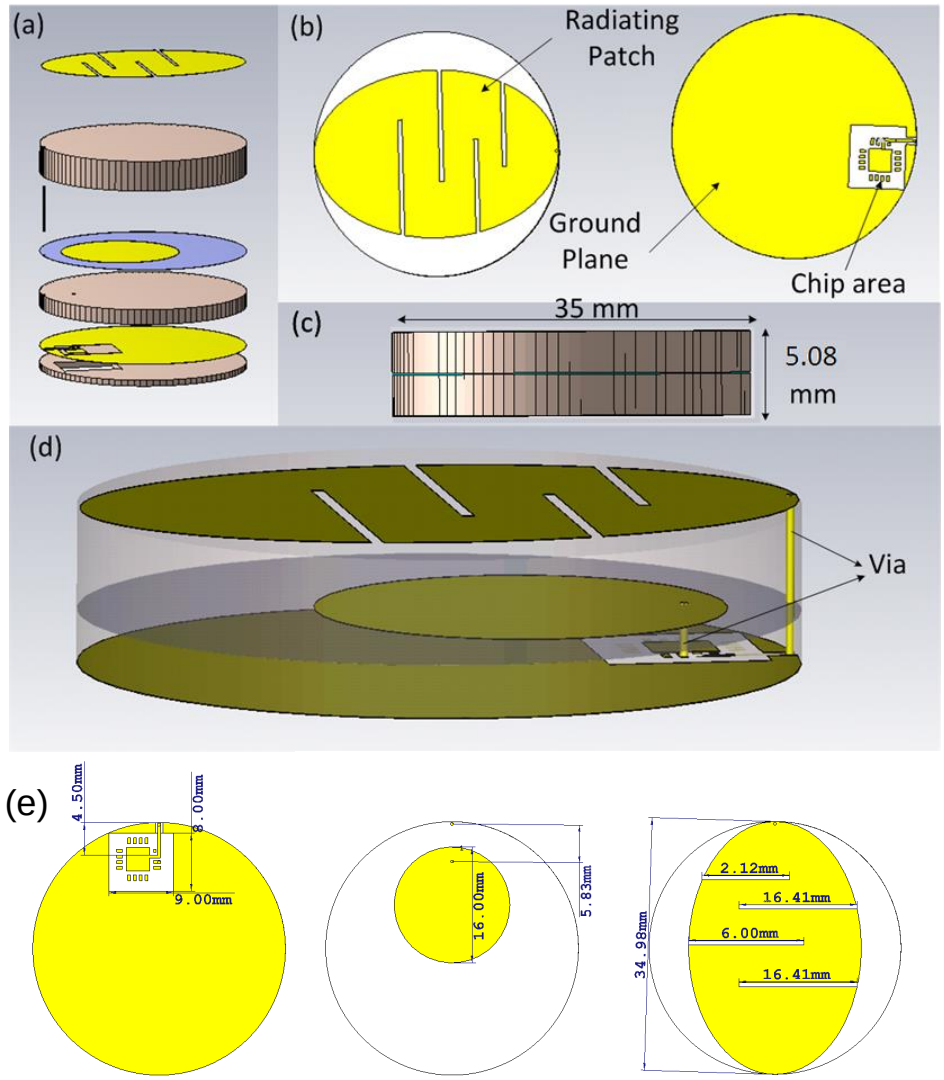

Figure 3.7: Circular RFID tag-antenna: (a) RFID tag-antenna profile, (b) RFID tag-antenna top and bottom view, (c) RFID tag-antenna dimension, (d) position of via, (e) dimension of each layer

The RFID tag-antenna is composed of three layers:

- *Top layer*: In the top layer is positioned the radiating patch with a number of slits in order to elongate the current path and reduce the physical dimensions. The top layer is connected through a metalized

via to the bottom layer realizing the connection to the RFID chip, as depicted in Fig. 3.7(d).

- *Middle layer*: In the middle layer there is a circular trace which acts as a capacitive feed and it is in parallel to the radiating patch. The distance between the middle layer and the top layer is dictated by the thickness of the substrate (2.54 mm). The size of the capacitive feed is impacting the impedance of the RFID tag-antenna as illustrated in Fig. 3.8. As the radius of the capacitive feed increases the resonance frequency shifts to lower values. A metalized via is connecting the middle layer to the bottom layer and the RFID chip.

- *Bottom layer*: In the bottom layer there is the ground plane and the designated space for the RFID chip. The connection between the via and the RFID chip is realized by a small transmission line with width 0.4 mm. The RFID chip is soldered at the bottom of the RFID tag-antenna leading to the need of a thin superstrate to keep the RFID tag in place (see Fig. 3.7(a)-(b)).

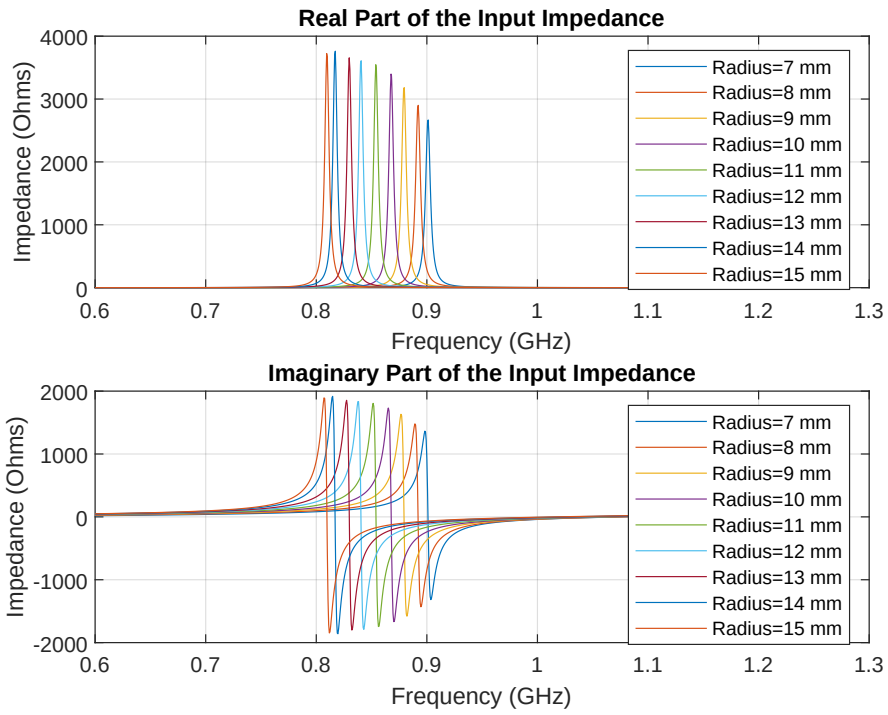

Figure 3.8: Real and imaginary part of the impedance of the circular RFID tag-antenna versus the radius of the circular feed

The radiation characteristics of the circular RFID tag-antenna are presented in Fig. 3.9 where the maximum gain of the RFID tag-antenna is -2.41 dBi at 868 MHz when operating on a metallic surface with

dimensions 20 $cm \times 20\ cm$, with radiation efficiency of 13% or -9 dB. The directivity, in this case, is 6.57 dBi.

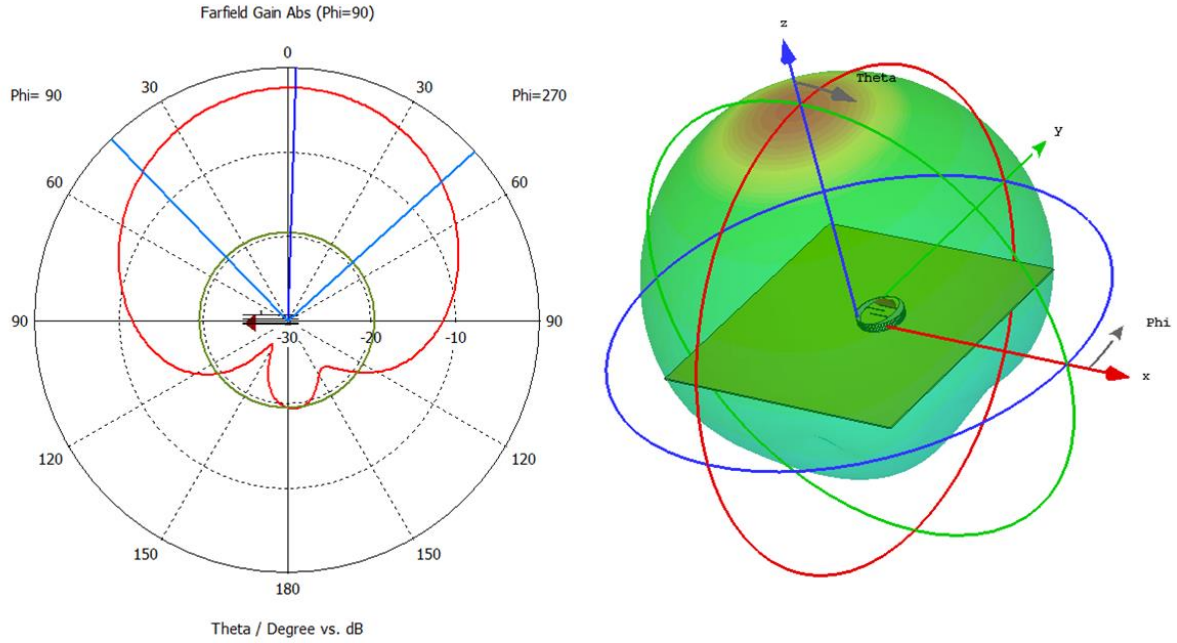

Figure 3.9: Radiation pattern of the circular RFID tag-antenna

The circular RFID tag-antenna was fabricated in the laboratory with a Computer Numerical Control (CNC) equipment. The substrate which was used is the Rogers RT6010.2LM [97] with permittivity of $\epsilon_r = 10.2$ (10.6 for designing) and losses $Tan\delta = 0.0023$. The fabricated prototype is illustrated in Fig. 3.10(a). The RFID tag was measured in the environment of an anechoic chamber to evaluate the maximum read range as depicted in Fig. 3.10(b). One advantage of the design of this particular RFID sensor tag, was the tuning capability due to the slits on the top layer. By using copper tape with conductive adhesive on the slits, a small tuning of the resonance frequency was possible. Due to this tuning, the resonance frequency could be corrected to be inside the 865-868 MHz frequency band.

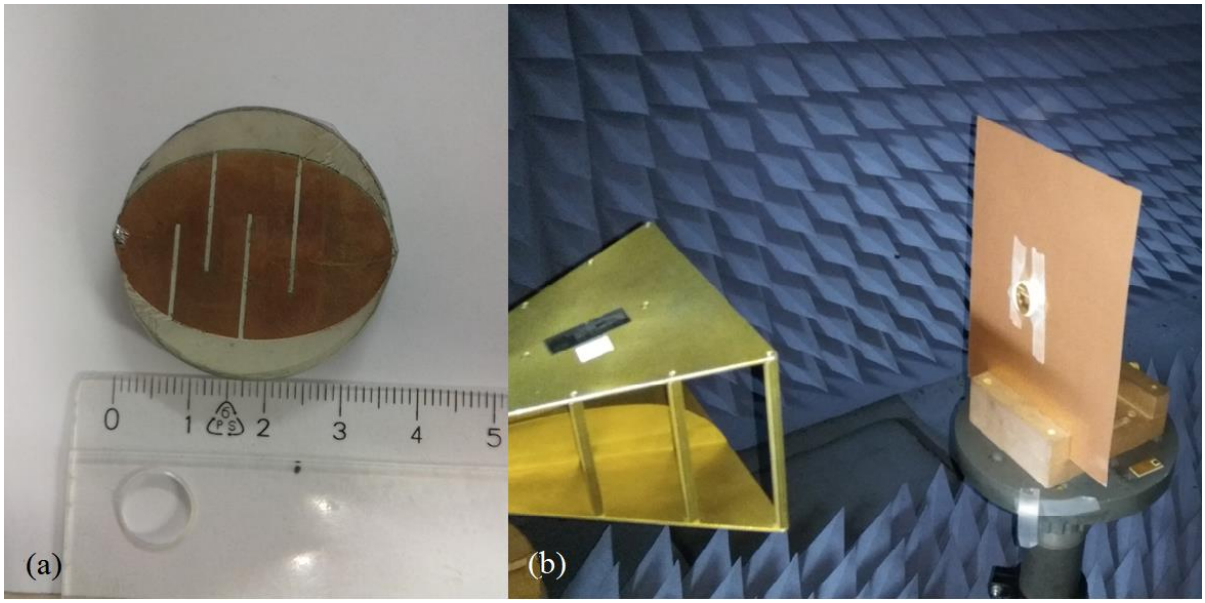

Figure 3.10: (a) Fabrucated prototype of the circular RFID sensor tag (b) Measurement of the read range in the anechoic chamber

The Tagformance Pro RFID reader was used to perform the measurements and the theoretical read range over frequency measured is presented in Fig. 3.11 compared to the read range expected from the simulation results, for different power thresholds of the RFID chip. According to the measurement results, there is a deviation between the calculated read range and the measured one. The reason for this deviation was attributed to the realization process, which was not as accurate as possible and to a possible polarization mismatch.

The read range of the circular UHF RFID sensor tag was based on the simulated data and was calculated by the following equation:

$$R = \frac{\lambda}{4\pi}\sqrt{\frac{EIRP \cdot G \cdot \tau}{P_t}} \tag{3.3}$$

Where R is the read range in meters, λ is the wavelength in meters, $EIRP$ is the effective isotropic radiation power transmitted by the RFID reader in watts, G is the gain of the RFID tag-antenna, τ is the coefficient of power transmission in the RFID chip and P_{th} is the power threshold for the RFID chip to activate in watts. In the above calculation it has been assumed that the RFID reader is transmitting the maximum allowed power according to the ETSI regulation, 2W Effective radiated power (ERP) which

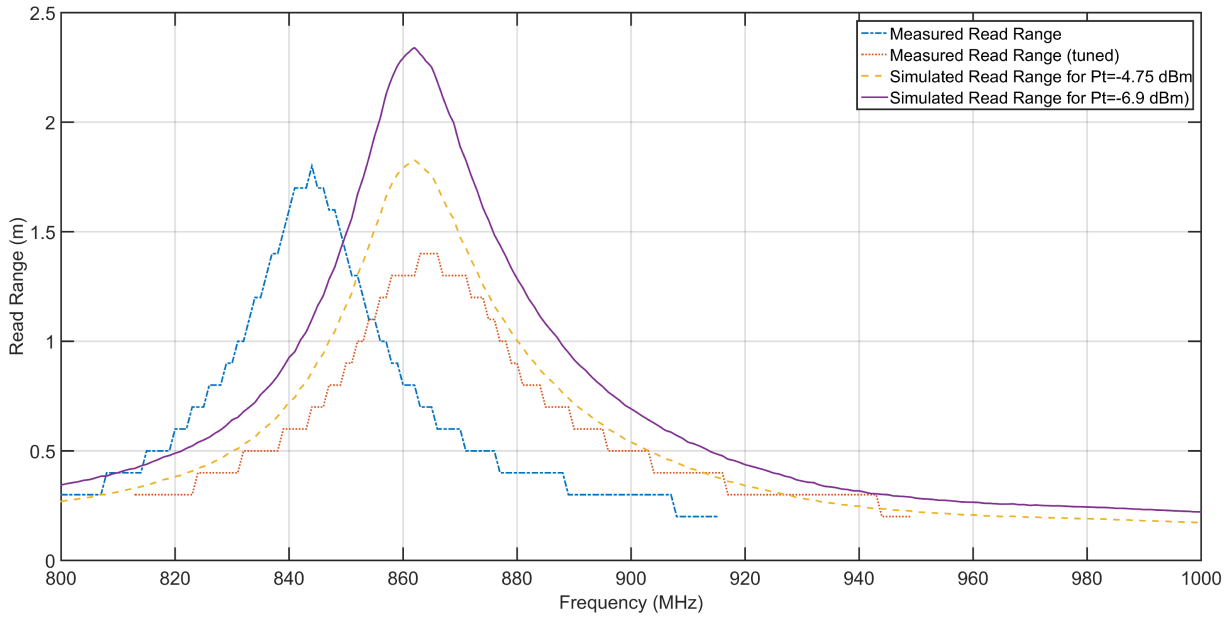

Figure 3.11: Measured theoretical read range and calculated read range from simulation results

corresponds to 33 $dBm + 2.15\ dB = 35.15\ dBm$ of EIRP. Also, it has been assumed that there will be no loses due to polarization mismatch.

In addition, as mentioned before, the input impedance of the RFID chip was a matter of confusion due to the variation of the nominal impedance value in the datasheets. Due to this confusion, the RFID tag-antenna was designed to be matched to the former value of impedance which yield different results than the latter value of impedance. This difference for the two values of impedances can be observed in Fig. 3.12.

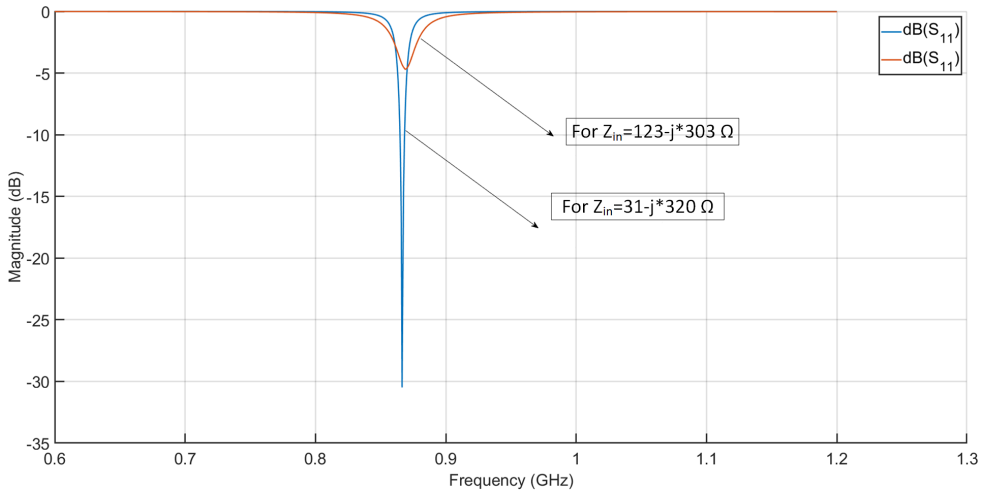

Figure 3.12: S11 parameters for different RFID chip input impedance values

3.4.2 Rectangular UHF RFID tag-antenna corresponding to $\lambda/2$ length

Besides the size and the performance attributes, another merit which should be taken into account is the ease of realization. The previously presented, circular design of RFID tag-antenna, poses a level of complexity which is enough to make the fabrication process more difficult and the cost of realization higher. From this perspective, another design was realized aiming to maintain more simplicity and to lower the cost of fabrication by utilizing two metallic layers and a simpler geometry.

Another RFID tag-antenna design attempt, was a rectangular design, utilizing a ground plane. The length of the RFID antenna-tag is relative to the $\lambda/2$ electrical length for the frequency of operation (in the 865-868 MHz ETSI frequency band). The substrate used in this design was the Rogers RT 6010.2LM, with thickness 2.54 mm, the permittivity of $\epsilon_r = 10.2$ and losses Tanδ = 0.0023. The design of the RFID tag-antenna is presented in Fig. 3.13.

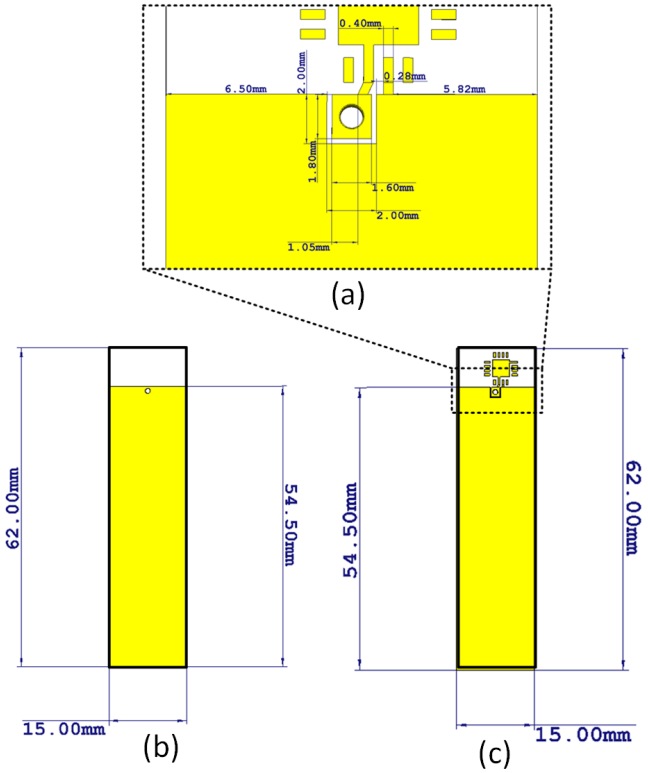

Figure 3.13: Rectangular RFID tag-antenna corresponding to λ/2 length. (a) the dimension of the feeding area (b) bottom view (c) top view

The overall length is exceeding by 2 mm the specification limit, but it is an acceptable deviation.

The presented RFID tag-antenna was designed and simulated with CST microwave studio to evaluate the performance regarding the parameters, S11, directivity, radiation efficiency, and gain. The simulation was conducted when the tag-antenna was placed on a metallic plate (copper) of size $80\ mm \times 120\ mm$.

One interesting feature for the used substrate value is the permittivity value. The RT6010.2LM substrate according to the respective datasheet has a permittivity of $\epsilon_r = 10.2$ and for the designing stage a higher value of around 10.6 should be used. However, this substrate is quite anisotropic and depending on the orientation and the strength of the electric field it can exhibit different permittivity values. For instance, the permittivity of the substrate for the z-axis is 10.6 but for the y-axis and x-axis the permittivity is 13.33. Hence, the permittivity value for designing purposes can vary from 10.6 to 11.4 as reported in [98]. This property was used after the initial fabrication of prototypes in order to compensate for any frequency shift between measured and simulated results. For this particular design the value of permittivity which was used is $\epsilon_r = 11.3$.

The results of the simulation are presented below in Fig. 3.14 –Fig. 3.16. The RFID tag-antenna is designed to be matched with the RFID chip of AMS SL900A.

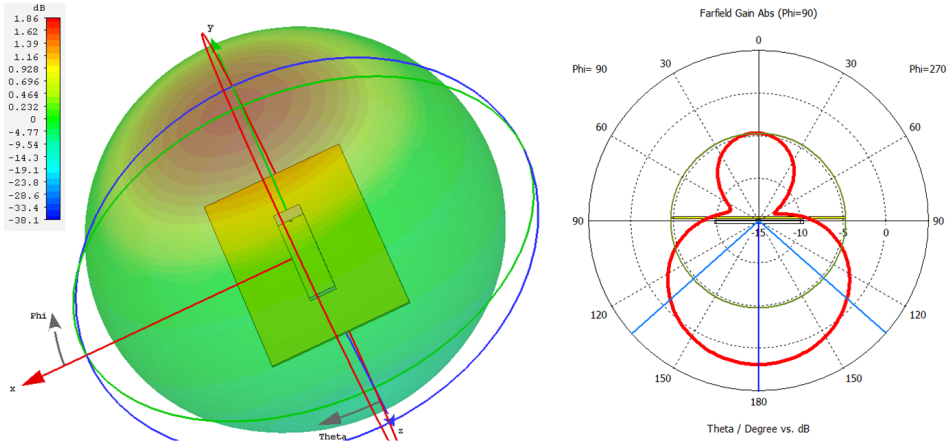

Figure 3.14: Gain of RFID tag-antenna

The maximum gain simulated for the RFID tag-antenna is 1.86 dBi (see Fig. 3.14) with the directivity at 4.97 dBi (see Fig. 3.15). The RFID tag-antenna has one main lobe vertical to the level of the radiating surface. The RFID tag-antenna is positioned with the top side (Fig. 3.13(c)) facing the metallic surface in the background. This configuration was selected due to the fact that with this positioning the RFID chip is attached to the metallic surface and thus the integrated temperature sensor of the RFID chip can monitor

better the temperature of the desired metallic surface. This characteristic will be further explored in §5.2 In a different configuration where the chip and metallic surface would be separated by the substrate material of the RFID tag-antenna the temperature measured by the sensor wouldn't be as accurate. This issue will be discussed in more extend later on.

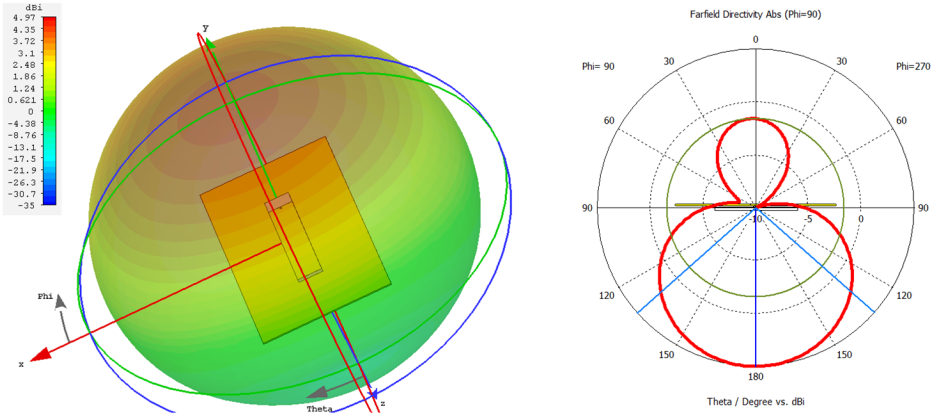

Figure 3.15: Directivity of RFID tag-antenna

In Fig. 3.16 the reflection coefficient (S11) is presented, where the minimum value of -9.5 dB is corresponding to 868 MHz.

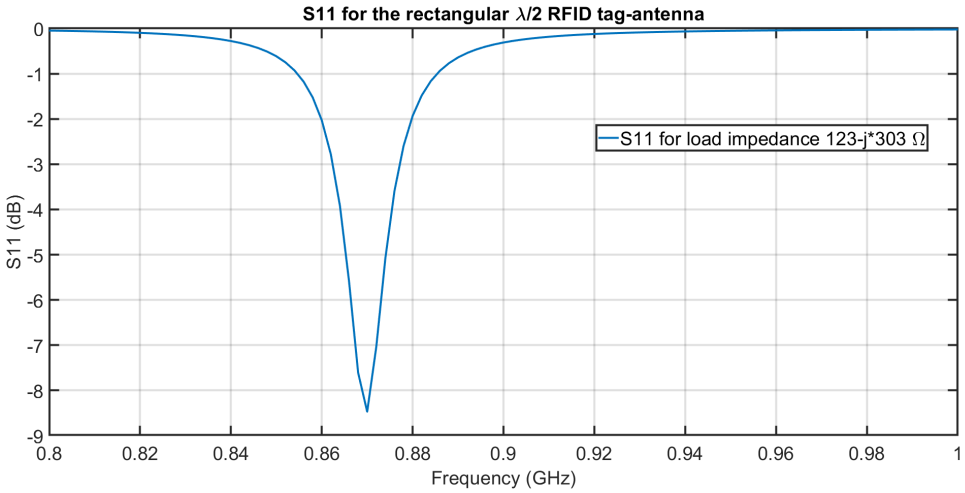

Figure 3.16: S11 of RFID tag-antenna

The gain and radiation efficiency are illustrated in Fig. 3.17 where the maximum gain is 2.2 dBi at 928 MHz and the radiation efficiency reaches 51%.

The proposed design of the RFID tag-antenna corresponding to $\lambda/2$ tag-antenna was fabricated and

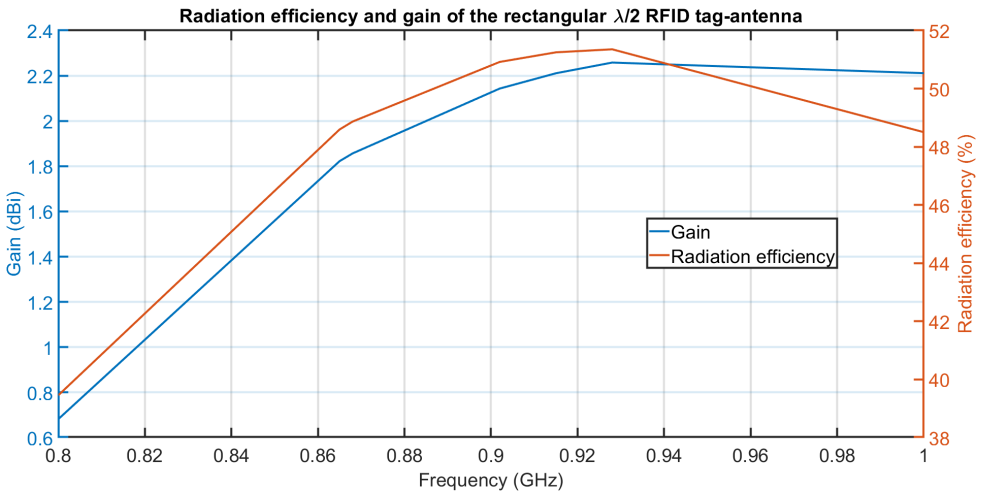

Figure 3.17: Gain and radiation efficiency of RFID tag-antenna

shown in Fig. 3.18. The measured read range is compared to the read range calculated from (3.3) by using the results of the simulation (see 3.19).

Figure 3.18: Fabricated $\lambda/2$ UHF RFID sensor tag

A deviation between the results of measurement and simulation is due to the value of threshold power reported in the RFID chip's datasheet (-6.9 dBm). From the measurements conducted in a series of prototypes the value of threshold power is closer to the value of -4.75 dBm which is actually matching the value reported in the datasheet if a dipole antenna with gain 2.15 dBi is connected to the chip.

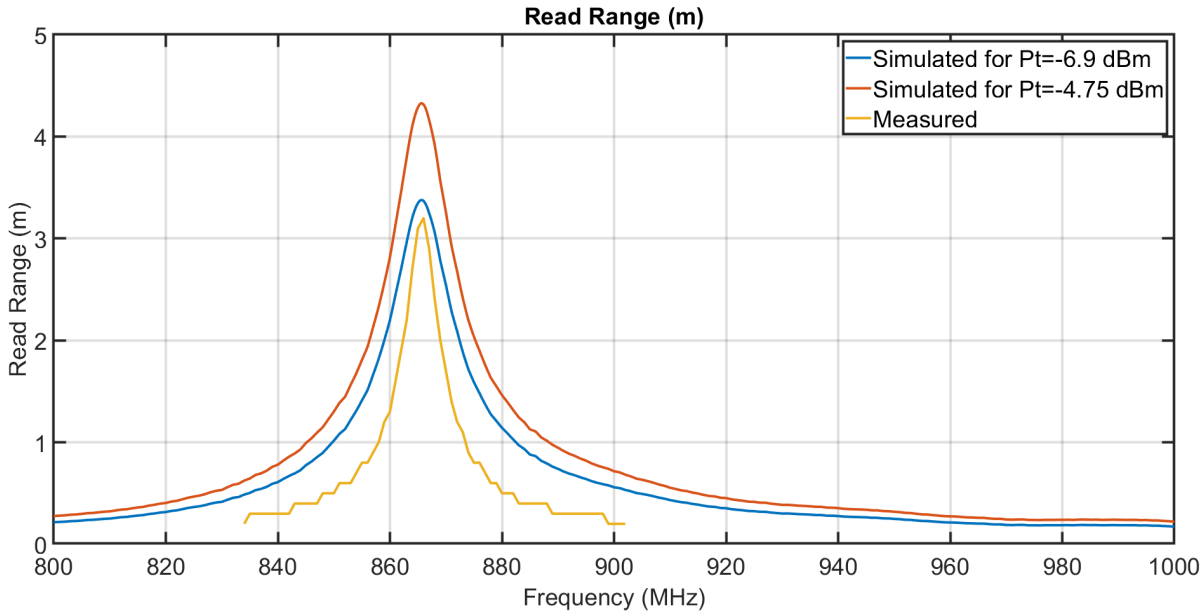

Figure 3.19: Read range of the RFID tag

3.4.3 Rectangular UHF RFID tag-antenna corresponding to $\lambda/4$ length

The next proposed UHF RFID antenna-tag is designed to exhibit the best performance when it is placed on a metallic surface, as the previous designs. In order to minimize the effects due to the impact of the nearby metal, the electric field in this antenna structure is confined between two parallel, with uneven length, copper plates. A set of metalized vias are connecting the top and the bottom layer of the RFID antenna in order to short-circuit these two layers and extend the length of the current path. The overall length of the tag-antenna corresponds to $\lambda/4$, where λ is the wavelength of the frequency of operation. A substrate with thickness 2.54 mm, permittivity ϵ_r = 10.2 (10.6 for designing) and losses Tanδ = 0.0023 (Rogers RT6010.2LM) was used. Hence, the design of the proposed antenna for the UHF RFID antenna-tag is mainly a $\lambda/4$ resonator as presented in Fig. 3.20.

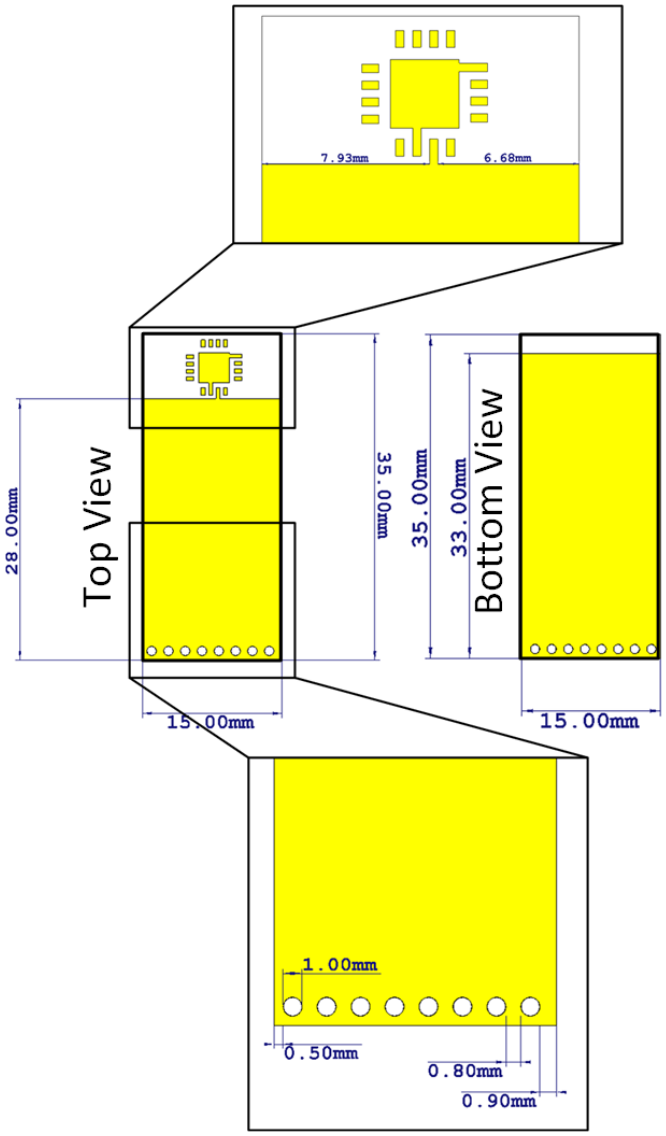

Figure 3.20: UHF RFID antenna-tag corresponding to $\lambda/4$

Flipping UHF RFID sensor tag

This RFID tag presents a quite interesting feature regarding the frequency operation. Flipping the tag in respect to a metallic surface, a dual-band operation can be achieved depending on which of the two sides of the tag is closer to the metallic surface. The uneven layers of the RFID antenna-tag present different capacitances, depending on which side is closer to the metallic plane, hence the impedance of the RFID antenna-tag differs in each case. The two cases are illustrated in Fig. 3.21.

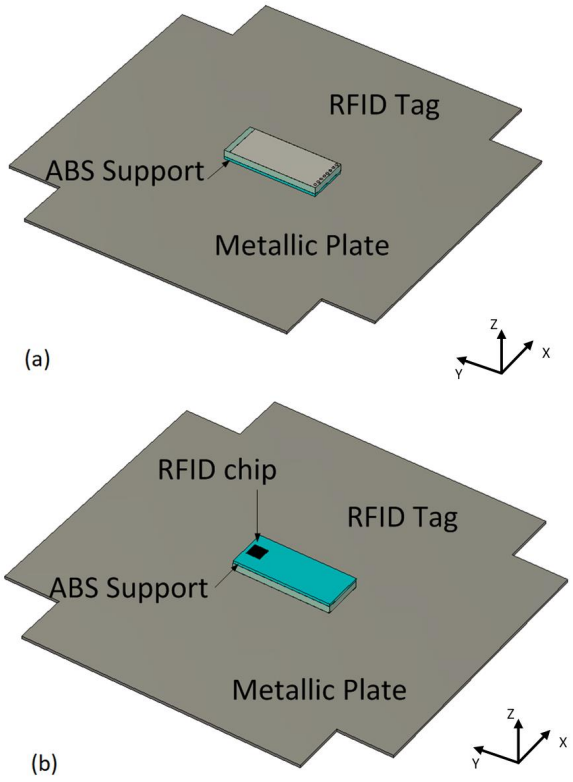

Figure 3.21: λ/4 UHF RFID antenna tag on a metallic plane (a) with the top side closer to the metallic plane (b) with the bottom side closer to the metallic plane

In the one side of the UHF RFID tag-antenna, there will be the RFID chip (AMS SL900A), hence for practical reasons and in order the UHF RFID sensor-tag to be positioned with either side (top or bottom) on a flat metallic surface, a support with thickness 1 mm and a square hole (to accommodate the RFID chip) was fabricated in a 3D printer made by the Acrylonitrile Butadiene Styrene (ABS) material. This support is visible in Fig. 3.21. Due to the 3D printing technique, the support is not homogeneous, having small air gaps across the whole surface. The permittivity and losses of the ABS support were measured in a DAMASKOS thin sheet tester cavity [99] to be ϵ_r = 2.29 and Tanδ = 0.005, respectively. The total dimensions of the UHF RFID sensor-tag are $35\ mm \times 15\ mm \times 3.54\ mm$, including the thickness of the RFID chip and the ABS support.

A numerical model of the RFID antenna was initially designed and simulated in the CST microwave studio 2016 [64]. In the simulation, a metallic plate surface with dimensions of $140\ mm \times 140\ mm$ was used. The simulations were performed when the metallic plate was placed either on the top side or the

bottom side of the RFID sensor-tag. In order to quantify the effects of the metallic plate on the RFID antenna, an exploration of the impact of the distance between them was performed. The two cases are called here in after as scenario (a) and scenario (b) and they are illustrated in Fig. 3.21. In addition, a third scenario will be examined regarding the operation of the RFID antenna in free space with the notation of "free space scenario".

For the scenario (a) the distance between the RFID antenna and the metallic plate was explored for increments of 0.25 mm from 0 mm to 1 mm, while in scenario (b) the exploration was performed for increments of 1 mm from 0 mm to 4 mm. This difference of explored distance ranges between the two scenarios is due to a set of preliminary simulations where the main effects of the metallic plate in each case have been dominant in the aforementioned ranges.

The change of the input impedance of the RFID antenna in both scenarios is presented in Fig. 3.22 and Fig. 3.23, respectively.

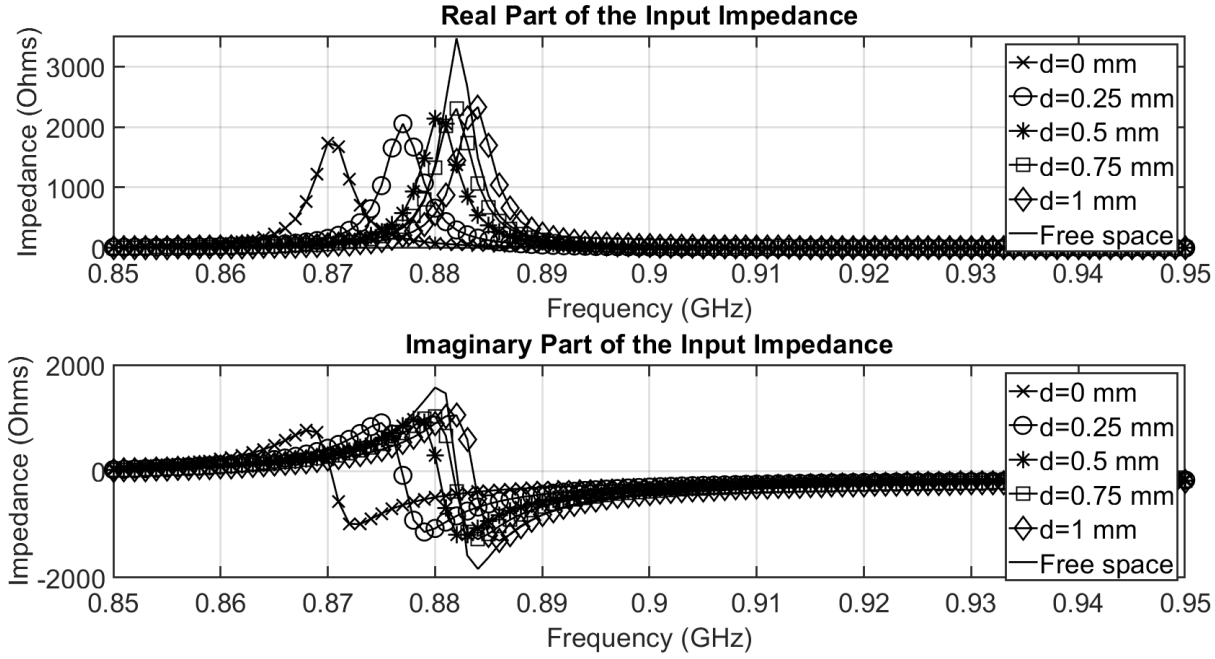

Figure 3.22: Simulated input impedance of the UHF RFID tag for scenario (a)

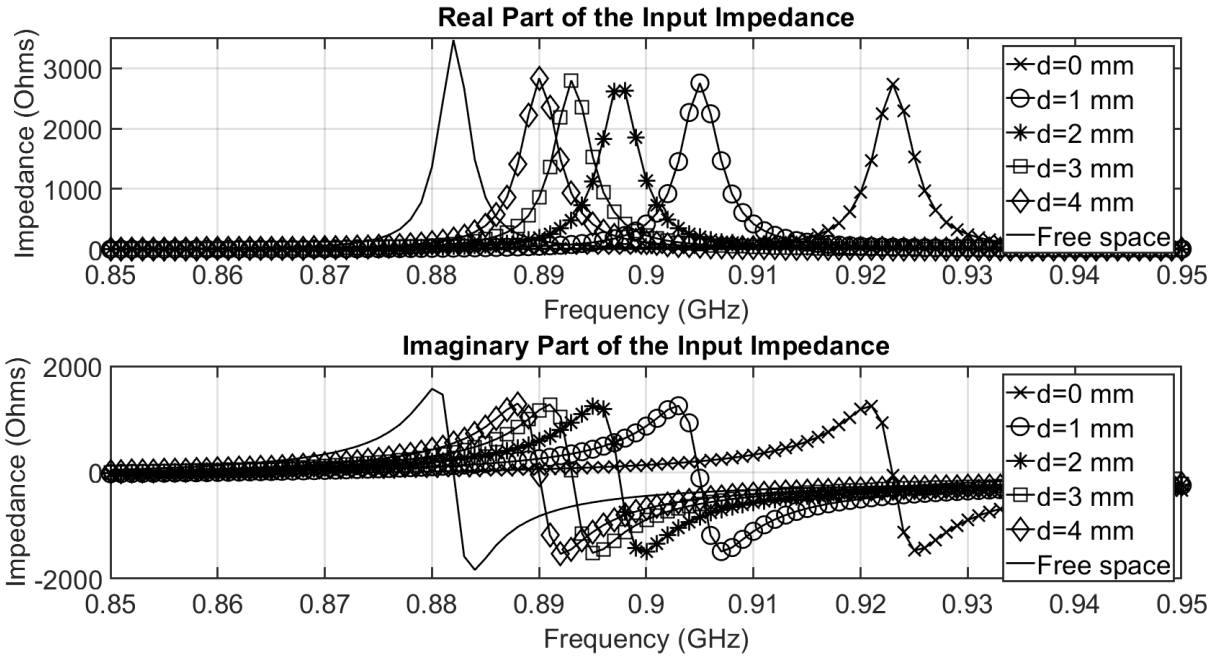

Figure 3.23: Simulated input impedance of the UHF RFID tag for scenario (b)

It is important to note that when the distance increases the resonance frequency follows opposite directions depending on the considered case. For the scenario (a) the resonance is moving towards higher frequency value, while for the scenario (b) the resonance is shifted towards lower frequency value. As the distance between RFID antenna and the metallic plate continues to increase further, the input impedance of the two scenarios will converge and match the case where the RFID antenna is simulated in a free space scenario. It is interesting to note that for scenario (a) the resonance frequency reaches 884 MHz at the distance of 1 mm and as the metallic plate moves further, decreases at the 882 MHz of the free space case. This behavior is due to the specific electromagnetic interaction between the metallic plate and the tag-antenna.

In addition, the gain of the RFID antenna for the proposed scenarios was simulated and presented in Fig. 3.24. For the free space scenario, the gain is considerably lower due to the fact that the RFID antenna was designed taking into consideration the existence of metallic surface in the vicinity. Such a metallic environment favors the reflections and eventually results in an increase of the directivity of the antenna ($5.63\ dBi$ for scenario (a), $5.69\ dBi$ for scenario (b) and $1.68\ dBi$ for free space scenario). The corresponding radiation efficiency is 0.282, 0.316 and 0.106, respectively.

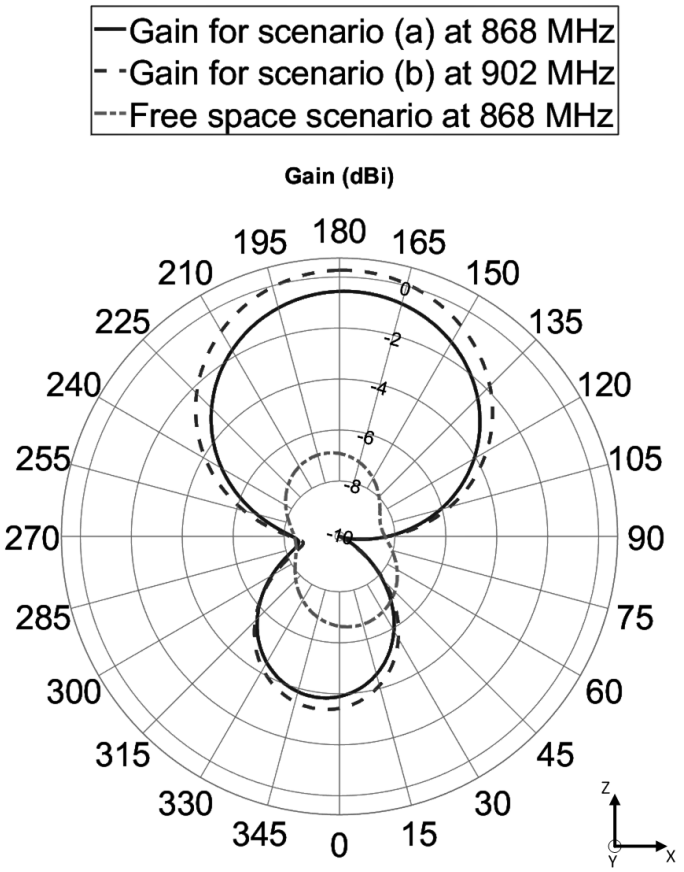

Figure 3.24: Radiation pattern for each scenario

Characteristics of the radiating properties of the UHF RFID antenna-tag

Aiming to provide a better understanding of the UHF RFID sensor tag behavior based on its position over a metallic plane, a further study was held. The two scenarios can be considered as two different antenna geometries and the geometry of the antenna has a major impact on the radiation characteristics.

When the RFID tag-antenna structure is included between perfect electric or magnetic conducting walls, standing waves with the appropriate wavelength can exist as long as the distance between the perfect conducting walls is a perfect product of the multiplication of the half-wavelength. Once such a solution has been discovered, more fitting solutions and their distribution can be predicted. The standing wave of the RFID tag-antenna structure inside the perfect conducting walls is referred to as Eigen-mode. The formulation of the described problem can be derived from Maxwell equations and the solutions can be predicted by 3D electromagnetic simulation. Two sets of solutions can be acquired. A set for $\omega = 0$ (static fields)

and a set for $\omega \neq 0$ for resonant solutions, where ω the angular frequency. Having a trivial solution such as $\omega = 0$ yields that the discretized equation matrix will have vanishing eigenvalues. By imposing additional constraints, non-static, numerical solutions can be extracted. The quantity ω is the eigenvalue while the vector of the electric field E is the eigenvector. More information regarding the numerical calculation of the resonance frequencies can be found in [100].

The goal was to see which are the eigenvalues or natural resonance frequencies of the first 3 modes of the RFID tag structure with the presence of metallic surface either according to scenario (a) or scenario (b). The natural resonance frequencies simulated are presented in Table 3.2

Table 3.2: Eigen-Mode simulation results

Mode	**Resonance frequency for scenario (a)**	**Resonance frequency for scenario (b)**
1	$0.782\ GHz$	$0.815\ GHz$
2	$2.292\ GHz$	$2.439\ GHz$
3	$3.084\ GHz$	$3.214\ GHz$

The difference of the natural resonance frequency of the first and dominant mode for the two scenarios (a) and (b) is 33 MHz (782 MHz and 815 MHz respectively). This difference of 33 MHz is quite convenient since the minimum difference between ETSI and FCC frequency bands is 34 MHz (upper ETSI frequency 868 MHz and lower FCC frequency 902 MHz). During the Eigen-mode simulation, no losses were taken into consideration and all the metallic parts were treated as PEC.

Equivalent circuit of the flipping UHF RFID tag-antenna

In order to explore further the effects of the metallic plate to the behavior of the RFID antenna, an equivalent circuit of the proposed tag was heuristically constructed based on the proposed model in [101]. The constraints for creating the equivalent model were oriented towards the agreement with the simulated data regarding the real and imaginary part of the input impedance and the quality factor Q, over the bandwidth around the resonance, when the RFID antenna was placed in a free space scenario. The selected circuit topology, which is a 5-elements parallel RLC circuit, is presented in Fig. 3.25.

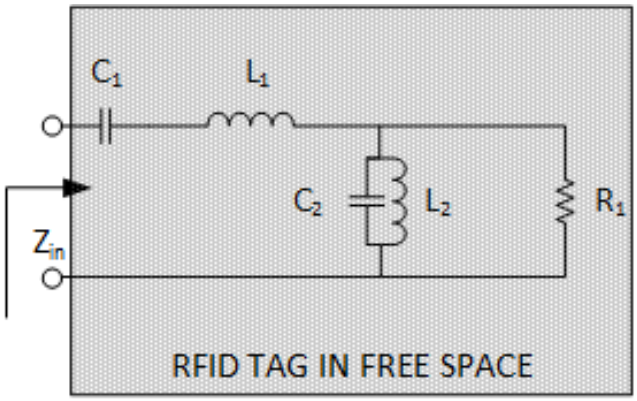

Figure 3.25: Equivalent circuit of the RFID tag in free space

The components C_2 and L_2 correspond to the reactance of the antenna and their parallel combination to the resonance frequency, while the value of R1 corresponds to radiation phenomena. The series component C_1 represents the reactance of the antenna in lower frequencies (compared to the resonance frequency) and the component L_1 the reactance at high frequencies.

The values of the components found in the free space scenario are presented in Table 3.3.

Table 3.3: Component values of the equivalent circuit of the RFID tag in a free space scenario

$C_1\ (pF)$	$L_1\ (nH)$	$C_2\ (pF)$	$L_2\ (nH)$	$R\ (k\Omega)$
0.9	15.6	14	2.325	3.4

The comparison between the real and imaginary parts of input impedance as well as the Q factor between the simulated model of the RFID antenna and the equivalent circuit in free space are illustrated in Fig. 3.26.

Previously, it was shown that depending on the distance of the RFID antenna and the metallic plate, the resonance frequency of the RFID antenna was shifting in both scenarios (a) and (b). As the metallic plate was moving further away, the result for both scenarios was to converge to the results of the RFID antenna in the free space scenario. Based on this result, the effects of the metallic plate could be modeled by adding an extra parallel RLC circuit to the equivalent circuit of the free space scenario, as it is illustrated in Fig. 3.27.

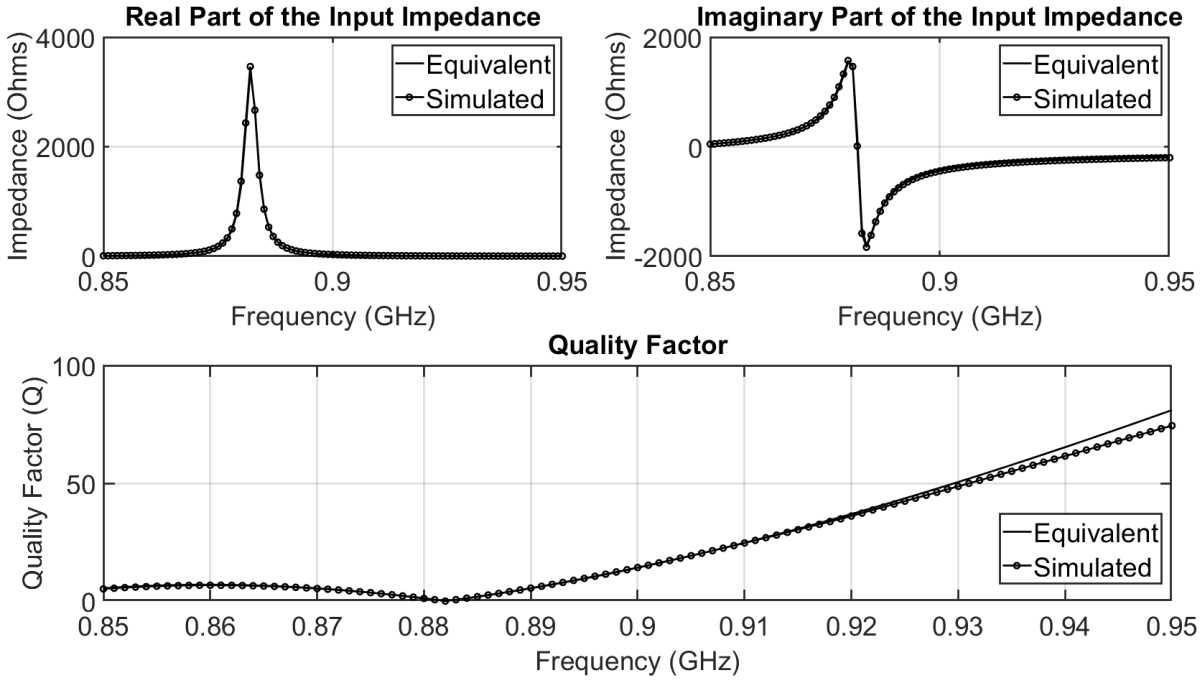

Figure 3.26: Comparison of simulated and equivalent model impedance and Q factor of the RFID tag in free space

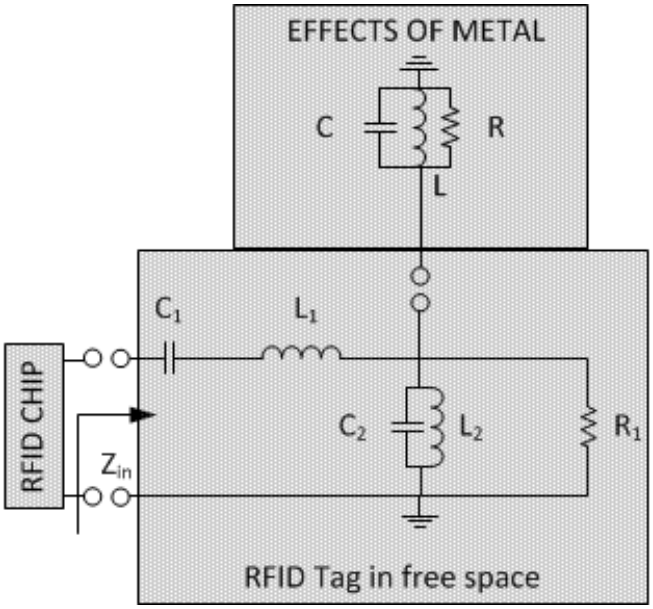

Figure 3.27: Equivalent circuit of the RFID antenna with the effects of the metallic plate as a parallel RLC circuit

The physical interpretation of the components C, L and R correspond to the additional capacitance, inductance and resistance, respectively, added to the antenna structure due to the metallic surface.

By adding the parallel RLC circuit, there will be a parallel combination of the two inductors (L_2 and L), the two capacitors (C_2 and C) and the two resistors (R_1 and R). Since in both scenarios there is a convergence towards the free space values, it can be seen that C should be decreased so that the parallel combination with C_2 will result eventually to C_2. Similarly, the L and R should be increased so that their parallel combination with L_2 and R_1 to converge to the reported values of the free space model.

To demonstrate this behavior, the simulated scenarios (a) and (b) for different distances with regard to the metallic plate, were modeled with the equivalent parallel topology and compared with the simulation results.

In Table 3.4 the values of each component of the parallel RLC circuit are reported.

Table 3.4: Values of the components of the RFID antenna equivalent model for different distances

Scenario (a)							
$Distance$ (mm)	$C\ (pF)$	$L\ (nH)$	$R\ (k\Omega)$	$C_p\ (pF)$	$L_p\ (nH)$	$R_p\ (k\Omega)$	$f_p\ (GHz)$
0	6.14	5.81	3.9	20.1	1.66	1.81	0.870
0.25	4.60	7.44	4.9	18.6	1.77	2.01	0.876
0.5	3.40	9.76	6.6	17.4	1.88	2.25	0.880
0.75	2.70	12.1	7.6	16.7	1.95	2.35	0.882
1	2.28	13.9	8.1	16.3	1.99	2.39	0.884
Scenario (b)							
$Distance$ (mm)	$C\ (fF)$	$L\ (nH)$	$R\ (k\Omega)$	$C_p\ (pF)$	$L_p\ (nH)$	$R_p\ (k\Omega)$	$f_p\ (GHz)$
0	1	25.1	9.68	14	2.12	2.51	0.922
1	1	43.5	9.77	14	2.20	2.52	0.905
2	1	63.1	10.0	14	2.24	2.54	0.898
3	1	92.0	11.0	14	2.26	2.60	0.893
4	1	130	11.4	14	2.28	2.69	0.889

Note:C_p, L_p, R_p, and f_p are respectively the capacitance, inductance, resistance and resonance frequency of the parallel combination

Table 3.4 shows that for the scenario (b) the capacitor C acquires very low values. The equivalent model matches the simulated data for zero capacitance in this case. For the sake of generality though, a very small value of capacitance was given in this case which is not affecting the parallel combination with the much higher values of C_2. In general, this kind of equivalent topology matches the characteristics of the simulated

data in the level of resonance frequency via the values of L_p and C_p according to (3.4). The value of R_p matches the value of the real part of impedance at the resonance frequency.

$$f_p = \frac{1}{2\pi\sqrt{L_p C_p}} \tag{3.4}$$

Overall, there is a very good agreement between the equivalent model of the RFID antenna and the results of the simulations for the different values of the distance. Finally, it is important to note that all the simulations presented so far were performed with a reference impedance of 50 Ω and the results presented so far should not be confused with the response of the RFID tag which will be presented according to the input impedance of the RFID chip. The comparison between the simulated data and the data of the equivalent circuit model (i.e., real/imaginary parts of impedance, Q-factor) for the two scenarios are presented in Fig. 3.28 and Fig. 3.29.

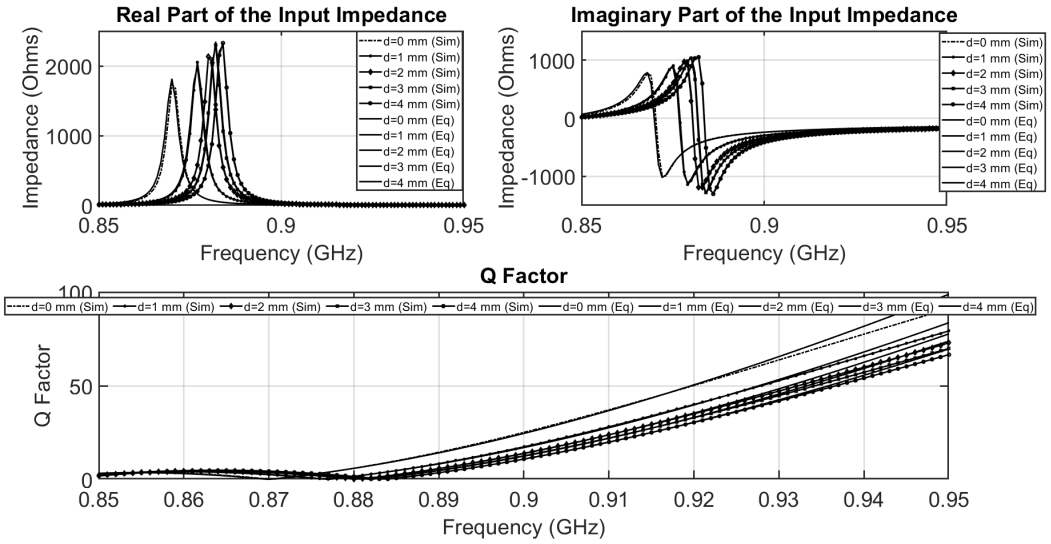

Figure 3.28: Comparison of the real and imaginary values of impedance and Q factor of the simulated RFID antenna and the equivalent circuit for scenario (a) for different values of distance between RFID antenna and metallic plate

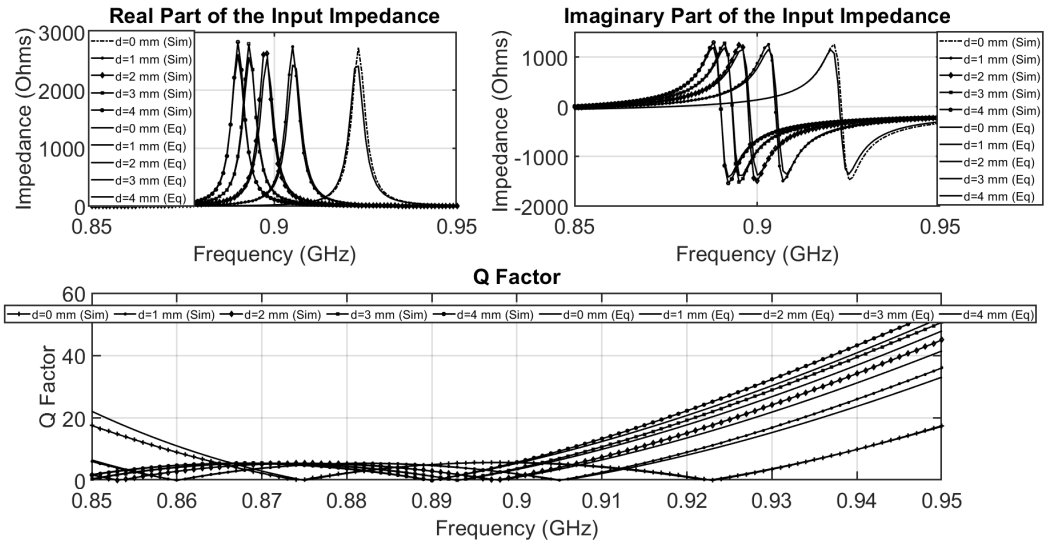

Figure 3.29: Comparison of the real and imaginary values of impedance and Q factor of the simulated RFID antenna and the equivalent circuit for scenario (b) for different values of distance between RFID antenna and metallic plate

Fabrication and measurements of the UHF RFID sensor tag

A number of prototypes of the designed RFID antennas were fabricated, with the RFID chip SL900A soldered, as it is presented in Fig. 3.30.

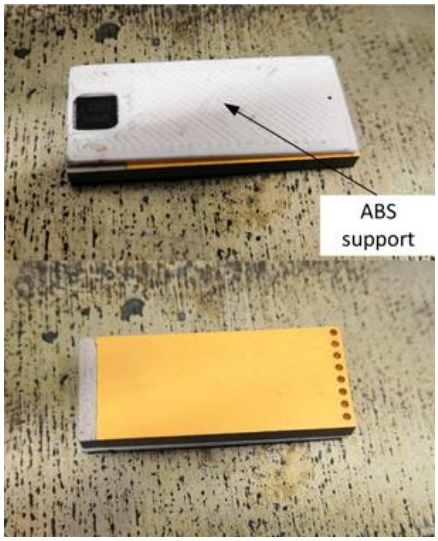

Figure 3.30: Fabricated UHF RFID tag

Initially, one of the prototype RFID antennas was connected to an SMA connector in order to be tested

with a VNA, aiming to compare the results of the measurement with the simulated results. In order to avoid discrepancies due to the existence of a metallic surface next to the SMA connector, the RFID antenna was measured only in a free space scenario.

In Fig. 3.31. the comparison between the S11 parameter and the real and imaginary part of the impedance of the measured and the simulated results are presented. There is a good agreement as far as the resonance frequency is concerned. However, there is a discrepancy regarding the maximum values of the real and imaginary part around the resonance. This discrepancy is due to the effects of the SMA connector as well as due to the addition of solder on the RFID antenna.

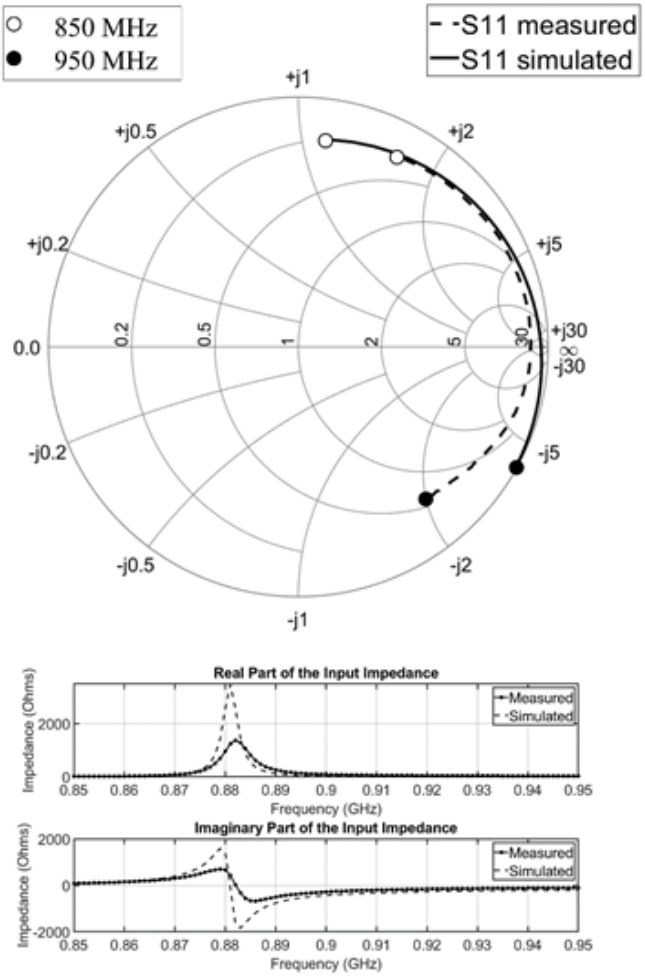

Figure 3.31: Measured and simulated results of the RFID antenna in a free space scenario

Afterward, the RFID antenna with the RFID chip mounted was tested in the two scenarios (a) and (b) as

well as in a free space scenario by using the Voyantic RFID reader Tagformance Pro. From this setup, the read range of the UHF RFID sensor-tag for each scenario was extracted and is presented in Fig. 3.32.

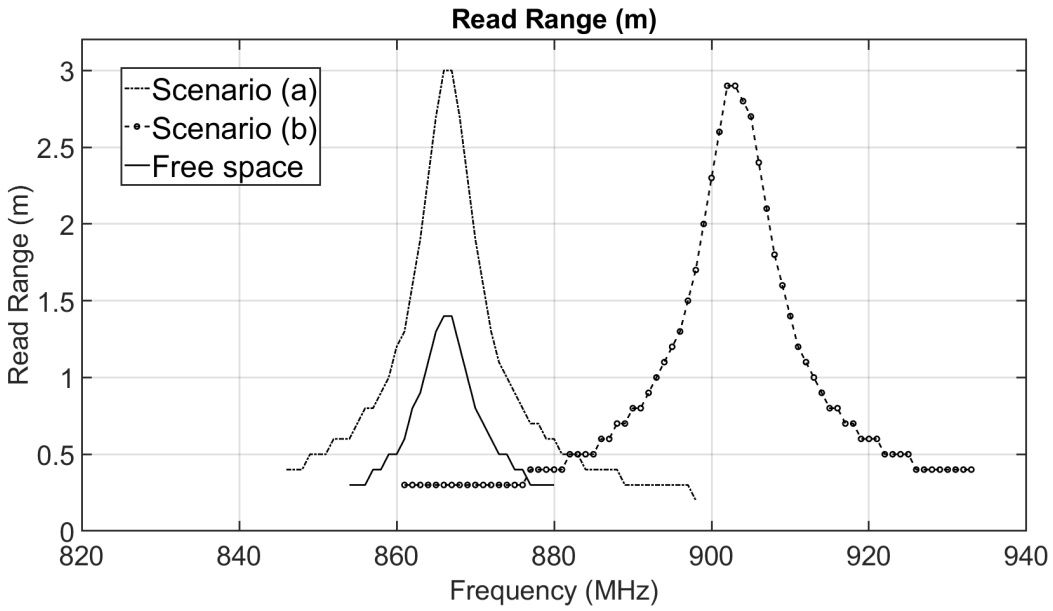

Figure 3.32: Measured read range of the RFID tag in scenario (a), scenario (b) and free space scenario

The results demonstrate that the proposed UHF RFID sensor-tag for the scenario (a) is operating inside the ETSI frequency band (868 MHz) as well as for the free space scenario. For the scenario (b) the UHF RFID sensor-tag is operating in the FCC band (902 MHz). The read range is 3 m for scenario (a) and $2.9\ m$ for scenario (b) while for the free space case is around $1.4\ m$. The performance of the UHF RFID sensor-tag in free space scenario is not as strong as in the other two scenarios since the gain of the antenna is considerably lower.

3.5 Conclusion

In this chapter, an exploration on the RFID chip with enhanced functionality was performed, aiming to reveal its characteristics and performance. In addition, a series of novel UHF RFID tag-antenna designs were presented. These designs are utilizing the same enhanced RFID chip (SL900A) and the most significant requirements were the operation on metallic surfaces and the highest possible read range, conforming to the initial size and weight specifications. The features of the three proposed UHF RFID sensor tags are summarized in Table 3.5.

Table 3.5: Summary of the proposed UHF RFID sensor tags

Feature	**Circular RFID sensor tag**	**λ/2 RFID sensor tag**	**λ/4 RFID sensor tag**
Read range (m)	~ 1.5	~ 3.1	~ 3
Length (mm)	35	62	35
Width (mm)	35	15	15
Height (mm)	5.08	2.54	2.54
Size (mm^3)	19550	2362	1333
Weight (grammars)	9	7	6

The λ/4 rectangular UHF RFID sensor tag had the best performance overall and hence this was the main device used for the rest of the thesis and for implementation in the real industrial environment. Moreover, the feature of this particular UHF RFID tag-antenna (i.e. dual band operation by flipping over a metallic surface) was elaborated by a detailed insight on its design process and operation. Furthermore, an equivalent circuit of this design was constructed, aiming to quantify the effects of the metallic surface on the impedance of the RFID tag-antenna relative to their distance. This equivalent circuit has the ability to account for the effects of the metallic surface, by introducing a parallel RLC combination. The values of the equivalent circuit, were then calculated heuristically, by using the impedance results of the simulated RFID tag-antenna.

CHAPTER 4
TWIN RFID SENSOR TAGS

4.1 Introduction

This chapter is mostly dedicated to the presentation of a developed RFID sensor tag concept, which comprises two RFID chips in one RFID tag structure. The initial motivation for such design was to discover the possibility of utilizing such a concept for better quality RFID sensing and in particular to sense several parameters in the same location, while in parallel to identify potential advantages and disadvantages of the concept.

Two different designs with different sizes were developed for this concept. The geometries of these designs are going to be presented as well as their simulation results regarding the S-parameters, radiation, field's distribution and read range. Some prototypes which were fabricated are going to be illustrated and their measured performance will be compared to the simulated results.

In addition to the twin RFID sensor tag concept, two antenna structures will be presented. These two antenna structures were designed and fabricated to serve as the RFID reader's antennas during measurements inside a large-scale generator.

4.2 Twin RFID sensor tag

The characteristics of the temperature accuracy and the temperature range, present inversely proportional performance. Consequently, if high accuracy in extended temperature range is required, the RFID sensor tag due to the characteristics of the RFID chip, will not be able to offer a good monitoring solution. Indeed, for the considered RFID chip SL900A there is a tradeoff between temperature range and its accuracy.

A possible solution could be to design an RFID sensor tag which will be exploiting two RFID chips, using the same initial size specifications. Each one of the RFID chips will be covering the half part of the temperature range offering thus superior accuracy. In this case, The RFID sensor tag will be transmitting two EPC codes for the identification of each RFID chip and the intended temperature range coverage and value can be associated with this EPC code.

The proposed RFID sensor tag will be referred to as the twin RFID sensor tag from now on and will be presented by describing the design of the antenna of the twin RFID sensor tag. The twin structure is, in fact,

two coupled RFID antennas with each one of the RFID chips connected to the input feed of each antenna.

4.2.1 Twin RFID tag antenna design

The design of the twin RFID tag antenna was based on the previously presented designs, and in particular on the rectangular $\lambda/2$ and $\lambda/4$ RFID tag antennas (§3.4.2 & §3.4.3). The numerical models of the twin RFID tag antennas were simulated with the CST Microwave suite in order to find their S-parameters, radiation efficiency, gain and calculate their expected read range. In addition, an exploration of the impact of the spacing between the two sub-antennas was carried out.

Design and fabrication of the $\lambda/2$ twin RFID sensor tag

The main idea for this concept was to design two coupled sub-RFID antennas, each one connected to an RFID chip and together forming the twin RFID sensor tag. The sensor tag was simulated for the substrate Rogers RT6010.2LM [97] with thickness 2.54 mm (as in the previously presented designs). The simulated structure is presented in Fig. 4.1.

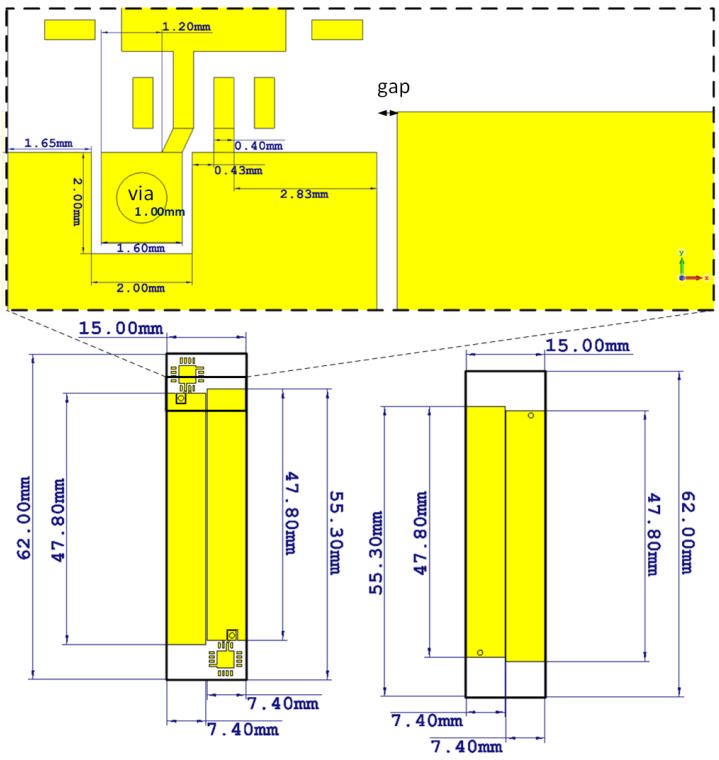

Figure 4.1: Twin RFID tag antenna based on the rectangular $\lambda/2$ design

The twin $\lambda/2$ RFID sensor tag antenna was simulated for the input impedance of the RFID chip SL900A and the S-parameters are presented in Fig. 4.2.

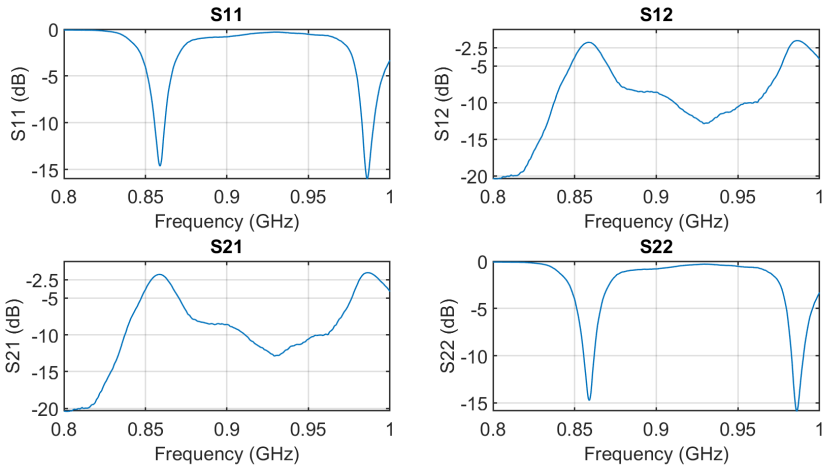

Figure 4.2: S-parameters of the $\lambda/2$ twin RFID tag antenna design

The twin $\lambda/2$ RFID tag presents two resonances, one at the region of 860 MHz and one at the region of 980 MHz. At these frequencies the transmission coefficients (S12, S21) acquire high value (-2.5 dB), indicating the fact that in these bands the coupling between the two sub-RFID antennas is stronger. Aiming to operate the two sub-RFID tags alternative, this coupling effect is exploited to offer better performance to the one operating sub-RFID tag at a time. This can be seen by examining the surface current distribution when only one sub-RFID tag has an input excitation signal (see Fig. 4.3). The excitation signal is feeding the point where the RFID chip 1 is positioned and it can be seen that the surface current distribution in the position of the RFID chip 2 is high (see Fig. 4.4 and Fig. 4.5). In this case, the RFID chip 2 is treated as an open circuit.

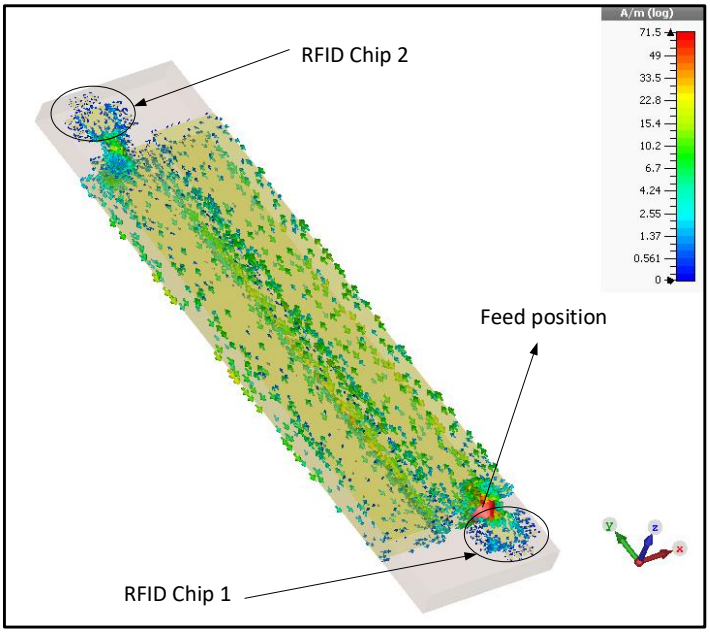

Figure 4.3: Distribution of surface current at 868 MHz for excitation only at the one sub-RFID antenna

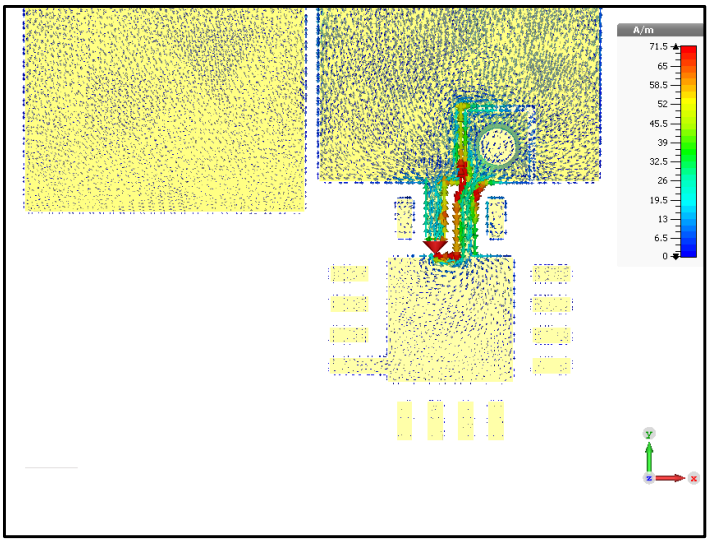

Figure 4.4: Distribution of surface current at 868 MHz at the RFID chip 1

The spacing between the two sub-RFID tags is an important factor as it has an impact on the impedance value of the sub-RFID antennas as well as on the coupling effect between them. This effect has been studied with a parametric simulation with a varying value of the gap (for 0.2, 0.4, 0.6, 0.8, 1 mm) between the two sub-RFID antennas (the total width of the twin RFID tag antenna was kept constant). The effect of the

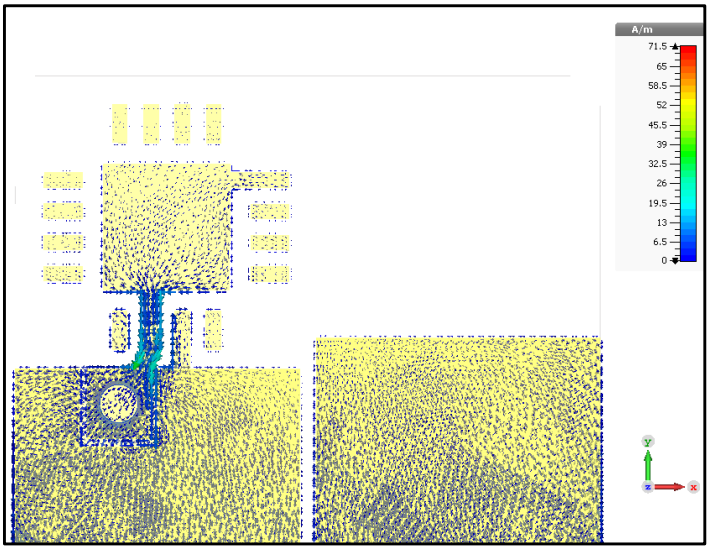

Figure 4.5: Distribution of surface current at 868 MHz at the RFID chip 2

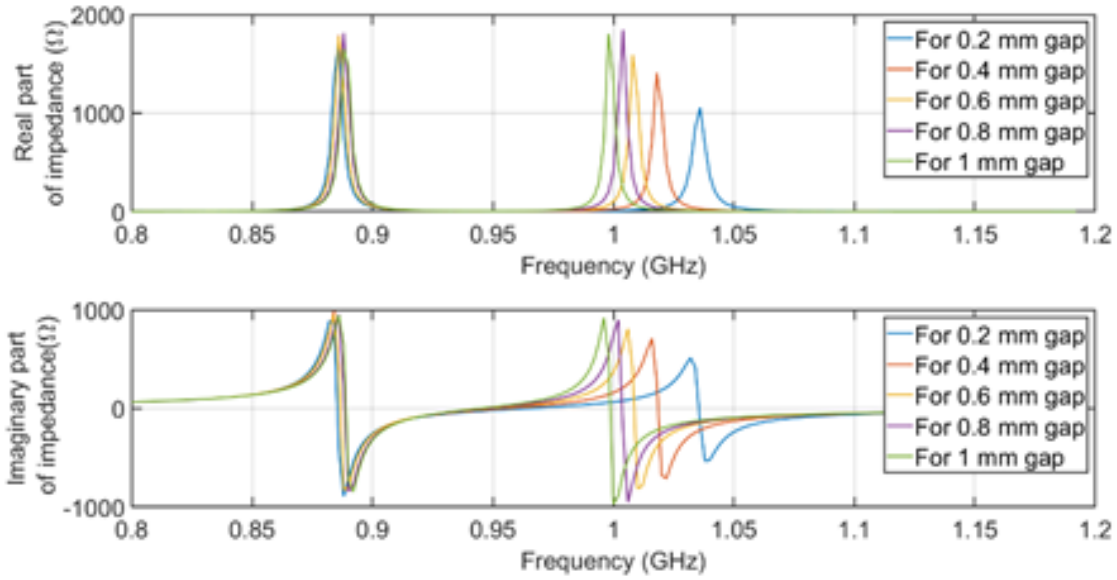

Figure 4.6: Variation of the real and imaginary part of the impedance of the $\lambda/2$ twin RFID tag

different spacing values is demonstrated in Fig. 4.6, by presenting the variation of the real and imaginary part of the complex input impedance of the sub-RFID antenna as well as the change of the radiation efficiency in Fig. 4.7.

The results of the parametric simulation show that the two resonances of the twin RFID sensor tag are shifting towards higher values of frequency with different rates. For the first resonance this variation is considerable smaller (from 885 to 889 MHz), while for the second resonance the frequency shift is quite larger (from 998 to 1030 MHz).

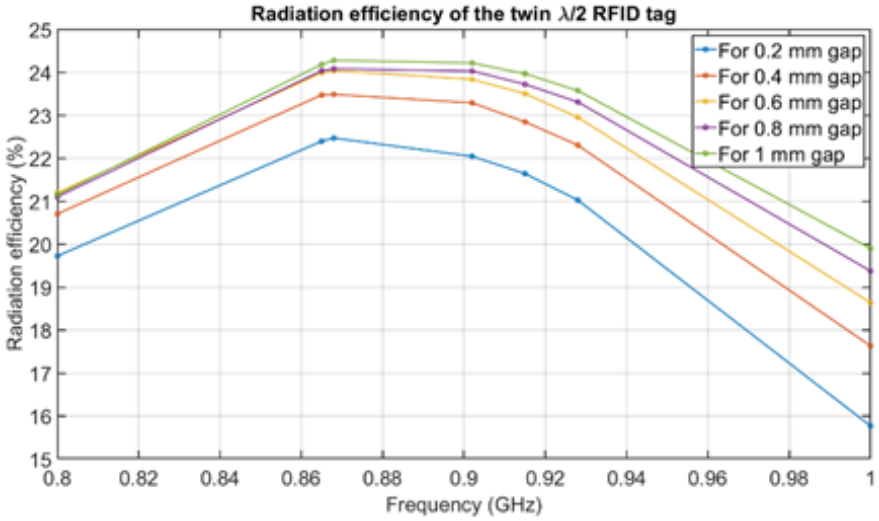

Figure 4.7: Radiation efficiency for different values of the gap for the $\lambda/2$ twin RFID tag

The radiation efficiency of the twin RFID sensor tag is increasing with the increase of the gap. For instance, for 868 MHz and for gap 0.2 mm the radiation efficiency is 22.5% while for gap 1 mm will be 24.2%.

The simulated gain of the twin RFID sensor tag is presented in Fig. 4.8. The maximum value that it is presenting at 868 MHz is 0.135 dBi. Also in Fig. 4.9 the electric field distribution is presented for different phase values of the excitation signal.

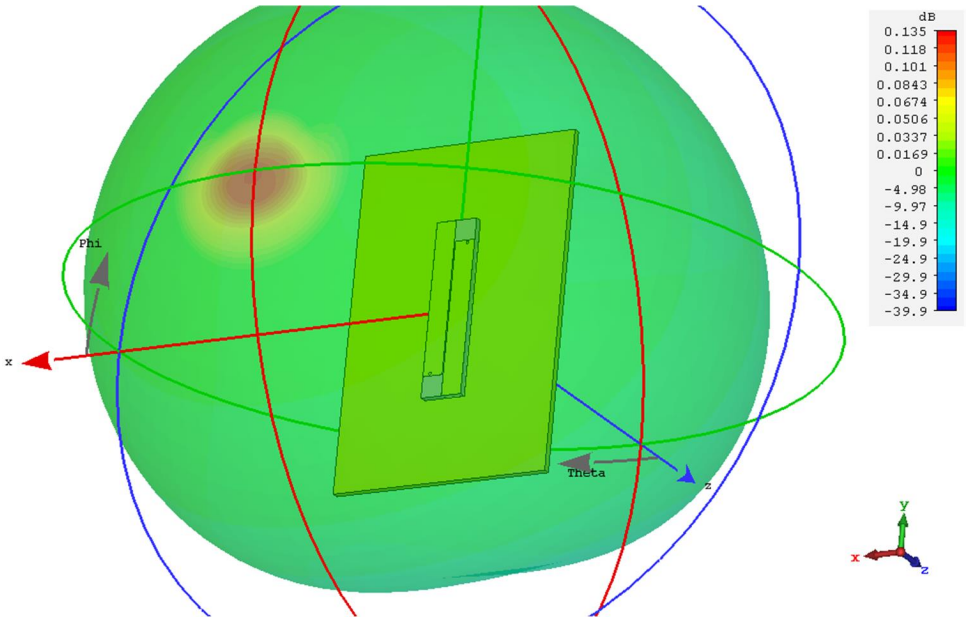

Figure 4.8: Simulated gain of the $\lambda/2$ twin RFID tag

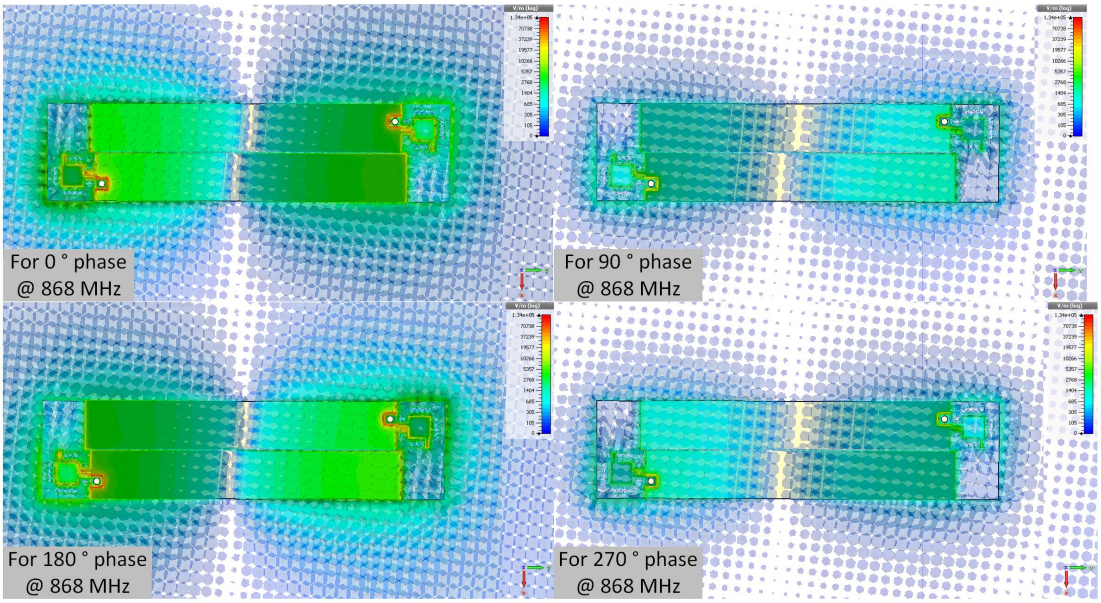

Figure 4.9: Electric field distribution for phase values $0°$, $90°$, $180°$ and $270°$ at 868 MHz

The twin $\lambda/2$ RFID sensor tag was fabricated, as it is presented in Fig. 4.10, and the read range calculated from the simulation results for the ETSI regulations was compared to the read range measured by the Tagformance Pro reader, Fig. 4.11.

At this point it is important to discuss the characteristics of the used substrate. As noted also in §3.4.1,

Figure 4.10: Fabricated $\lambda/2$ twin RFID tag with the trimmed areas marked

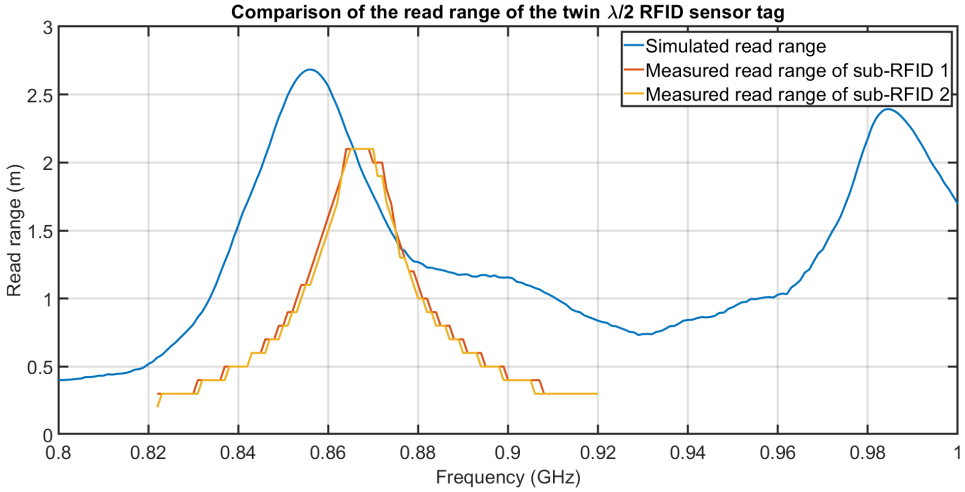

Figure 4.11: Read range comparison of the $\lambda/2$ twin RFID tag

the RT6010.2LM is an anisotropic substrate with the value of permittivity being difficult to know beforehand with certainty. In this design the initial value of permittivity used for the twin $\lambda/2$ RFID sensor tag was ϵ_r = 10.2. This value lead to the initial fabricated prototypes to have a resonance frequency around 770 MHz. This result yield that the real permittivity value would be quite higher and in fact it was found to be 11.3. The fabricated prototypes were tuned to resonate at the ETSI frequency band by trimming parts of the antenna structure (Fig. 4.10). The simulation presented so far are for the new permittivity value of 11.3 and the design was re-simulated to match the trimmed fabricated prototype. The measurements of the read range of the twin $\lambda/2$ RFID sensor tag were performed by selecting the EPC code of the one RFID chip and reading only this RFID chip. At the next instance the EPC of the other RFID chip would be selected

and the same measurement would be repeated. During this procedure both RFID chips are powered-up but only one is responding to the reader's commands. The measurements of the read range have some deviation from the calculated read range which can be justified by the limited trimming accuracy of the twin $\lambda/2$ RFID sensor tag and from the fact that during the simulation, there was the assumption that both RFID chips are presenting exactly the same impedance which does not applies in reality. The maximum measured read range was $2.2\ m$ while the maximum calculated was $2.7\ m$. At this point it is important to mention that the presented read range is corresponding to the read range of the twin RFID sensor tag when it receives the query command. The response of the twin RFID sensor tag in this case is to transmit the corresponding EPC value for the specific sub-RFID chip which is selected. When the twin RFID sensor tag receives a command regarding the output of the integrated ADC, then more power is consumed to operate resulting in a degradation of the read range. In this case for transmitting the value of the ADC circuit the read range was around $1\ m$.

Design and fabrication of the λ/4 twin RFID sensor tag

Similarly, the design and fabrication of theλ/4 twin RFID sensor will be presented in this subsection. In Fig. 4.12 the geometry and the dimensions of the λ/4 twin RFID sensor tag are presented.

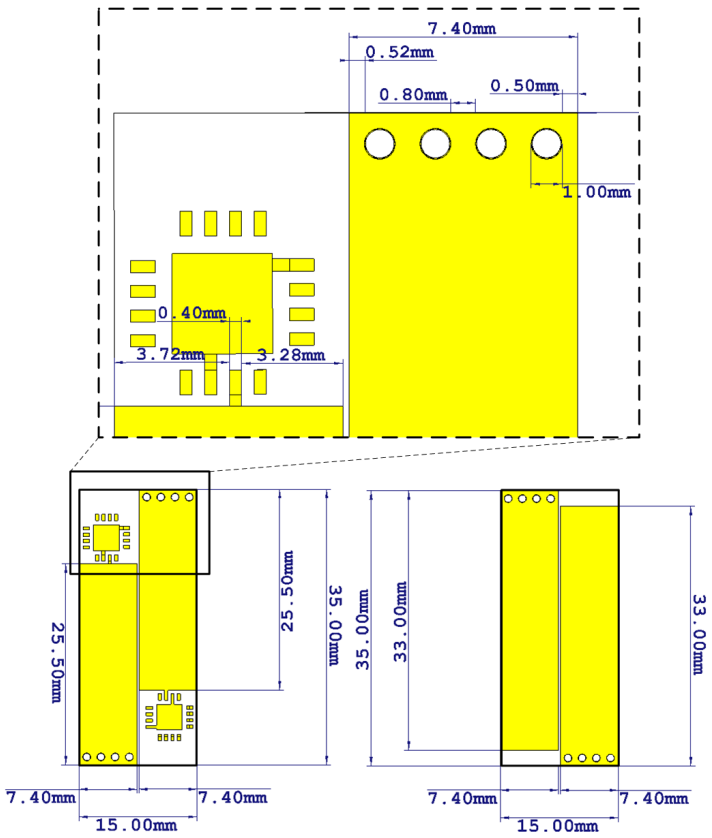

Figure 4.12: Twin RFID tag antenna based on the rectangular λ/4 design

The simulated S-parameters for the RFID antenna impedance of the λ/4 twin RFID sensor tag are presented in Fig. 4.13.

The gap between the two sub-RFID tag antennas is $0.2\ mm$ and as demonstrated also for the λ/2 twin RFID sensor tag the distance between the two sub-RFID tag antennas has an impact on the characteristics of the structure overall. A parametric simulation with the value of the gap between $0.2\ mm$ and $1\ mm$ with step of $0.2\ mm$ was performed. The results of the parametric simulation are presented in Fig. 4.14.

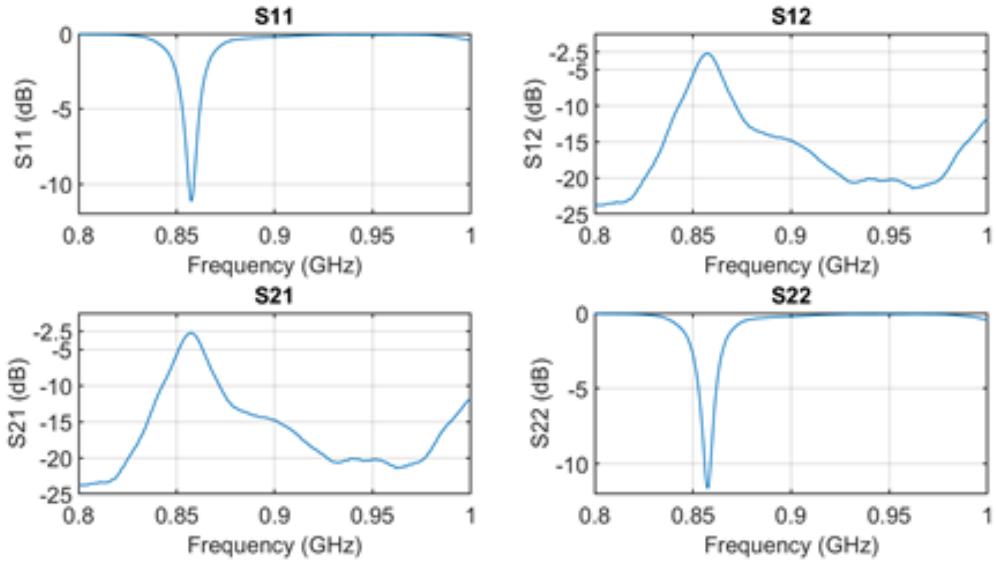

Figure 4.13: S-parameters of the $\lambda/4$ twin RFID tag antenna design

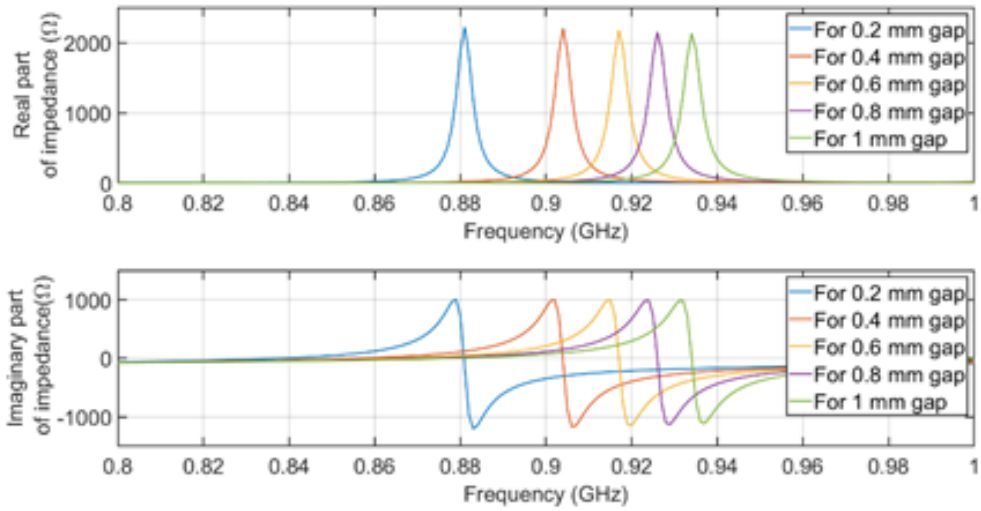

Figure 4.14: Variation of the real and imaginary part of the impedance of the $\lambda/4$ twin RFID tag

The parametric simulation shows that the resonance frequency is shifting towards higher frequency

value and more specifically from 882 MHz to 935 MHz. Furthermore, the radiation efficiency of the twin $\lambda/4$ RFID sensor tag antenna is varying according to Fig. 4.15.

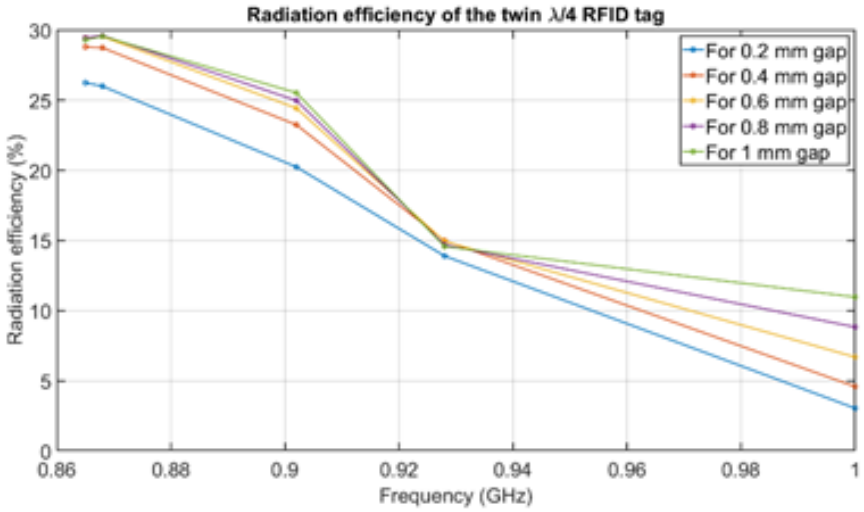

Figure 4.15: Radiation efficiency for different values of the gap for the $\lambda/4$ twin RFID tag

The radiation efficiency for the minimum value of gap is at 26 % for 868 MHz and as the gap increases to 1 mm the value of radiation efficiency reaches to 30%. Moreover, the case where one of the two sub-RFID tag antennas is fed with an excitation signal was simulated in order to observe the effect at the other sub-RFID tag antenna. In Fig. 4.16 the surface current distribution is illustrated, and in Fig. 4.17 and Fig 4.18 the current at the input of the RFID chips is presented. Similar to the case of the $\lambda/2$ twin RFID tag antenna, when the one sub-RFID antenna is excited, higher current is presented in the input of the other sub-RFID antenna.

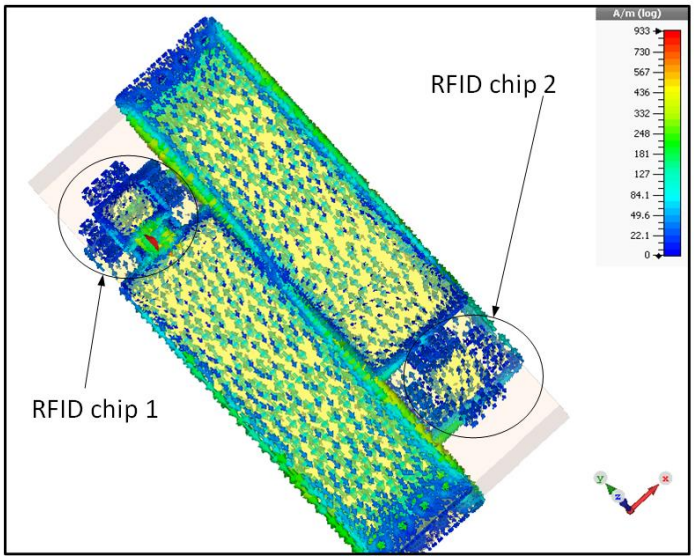

Figure 4.16: Distribution of surface current at 868 MHz for excitation only at the one $\lambda/4$ sub-RFID antenna

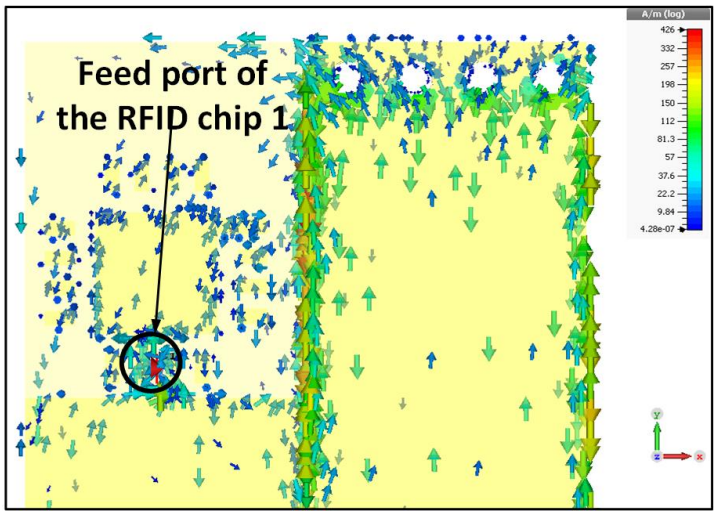

Figure 4.17: Distribution of surface current at 868 MHz at the input of the RFID chip 1 (with the excitation applied)

As in the case of the twin $\lambda/2$ RFID sensor tag, the two sub-RFID tags are coupled and with this behavior every time the whole structure is utilized to power up each one of the RFID chips.

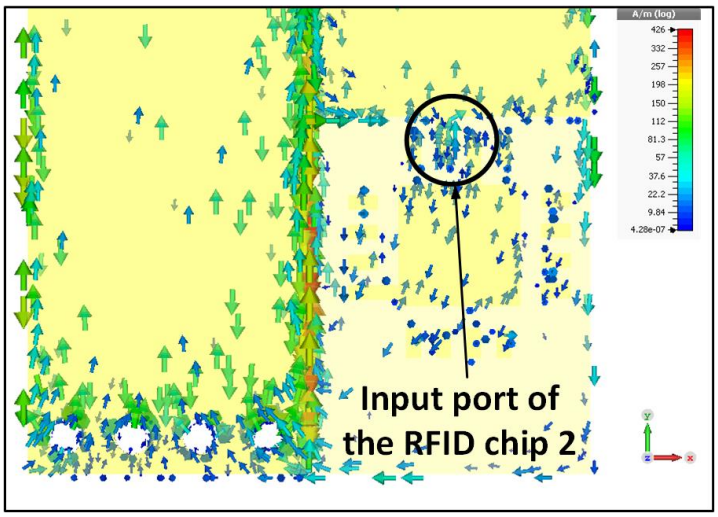

Figure 4.18: Distribution of surface current at 868 MHz at the input of the RFID chip 2

Also, in Fig. 4.19 the distribution of electric field for different values of phase is presented.

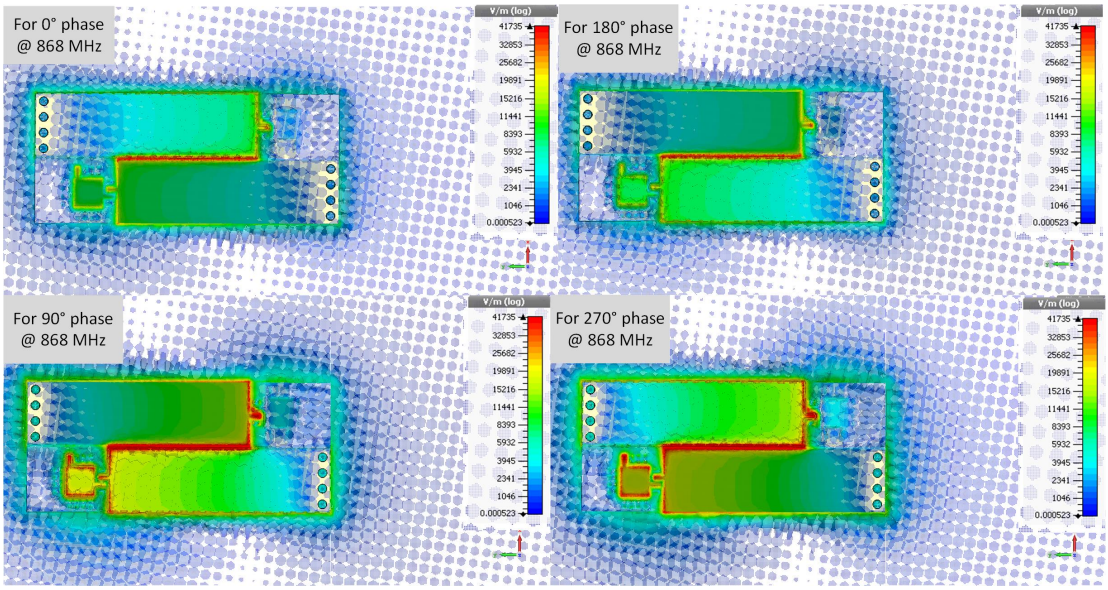

Figure 4.19: Electric field distribution for excitation signal phase values 0°, 90°, 180° and 270° at 868 MHz

The simulated gain of the structure is presented at Fig. 4.20.

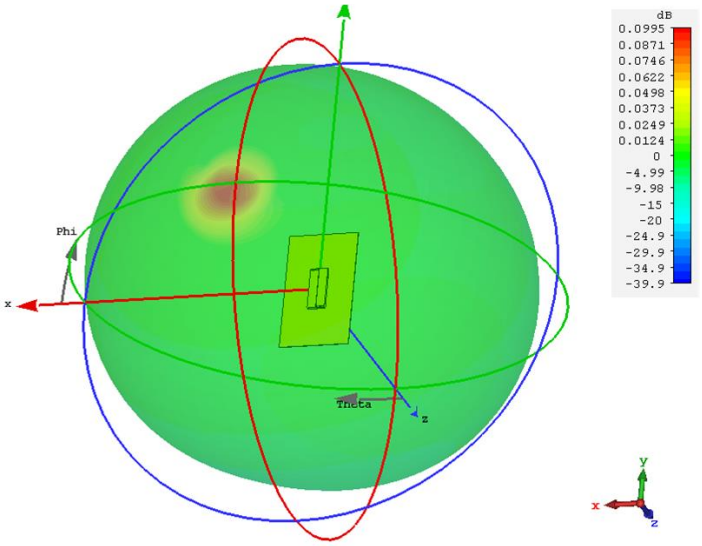

Figure 4.20: Simulated gain of the $\lambda/4$ twin RFID tag

The $\lambda/4$ twin RFID sensor tag was fabricated (see Fig. 4.21) and the permittivity of the substrate which was found after the realization was 10.8.

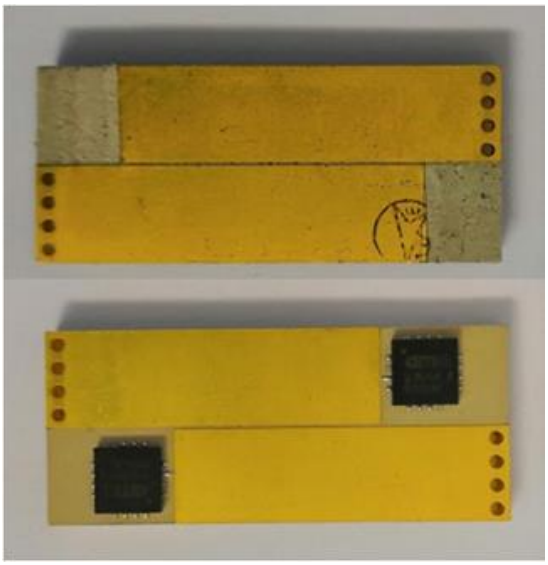

Figure 4.21: Fabricated $\lambda/4$ twin RFID tag with the trimmed areas

The $\lambda/4$ twin RFID sensor tag was tuned the same way as in the previous case of $\lambda/2$ twin RFID sensor

tag (by trimming part of the copper cladding) to exhibit a resonance frequency at ETSI band. In Fig. 4.22 the comparison of the calculated read range with the measured is presented.

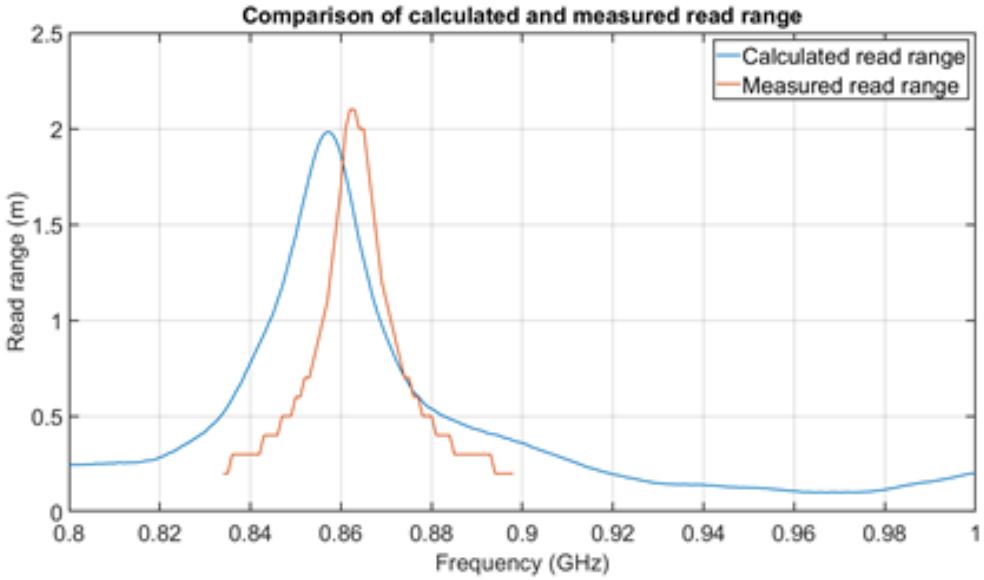

Figure 4.22: Read range comparison of $\lambda/4$ twin RFID tag

The twin $\lambda/4$ RFID sensor tag exhibits a measured read range of $2.1\ m$, very close to $2\ m$ calculated from the simulation results. As previously stated, the read range presented here is regarding the ability of the RFID sensor tag to correspond to read command sent by the RFID reader. If the twin RFID sensor tag receive a command to transmit the output value of the integrated ADC circuit, the read range will be lower and it was found to be around $0.8\ m$ for this twin $\lambda/4$ RFID sensor tag.

4.3 Antenna designs for the RFID reader

Another important task which came up during the study of the environment of the generator is the need of specially designed antennas for the RFID reader. The generator structure acts as Faraday cage and in order to communicate with the RFID sensor tags installed in the interior, the antenna of the RFID reader should also be inside the generator. The available space in the generator is quite limited and hence the standard antennas which are used for RFID readers would not be able to fit. Consequently, new antennas with matching specifications to the exact geometry and size of the generator should be designed and used.

More information about the exact installation method used will be presented later on. In this section the specifications and the designs of the antennas for the RFID reader will be presented.

4.3.1 Specifications of the antennas of the RFID reader

The main specifications for the antennas of the RFID reader concern their size. The places which were selected to install these antennas would allow antenna structures with maximum length of 10 cm, width of 3 cm and thickness less than 0.5 cm. In addition, these antennas would be installed on metallic surfaces and they would require operating in the ETSI frequency band.

4.3.2 Design of RFID reader antenna with lumped component

The antenna illustrate in Fig. 4.23 was designed to operate as antenna for the RFID reader.

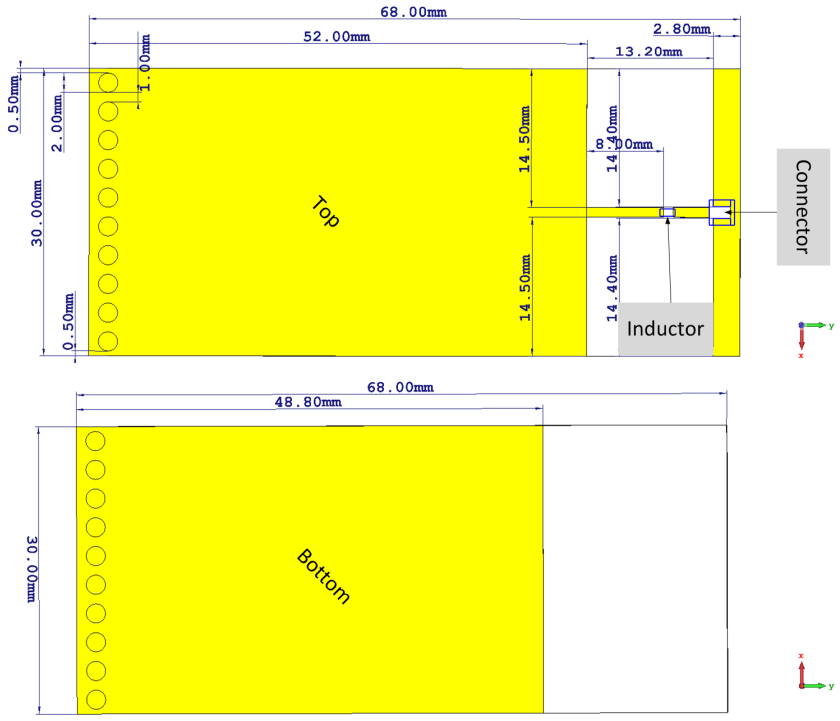

Figure 4.23: RFID reader antenna with lumped component

The total dimensions are 68 $mm \times 30\ mm \times 1.524\ mm$ ($Length \times width \times thickness$). An inductor was used for matching purposes with value of 33 nH (coilcraft 0805HP-33NXJRB [102]). The simulation results of the S-parameters as well as the realized gain and the radiation efficiency are presented in Fig. 4.24, Fig. 4.25 and Fig. 4.26 respectively.

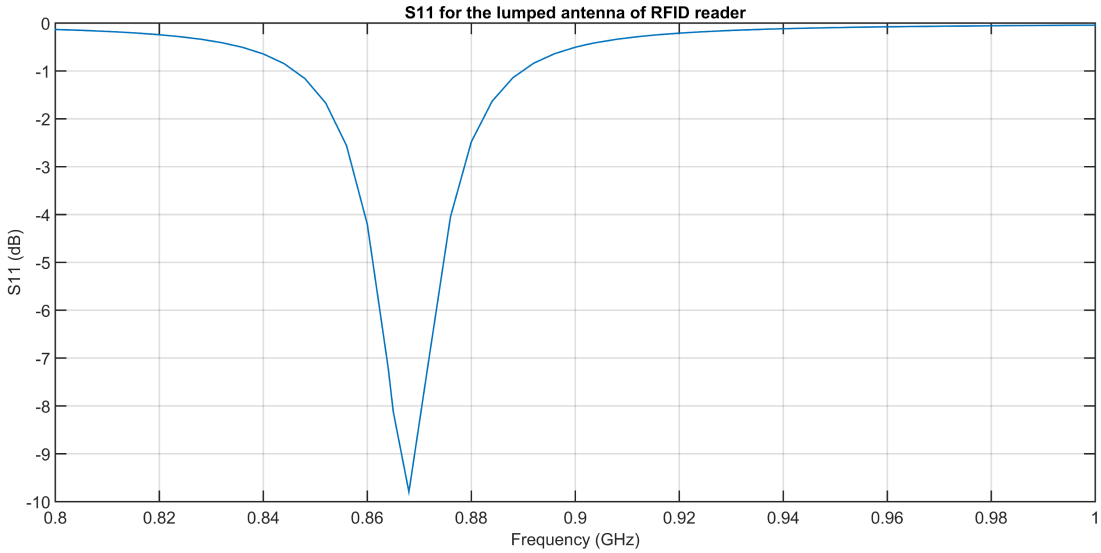

Figure 4.24: S11 parameters for the RFID reader antenna with lumped component

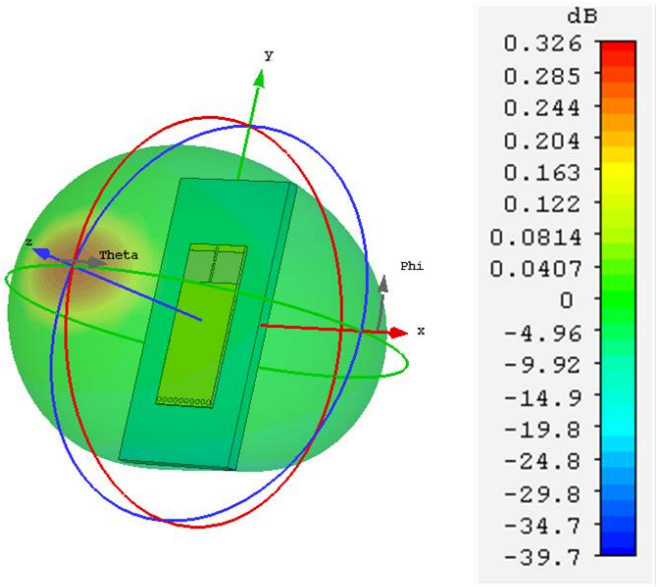

Figure 4.25: Realized gain of the RFID reader antenna with lumped component at 868 MHz

Regarding the S-parameters, the reflection coefficient is around 10 dB for the ETSI frequency band while the realized gain at 868 MHz is 0.326 dB. The radiation efficiency at 868 MHz is 48%. The antenna was fabricated on the Rogers RO4003C [103] substrate with permittivity of 3.38 (3.55 for design) with Tanδ 0.0027 and thickness 1.524 mm. The copped cladding was 1 oz. (35 μm). In Fig. 4.27 a fabricated prototype

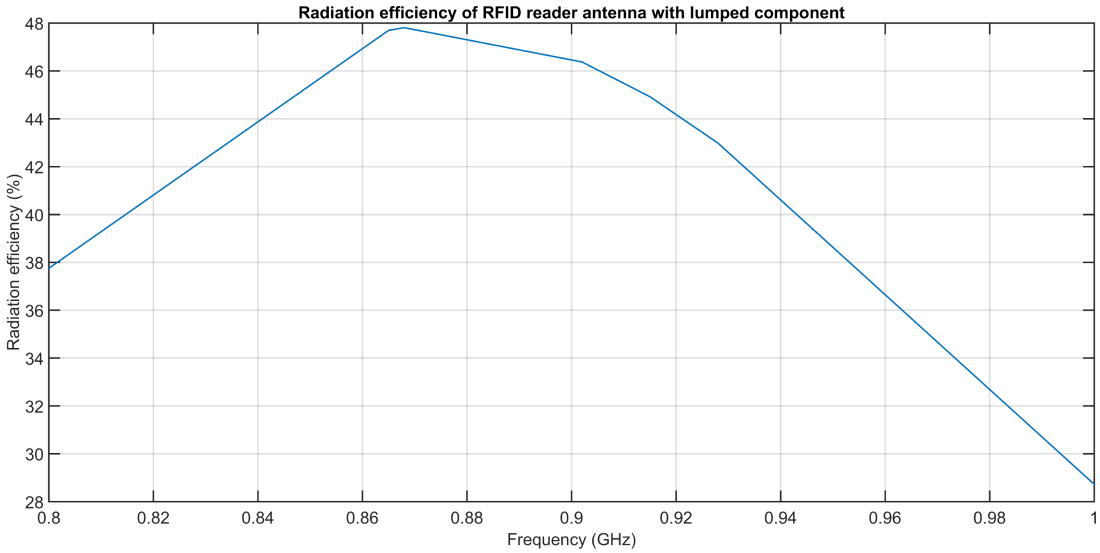

Figure 4.26: Radiation efficiency of the RFID reader antenna with lumped component

of the antenna is illustrated. The antenna is connected with an ultra- miniature coax connector (UMCC).

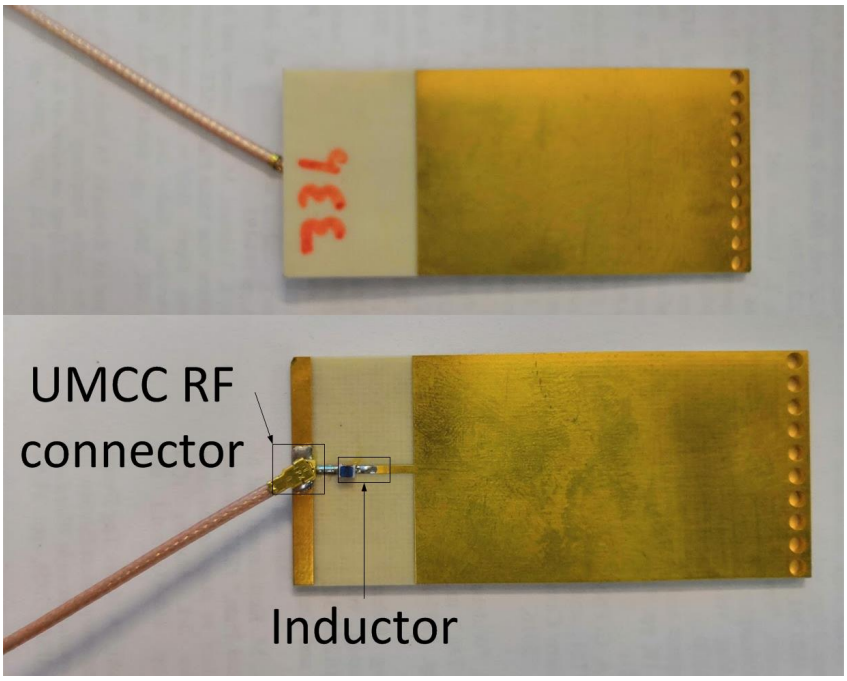

Figure 4.27: Fabricated prototype of the RFID reader antenna with lumped component

The input reflection coefficient of the RFID reader antenna was measured by means of a VNA (Field-Fox N9918A) [104] and a comparison between measured and simulated results is presented in Fig. 4.28.

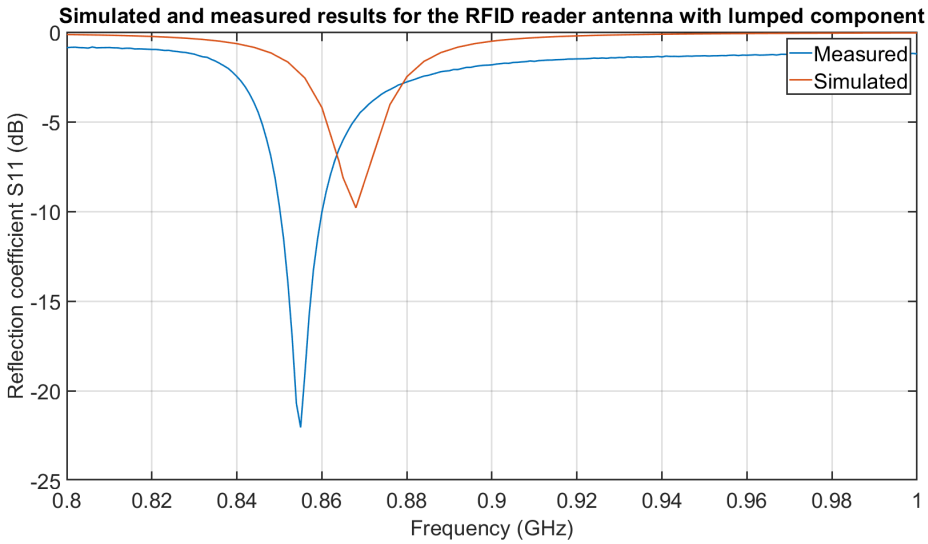

Figure 4.28: Comparison of input reflection coefficient between simulated and measured results

It can be observed that there is a discrepancy between measured and simulated input reflection coefficient. This is due to the value of the inductor which is not very accurate in the electromagnetic simulation, since there was no model for the inductor. Consequently, parasitic effects due to the inductor package are not taken into account. In the simulation, only the value of inductance was taken into account. Moreover, the bandwidth of the antenna is quite limited, around 4 MHz, which is something expected due to the limited size of the antenna as well as due to the ground plane.

4.3.3 Design of RFID reader antenna with the inset technique

Another antenna structure designed and later on fabricated to act as the RFID reader antenna is presented in Fig. 4.29.

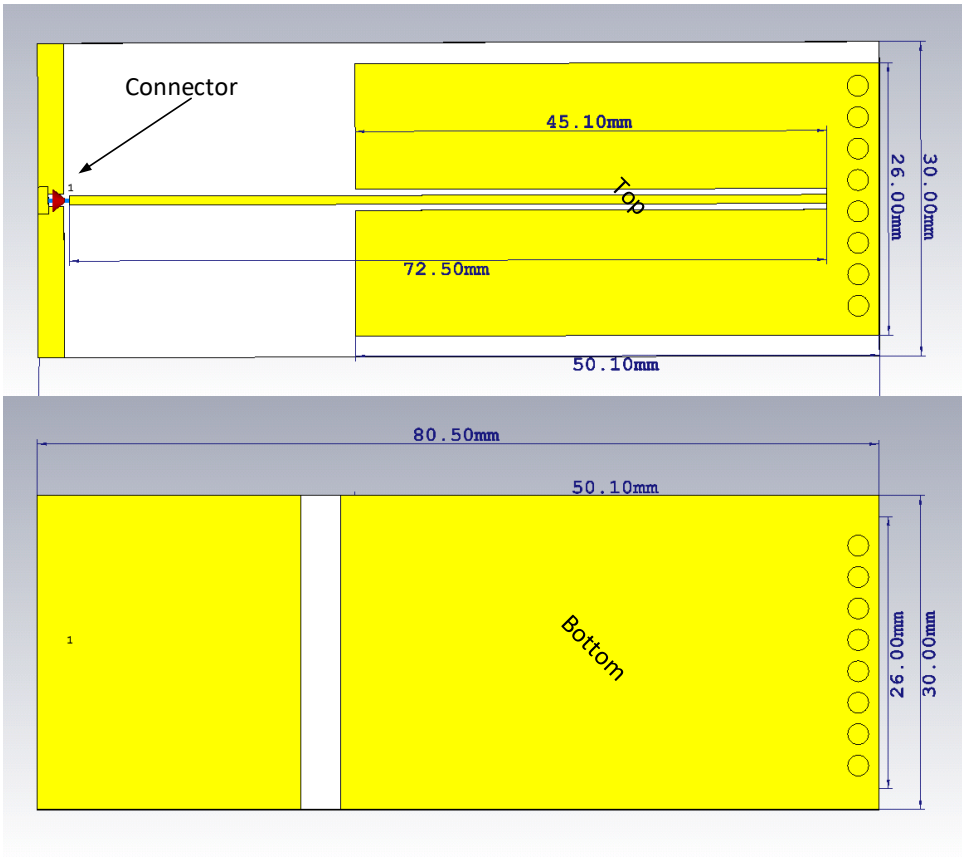

Figure 4.29: Inset RFID reader antenna

This antenna has similar geometry with the previously presented antenna, but in this case the inset technique was used for matching purposes. This variation was selected in order to avoid the usage of an inductor, due to the high magnetic field in the area of installation, and to reduce the complexity of the antenna overall. In Fig. 4.30, Fig. 4.31 and Fig. 4.32 the simulated input reflection coefficient, realized gain and radiation efficiency are presented respectively.

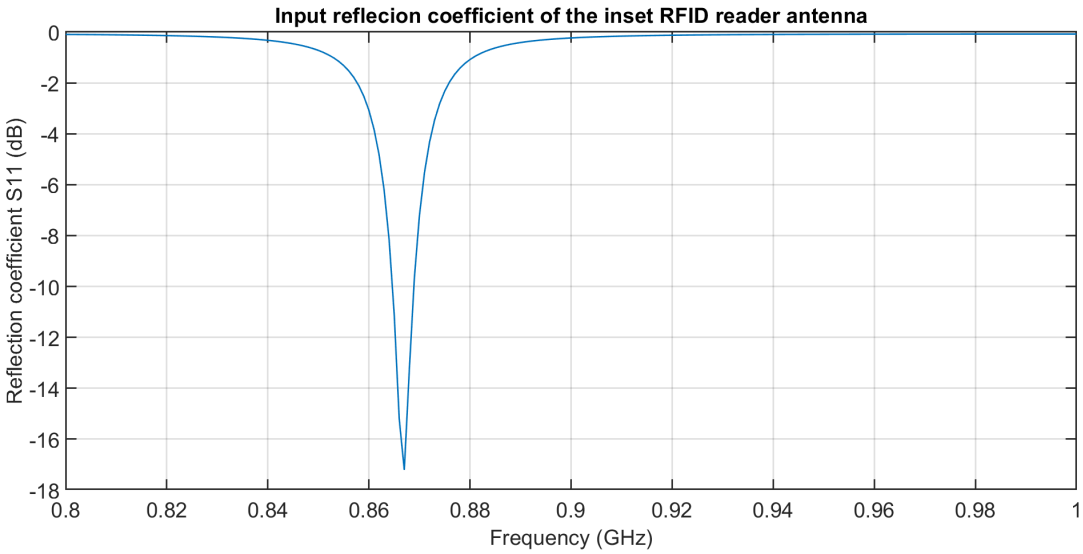

Figure 4.30: Input reflection coefficient of inset RFID reader antenna

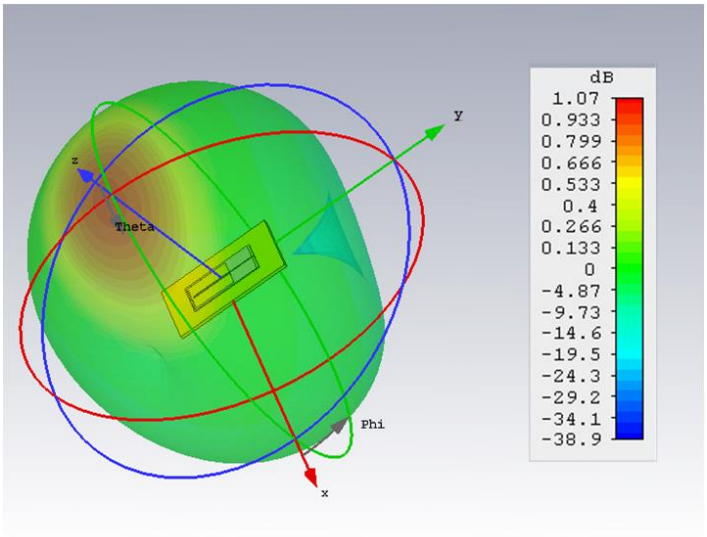

Figure 4.31: Realized gain of the inset RFID reader antenna at 868 MHz

The overall dimensions of this design are 80.5 mm $\times$ 30 mm $\times$ 1.524 mm ($Length \times width \times thickness$).

For this antenna, the input reflection coefficient is -17 dB in the ETSI frequency band while the realized gain at 868 MHz is 1.07 dB. The radiation efficiency reaches up to 53%.

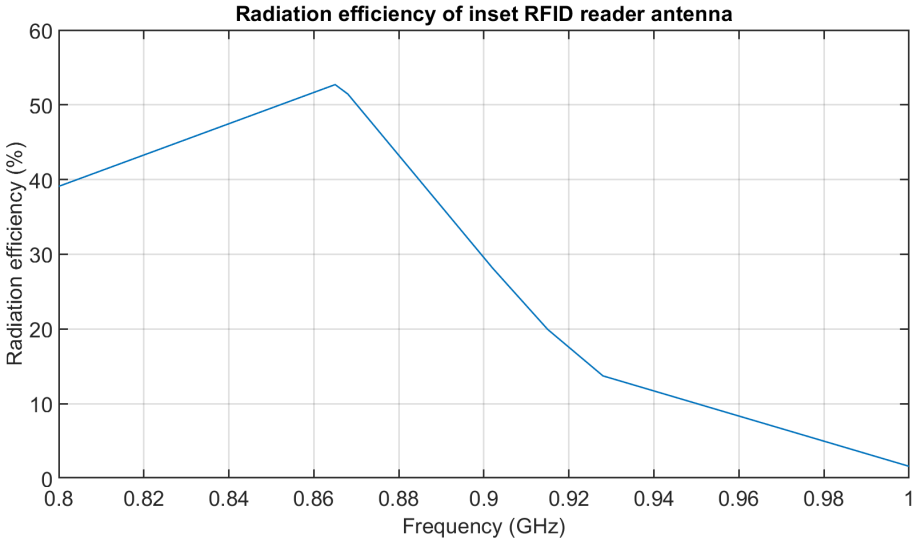

Figure 4.32: Radiation efficiency of inset RFID reader antenna

The antenna was fabricated using the same substrate with the previous design (Rogers RO4003C) with the same characteristics. The fabricated antenna is presented in Fig.4.33. The input reflection coefficient was measured by means of the VNA (Field Fox N9918A). The initial measured input reflection coefficient was found to be a little lower that the ETSI frequency and a copper tape was used for tuning aiming to increase the resonance frequency. The comparison between measured and simulated results is presented in Fig. 4.34.

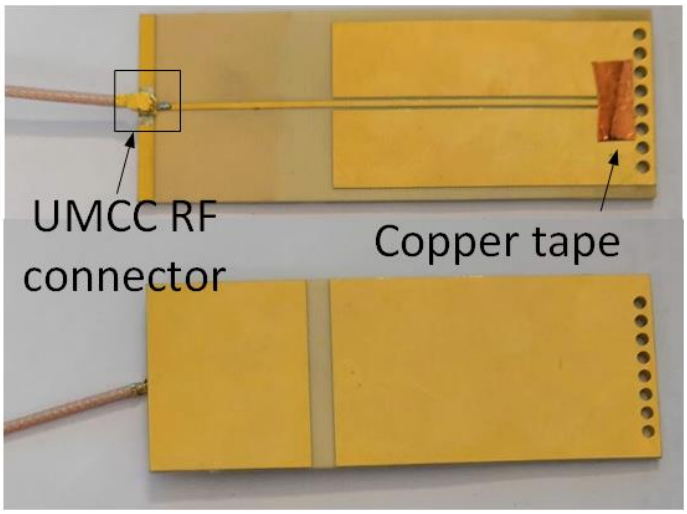

Figure 4.33: Fabricated prototype of the RFID reader antenna with lumped component

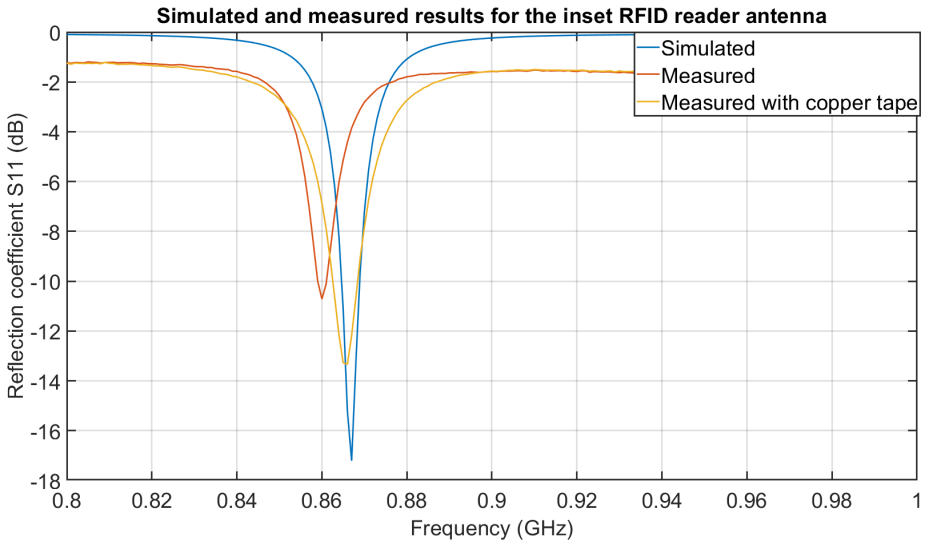

Figure 4.34: Comparison of input reflection coefficient

The bandwidth of this antenna is similar to the bandwidth presented by the previous antenna with lumped component and it is around 5 MHz.

4.4 Conclusion

In this chapter the twin RFID sensor tag concept was introduced. The motivation of designing such an RFID sensor tag concept was the need of high accuracy in combination of wide temperature measuring range. The design of the twin RFID sensor tags was inspired by the $\lambda/2$ and $\lambda/4$ rectangular RFID tag-antennas which were presented in the previous chapter. The study of the twin RFID sensor tags included their simulation as well as their fabrication and measurement. An initial problem has been the uncertainty regarding the permittivity value of the substrate. This problem was solved by fabricating prototypes and then through measurements the actual value of permittivity was deduced by comparing the simulated and measured results. The twin RFID sensor tags are displaying a read range of more than $2\ m$, for identification applications and around 0.8 to $1\ m$ for sensing applications. Since the twin RFID sensor tag is in the far-field of the RFID reader, the incoming electromagnetic waves can be treated as plane waves. In this case at any time both sub-RFID tags of the twin sensor are activated and by using the EPC command "*select*" , one of the two RFID chips is responding. While the one RFID chip will be responding the other one will also be activated, presenting similar input impedance with the RFID chip which is responding.

In addition, two designs regarding RFID reader antennas were presented. The nature of the project of

this thesis, (i.e. sensing in harsh environment) required specially designed antennas for the RFID reader conforming to size limitations as well as to metallic environment operation. The designed antennas for the RFID reader due to their size have inferior performance compared to the standard commercially available antennas (typically 6dBi gain, circular polarization, bandwidth covering both ETSI and FCC frequency bands). The RFID reader antennas as it will be shown later on, were used for an installation inside a large-scale generator.

CHAPTER 5
TEMPERATURE AND STRAIN MEASUREMENTS IN THE LAB

5.1 Introduction

Having established a series of different UHF RFID antenna tag designs the next goal was to evaluate their performance regarding sensing functions. Initially, two case studies on the thermal conductivity issues are going to be presented with upper goal to explain the positioning of the RFID chip in the bottom side of all the RFID sensor tags presented so far. Since the temperature sensor is integrated in the RFID chip, a better thermal transfer to the temperature sensor can be achieved if the RFID chip is in contact with the surface of interest. These case studies will present a comparison by using one of the designed RFID sensor tags positioned either with the RFID chip on top of the RFID sensor tag or on the bottom.

Moreover, using the fabricated prototypes of the presented so far designs, a series of measurements in the controlled environment of the laboratory were conducted aiming to study the performance regarding measurements of temperature and strain. All the designs were developed with the usage of the RFID chip SL900A; hence the sensing evaluation will be actually an evaluation of the sensing capabilities of the specific RFID chip.

Furthermore, since the high accuracy of the measured temperature is something required according to the specifications, a solution offering higher accuracy was developed and is presented based on the twin RFID sensor tags presented in the previous chapter (§4). The superior accuracy is demonstrated through measurements in the laboratory environment.

Finally, a demonstration of measurements of stress is included, by utilizing some of the advantages of the used RFID chip. Overall, this chapter is focusing on the sensing part of the designed RFID sensor tags.

5.2 Considerations on thermal conductivity issues

The RFID sensor tags have been designed with the RFID chip in the bottom side in order to be in direct contact with the surface whose temperature is being measured. The initial thoughts on this issue were that if the substrate is interfering between the surface of interest and the integrated temperature sensor of the RFID chip, the temperature measurement will not be accurate enough. In order to verify this issue, a thermal simulation in the CST microwave suite was performed. A mockup of a part of a generator was designed and

one of the designed RFID sensor tags ($\lambda/4$ rectangular RFID sensor tag) was used. The simulated setup is presented in Fig. 5.1.

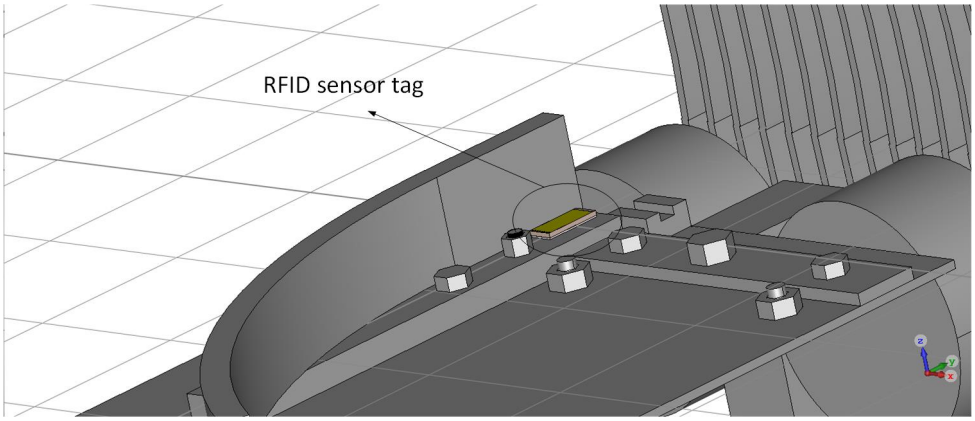

Figure 5.1: Mockup of generator with the RFID sensor tag

A thermal source was then added to the setup and by using temperature probes on the surface below the RFID sensor tag and on the RFID chip the temperature values were recorded. The temperature distribution of the simulation is presented in Fig. 5.2. In the simulation it can be seen the temperature degradation, as the distance from the thermal source is increasing. The temperature value of the source was set to be 100 °C.

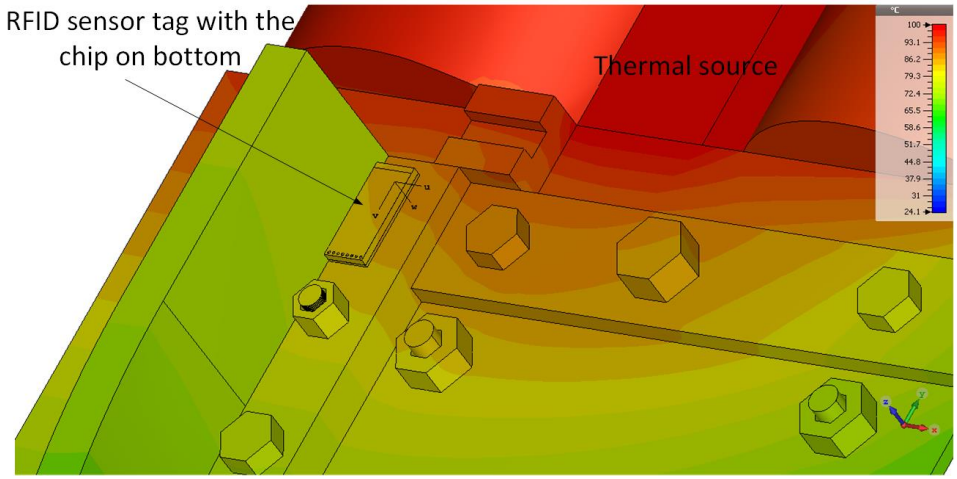

Figure 5.2: Temperature distribution with the RFID chip on bottom of the RFID sensor tag

The simulation was repeated with the RFID sensor tag now positioned with the RFID chip on top. The distribution of temperature in this case is presented in Fig. 5.3.

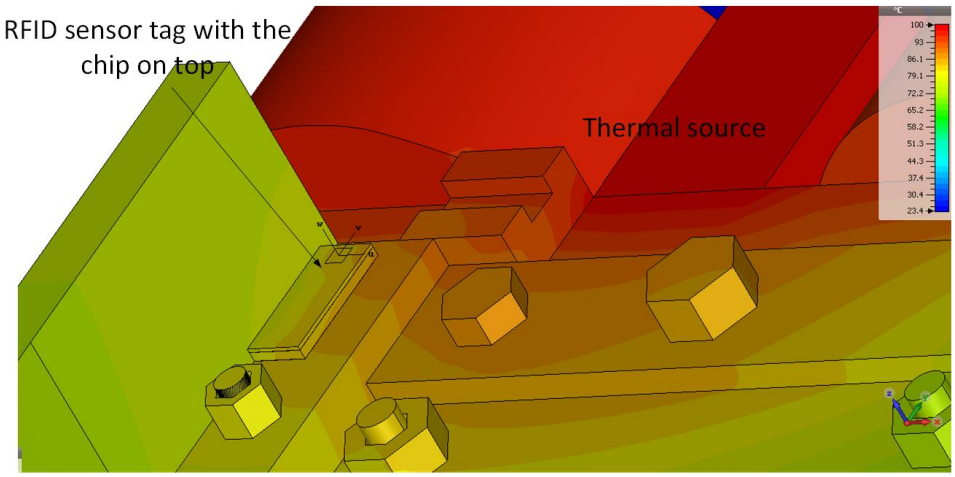

Figure 5.3: Temperature distribution with the RFID chip on top of the RFID sensor tag

The materials used for the simulation were iron, for the generator part mockup, copper and the RT6010.2LM substrate for the RFID sensor tag and silicon for the RFID chip model. All these materials are specified with thermal properties in the thermal simulator of CST microwave suite.

In each simulation three temperature probes were added: a temperature probe on the thermal source, a temperature probe on the surface close to the RFID sensor tag and a temperature probe on the RFID chip. From Table 5.1 it can be seen that in the case where the RFID chip is at the bottom side of the RFID sensor tag a more accurate measurement of temperature can be achieved.

Table 5.1: Values of the temperature probes for each case study

Temperature probe placement	Case study 1 (RFID chip on bottom)	Case study 2 (RFID chip on top)
Source	100°	100°
Surface close to RFID tag	86.88°	86.795°
RFID chip	85.1°	82.74°

The temperature probes in both case studies for the thermal source have the same result, something which is expected. For the surface close to the RFID sensor tag the difference is quite small between the two simulation and this variation is due to the mesh setup in each case. The value of temperature at the RFID chip in the case when the RFID chip is on the top is 4.55 °C lower than the nearby surface while in the case

where the RFID chip is at the bottom this difference is 1.7 °C.

Based on these simulations, the choice to design the RFID sensor tags with RFID chip at the bottom side could potentially offer better temperature measurement accuracy.

5.3 Sensing capabilities of the SL900A RFID chip

As mentioned already, the SL900A RFID chip includes an integrated temperature sensor and some extra functionalities such as a 10-bit integrated Analog to Digital Converter (ADC) as well as two external analog ports for connecting various external sensors. More information and details can be found in the corresponding datasheet [31]. These feature of the RFID chip will be exploited by using the integrated temperature sensor for temperature measurement, and by utilizing the analog ports to connect a strain gauge for stress measurements.

5.3.1 Temperature measurements with the integrated sensor

The maximum temperature range which can be sensed from the integrated sensor is from -40 °C to 125 °C. The integrated temperature sensor utilizes the DC voltage generated from the RF rectifying circuit, after it is regulated, in order to set the reference voltages to perform the sampling in the ADC. To set the temperature range, and the resolution of the sensor, two reference voltages are required and these values are adjustable. The two voltages will be referred from now on as V_{REF1} and V_{REF2}. The possible values which these two voltages can acquire are presented in Table 5.2.

Table 5.2: SL900A ADC reference voltages

Reference Voltage 1 (mV) (V_{REF1})	Reference Voltage 2 (mV) (V_{REF2})
160 mV	260 mV
210 mV	310 mV
260 mV	360 mV
310 mV	410 mV
360 mV	460 mV
410 mV	510 mV
460 mV	560 mV
510 mV	610 mV

The lowest possible temperature detection is set by the value of V_{REF2} according to Table 5.3. The resolution of the temperature sensing is limited by the 10-bit ADC, hence by the difference $(V_{REF2} - V_{REF1})/2^{10}$. In Table 5.4 the temperature measuring range is presented in contradiction to the difference between the reference voltages, as well as the calculated resolution.

Table 5.3: SL900A theoretical lower temperature limit

Reference voltage 2 (mV) (V_{REF2})	*Lower temperature limit** (°C)
$260\ mV$	$-118.9°C$
$310\ mV$	$-89.3°C$
$360\ mV$	$-59.6°C$
$410\ mV$	$-29.0°C$
$460\ mV$	$0.3°C$
$510\ mV$	$29.3°C$
$560\ mV$	$59.0°C$
$610\ mV$	$88.7°C$

** The lowest measurable temperature is -40 °C. Lower values are only theoretical and are not applicable.*

Table 5.4: SL900A reference voltage difference, resolution and measuring range

Difference between reference voltages (mV) (V_{REF2}-V_{REF1})	*Resolution* (°C)	*Measuring range** (°C)
$50\ mV$	$0.029°C$	$29.7°C$
$100\ mV$	$0.058°C$	$59.3°C$
$150\ mV$	$0.086°C$	$88.0°C$
$200\ mV$	$0.116°C$	$118.6°C$
$250\ mV$	$0.145°C$	$148.3°C$
$260\ mV$	$0.151°C$	$154.2°C$
$300\ mV$	$0.174°C$	$177.9°C$
$310\ mV$	$0.180°C$	$183.9°C$
$350\ mV$	$0.203°C$	$207.6°C$
$360\ mV$	$0.209°C$	$213.5°C$
$400\ mV$	$0.232°C$	$237.2°C$

**The maximum measuring range is from -40 °C to 125 °C. The values which correspond to higher measuring range are not applicable.*

The accuracy of the temperature measurement is reported to be ± 1 °C, for the default setting of the RFID

chip which is for the temperature range between -29 °C to 58 °C. If the reference voltages are changed for wider temperature range measurements, a lower temperature accuracy will apply ($> \pm 1$ °C) and the sensor will need a re-calibration. Generally, a higher measuring range results in inferior accuracy. The relation between temperature range and accuracy was tested in practice by changing the reference voltages of the RFID chip for two different temperature measuring ranges and by evaluating the accuracy achieved for each range. The temperature sensor was then re-calibrate by utilizing a high accuracy (± 0.1 °C) Resistance Temperature Detector (RTD) probe.

The equation (5.1) below is used for the calculation of the temperature in °C:

$$T = \frac{V_{REF2}[mV] \cdot (code + 1024) - code \cdot V_{REF1}[mV]}{1024 \cdot 1.686} - 273.15 \tag{5.1}$$

, where $code$ is the output binary code of the integrated ADC which value is read by sending the appropriate command to the RFID chip via an RFID reader. For the tests performed, there were two cases studied according to:

- Case study 1: V_{REF1} = 360 mV and V_{REF2} = 560 mV. These values correspond to a minimum temperature limit of 59.0 °C and a temperature range ($V_{REF2} - V_{REF1}$) of 118.6 °C, hence from 59.0 °C to 177.6 °C (applicable up to 125 °C).

- Case study 2: V_{REF1} = 460 mV and V_{REF2} = 560 mV. These values correspond to a minimum temperature limit of 59.0 °C and a temperature range ($V_{REF2} - V_{REF1}$) of 59.3 °C, hence from 59.0 °C to 118.3 °C.

The (5.1) will be used for the conversion of the ADC output ($code$ value) to temperature, but also there will be a two-point calibration in order to find a curve fitting the data. This is quite important since the RFID chip is calibrated for the default values of reference voltages and a potential change of these voltages will require a re-calibration. The curve which will be used to fit the data will acquire the form $T(^\circ\text{C})=a \cdot code(binary) + b$.

The temperature measurement setup which was used contains a hot plate [105], a high accuracy RTD temperature sensor [106], the RFID reader and its antenna, a copper block piece with a small hole at the middle in order to insert the RTD probe and the RFID sensing tag. The measurement setup is presented in Fig. 5.4

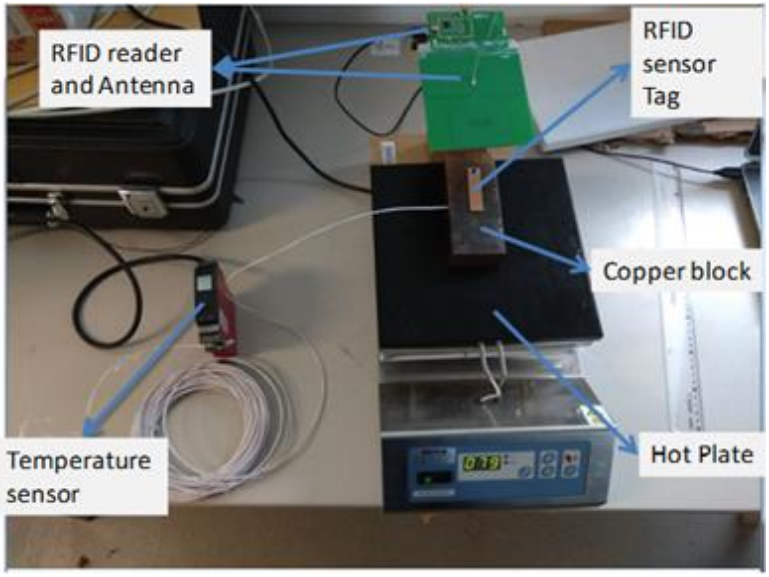

Figure 5.4: Temperature measurement setup

The results for each different configured temperature range are presented in Fig. 5.5 and Fig. 5.6.

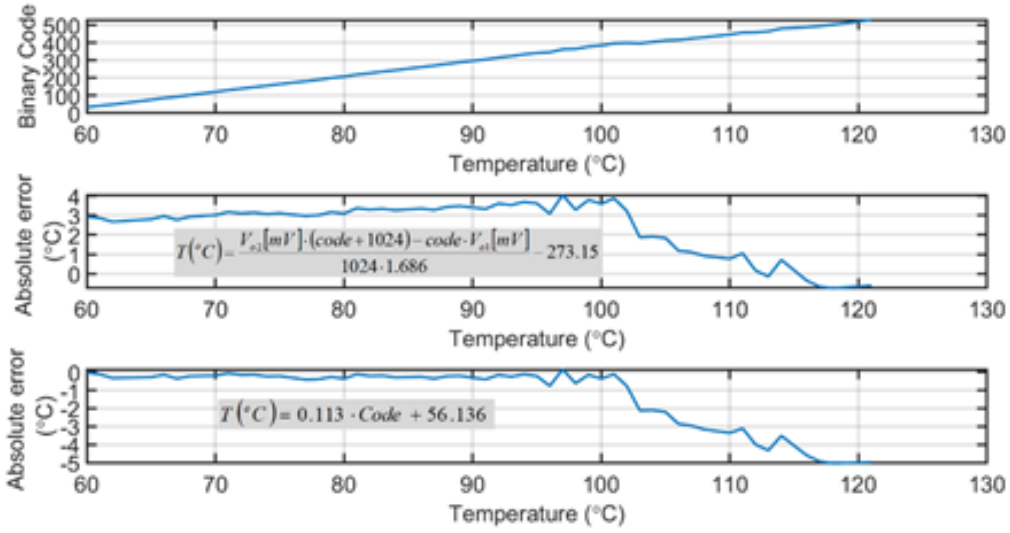

Figure 5.5: Case 1: output code and absolute error using the 5.1 and 2-point calibration

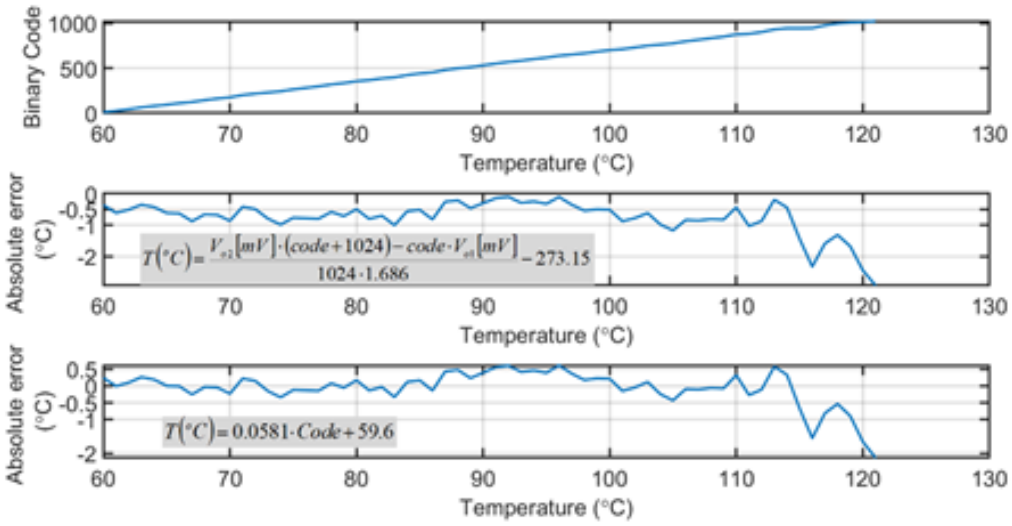

Figure 5.6: Case 2: output code and absolute error using the 5.1 and 2-point calibration

For the first case, where the temperature range is 118.6 °C, the absolute error which results from using the 5.1 is quite high, with values from 2.5 °C up to 4 °C for temperature values from 60 °C to 100 °C. By using the fitting curve, which was extracted by the 2-point re-calibration, the result can be more accurate resulting in absolute error from 0 °C to 1 °C from 60 °C to 100 °C and up to 5 °C for 100 °C to 120 °C. The curve extracted in this case was: $T(°C) = 0.113 \cdot code + 56.136$. For the second case, the temperature range is 59.3 °C. The absolute error found by using the 5.1 acquired values up to 0 °C to 1 °C for the interval 60 °C to 100 °C and up to 3 °C for 100 °C to 120 °C. The fitting curve found from the 2-point re-calibration, in this case, was the $T(°C) = 0.0581 \cdot code + 59.6$. By applying this curve for the temperature conversion the absolute errors that is calculated is from -0.5 °C to 0.5 °C for the interval 60 °C to 100 °C and up to -2 °C for 100 °C to 120 °C.

Finally, from the fitting curves it is shown that their general form is: $T(°C) = resolution \cdot code + Lower\ temperature\ limit$, where the values of resolution and lower temperature limit are close to the theoretical values (Table 5.3 and Table 5.4) needing a correction, from the 2-point calibration.

5.3.2 Stress measurements using an external strain sensor

Detecting deformation is an important parameter to be monitored, especially when it concerns structural health. One approach on utilizing RFID sensing technology to detect deformation was proposed in [107], where the bending state of a material could be sensed with an internal type RFID sensor. Another approach is to utilize a strain gauge and form an external type RFID sensor, similar to [108]. This approach with the external strain gauge is the selected option in this case. One of the advantages of the particular selected RFID chip is the possibility of connecting a sensor to either one of the two available external ports. This feature was exploited in order to operate the RFID sensor tag as a stress sensor by utilizing a strain gauge.

A strain gauge is a device capable to detect deformation of the materials on which it is attached (see Fig. 5.7). As the gauge is stressed, a different variation of resistance is being presented on its input, linking this resistance variation to the level of stress. The strain gauge has some characteristic values, such as the gauge factor (GF) which describes the correlation between strain and resistance variation (ΔR) and the characteristic resistance R_0. The strain can be calculated from the 5.2:

$$\epsilon = \frac{\Delta R}{GF \cdot R_0} \tag{5.2}$$

where ϵ is the strain in μstrain.

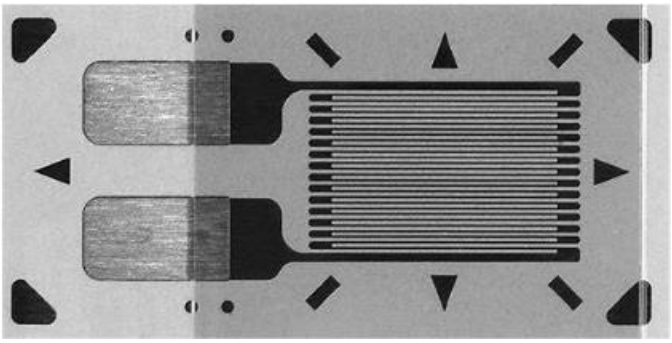

Figure 5.7: Strain gauge from Micro Measurements company [109]

For the strain gauge used here [6], the GF is 2.155 and the R_0 is 350 Ω resulting in a variation of the strain versus the resistance variation according to Fig. 5.8.

Having established the basic properties of the strain gauge the next step would be to connect it with the RFID sensor tag and in particular with the RFID chip. The RFID chip besides the two external ports for

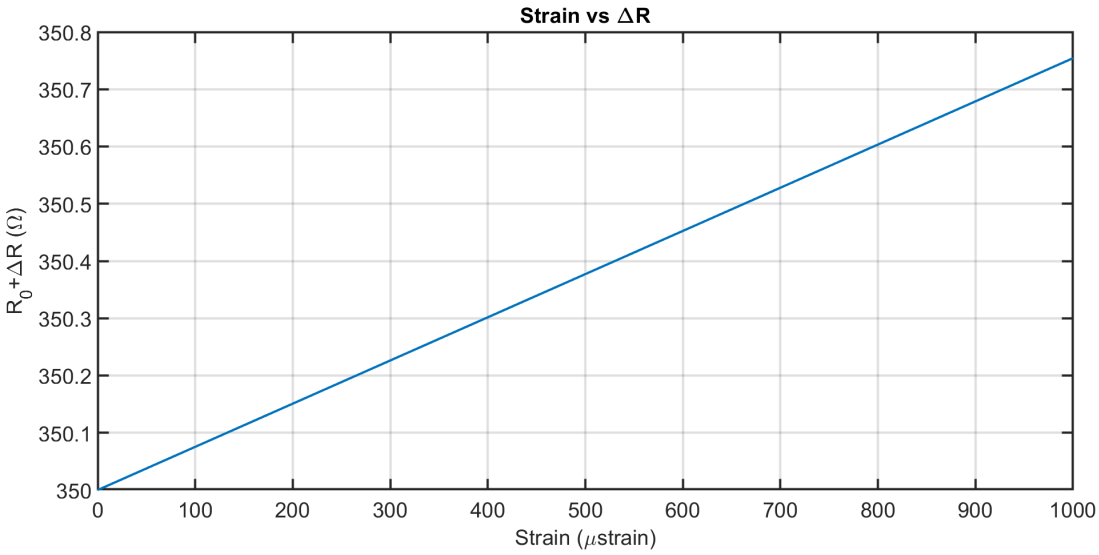

Figure 5.8: Strain versus ΔR for the used strain gauge

connecting sensors, among others, contains a port supplying a reference voltage with AC excitation as well as a ground port. Based on the specific characteristics of the RFID chip, two possible connections were identified:

- By using a Winston bridge, with appropriate resistance values and replacing one resistor with the strain sensor. The input ports of the Winston bridge are connected to the reference voltage port and the ground port. Then by utilizing both the external ports of the RFID chip connecting them to the output ports of the Winston bridge the voltage difference variation can be acquired. From this difference variation, the resistance variation can be deduced and consequently the strain value.
- By using only one external port and the voltage reference port. In this setup, the resistance variation is detected through the voltage difference variation at the external port for constant current feed.

To test the sensing performance of the RFID sensor tag with the strain gauge in practice, a measurement setup was prepared as illustrated in Fig. 5.9.

The measurement setup contained the RFID sensor tag, the strain gauge glued to an aluminum plate, a control knob to achieve small variations of strain and an electronic multimeter [110] with a resolution of 0.01 Ω. In addition, an RFID reader was positioned opposite to the measurement setup to interrogate the RFID sensor tag. The value of the strain gauge output for different control knob states was obtained by the RFID reader with the appropriate software interface and at the same time, the value of the resistance of the

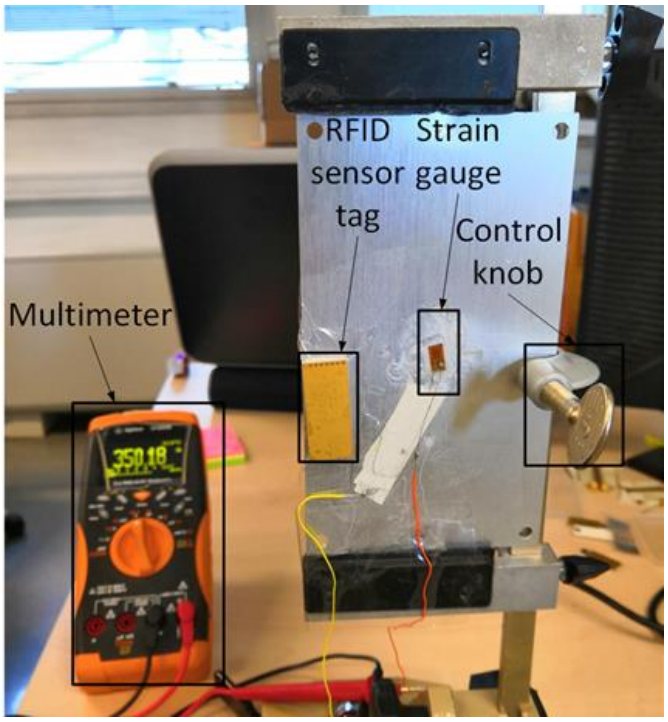

Figure 5.9: Strain measurement setup

strain gauge was reported from the multimeter. The values captured by the RFID reader were not stable, due to accuracy limitations, and for this reason for every state 10 values were captured and the average value was used for plotting the data. In Fig. 5.10 the strain measured by the RFID sensor tag is presented.

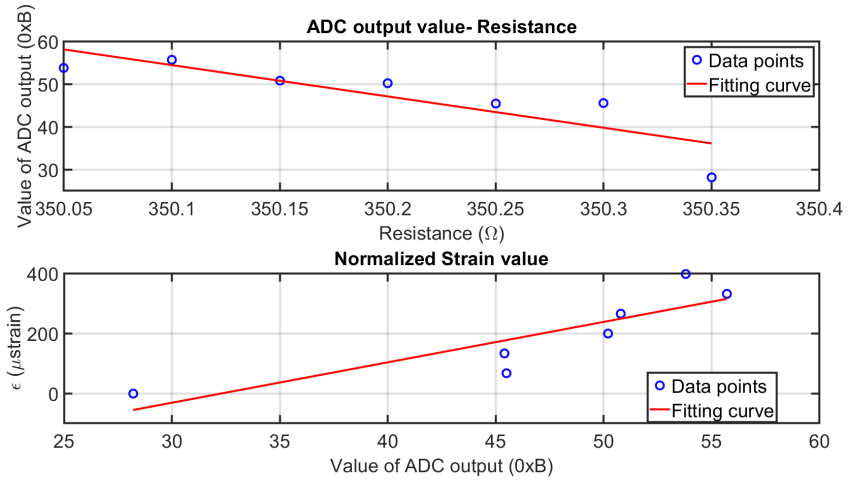

Figure 5.10: Resistance versus ADC output and normalized strain measured by the RFID sensor tag

The presented strain measurements are considered to be in stable temperature conditions, since they were all performed in room temperature in a time duration of several hours. In the case of a real environment application, the temperature can play a major role in the accuracy of the system, since the output of the strain gauge is temperature dependent [111]. This can be solved quite easily with the current RFID chip since the integrated temperature sensor can be used to monitor the temperature at each measurement. By transmitting the appropriate command to receive the temperature value at each stress measurement, a temperature stamp can be attached to each data point, allowing this way a temperature compensation.

Finally, a comparison between the measured data and theoretical data must be concluded in order to demonstrate the validity of these measurements. The strain gauge during the measurements acquired values between $350.35\ \Omega$ to $350.05\ \Omega$ with ΔR= $0.30\ \Omega$. This resistance variation corresponds to a variation of the strain of $400\ \mu$strain according to Fig. 5.8. In Fig. 5.10 at the bottom diagram the data points span from 0 to $400\ \mu$strain and the fitting curve reaches a value of approximately $350\ \mu$strain. The accuracy of the stress measurements can be improved by using the first approach (i.e., Winston bridge) but this concept has not been explored at the time.

5.4 Temperature measurements with the twin RFID sensor tag

Previously, it was demonstrated that the temperature accuracy and the temperature range present performance inversely proportional. Consequently, if high accuracy in extended temperature range is required, the RFID sensor tag will not be able to offer a good monitoring solution.

To solve this issue, an analog external temperature sensor with better accuracy could be added to an external port of the RFID chip and its value to be converted by using the 10-bit integrated ADC circuit. Another solution could be to utilize a digital temperature sensor connected to a complementary microcontroller and to communicate its value to the RFID chip by a Serial Peripheral Interface (SPI) bus. The microcontroller is needed to act as the SPI master unit since the RFID chip contains an SPI interface, but it can only operate as a slave unit. These conventional solutions have the disadvantage to increase the complexity of the RFID sensor tag and in the intended harsh environment is something that should be avoided.

For the above mention problem, a possible solution could be to exploit the twin RFID sensor tag. Each one of the RFID chips will be covering the half part of the temperature range offering thus superior accuracy. The twin RFID sensor tag, will be transmitting two EPC codes for the identification of each RFID chip and the intended temperature range coverage and value can be associated with this EPC code.

The twin RFID sensor tag was studied in a temperature measurement setup in the laboratory. In order to showcase the performance regarding the temperature sensing accuracy, it will be compared with an RFID sensor tag utilizing one RFID chip (from now on referred as single RFID sensor tag) and for the same temperature range. The exact settings for both the RFID sensor tags can be viewed in Fig. 5.11 below.

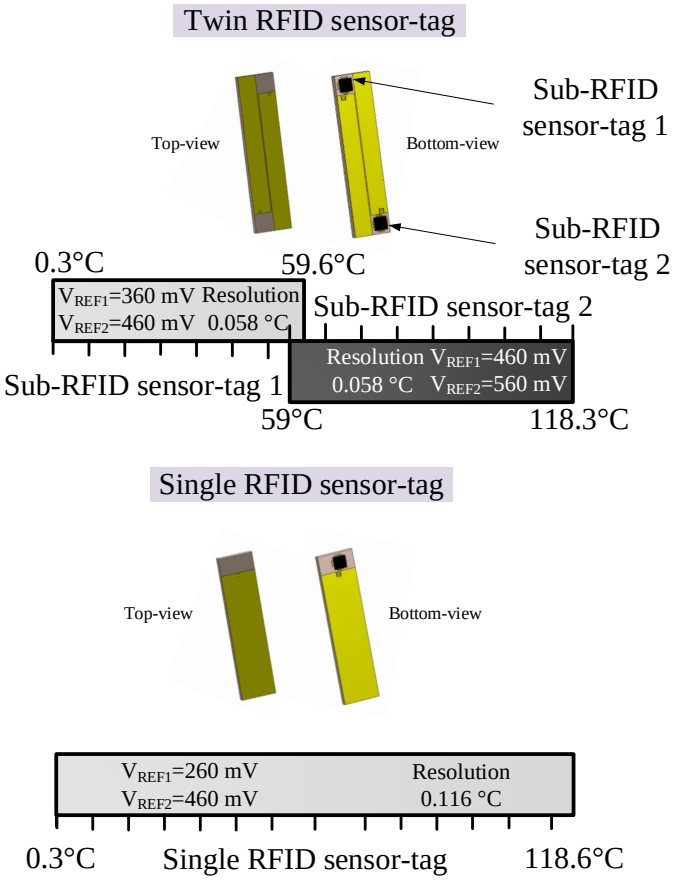

Figure 5.11: Twin and single RFID sensor tags settings

The first sub-RFID sensor tag was set with $V_{REF1} = 360\ mV$ and $V_{REF2} = 460\ mV$ which yields in lower temperature limit of 0.3 °C and a measuring range of 59.3 °C. The second sub-RFID sensor tag was set with the V_{REF1}= 460 mV and V_{REF2} = 560 mV, which yields in lower temperature limit of 59.0 °C and a measuring range of 59.3 °C. With this configuration, the temperature range between 0.3 °C to 118.3 °C is covered. The single RFID sensor-tag was set with V_{REF1} = 260 mV and V_{REF2} = 460 mV, resulting in a lower temperature limit of 0.3 °C and a temperature range of 118.6 °C. With this configuration, the two different sensor tags offer very similar temperature range, 118 °C and 118.3 °C respectively. The experimental setup to perform temperature measurements is presented in Fig. 5.12. It comprises a hot plate,

a Pt-100 temperature sensor with an RTD probe, a copper block and the antenna of the RFID reader. For each recorded temperature value by the Pt-100 temperature sensor, the corresponding value of the ADC of the RFID chip would be captured. The temperature intervals were 1 °C.

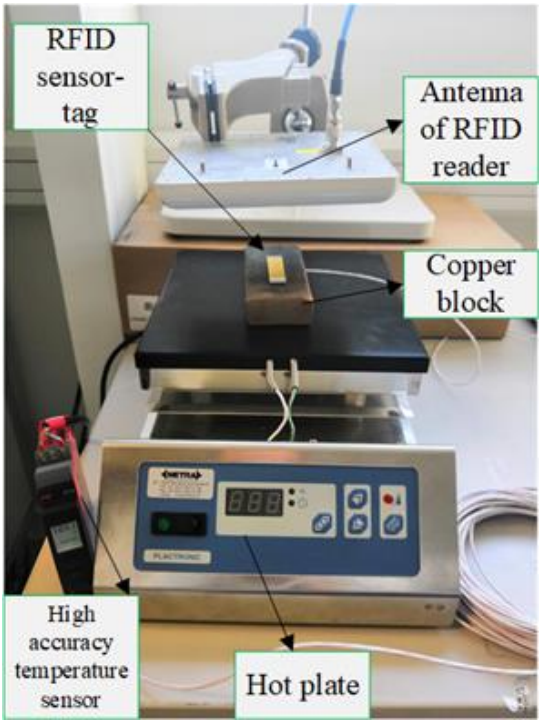

Figure 5.12: Experimental setup for temperature measurement

The copper block in the middle of the hot plate has a small hole, big enough for the RTD probe to fit in. Positioning the RFID sensor tags on top of the probe can ensure the highest possible accuracy between the reading of the temperature sensor and the RFID tag (see Fig. 5.13(b)).

The twin RFID sensor tag was trimmed at the sides for tuning purposes, aiming to resonate inside the ETSI frequency band (see Fig. 5.13(a)).

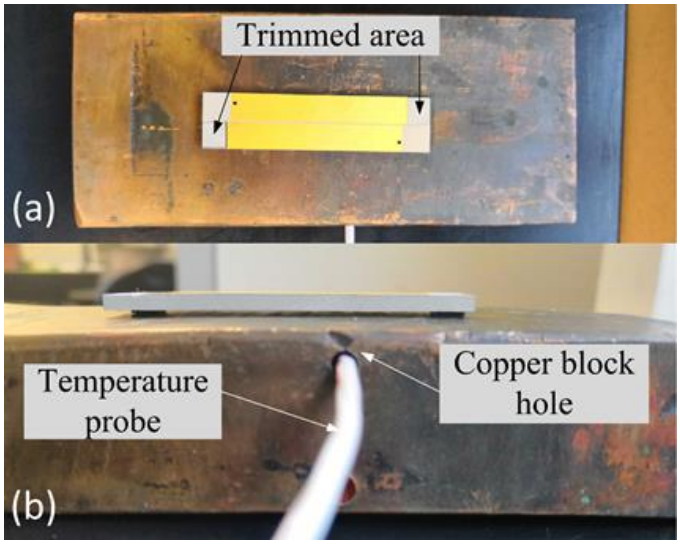

Figure 5.13: Details of measurement setup(a) Trimmed twin RFID sensor tag (b) RTD probe in the hole of the copper block

For the case of the twin RFID sensor tag, the ADC output values were captured initially from the one RFID chip (with a temperature range up to 59 °C) and the other RFID chip was read for higher values of temperature (with a temperature range up to 118.3 °C). The values of the ADC output were registered and they are presented in Fig. 5.14.

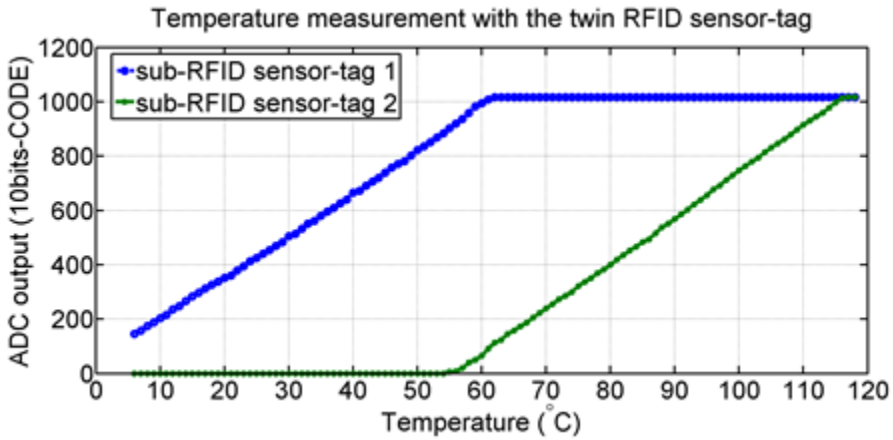

Figure 5.14: RTD probe in the hole of the copper block

The outputs of both ADCs are following a quite linear behaviour and when the first RFID chip saturates

at 60 °C (1 °C higher than the theoretical value), the other RFID chip is read. From the registered values a 2-point calibration was performed based on the value of temperature read by the Pt-100 temperature sensor. The calibration curves for the ADC outputs are:

$$T_1 = 0.0630 \cdot (AD_{CODE}) - 2.176 \tag{5.3}$$

for the first RFID chip in the low-temperature region and:

$$T_2 = 0.0597 \cdot (AD_{CODE}) + 55.52 \tag{5.4}$$

From the calibration curves, the absolute temperature error found for the twin RFID sensor tag is illustrated in Fig. 5.15.

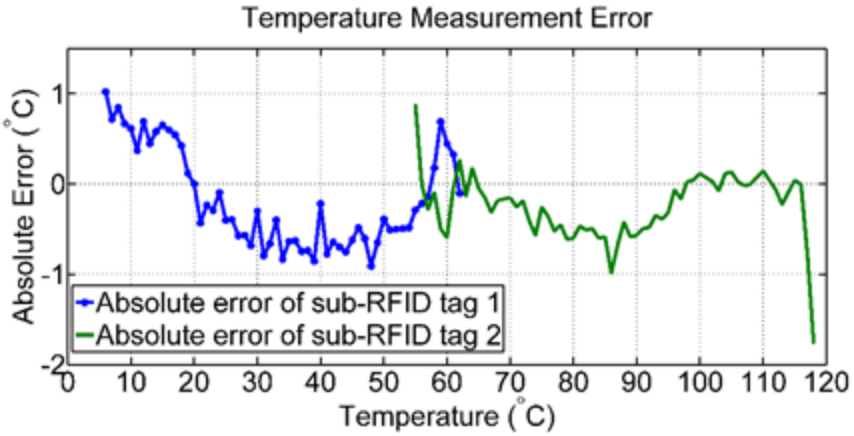

Figure 5.15: The absolute error of the temperature measurement for the twin RFID sensor tag

As it can be observed in Fig. 5.15, the absolute error through the whole temperature range is less than ±1 °C. At the end of the curve, near the 120 °C mark, the error is increasing due to the fact that the output of the ADC of the RFID chip was saturated in this point at around the 117 °C mark (1 °C less than the expected theoretical). In the region around 60 °C, both sub-RFID sensor tags are transmitting data without being in saturation, making this region able to operate as a cross-reference region.

The same procedure was followed and for the case of the single RFID sensor tag. The measurements were conducted for the same temperatures with the same temperature intervals of 1 °C. The results of the ADC output of the chip in comparison to the temperature are reported in Fig. 5.16.

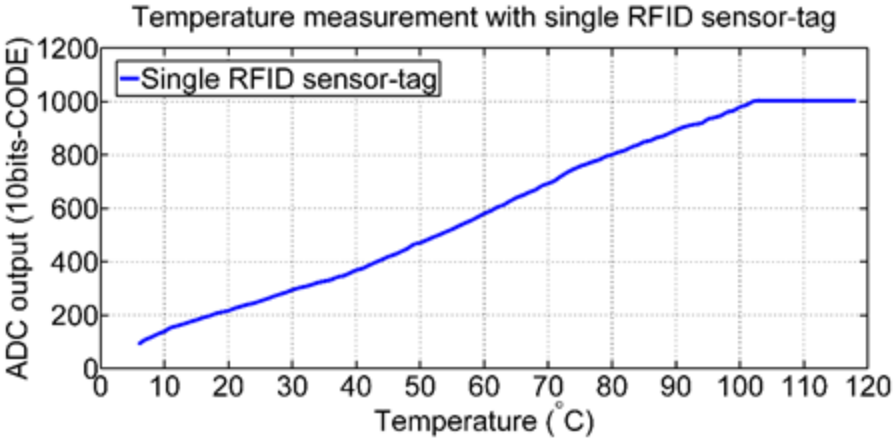

Figure 5.16: The ADC output of the single RFID sensor-tag versus the measured temperature

The 2-point calibration curve which was extracted from the results of Fig. 5.16 was:

$$T_1 = 0.107 \cdot (AD_{CODE}) - 5.12 \tag{5.5}$$

The ADC output of the chip is saturated at the 103 °C mark, much lower than the 118.6 °C which was anticipated. The absolute error which is corresponding to the single RFID sensor tag is presented in Fig. 5.17.

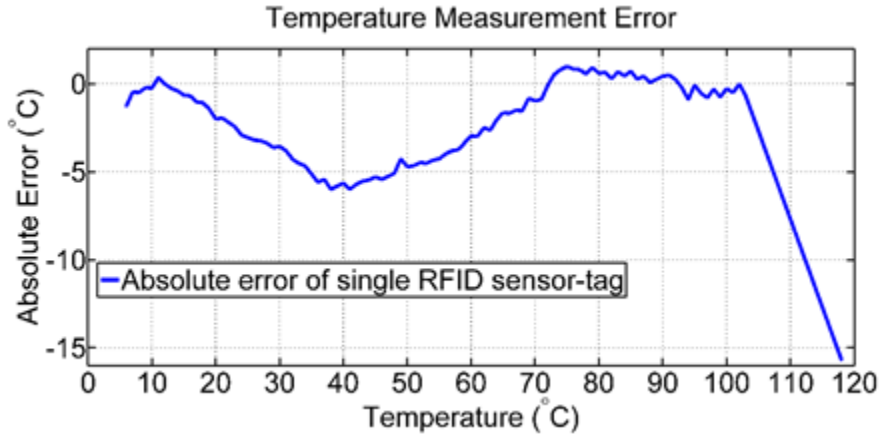

Figure 5.17: Absolute temperature error of the single RFID sensor-tag

The absolute error in the case of the single RFID sensor tag is much higher than in the case of the twin

RFID sensor tag.

Concluding this section, the twin RFID sensor tag concept can be utilized as the mean for sensing multiple parameters simultaneously. With such setup up to 5 parameters could be potentially sensed (2 external ports for every RFID chip and the integrated temperature sensor) maintaining a small form factor.

5.5 Conclusion

In this chapter the main focus was set on measurements in the laboratory environment. Initially, an exploration on the impact of the RFID chip placement on the RFID sensor tag was performed by means of a thermal simulation in the environment of the CST microwave suite. The results showed that the RFID sensor tag can offer higher accuracy if it is designed with the RFID chip in direct contact to the surface it wants to measure.

Following, information regarding the sensing capabilities of the used RFID chip were presented, by introducing the reference voltages which control various characteristics of the sensing functions of the RFID chip (such as resolution, temperature range etc.). The designed RFID sensor tags which were presented so far were tested in a temperature measurement setup in order to showcase potential configurations for the particular RFID chip.

In addition, in a stress measurement setup, the RFID sensor tag was tested by adding an external strain gauge and it was evaluated in its capabilities to operate as stress sensor.

Finally, the previously designed and presented twin RFID sensor tag was studied in a temperature measurement setup. The goal of this measurement was to underline the advantage of the twin RFID sensor tag regarding its temperature measurement capabilities. This was achieved by comparing the twin RFID sensor tag to an RFID sensor tag operating with one RFID chip.

CHAPTER 6
DIFFERENT APPROACHES ON RFID SENSING

6.1 Introduction

Besides the choice of using RFID chips with enhanced operation (i.e. integrated sensors or possibility of connecting a sensor), the technique discussed earlier and presented as internal sensing was explored. In this context, alternative structures were designed and tested, aiming to evaluate their performance as possible solutions in an RFID sensing setup.

In this chapter, a technique which is actually a fusion between the external and internal type of RFID sensing is proposed, by utilizing a supplementary circuit of self-tuning integrated in some commercially RFID chips. This technique is evaluated by measurements in a temperature varying environment and useful conclusions are extracted. In addition, a method to improve the performance of such technique is proposed. The joint exploitation of internal and external sensing is of great interest for future development of RFID.

Furthermore, some chipless RFID designs are explored, aiming to assess their robustness and performance in a temperature and humidity sensing concept as well as for an angular motion sensing concept. Finally, the possibility of using Software Defined Radio (SDR), operating in the regulated frequency band (ISM band) for reading chipless RFID sensors is also explored and evaluated. Finally, it is important to mention that the chipless RFID sensing approaches will be presented without getting into much details. This is due to the fact that the work regarding the chipless RFID sensors was led by a post-doctoral researcher with the author's participation.

6.2 Self-tuning RFID chips

Recently, RFID chips from different manufacturers (e.g. Impinj Monza R6 [112], NXP UCODE 8 [113]) have been developed with an integrated self-tuning circuit. The purpose of this circuit is to better match the RFID integrated circuit (IC) with the tag's antenna impedance and achieve higher bandwidth of operation, and so, the best possible performance in case of de-tuning due to environmental effects. An example of the effect of the self-tuning circuit is demonstrated in Fig. 6.1.

Here the Monza R6 RFID chip from Impinj will be the main focus and subject of research. The function of the self-tuning circuit (named as auto-tune in the particular chip and this term will be used interchange-

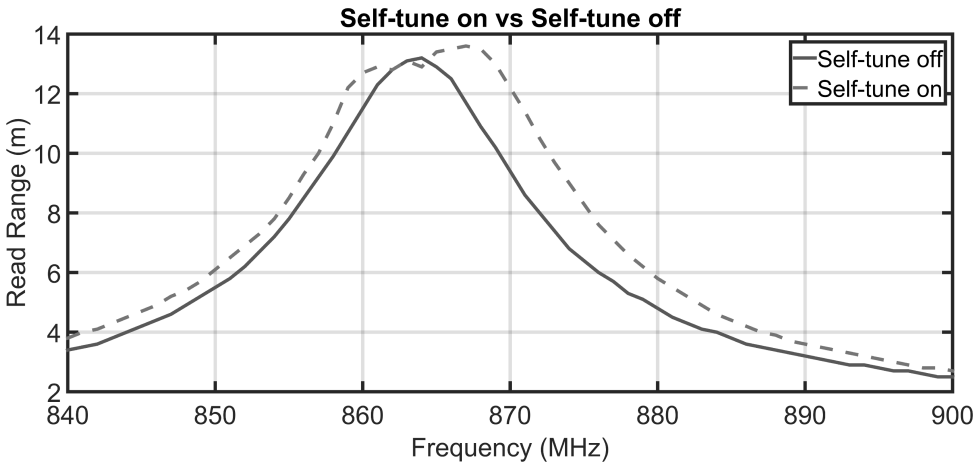

Figure 6.1: Self-tuning effect on the read range of an RFID tag

ably) is to sample the power at the input ports of the chip for different, predefined capacitance values. When a value of capacitance is detected to ensure the maximum input power then this value of capacitance is selected and stored in the memory bank of the RFID chip. The value of the chosen capacitance can then be accessed from an RFID reader simply by reading the specified memory slot which this value is stored. The self-tuning circuit of this chip [114] requires lower power than the RFID IC to operate and it maximizes the power extraction efficiency by adding or subtracting two different, fixed values of capacitance according to Table 6.1. A presentation of the operation of the self-tuning circuit for the Monza R6 RFID chip is presented in Fig. 6.2.

Table 6.1: Capacitance values of auto-tune circuit of Monza R6

Memory Value (hexadecimal)	*Input capacitance value difference (fF)*
0000	-100
0001	-40
0002	0
0003	40
0004	100

6.3 Self-tuning circuit for sensing operation

Using conjointly the self-tuning circuit integrated in some RFID chips and a transducer it can be possible to offer a mixture of the two main sensing approaches (see §Chapter 1), where the sensing is performed with

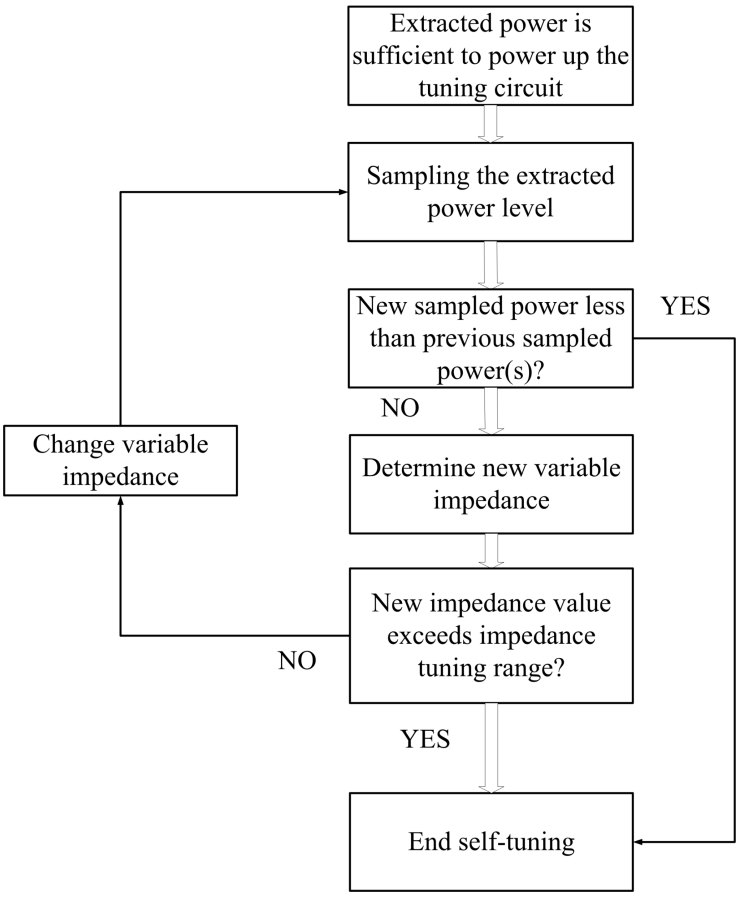

Figure 6.2: Operating principle of the auto-tune circuit

analog way and the communication digitally. This approach can be relevant notably for low-cost wireless sensing. Also, some specialized IC have been developed by the RF-Micron company in [115], where the IC has greater capabilities as far as the self-tuning range is concerned. These RFID chips are more sensor-application oriented, since they include an integrated temperature sensor. Some commercial products with the RF Micron ICs offer temperature and humidity sensing solutions (e.g. [116]). In addition, works related to this concept have been published recently in [117] and [118]. In these publications, a formulation of the RFID sensing problem is presented and discussed. Moreover, a complete model based on a commercially available shelf-tuning IC ([4]) is proposed and experimentally verified in both linear and non-linear regimes.

The approach presented in this section is regarding the utilization of an RFID chip with self-tuning capabilities and an RFID antenna formed by a temperature sensitive material. The temperature change will result in a variation of the complex impedance of the antenna structure, which will result in a frequency shift of the RFID tag resonance frequency, resulting in triggering the self-tuning circuit of the RFID chip;

and this, assuming that the RFID chip is relative insensitive to the variation of temperature. By reading the value of the self-tuning circuit stored in the memory of the RFID chip, the temperature of the RFID tag can be assessed.

6.3.1 Selection of substrate

One of the main characteristics of substrate materials is the thermal coefficient of relative permittivity. This coefficient describes the variation of relative permittivity according to the temperature variation and it differs for different substrate materials. From Table 6.2, it can be seen that the substrate RT 6010.2LM from Rogers (the substrate which has been used in this thesis so far) presents the higher thermal coefficient of relative permittivity and this is the substrate which will be used. Moreover, the thermal expansion of the substrate is a secondary contributor to the overall sensitivity to the variation of temperature, since it is contributing to the change of the overall size of the tag.

In addition to the substrate acting as a temperature transducer, the copper which is used for the realization of the tag presents a coefficient of thermal expansion of 16 $ppm/^{\circ}C$ adding a variation to the length of the tag and to the complex impedance overall.

Table 6.2: Properties of common used substrate materials

Substrate	*Coefficient of thermal expansion x/y/z-axis*	*Thermal coefficient of relative permittivity* ϵ_r
RT6010.2LM	$24/24/47\ ppm/^{\circ}C$	$-425\ ppm/^{\circ}C$
RT6006	$47/34/117\ ppm/^{\circ}C$	$-410\ ppm/^{\circ}C$
RO4350B	$10/12/32\ ppm/^{\circ}C$	$+50\ ppm/^{\circ}C$
RO4003C	$11/14/46\ ppm/^{\circ}C$	$+40\ ppm/^{\circ}C$
RT5870	$24/24/47\ ppm/^{\circ}C$	$-115\ ppm/^{\circ}C$
RT5880	$31/48/237\ ppm/^{\circ}C$	$-125\ ppm/^{\circ}C$

Assuming a linear dependency between the relative permittivity ϵ_r and the temperature, an empirical equation can be deduced (6.1):

$$\epsilon_r(T) = \epsilon_{r0} + k \cdot T \tag{6.1}$$

where T is the temperature in $^{\circ}C$, ϵ_{r0} is the relative permittivity at $0^{\circ}C$ and k is the thermal coefficient of relative permittivity. The variation of the relative permittivity versus the temperature is presented in Fig.

6.3.

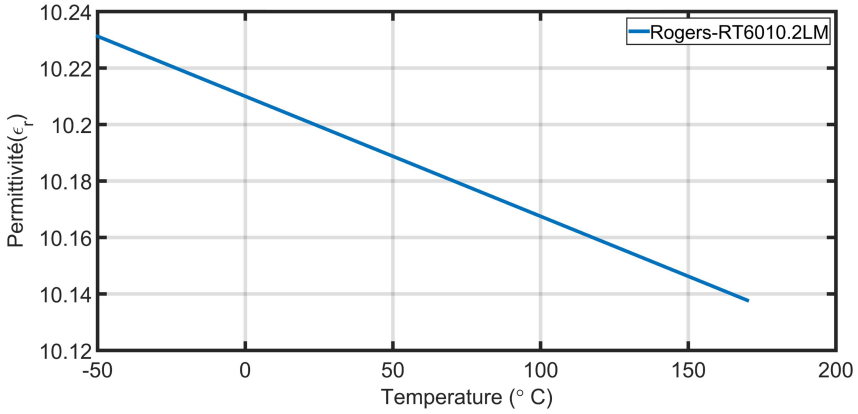

Figure 6.3: Dependency of thermal coefficient of relative permittivity versus the temperature for the RT 6010.2LM substrate

Summing up, the temperature variation affects the complex impedance of the antenna of the RFID tag due to the sensitivity of the substrate and of the metallic parts. This leads to a mismatch between tag's antenna and RFID chip and this mismatch is attempted to be corrected automatically by the self-tuning circuit of the UHF RFID chip. By acquiring the values of the self-tuning circuit from the memory bank of the UHF RFID chip for known values of temperature, the UHF RFID sensor tag can be calibrated and operate as a temperature sensor.

6.3.2 Simulation of the proposed RFID sensor tag

In order to validate the impedance variation due to the effects of temperature a UHF RFID tag was designed by means of a 3D numerical model in the CST Microwave studio. The variation of the relative permittivity of the substrate, as well as the variation of the size of the substrate and of the copper parts due to a variation of temperature, were imported as parameters and the simulation was performed for different values of temperature. The RFID tag was designed to be placed on a metallic surface and for this reason a copper block was included as part of the simulation. In this point it is important to mention the fact that even though this study is focusing on a UHF RFID tag designed to be attached on metal does not affect the generality of the proposed technique. The dimensions of the UHF RFID tag are $57\ mm \times 15\ mm \times 1.27\ mm$ and of the copper block are $140\ mm \times 60\ mm \times 26\ mm$, see Fig. 6.4 and Fig. 6.5.

The input impedance of the used RFID chip can be calculated from a linearized RC model which consists of a resistor $R_p = 1.2\ k\Omega$ in parallel with two capacitors with values $C_p = 1.23\ pF$ and $C_{mount} = 0.21\ pF$

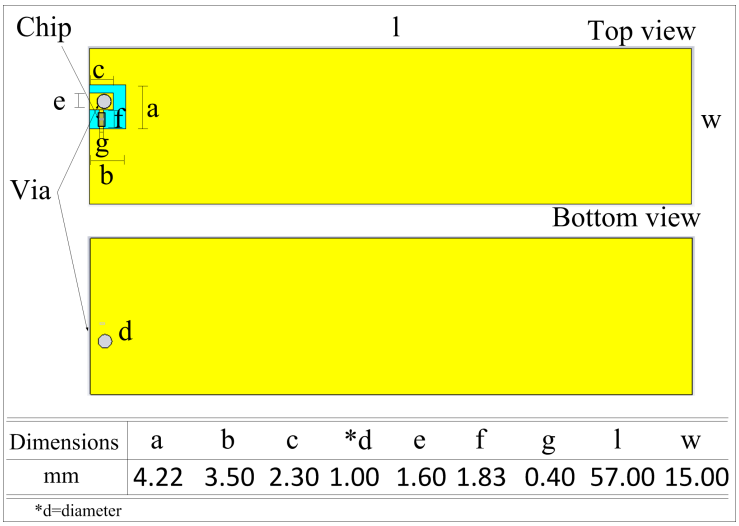

Dimensions	a	b	c	*d	e	f	g	l	w
mm	4.22	3.50	2.30	1.00	1.60	1.83	0.40	57.00	15.00

*d=diameter

Figure 6.4: Layout of the proposed RFID sensor tag

respectively. For the frequency of 866 MHz the input impedance of the chip is $Z_{in} = (13.42 - j \times 126.2)\Omega$.

A subminiature version A (SMA) connector, as well as a coaxial cable, are added to the 3D model in order to take into account discrepancies which arise when conducting this type of measurements. Indeed, when electrically small antennas with ground plane are being measured with the usage of a coaxial cable, serious discrepancies can occur [119]. This is due to the placement of the coaxial cable in the near-field of the antenna, interfering with the radiation characteristics. Also the small ground plane cannot be treated as an infinite ground plane and thus currents can flow back through the surface of the cable causing the cable to radiate. In addition, interference can arise from the SMA connector soldered on the body of the tag. The complete simulation setup is presented in Fig. 6.5.

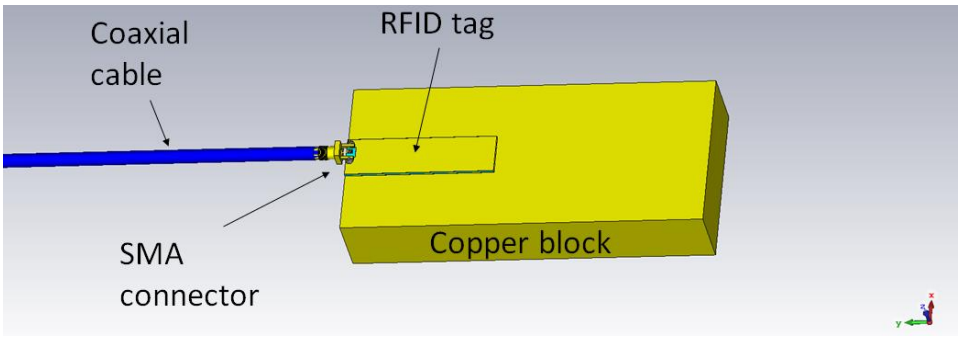

Figure 6.5: Complete simulation setup including the RFID tag, the SMA connector, the coaxial cable and the copper block

The designed setup was simulated aiming to acquire the real and imaginary parts of the impedance of the tag antenna as if the structure was in an environment with temperature between 30 °C and 80 °C and for every 10 °C. The results of the simulation are presented in Fig.6.6. The values of real part for the frequency of 868 MHz vary between 202 Ω and 211 Ω. For the imaginary part and for the same frequency the values vary between 65 Ω and 80 Ω. The results are following the expected behavior described in the principle of operation section, since the simulated effects of temperature are enough to create notable variations in the complex impedance of the antenna-tag.

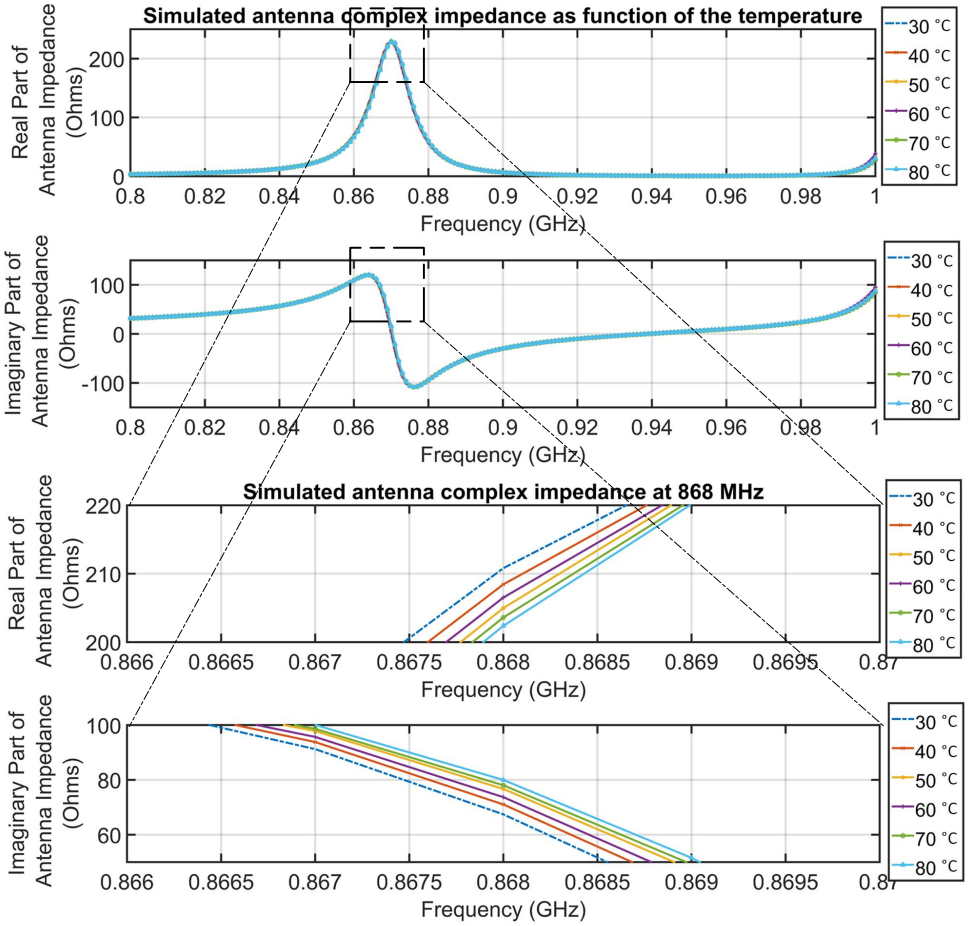

Figure 6.6: Simulated complex impedance of the antenna as function of temperature and span of real and imaginary values of the impedance at 868 MHz

6.3.3 Fabrication and measurements of the self-tuning RFID sensor tag

The self-tuning RFID sensor tag was fabricated and the prototype is illustrated in Fig. 6.7. A prototype, with an SMA connector in the place of the RFID chip was used to perform measurements in comparison to

the simulation results.

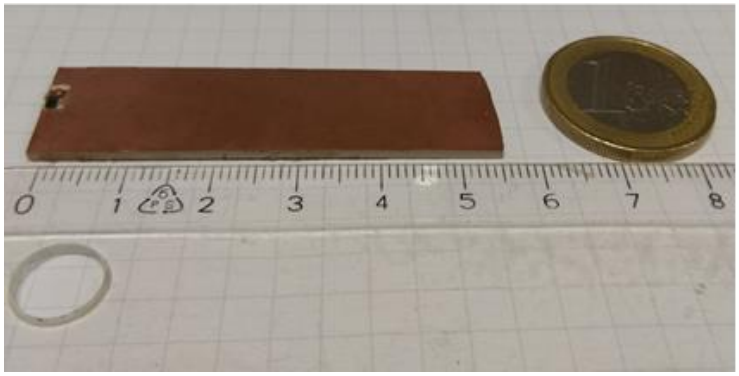

Figure 6.7: Fabricated self-tuning RFID sensor tag

The measurements were performed focusing on exploring the input impedance of the RFID chip and the complex impedance of the antenna as function of temperature. The measurements were performed by using the Agilent PNA network analyzer N5222A. A custom calibration kit was realized and used in order to calibrate the network analyzer and transfer the reference plane of the measurements to the edge of the SMA connector. For ensuring correct calibration, two reference circuits with known complex impedances were used to verify the calibration and adjust the offset delay from the de-embedding menu of the network analyzer. The reference circuits were two different combinations of a resistor in parallel with a capacitor soldered in an SMA connector. Before any measurement session the two reference circuits would be measured and used for verification, after the calibration, in order to set the offset delay from the de-embedding menu to the correct value.

Measurement of the RFID chip

Besides the exploration on the complex impedance of the RFID antenna structure, an exploration of the effects of temperature on the RFID chip was also performed, to ensure the initial assumption namely, the input impedance of the RFID chip is relative insensitive to the temperature variation.

Three Impinj Monza R6 RFID chips were soldered on SMA connectors and connected to the network analyzer while attached on a copper block which was positioned on a hot plate, see Fig. 6.8.

An RTD probe of the Pt-100 temperature sensor was inserted through a small hole in the middle of the copper block. The temperature accuracy of the Pt-100 temperature sensor is $\pm 0.1^{\circ}$C.

The network analyzer was set on power sweep mode with frequency 868 MHz and measurements of

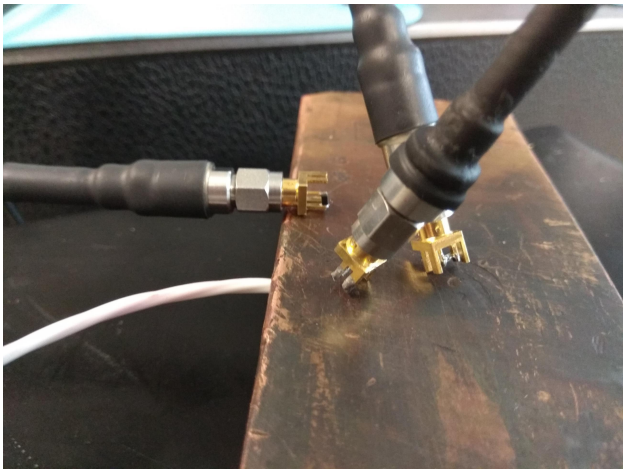

Figure 6.8: The RFID chips on the copper block on the hot plate

the impedance of the three RFID chips were acquired for temperature values between 30 °C and 80 °C, with intervals of 10 °C. The measurements where repeated multiple times for verification purposes. It was observed that the behavior of the chips was consistent and very similar for the three different RFID chips. The results of the measurement of the input impedance value of one of the RFID chips are shown in Fig. 6.9.

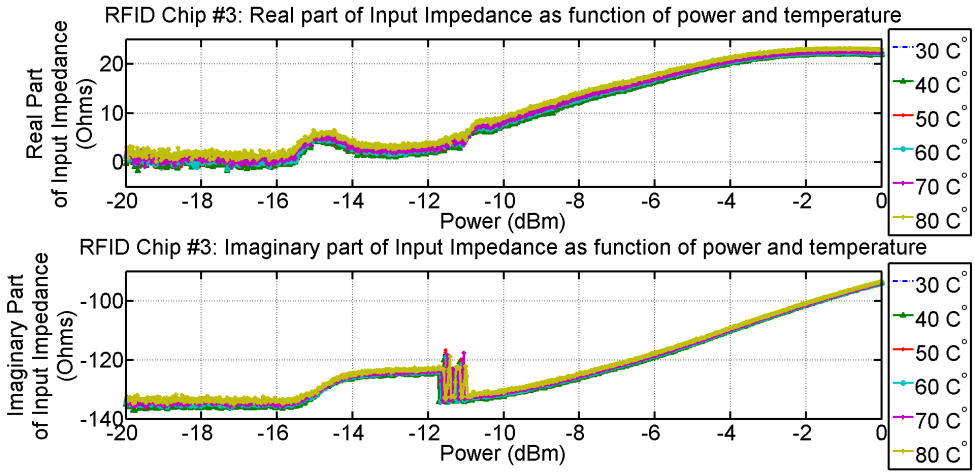

Figure 6.9: Real and imaginary part of the impedance of the RFID chips versus the temperature

From the measurement results of the RFID chips the activation power can be observed, around -15 dBm, which is consistent for all three measured RFID chips. The activation power in the datasheet is reported at -22.1 dBm but in the measurement setup the RFID chips were attached to 50 Ω connectors, downgrading the absorbed power levels. Thus, such deviation between measurement and datasheet is expected. Furthermore,

after the activation of the RFID chips, the real part of the impedance has a value between 1.1 Ω and 20 Ω depending on the input power. For the same range of input power, the imaginary part of the input impedance of the chips is between -130 Ω and -100 Ω. These values are also consistent for the three tested RFID chips and close to the reported values of the datasheet ($Z_{in} = 13.42 - j \times 126.2\ \Omega$).

As it can be seen in Table 6.3, the temperature affects the value of the input impedance of the RFID chips, increasing by a small amount the real part leaving the imaginary part almost unaffected. The imaginary part of the impedance remains constant due to the self-tuning circuit. The real part of the impedance of the RFID chips has a small deviation between the 3 UHF RFID chips, probably due to the amount of solder used in each case and which is inconsistent for the three RFID chips. Generally, the variation of the impedance of the RFID chip can be regarded as negligible in contrast to the variation of impedance of the antenna due to temperature variation.

Table 6.3: Complex impedance of the 3 RFID chips as function of temperature

Temperature $(^{\circ}C)$	*Real part of impedance* (Ω)			*Imaginary part of impedance* (Ω)		
	#1	#2	#3	#1	#2	#3
30	6.85	8.03	7.45	−139	−134	−132
40	7.40	7.34	7.46	−138	−135	−132
50	7.53	8.50	7.81	−138	−133	−131
60	7.69	8.60	8.16	−138	−133	−131
70	7.30	8.66	8.23	−134	−134	−131
80	8.52	8.79	9.34	−138	−133	−131

Measurement of the RFID tag antenna

The measurement of the complex impedance of the antenna-tag was the next goal of this study. In order to be able to make a comparison with the simulated results, the measurement setup was as close as possible to the simulated setup. The measurement setup is presented in Fig.6.10. The antenna is positioned on the copper block and from 30 °C to 80 °C for every 10 °C a measurement of the impedance of the antenna is performed.

In Fig. 6.11, the results of the measurements are presented. It was observed, in comparison with the simulated results, that there is a shift of the resonance frequency of the RFID tag of around 4 MHz between

Figure 6.10: Measurement setup of the RFID antenna tag

the results. For the simulation results this frequency was 868 MHz and for the measured results was 864 MHz.

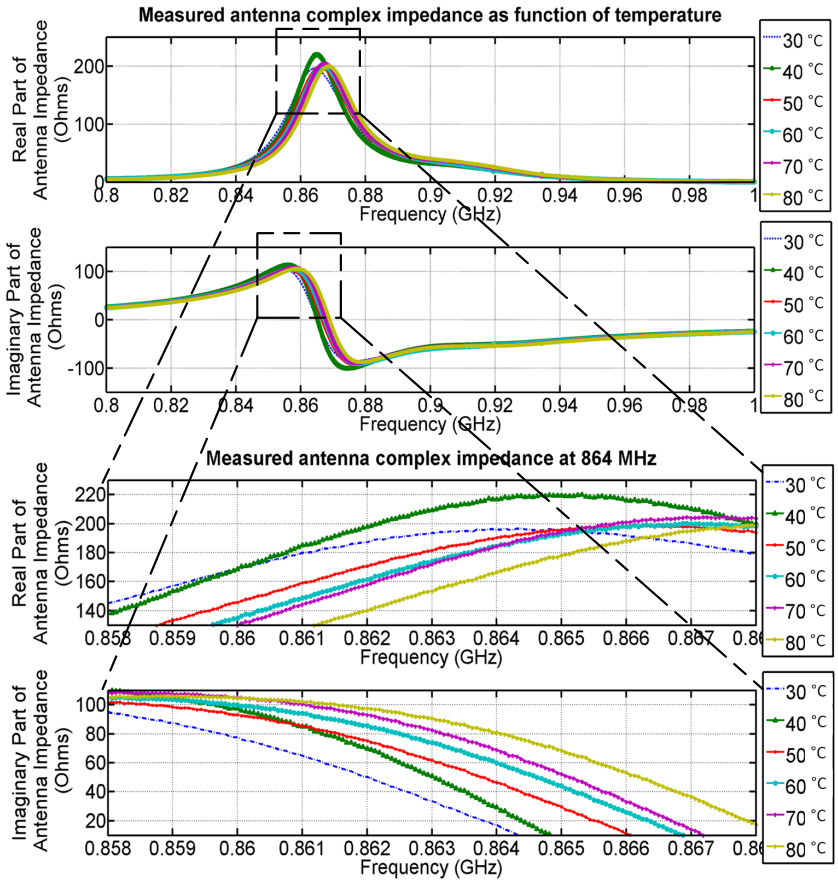

Figure 6.11: Measured complex impedance of the antenna as function of temperature and span of real and imaginary values of the impedance at 864 MHz

The value of the real part of the complex impedance for the frequency of 864 MHz is between 166 Ω

and 216 Ω while for the imaginary part, the value is between 17.2 Ω and 80.9 Ω.

It is important to note that the measurements have confirmed the initial analysis, presented in the section §6.3.2. Indeed, the imaginary parts of the complex impedances are monotonically depended on the temperature. It can be observed that there is a deviation between the results of the simulation and the measurement, but such deviation is expected when such a complex, temperature varying system is being study. The imaginary part of the impedance in both the simulated and measured data is increasing with the temperature and this is crucial for the discussed application. The self-tuning circuit of UHF RFID chip is trying to correct the imaginary part deviation of the impedance and the value stored in the memory bank of the chip is correlated with this increasing variation. Another important remark is that the system antenna and UHF RFID chip is a dynamic system where both parts are varying their impedances according to temperature. This variation occurs with different rates, as it was shown from the results of this study, and thus the main transducer of the system is the antenna part.

The comparison between the simulated and measured results is given in Table 6.4.

Table 6.4: Comparison between simulated and measured impedance of the RFID tag antenna

Temperature *(°C)*	*Simulated impedance at 868 MHz* *(Ω)*	*Simulated impedance at 864 MHz* *(Ω)*
30	$211 + j65$	$196 + j17.2$
40	$208 + j68$	$216 + j29.2$
50	$206 + j70$	$190 + j46.4$
60	$205 + j75$	$185 + j60.1$
70	$203 + j78$	$184 + j68.8$
80	$202 + j80$	$166 + j80.9$

6.3.4 Application on temperature sensing

The presented technique was tested in practice in a real application of temperature sensing. The RFID sensor tag with the Impinj Monza R6 RFID chip soldered was tested to confirm the validity of the presented study. The frequency band of interest is the ETSI band (865 MHz - 868 MHz). The preliminary measurements showed that in order to trigger effectively the self-tune circuit and change the value of the internal capacitance, the tag should be quite frequency selective and its resonance frequency should be a little higher (i.e., 870 MHz) from the interrogation frequency.

Designing the RFID tag with a little higher frequency enables the fast degradation of the read range in the EU band and consequently the extracted power of the chip, (see Fig. 6.12).

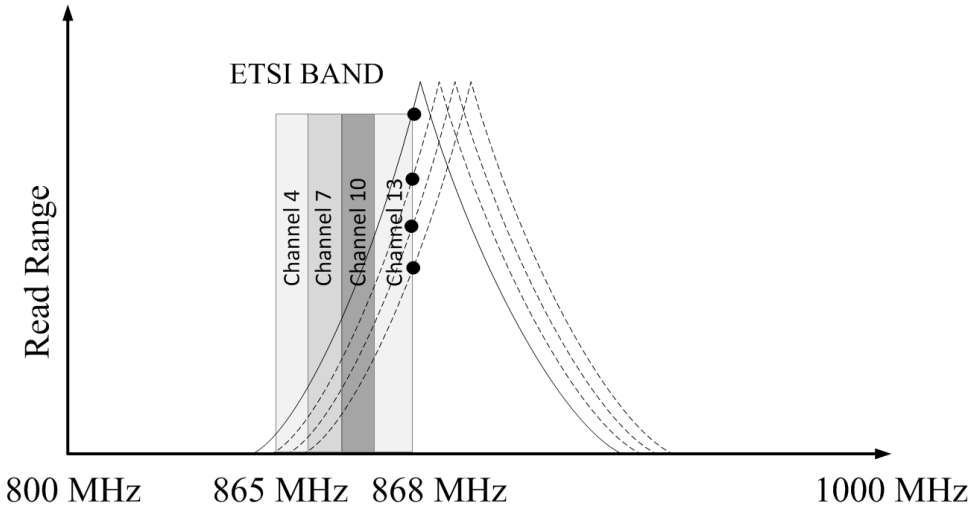

Figure 6.12: Change of resonance frequency due to temperature change and different power extracted level

This results to variations capable to trigger the self-tune circuit. In case of a broadband RFID tag, these changes would be much smaller and probably not enough to vary the self-tune circuit. Another option with this technique could be to have the resonance frequency inside the EU band and exploit every time a different single channel. In this way the total bandwidth of the EU band could be better exploited and the sensor could be used for a wider temperature range span. This kind of technique could be much better to be exploited in the FCC frequency band, since it offers much wider frequency bandwidth and 50 channels with 500 kHz bandwidth each.

The RFID tag was tested in a similar temperature measurement setup as presented previously. The Voyantic Tagformance RFID system was used to perform measurements of the read range of the UHF RFID temperature sensing tag for every 10 $^{\circ}C$ from 30 $^{\circ}C$ to 80 $^{\circ}C$. In Fig. 6.13 the measured read range is illustrated.

The read range is degrading with the increase of temperature due to the variation of the impedance and resonance frequency is shifting towards higher values as expected. The specific measurement was repeated, but this time the value of the self-tune circuit stored in the memory bank of the RFID chip was acquired. The values of the self-tuning circuit which were registered at each temperature can be found in Table 6.5. For 30 $^{\circ}C$ the self-tuning circuit is saturated to the lowest capacity value and when the temperature rises

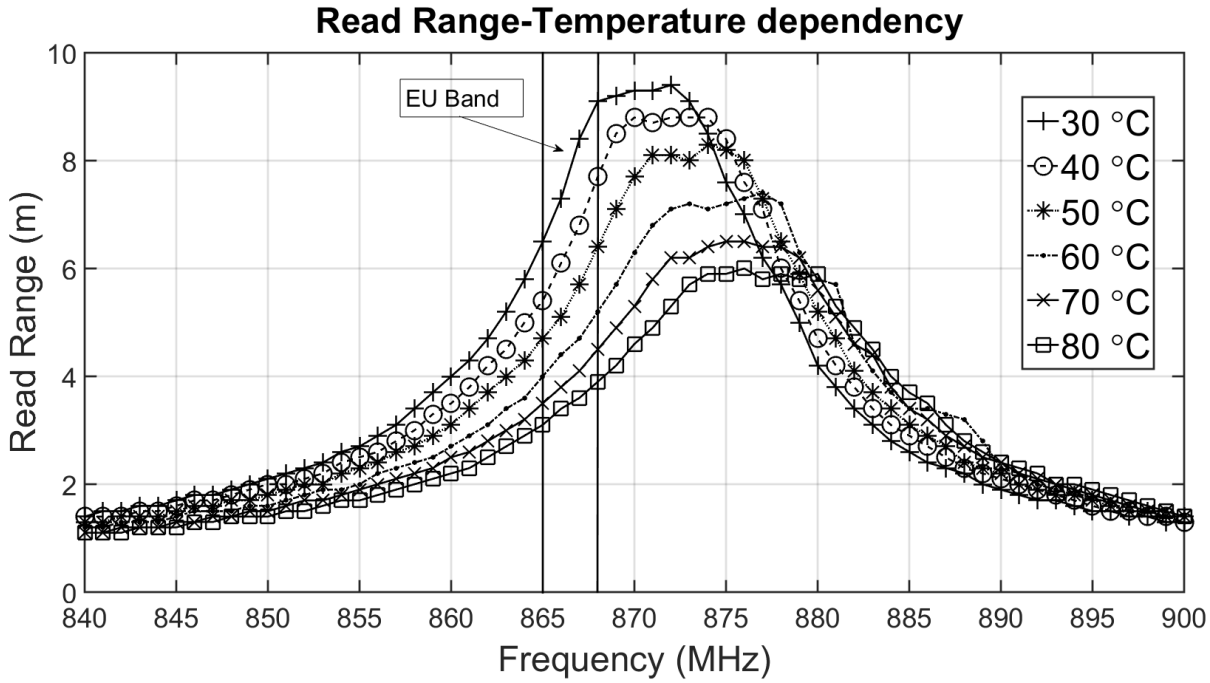

Figure 6.13: Measured read range for different temperature values

to 40 $^{\circ}C$ the difference of the power extracted by the chip is not enough to drive the self-tuning circuit to change the value of capacitance.

Table 6.5: Self-tune value versus temperature

Memory Value(hexadecimal)	*Temperature ($^{\circ}C$)*
0000	30
0000	40
0001	50
0002	60
0003	70
0004	80

In addition, the transmitted power of the reader was swept from 10 dBm to 30 dBm, in order to explore the impact of transmitted power on the self-tune value, considering that the input impedance of the RFID is a function of both frequency and received power. The results are showcased in Fig. 6.14.

It can be observed that for the maximum and minimum transmitted powers the self-tuning circuit is saturated to the lowest and highest capacity value, respectively. For the part which there is no response the maximum value of the self-tuning circuit was set (0004) but the power received by the chip was not enough

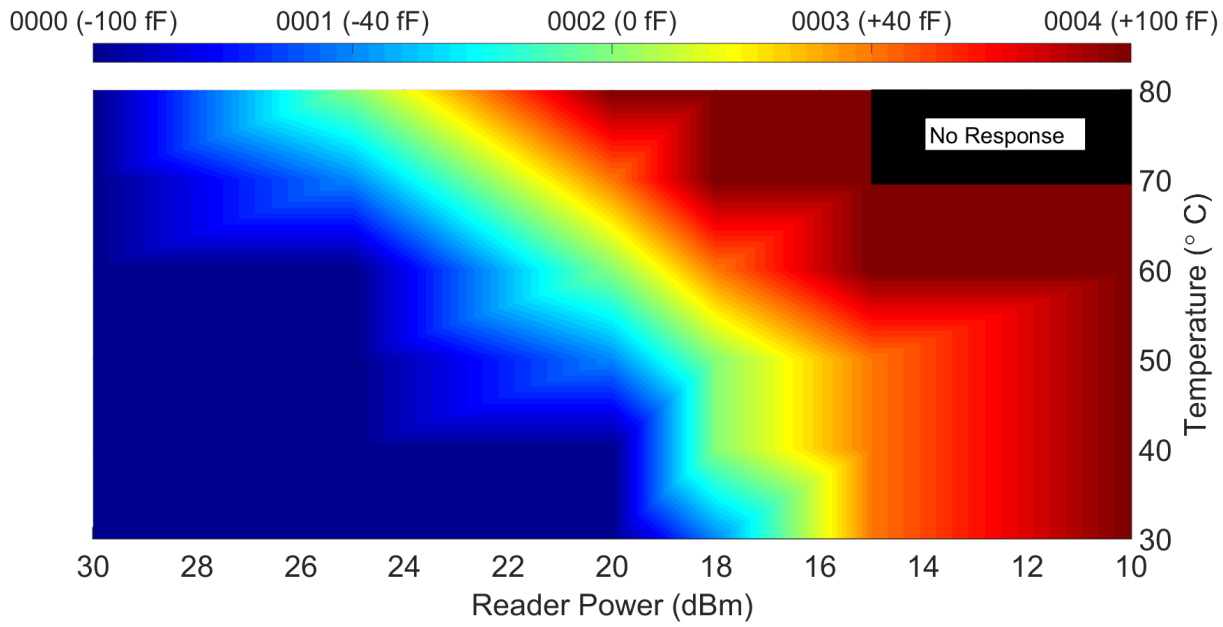

Figure 6.14: Self-tune value vs reader power vs temperature. (* In the black area there was no response from the tag)

for it to respond. Also it can be seen that the self-tuning circuit exhibits a partially linear response in the middle of the graph (light blue-green-yellow-light red parts) where actually the change of the impedance due to change of temperature is cancelled out by the change of the impedance due to the different power received. In case of lower temperatures, the self-tuning circuit would be saturated and the value of 0000 would be read all the time from the memory bank of the IC. If the tag is designed with the appropriate resonance frequency can be set to detect lower temperatures in the same manner that it was presented in this section. In addition, if a single channel of the reading band is exploited, this RFID tag could be used for sensing different temperatures ranges including lower temperature values. Since the specifications of the IC are limited to a temperature of 80 $°C$, higher values of temperature could have an impact to the proper functionality of the IC or even destroy it.

This RFID temperature sensing tag exploits 5 different capacitance levels resulting in a limited resolution. In addition, the difference between these 5 capacitance values is not fixed. For instance, the value 0000 corresponds to $100fF$ subtraction to the input impedance of the chip while the value 0001 corresponds to a subtraction of $60fF$, meaning a difference of $40fF$. For the 0002 value there is no change to the nominal input impedance of the chip resulting in a difference of $60fF$ between the value 0002 and the value 0001. According to this fact, the resolution will not be consistent. Moreover, during the reading of the self-tuning

circuit values for a specific temperature there were some errors regarding the captured value. For instance, for 60 $^{\circ}C$ the captured value could change between 0002 and 0003 every time the self-tuning value would be captured. The value which was finally noted was the one appearing more often. The testing of the tag was also performed in a cooling scenario and the results were consistent with the heating procedure. Overall, it is tedious to set the characteristics of this sensor tag in a context of a typical sensor characteristics since this concept is based on an indirect measurement of the temperature through the received power which is sampled by the RFID chip.

One problem that can arise using the proposed technique is the fact that the substrate or the radiating properties of the antenna can be sensitive to multiple environmental factors (e.g. deformation, proximity of metallic parts). In this way the impedance variation will not be only connected to temperature variation but to the environment overall giving false temperature measurements. Such a problem is very common in UHF RFID tags practical implementations. One option to overcome this drawback is to adopt calibration measurement procedures and reference tags (e.g. [117]).

Overall this sensing technique is based on creating in a controlled environment, a controlled change of the matching between antenna and RFID chip, which leads to different extracted power levels during the sampling instances of the self-tuning circuit.

6.3.5 90° Hybrid coupler concept for insensitive to power received self-tuning RFID sensor tag

One of the main vulnerabilities of the self-tuning RFID sensor tag is the dependency of the input impedance of the RFID chip on the power received. As it was demonstrated in the previous section, if the power received by the RFID chip is varying, then false information regarding the desired physical parameter (i.e. temperature in the presented case) can be extracted. One solution can be to control the power transmitted by the RFID reader, based on the RSSI information of the targeted RFID sensor tag. In this case the power transmitted to the input of the RFID chip will be adapting to the random environmental conditions and thus the RFID chip will be operating in the linear regime.

This concept is proposed in [117], and in this way the sensing mechanism can be independent from random fluctuation of input power. Such solution can easily operate when a single self-tuning RFID sensor tag is in the field of the RFID reader. However, in a scenario where multiple RFID sensor tags are needed to operate within a single RFID reader's field, then such approach becomes more challenging. Even more, when a scenario of moving items tagged with RFID sensor tags is considered. The processing capabilities of

the RFID reader will potentially rise to a high complexity level and a real time RFID sensing system might fail to operate.

One potential solution to this problem would be to attempt to solve it at the level of the RFID sensor tag. Elaborating, a concept that could tackle such a problem would be to utilize a 90° hybrid coupler. The 3-dB 90° hybrid coupler has been used in the past for different concepts in RFID systems, such as the passive retro-directive wireless sensor in [120].

The behavior that demonstrates the 3-dB 90° hybrid coupler when two identical impedances are present to the direct and coupled ports could be utilized. In this case the reflected signals of the two ports have the same phase and they are added in the isolated port presenting the reflection coefficient Γ of the identical impedances, as it is demonstrated in Fig. 6.15. At the same time at the input port the reflected signals are canceling each other out resulting in no signal.

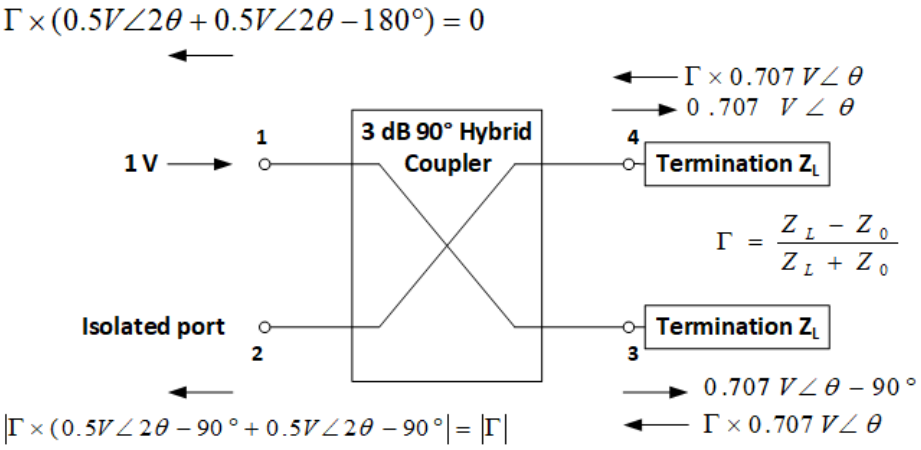

Figure 6.15: 3-dB 90° Hybrid coupler for equal impedance terminations

Based on the proposed concept, if in the place of the two terminations of the ports 3 and 4 (see Fig. 6.14) were two identical self-tuning RFID chips then regardless the input power, both RFID chips would present the same reflection coefficient and thus the isolated port would have Γ as output. The value of Γ is depending on the characteristic impedance of the 3-dB 90° hybrid coupler, which is usually 50 Ω, and the value of the impedance of the RFID chips and not by the input power. Between the ports of the 3-dB 90° hybrid coupler and the RFID chips should exist an impedance matching network which would acquire the sensing function in this case. For instance, if the matching circuit was fabricated with a temperature sensitive material, then it could act as the temperature transducer of the sensing system. Finally, in order to

isolate the input of the system (i.e., the port 1) with the output (i.e., port 2). This can be achieved by adding a circulator in the input of the system, as it is displayed in Fig. 6.16.

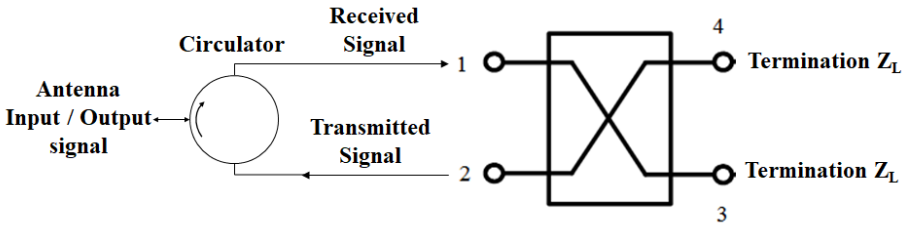

Figure 6.16: 3-dB 90° Hybrid coupler system with the addition of a circulator

This concept was tested by fabricating a 3-dB 90° hybrid coupler circuit, with two additional boards including a matching circuit and a Monza R6 RFID chip. The role of the matching circuit was to transform the impedance of the chip to the 50 Ω value. The fabricated circuits and the system overall are presented in Fig. 6.17.

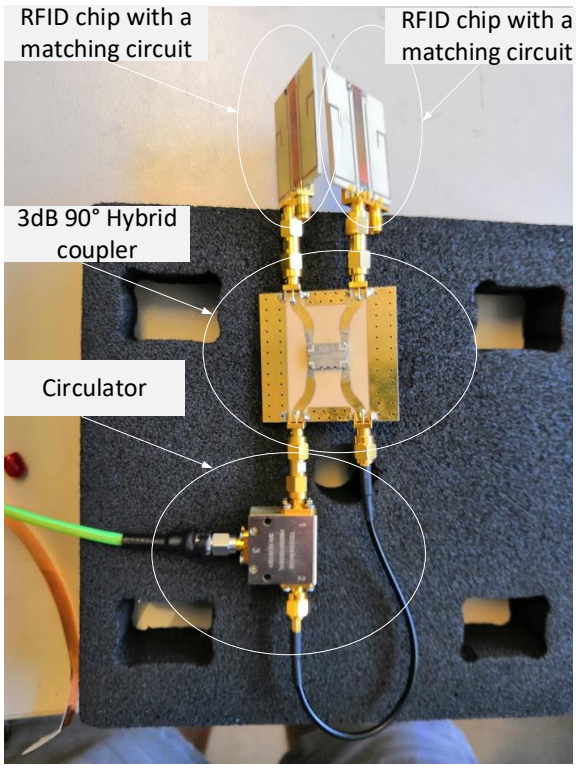

Figure 6.17: Fabricated system with the circulator, 3-dB 90° hybrid coupler and the RFID chips with the matching circuits

One of the measurements to explore the operation of the proposed system would include initially to connect an RFID reader (Impinj R420) to the board of the RFID chip with the matching circuit. The transmitted power of the RFID reader would be then swept for a span of values from -15 to 15 dBm with steps of 1 dBm. For every power level, the value of the auto-tuning circuit would be noted. The same measurement was repeated but this time the complete circuit would be tested. In this procedure only one of the RFID chips would be read and the value of the auto-tuning circuit would be noted. The results of this measurement are presented in Fig. 6.18.

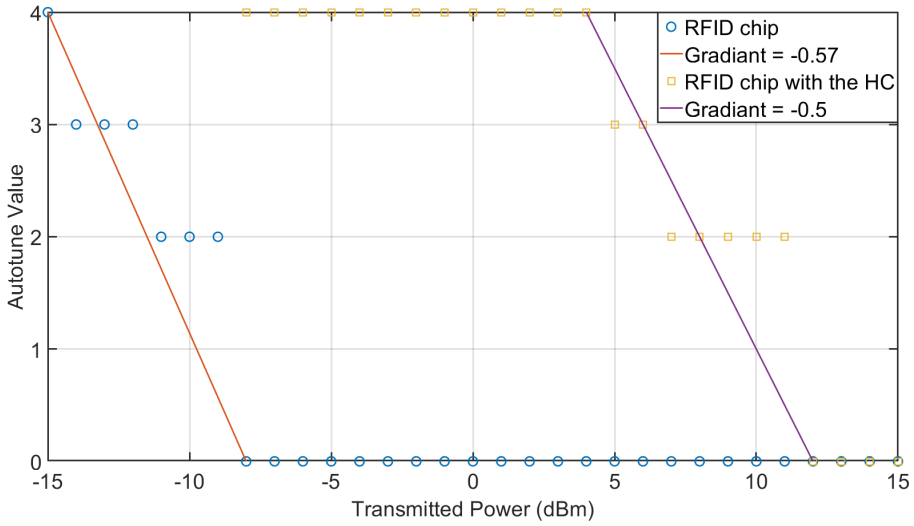

Figure 6.18: Self-tuning value versus transmitted power

The results showed that the difference between the two cases was little to none. If the proposed circuit operated as expected the gradient of the auto-tune value would have much smaller value. Due to time limitation this concept was not able to be explored in more depth at the time. Some possible points of failure could be the limited bandwidth of the matching circuit resulting in a variation of the impedance of the two RFID chips seen by the hybrid coupler. Finally, this concept could potentially find better application in an integrated design were the whole system could be in a chip.

6.4 Chipless RFID sensing approaches

Besides the traditional RFID sensor tag solutions, which include an RFID chip, some chipless RFID tags were developed aiming to perform sensing functions. This part will be a presentation of the main outcomes of this work. The chipless RFID sensor tags which will be presented, were designed to sense temperature,

humidity or rotational speed. An interesting point in this work is the frequency band of operation. The ISM and ETSI frequency bands and especially the 866 MHz, the 2.45 GHz and 5.8 GHz frequencies received the main attention. In addition, the possibility to read such chipless RFID sensor tags with a software defined radio (SDR) equipment was explored.

6.4.1 Threshold temperature sensing chipless RFID tag

A chipless RFID sensor tag including two C-like resonators (Resonator 1 and Resonator 2) is designed to resonate in the allocated frequency bands, ETSI and ISM bands respectively as shown in Fig. 6.19. Sensing the temperature threshold happens when the temperature shifts the resonance inside the band leading to a change in the backscattered signal amplitude. This change can be mapped to the temperature range and hence, indicating the threshold value of the temperature. Fig. 6.19 (b) illustrates the principle of temperature threshold sensing using ETSI and ISM 2.45 GHz bands. The structure has been designed on Rogers RT 6010.2LM substrate with thickness $h = 1.27\ mm$ which has a high thermal coefficient in the temperature range of -50 to 170 $^{\circ}C$. The temperature threshold sensing has been verified experimentally for ETSI and ISM 2.45 GHz bands as shown in Fig. 6.20 [121].

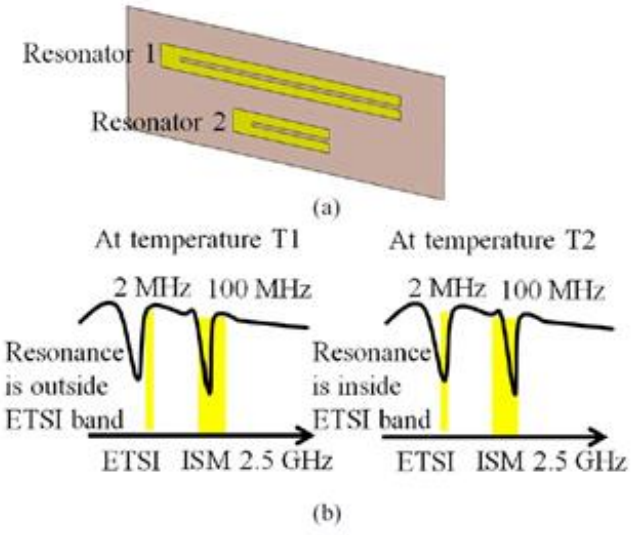

Figure 6.19: Temperature threshold chipless RFID tag(a) The chipless RFID sensor tag structure (b) operation for different temperature values

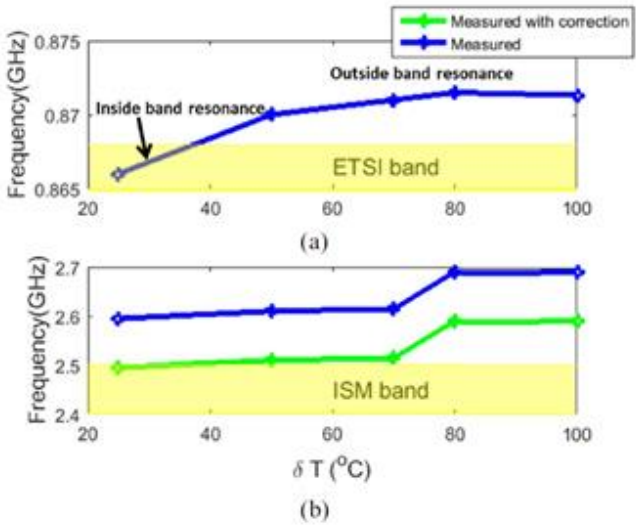

Figure 6.20: Measurement of the shift of the resonance peak inside (a-top) ETSI band (b-down) ISM band

6.4.2 Dual chipless RFID threshold sensor for temperature and humidity

The proposed chipless sensor for dual detection of temperature and humidity is shown in Fig. 6.21.

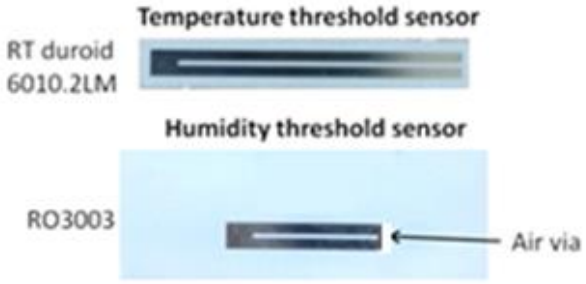

Figure 6.21: The dual chipless threshold sensor structure

It is actually a combination of two C-shaped resonators, one similar to the one presented in the previous subsection with the addition of another resonator for humidity detection. The sensor is composed of two different substrates each of which is used to realize each one of the C-shaped resonators. The choice of the substrates is based on the thermal coefficient of permittivity which is lower in the case of the RO3003

(-3 ppm/$^{\circ}C$) than the RT Duroid 6010.2LM (-425 ppm/$^{\circ}C$). To have a compact size sensor, the substrate RT Duroid 6010.2LM which has a permittivity of 10.2 is used for resonance in ETSI band while RO3003 has a permittivity of 3 is used for resonance in ISM 2.45 GHz band. Since RO3003 has very small thermal coefficient of permittivity, an air via has been introduced at the capacitive end of the C-shaped resonator to increase its selectivity to humidity variation.

The structure has been designed using CST Microwave Studio using time domain method by illuminating the structure with a linearly polarized plane wave. The backscatter signal is collected by probes placed 10 cm away from the structure and the radar cross section (RCS) is used as a metric for the performance evaluation.

The measurement setup was installed in the environment of an anechoic chamber. The temperature and humidity levels would be monitored by dedicated sensors. A heater or a container with boiling water would affect the levels of temperature and humidity, respectively and their variation measured with the sensors would be linked to the resonance frequency shift in the ETSI and the ISM 2.45 GHz bands measured by a VNA connected to an antenna. The measurement setup is described in Fig. 6.22.

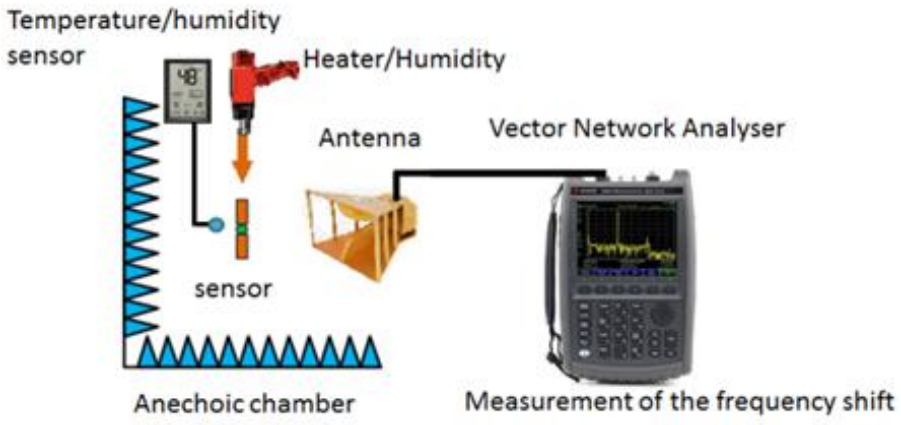

Figure 6.22: Measurement of the dual chipless RFID threshold sensor

Since the reflection coefficient is of interest, the measurement procedure starts by measuring the S11 parameter of the background without the presence of the dual sensor structure. Then, the sensor structure is placed in front of the antenna. The effect of the background has been removed by subtracting the S11 of the background from the S11 of the measured sensor. Fig. 6.23 shows the measurement results for the case of

temperature and humidity in their frequency bands.

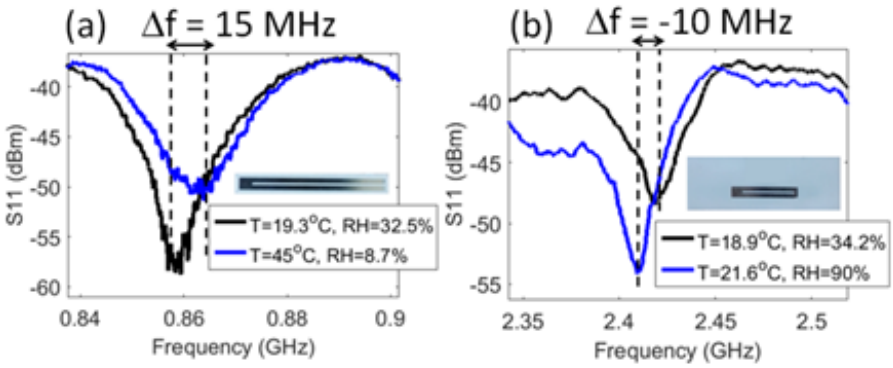

Figure 6.23: Measurement results (a) temperature threshold sensor (b) humidity threshold sensor

6.4.3 Rotational motion sensing

In this sub-section, a chipless sensor design for angular speed sensing compliant with UHF RFID standards is presented. The concept is based on using the geometric configuration of an aperture antenna [122] as chipless sensor structure. Depending on the relative orientation of the interrogator antenna and the chipless structure, backscattered power pattern is generated as the aperture is rotating due to polarization mismatch [123]. The basic aperture structure considered in this section for chipless sensing is formed from a narrow rectangular slot of size $a \times b$ ($b \ll a$) in a metal film patched on a dielectric substrate of permittivity ϵ_r. The aperture structure is placed in the x-y plane with the origin of the coordinate system is at the center of the aperture as shown in Fig. 6.24. The aperture length a is $\lambda_g/2$ where $\lambda_g = \lambda/\sqrt{\epsilon_r}$ and λ is the free space wavelength. The structure is designed to operate at 866.7 MHz, which is in European RFID band, and to comply with ETSI regulations.

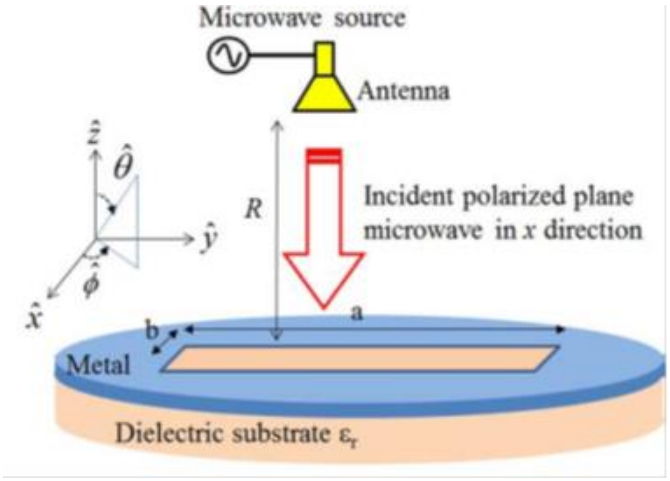

Figure 6.24: Rotational motion sensing chipless RFID sensor

The structure was fabricated and tested experimentally to compare the simulated RCS with the experimental results. Fig. 6.25 shows the experimental setup for measuring the RCS of the sensor structure.

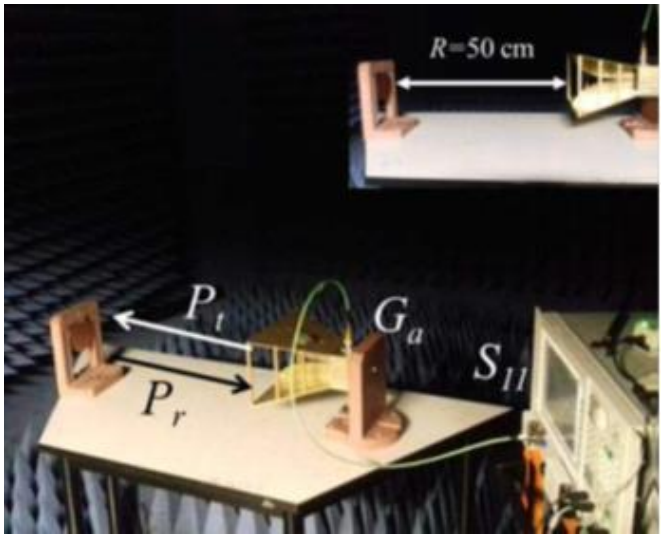

Figure 6.25: Measurement setup for the rotational motion sensor

The monostatic setup is constituted with a linearly polarized horn antenna connected to the vector network analyzer PNA-X Series N5222A and separated of tags at the distance $R = 50\ cm$. The reflection coefficient S11 is measured as a function of the angle ϕ between 0 and 360°C The measured S11 is used to

deduce the RCS using the classic monostatic radar equation given by [124]:

$$\frac{P_r}{P_t} = |S_{11}|^2 = \frac{G_\alpha^2 \lambda^2}{(4\pi)^3 R^4} RCS \tag{6.2}$$

where P_r is the received power, P_t is the transmitted power, G_α is the gain of the transmitting antenna and λ is the transmitted wavelength. The RCS is found by the measurement of the S11 parameter since the rest of the values of the (6.2) are already known. The results of the measurements compared with the simulated results are presented in Fig. 6.26.

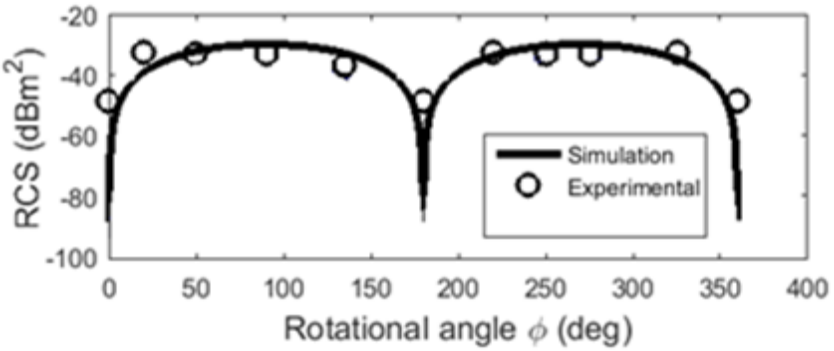

Figure 6.26: Measurement and simulated results of the rotational motion sensor

6.4.4 Chipless sensor reader architecture and operation principle

A generic block diagram of the proposed reader architecture for chipless sensors reading is presented in Fig. 6.27. The reader sends a baseband signal $s_t(t)$ with bandwidth B that is modulated to occupy either the ETSI band with $B = 2\ MHz$ or ISM 2.45 GHz band with $B = 100\ MHz$. This signal is swept using a voltage-controlled oscillator (VCO).

The detection process starts by demodulating the backscattered signal received from the sensor then processing the received baseband signal $s_r(t)$ in the reader. The processing is done through arithmetic operation by subtracting the transmitted baseband $s_t(t)$ from the demodulated signal received $s_r(t)$ in the frequency domain. To illustrate the operation principle of the proposed reader, the spectrum representations of the transmitted and received signals are shown in Fig. 6.28 (a) and Fig. 6.28 (b) respectively. Initially, the reader transmits a wideband signal $s_t(t)$ with the spectrum $S_t(f)$ shown in Fig. 6.28 (a) which have the

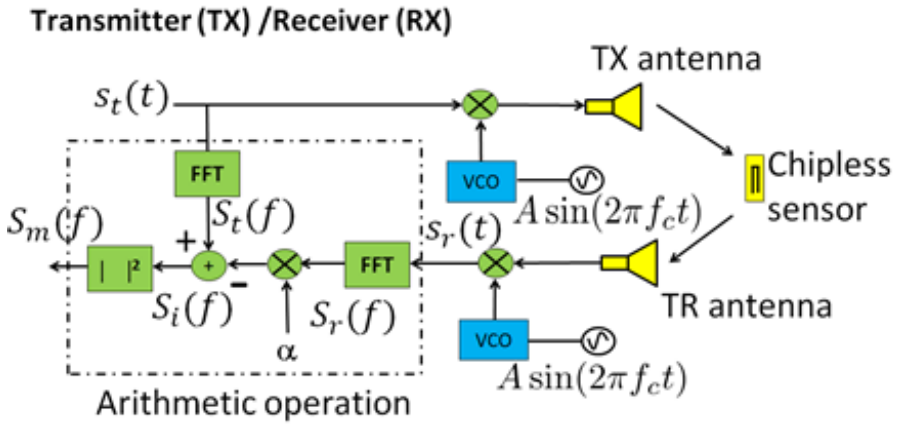

Figure 6.27: Generic block diagram of the proposed chipless sensors reader

amplitude a. Since the chipless sensors are resonant structures, the backscattered signal $s_r(t)$ will be same as the transmitted signal $s_t(t)$ but with a missing amplitude at the resonance frequency. This is under the condition that the sensor is resonating in the band. Fig. 6.28 (b) shows the spectrum $S_r(f)$ of the received signal in the frequency domain. To detect the amplitude difference at reception, the received demodulated backscattered signal is subtracted from the transmitted baseband signal as it shown in Fig. 6.28 (c). It is important to notice that there is a level difference between $S_t(f)$ and $S_r(f)$ due to path loss so; the level of the signal needs to be adjusted by a scaling factor α to compensate the losses that are not related to the resonance nature of the chipless sensor structure.

For instance, in the case presented in Fig. 6.28, the reader transmits a signal with band B having level α in the frequency domain, and receives the backscattered signal with level b, where $b < a$.

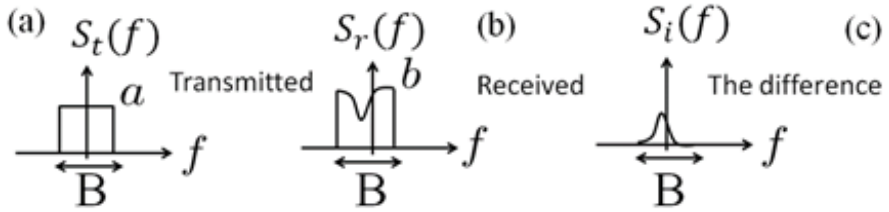

Figure 6.28: The Fourier transform of the signal with bandwidth B (a) transmitted and (b) received backscattered signals from the proposed chipless sensor, (c) is the output calculated signal in frequency domain after processing by the arithmetic operation

Hence, by multiplying $S_r(f)$ by α such that $\alpha \cdot b = a$ the calculated signal $S_m(f)$ will be:

$$S_m(f) = |S_t(f)|^2 = |S_t(f) - \alpha S_r(f)|^2 \tag{6.3}$$

The square of the magnitude has been taken since the absolute value of the difference is of interest as shown in Fig. 6.26 (c). In case where the resonance is outside the band, (6.3) will give theoretically zero.

6.4.5 SDR chipless RFID reader

The universal software radio peripheral (USRP) is a SDR platform for research and development in radio and wireless communications as well as in reconfigurable radio platforms. The USRP consists of two main features: 1) the hardware; and 2) the software. In this section, the used model of the USRP, and the software is described. Finally, the utilization of such platform to read the already presented chipless RFID sensors will be demonstrated.

USRP Description and specifications

The USRP 2900 from National Instrument was used in this demonstration. The USRP is a hardware platform interfaced to a host computer through USB 2.0 port. Open-source GNU radio software is used to create the reader functionality by graphical programming. The USRP hardware contains a Field Programmable Gate Array (FPGA) for high-speed signal processing, two 12 bits high-speed analog-to-digital converters (ADC), two 12 bits high-speed digital-to-analog converters (DAC), and auxiliary analog and digital input/output (IO) ports. The maximum output power of the USRP 2900 is 20 dBm. There is a programmable gain amplifier (PGA) at the radio frequency (RF) output to amplify weak output signals. USRP 2900 operates in the frequency range of 70 MHz – 6GHz with a maximum instantaneous real-time bandwidth of 56 MHz.

USRP implementation of the chipless sensor reader architecture: Transmitter path implementation

The host computer running GNU Radio is used to develop the signal processing software [125], which is transmitted to the USRP's FPGA memory prior to operation using the USB port. The software signal-processing interface is created using graphical programming from the GNU Radio library. In the case of ETSI band, the VCO was not needed to generate a 2 MHz band signal since this can be generated by adjusting the sampling rate. According to Nyquist criterion, the maximum frequency to avoid aliasing is equal to half of the sampling rate f_s. Since complex samples are used the range of non aliasing is extended

from $-f_s/2$ to $+f_s/2$ centered at zero for the baseband signal. By setting $f_s = 2M$ samples, a 2 MHz bandwidth centered at zero is obtained. To generate the ETSI band, the 2 MHz baseband signal is modulated automatically by the RF unit of the USRP using 865 MHz carrier frequency. Implementing the ISM 2.45 GHz band (B=100MHz) using USRP 2900 cannot be done by adjusting the sampling rate as in the previous case. The reason is due to the maximum bandwidth limitation of the USRP 2900 (56 MHz). In order to avoid this limitation, the VCO is used. By adjusting f_s to 10 M samples, a 10 MHz band of the baseband signal is obtained. This band is modulated at 2.45 GHz while sweeping the modulating frequency in the ISM band by the VCO [126] as shown in Fig. 6.29.

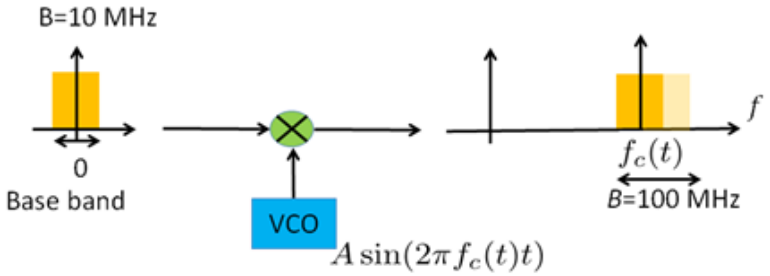

Figure 6.29: Modulating the 10 MHz base band signal using VCO to generate the ISM 2.45 GHz band by USRP 2900

To verify the USRP signal output, a spectrum analyzer has been connected to the TX output of the USRP to measure the output-modulated signal at the ISM 2.45 GHz band (see Fig. 6.30).

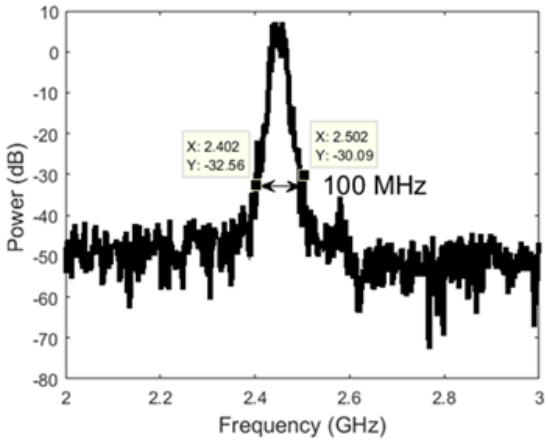

Figure 6.30: TX/RX output of the USRP 2900 for the 100 MHz ISM 2.45 GHz band

USRP implementation of the chipless sensor reader architecture: Receiver path implementation

The receiver path is the inverse of the transmission path. The demodulation is taken place automatically to obtain the received baseband signal. The baseband signal is then manipulated directly by the GNU radio interface to get the sensed value from the received backscattered signal. To do so, a post-processing of the received signal is achieved after demodulation by the arithmetic operation given in equation (6.3). The factor $\alpha$is an environment dependent and needs to be readjusted if the experimental setup is changed, so, it is defined as a variable in the GNU radio interface. This enables the user to modify it based on the interrogation setup. Since the signal generated by the GNU radio is complex, the final stage is to take modulus square to get the amplitude of the signal in the frequency domain which contains the sensed information.

Experimental results

The experimental setup used to measure the chipless sensing system consists of two identical horn antennas connected to the USRP 2900 device in a bi-static configuration. One antenna is for the TX port and the other for the RX port. The USRP is connected to a host computer running GNU radio, as in Fig. 6.31. Matlab is used for post-processing and signal plotting.

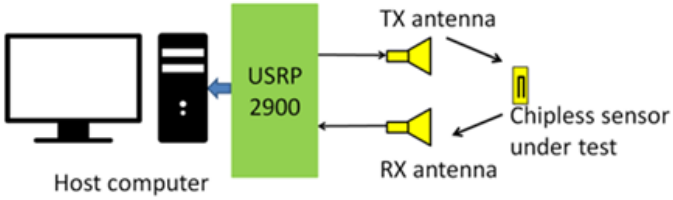

Figure 6.31: Schematic diagram of the experimental setup for the sensing system

The SDR chipless RFID reader was used for two of the previously presented chipless RFID sensors: the temperature threshold chipless RFID sensor and the rotational motion sensor.

Measurement of temperature threshold chipless RFID sensor

The chipless threshold temperature sensor is placed at a distance of 15 cm from the USRP antennas at room temperature. Then, the sensor is interrogated while heating the sensor structure using a heat gun to a maximum nozzle temperature of around 40 $^{\circ}C$. The temperature of the sensor was monitored using an infrared thermometer. The acquisition time was monitored while the structure is heating to reach a maximum ambient temperature of 35 $^{\circ}C$. The temperature attained was less than the nozzle temperature since the structure was heated in a non-isolated environment. The relation between the signal amplitude and the temperature is achieved through the correspondence between heating time and the acquisition time. The results of the temperature threshold measurements are shown in Fig. 6.32.

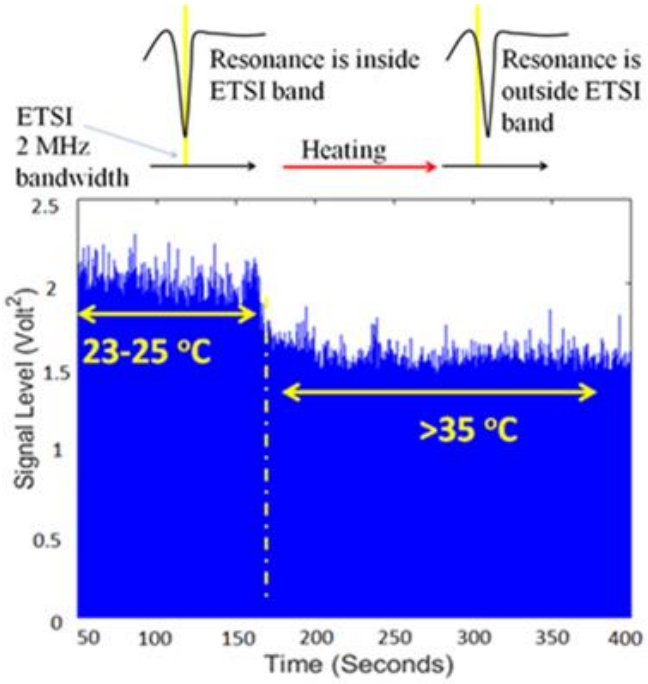

Figure 6.32: (up) Illustration of the resonance frequency shift due to heating (down) The measurement results for the chipless temperature threshold sensor in the ETSI band

Measurement of the chipless RFID rotational motion sensor

The chipless rotational motion sensor is placed on a rotating platform with an adjustable rotational speed motor. The experimental result is shown in Fig. 6.33.

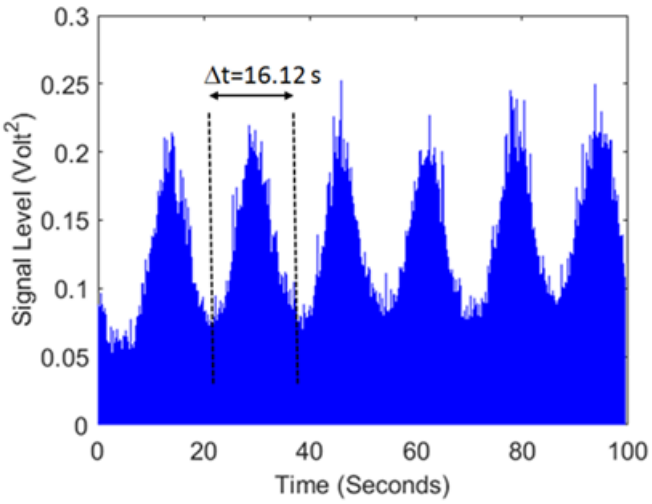

Figure 6.33: The measurement results for the chipless rotational motion sensor in the ETSI band by the USRP. The time interval between two minima represents one cycle

The angular velocity of the object can be deduced from the power pattern. The time interval between two minima in Fig. 6.33 corresponds to the angular difference between two minima in the RCS pattern of Fig. 6.26. The presented chipless rotation motion sensor has one slot resulting in a 180° angel difference between two minima. Hence, by knowing the time interval between the two minima Δt_{min} from the pattern, the angular velocity ω can be calculated by:

$$\omega = \frac{180^\circ}{\Delta t_{min}} \tag{6.4}$$

From (6.4) and for $\Delta t_{min} = 16.12\ s$ the angular speed will be $11.16\ ^\circ/s$ or $0.195\ rad/s$.

6.5 Conclusion

In this chapter, various approaches on RFID sensing were presented. Initially, a proposed scenario on how to exploit the self-tuning circuit of an RFID chip to perform sensing functions was described. An application on temperature sensing based on this scenario was then presented, including simulations, measurements and the fabrication of a prototype RFID temperature sensor. The self-tuning RFID temperature sensor presented the expected behaviour enabling sensing based on the value which the self-tuning circuit acquired. The performance of this self-tuning RFID temperature sensor was limited by the total available self-tuning states offering low accuracy. In addition, the received power and input impedance dependence of the RFID chip resulted in a limitation of the possible application scenarios, restricting the usage of such sensor in fixed positions applications. Also a limiting factor of the performance of the self-tuning temperature RFID sensor is the limited operating frequency bandwidth (ETSI in this case). In a case where FCC frequency band is utilized the potential of this kind of sensor could be better exploited.

Furthermore, a concept to ameliorate the performance of the self-tuning RFID temperature sensor was elaborated including a 3dB 90° hybrid coupler. According to this concept an RFID sensor based on the self-tuning technique could operate more reliable without being subject of the received power and input impedance dependency. This concept was not fully explored but laid the ground for future work.

Finally, a series of chipless RFID sensors were introduced, aiming to sense properties such as temperature, rotational speed and humidity. Their structures are based on resonators and by utilizing intrinsic phenomena of the used substrates, their operation as sensors can be achieved. Also, the polarization mismatch between RFID reader and RFID chipless sensor was used in the case of the rotation motion sensor. Moreover, an RFID reader architecture is proposed and realized by using a SDR device to perform the reading tasks in the ISM band.

CHAPTER 7
INSTALLATIONS AND MEASUREMENTS IN INDUSTRIAL SITES

7.1 Introduction

In this chapter, a more practical and close to real applications aspect of the thesis work will be presented. As the subject of the thesis in the context of the Innov'Hydro project was to explore the possibility of monitoring industrial sites and especially large scale generators using the RFID technology, the exploration of such sites was very important. In order to succeed in this aspect, visits to industrial sites of the Electricité de France (EDF) company were performed. Different hydroelectric power plants were visited with a variety of different large scale generators and several tests and measurements were conducted. After the first exploration of the geometry of the generators, the possible positions for each part of the RFID sensing system were pointed out, aiming to customize each part according to the exact specification of each generator geometry. This customization included the RFID sensor tags as well as the type and positioning of the antennas of the RFID reader, the used cables and other precautions needed.

In addition, an opportunity to test the developed RFID sensing system on the transformers installation of a power plant appeared. This occasion was very useful in order to extract some very important conclusions of the overall operation of the RFID sensing system.

Furthermore, besides the importance of the development of the RFID sensor tags, the selection of the specific model of the RFID reader, as well as the development of the necessary software for acquiring the sensing data will be presented. Concluding, in this chapter different aspects of the overall system will be discussed and presented.

7.2 Visits in different industrial sites

In the duration of this thesis 7 hydroelectric power-plants were visited. All the visited sites had different types of generators, varying in size, geometry and complexity. In chronological order the sites visited were:

1. Hydroelectric power-plant of *Châteauneuf-sur-Isère (6/2016)*
2. Hydroelectric power-plant of *Prévenchères (11/2016)*
3. Hydroelectric power-plant of *Beauvoir (12/2016)*

4. Hydroelectric power-plant of *Saint-Chamas (12/2017)*

5. Hydroelectric power-plant of *Grand'Maison (7/2018-4/2019)*

6. Hydroelectric power-plant of *Super-Bissorte (10/2018)*

7. Hydroelectric power-plant of *Aussois (1/2019-3/2019)*

In the industrial sites where there was an installation of RFID sensor tags there were multiple visits to carry out necessary work. In the next sections, information about the different industrial sites and about the work and the outcome of each visit will be presented.

7.2.1 Visit in the hydroelectric power-plant of *Châteauneuf-sur-Isère*

The visit in this site was the first contact with the industrial site of a hydroelectric power plant and the generators which are operating in its premises. The goal of this visit was to observe the structure and geometry of the generator and acquire a first impression of the industrial environment overall. In this visit, there were no tests or measures conducted neither any equipment was carried. In the Fig. 7.1, Fig. 7.2 and Fig. 7.3 the generator and some internal components such as the rotor, the stator and the interpolar connections are illustrated.

Figure 7.1: Outer view of the generator at the power-plant of *Châteauneuf-sur-Isère*

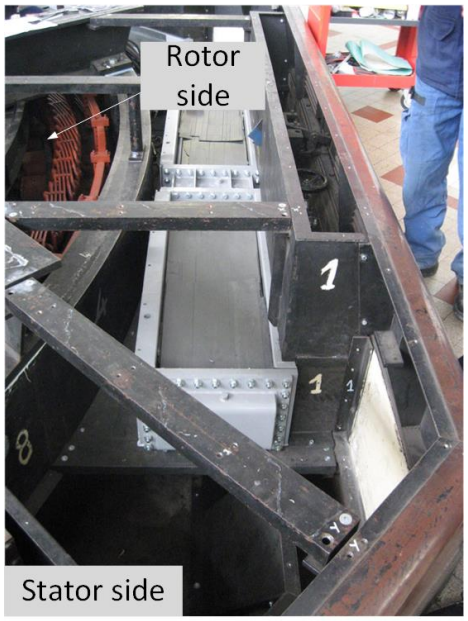

Figure 7.2: Inside view of the generator at the power-plant of *Châteauneuf-sur-Isère*

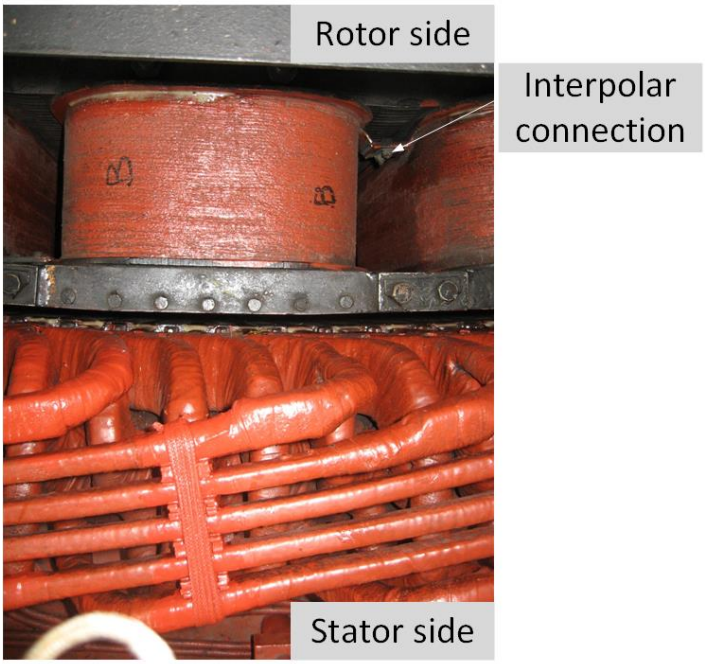

Figure 7.3: Interpolar connection at the hydroelectric power-plant of *Châteauneuf-sur-Isère*

7.2.2 Visit in the hydroelectric power-plant of *Prévenchères*

In the visit in this hydroelectric power-plant the goal was also to observe the quite different geometry of the generator (see Fig. 7.4) and to test a commercial available RFID sensor tag which was utilizing the RFID chip SL900A [31]. In fact, the RFID sensor tag was a dipole design which is not specially design to operate on metallic surface and thus a spacer was used to offer better performance and acquire some initial measurements. These measurements were qualitative and the goal was to see if the value of temperature could be read by the used RFID reader (AMS AS3993 Femto reader). This test was performed in various positions using the RFID sensor tag in passive and semi-passive mode. The RFID sensor tag was read but with limited read range. Two of the positions which the RFID sensor tag was tested are presented in Fig. 7.5 and Fig. 7.6.

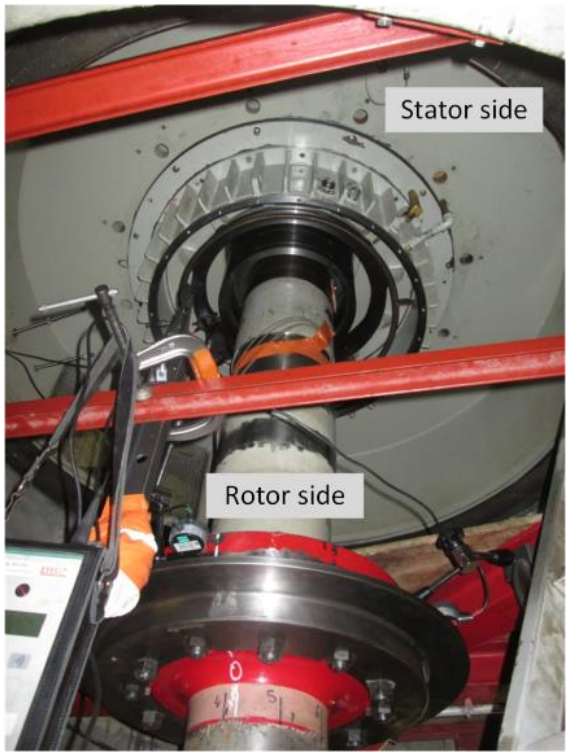

Figure 7.4: Outer view of the generator at power-plant of *Prévenchères*

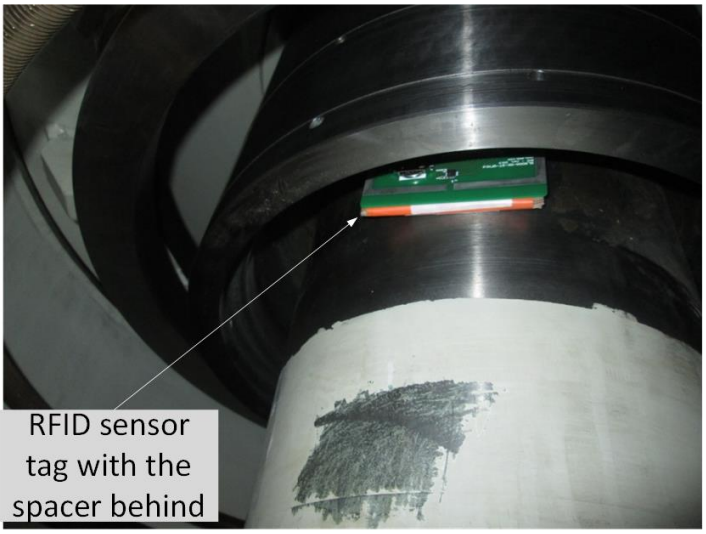

Figure 7.5: Position 1 of the RFID sensor tag

Figure 7.6: Position 2 of the RFID sensor tag

7.2.3 Visit in the hydroelectric power-plant of Beauvoir

In the hydroelectric power-plant of Beauvoir the opportunity to make some more measurements arisen. Therefore, a variety of commercially available RFID tags (without sensing capabilities) were tested by placing them in different positions in the interior area of the generator and by using the Tagformance pro RFID reader, these tags were tested regarding their readability and backscatter power. In Fig. 7.7 the generator geometry in the power-plant of Beauvoir is illustrated and in Fig. 7.8 and Fig. 7.9 some measurement setups with RFID tags in different (possible for installation) positions are presented.

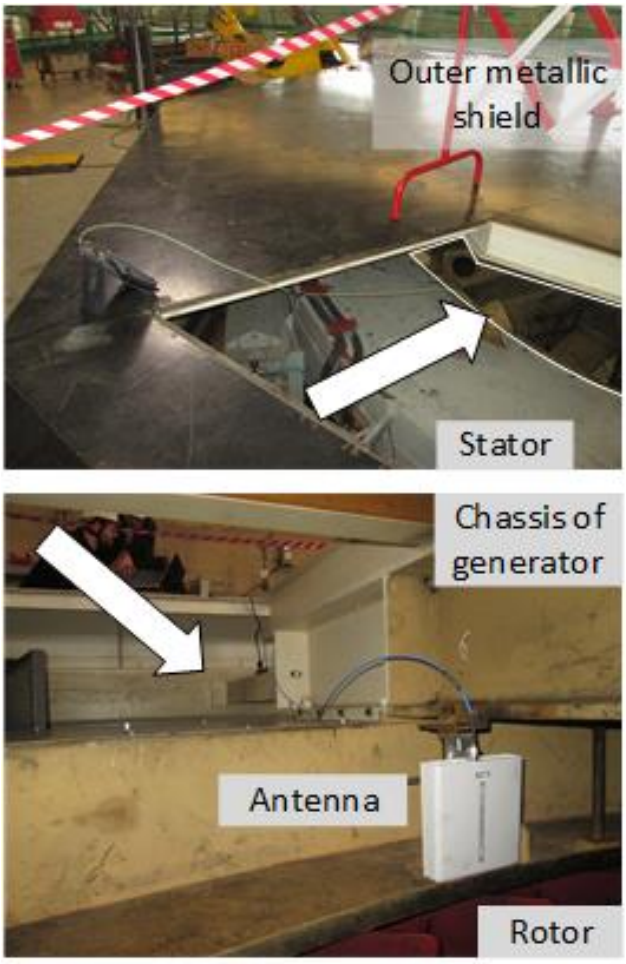

Figure 7.7: Generator geometry in hydroelectric power-plant of Beauvoir

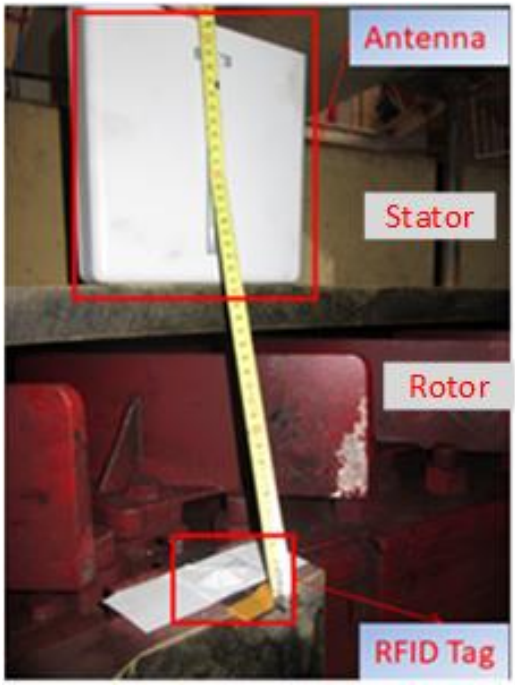

Figure 7.8: Example position of the RFID sensor tag and reader's antenna inside the generator

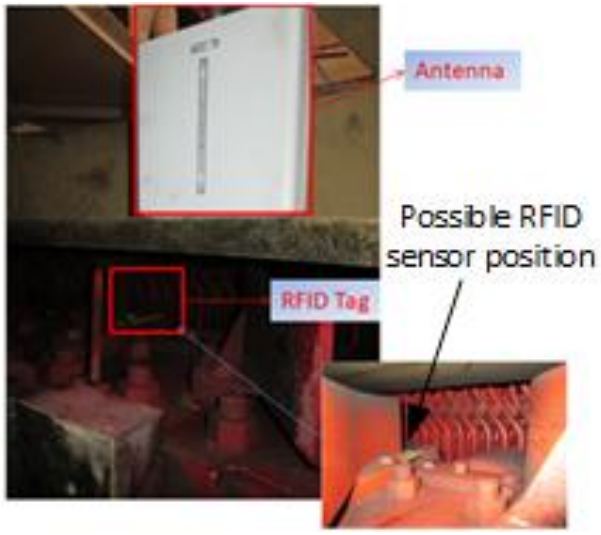

Figure 7.9: Example position of the RFID sensor tag and reader's antenna inside the generator

Moreover, in this visit, the opportunity to rotate manually (thanks to the power-plant workers) the generator showed up, and measurements regarding the propagation of the RF signal in the interior of the generator were conducted (see Fig. 7.10).

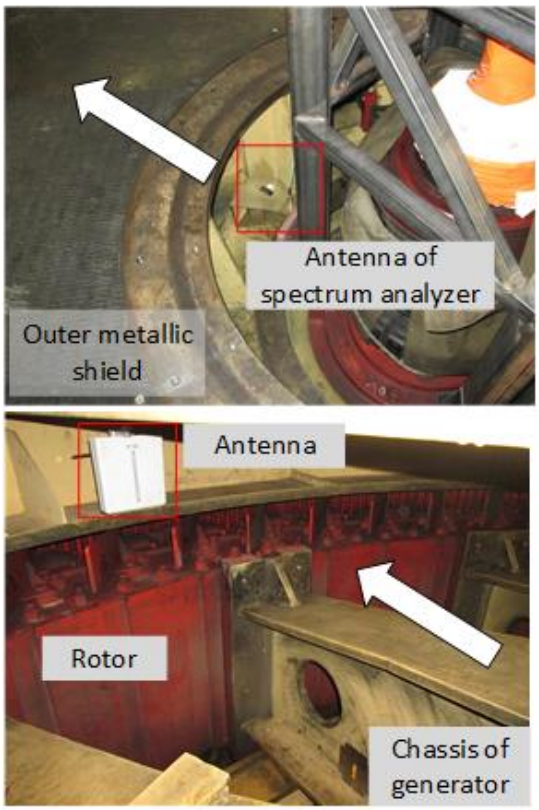

Figure 7.10: Position of the antenna of spectrum analyzer (SA)

For the rotating tests, the Tagformance pro RFID reader was used and it was mounted on the stator, while an antenna connected to a spectrum analyzer was positioned in the center of generator (not rotating). The two antennas were not in line of sight and their communication was depending on the reflections on the metallic walls of the interior part of the generator. The RFID reader would transmit a carrier wave at 866 MHz and with the antenna connected to the spectrum analyzer the power level of the received signal would be evaluated while the rotor was slowly rotating.

The main conclusions of the measurement in the hydroelectric power-plant of Beauvoir were:

1. Due to multipath phenomena, several RFID tags were able to respond to the RFID reader commands, even if they were positioned perpendicular towards the linear polarized antenna of the RFID reader

Tagformance Pro. Moreover, in some cases RFID tags were able to be read solely due to reflections. It is important to note here that these RFID tags were only for identification functions and no sensing data were transmitted.

2. The rotating test of the generator showed that the level of the power of the received signal at the spectrum analyzer would have a varying value depending on the position of the generator during the rotation. This variation was spanning in values ± 1 dB from the median value of the received power (see Fig. 7.11). For this test the transmitted power of RFID reader was 36 dBm.

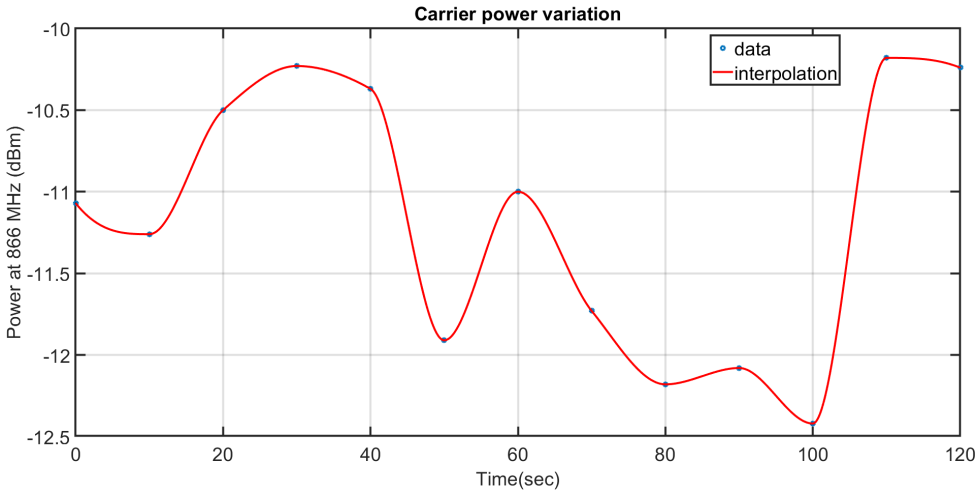

Figure 7.11: Received power during the rotation of the generator

7.2.4 Visit in the hydroelectric power plant of Saint-Chamas

Another stop in the industrial sites visitation journey was to the hydroelectric power-plant of Saint-Chamas. In this power-plant a different type and geometry generator was explored. In fact, the type of the generator could potential be more advantageous for installing an RFID sensing system due to the fact that it was not enclosed in a metallic shell, but it had a plexiglas cover as it is demonstrated in Fig. 7.12. Hence, a LOS scenario between RFID sensors and RFID reader's antenna can be quite easily applicable. During this visit, there was not the possibility to perform meaningful measurements due to fact that the generators were disassembled quite fast. Hence, the main outcome of this visit was to observe the specific type of generator and explore possible setups for future measurements or installations of RFID sensing system.

Figure 7.12: Generator at Saint-Chamas power-plant

In Fig. 7.13 is illustrated an interpolar connection of the specific generator type as well as the stator and rotor configuration.

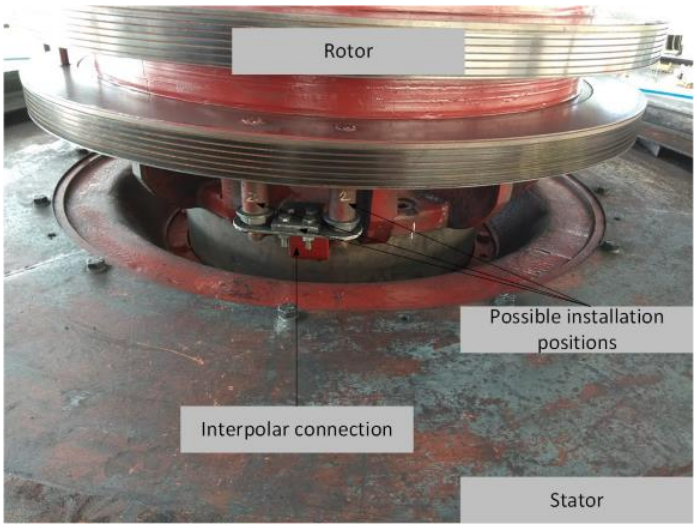

Figure 7.13: Interpolar connections in Saint-Chamas power-plant

In this type of generator, an RFID sensing system could potentially have the interpolar connections tagged with the RFID sensor tags and the RFID read with the antenna in a position at the exterior of the generator with the antenna focused on the position of the RFID sensor tags. However, up to the ending of the thesis there was no possibility to install and test the RFID sensing system in such generator.

7.2.5 Visit in the hydroelectric power-plant of Grand'Maison

In the hydroelectric power-plant of Grand'Maison, the first opportunity to make an installation was presented. The installation did not concern the interpolar connections in the interior of a generator but the transformer connections which were connecting the generator's output to the main power network. The transformer equipment needed a maintenance after some failure problem and thus the opportunity to test the fabricated RFID sensor tags and eventually the RFID sensing system appeared. In the same way that the RFID sensing system would operate inside the generator, where if it would detect high temperature values it would indicate a high failure possibility, the same principle is applied to the transformers. If abnormally high temperature is detected in the transformers, then the possibility of failure is high. It is important to notice that the opportunities to make installations in industrial sites relied on the maintenance operations of the EDF company. When maintenance operations would take place, the systems would shut down and in order to install any RFID sensor tags the system of interest should not be operating for security reasons.

The visit in the hydroelectric power-plant of Grand'Maison was divided in two parts: The installation part and the measurement part. The installation part was performed in July 2018 and the measurement part in April 2019.

Installation of RFID sensor tags in the transformers of the Grand'Maison power-plant

The design of the $\lambda/4$ rectangular RFID sensor tag was used for an initial production of 50 RFID sensor tags. The transformer structure is presented in Fig. 7.14. The transformer has 3-phases connections and thus RFID sensor tags would be installed in each one.

The part where the RFID sensor tags needed to be installed was below a black rubber cover (called "soufflet" in French). This position was advantageous since after the installation it would be possible to use an antenna at this point to potentially read the RFID sensor tags.

In each phase connection 7 RFID sensor tags were installed, each one in different position. A strong glue (Loctite 9492) for metallic items was used to keep the RFID sensor tags in place. One of the fabricated RFID sensor tags and the placement with the glue is presented in Fig. 7.15.

Figure 7.14: Transformers in hydroelectric power-plant of Grand’Maison

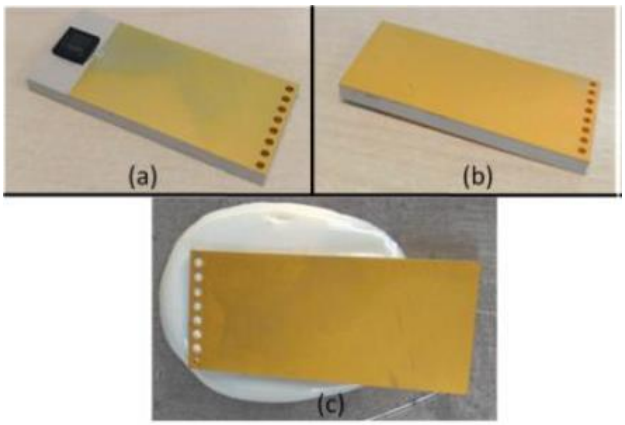

Figure 7.15: Fabricated RFID sensor tag (a) bottom view (b) top view (c) placement with the glue

In Fig. 7.16 the placement of some RFID sensor tags in the transformer can be viewed.

Each RFID sensor tag had the EPC value renamed according to its placement. The name would include

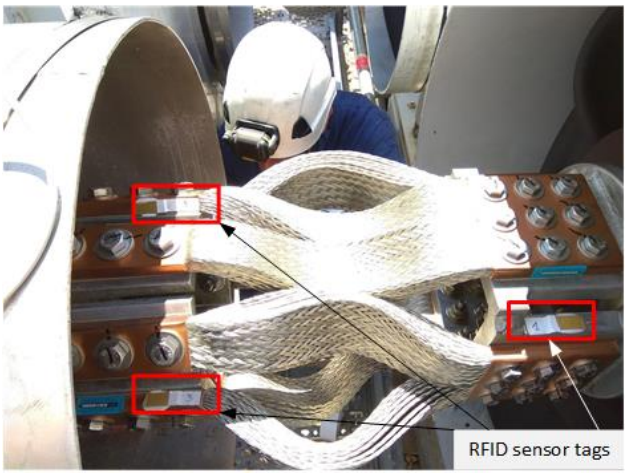

Figure 7.16: Transformer with RFID sensor tags in various installation positions

which transformer it was installed and at which position. All the seven positions which were utilized in this installation are presented in Fig. 7.17.

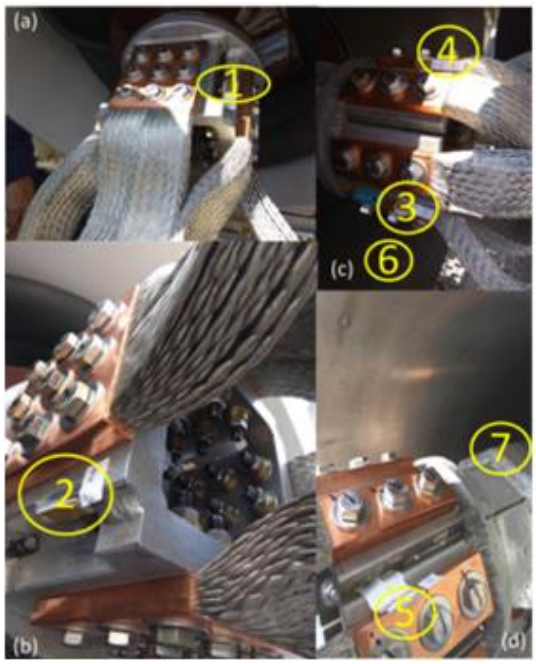

Figure 7.17: Installation positions of the RFID sensor tags in each transformer connection (seven positions overall)

One very important issue during the installation of the RFID sensor tags was the fact that each position had different geometry and the metallic surfaces in the proximity would pose a different effect on the RFID sensor tag-antenna. This had an impact on the resonance frequency of the RFID sensor tag, resulting not to operate with the best performance in the ETSI frequency band. This issue had to be considered even more since the designed RFID sensor tags exhibit a narrow band operation and the fact that the ETSI frequency band has only 2 MHz of bandwidth. To address this problem, the following procedure was adopted. Initially the RFID sensor tag was placed in the specific position it would be installed. The performance of the RFID sensor tag would be evaluated by using the Tagformance Pro RFID reader. The RFID sensor tag would be trimmed gradually until the resonance would correspond to the ETSI frequency band. Then the RFID sensor tag would be permanently installed.

By trimming the RFID sensor tag-antenna, the resonance frequency can only vary towards higher frequency values. The potential tuning of the RFID sensor tags was anticipated and thus the RFID sensor tags were fabricated to resonate a little lower of the ETSI frequency band (860 MHz) taking into account the possibility of tuning them to the desired frequency.

In addition to the impact of the nearby metallic structures on the resonance frequency of the RFID sensor tag, the radiation properties of the RFID sensor tag would be affected, downgrading the performance and the read range of the RFID sensor. Specifically, the RFID sensor tags were positioned on different sized metallic surfaces. Larger metallic surfaces are resulting in a higher directivity and thus higher read range.

After the installation of the RFID sensor tags, and a time interval for the maturation of the glue, some measurements of the temperature were conducted. For these measurement the Thingmagic M6e reader [127] was used. The SL900A RFID chip in order to transmit the value of the output of the integrated temperature sensor, needs to receive a custom command. The M6e reader operates with the Mercury application programming interface (API) which already includes libraries with the custom commands that the RFID chip requires to respond the value of the integrated temperature sensor. Hence, an interface including the standard EPC commands as well as the custom commands of the SL900A RFID chip was developed using the C# programming language for this specific application [128].

In Fig. 7.18 a screenshot of the developed interface is presented, when the M6e RFID reader was reading one of the installed RFID sensor tags. The interface contains two main windows. In the left one (with the green graph) the output of the ADC value of the RFID chip is appearing. In the right window (red graph) the value of the temperature can be seen after the appropriate data processing completes (according to §5.3.1, eq.

5.1). For instance, in the Fig. 7.18 the average value transmitted was 675 which according to the reference voltages of the RFID chip corresponds to 32.2 $°C$.

Figure 7.18: Developed interface for acquiring the output value of the integrated temperature sensor of the SL900A RFID chip

Measurement of the installed RFID sensor tags in the transformers of the Grand'Maison power-plant

The RFID sensor tags which were installed in the hydroelectric power-plant of Grand'Maison stayed idle until the opportunity to conduct measurements while the transformers were operating arisen. This was a first class opportunity to test the operation of the RFID sensor tags under high electric and magnetic field conditions. In order to perform the measurements, some very important precautions should be taken into account. When the transformers are operating a very high electric and magnetic field surrounds them, thus the antenna and the RFID reader which is needed to be in close proximity should be shielded to avoid the

generation of high current passing through the equipment. For this reason, a measuring setup was developed in cooperation with the team of the EDF company. The measuring setup is presented in Fig. 7.19.

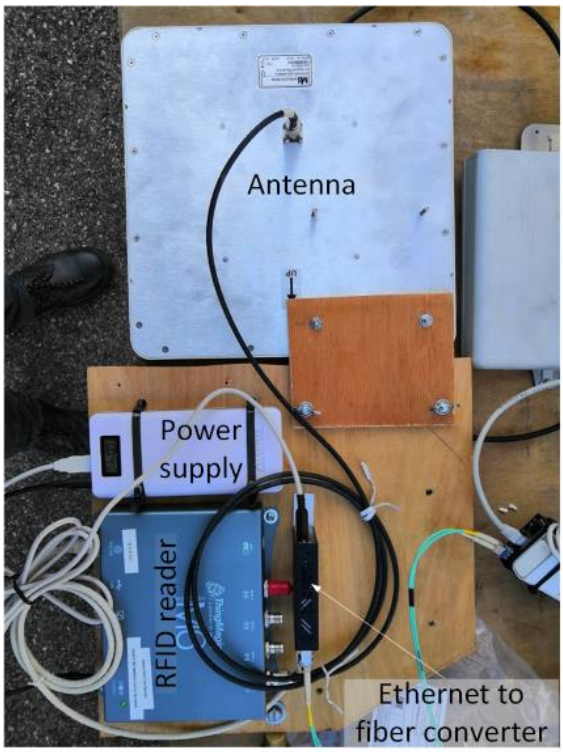

Figure 7.19: Shielded measurement setup

The measurement setup contains the RFID reader ThingMagic M6 [129] with right-handed circular polarized antenna with gain 6 dBi, an Ethernet to optical fiber converter and a power supply [130] which was powering up the RFID reader and the converter. The whole measurement setup was positioned on a wooden base attached to an insulated stick.

Moreover, the position of the antenna in order to read the RFID sensor tags was an issue which was given the appropriate attention. The antenna was positioned around the rubber cover (soufflet) since the rest of the transformer cover was metallic. However, as presented previously, the RFID sensor tags were installed in different sides of the transformer. With such placement the RFID sensor tags positioned at the other side of the antenna could potentially be unreadable due to the intervention of the transformer body. For this issue during the measurements the antenna of the RFID reader was tested in different positions to identify the case where the highest amount of RFID sensor tags was read. The positions were the antenna

was tested are presented in Fig. 7.20.

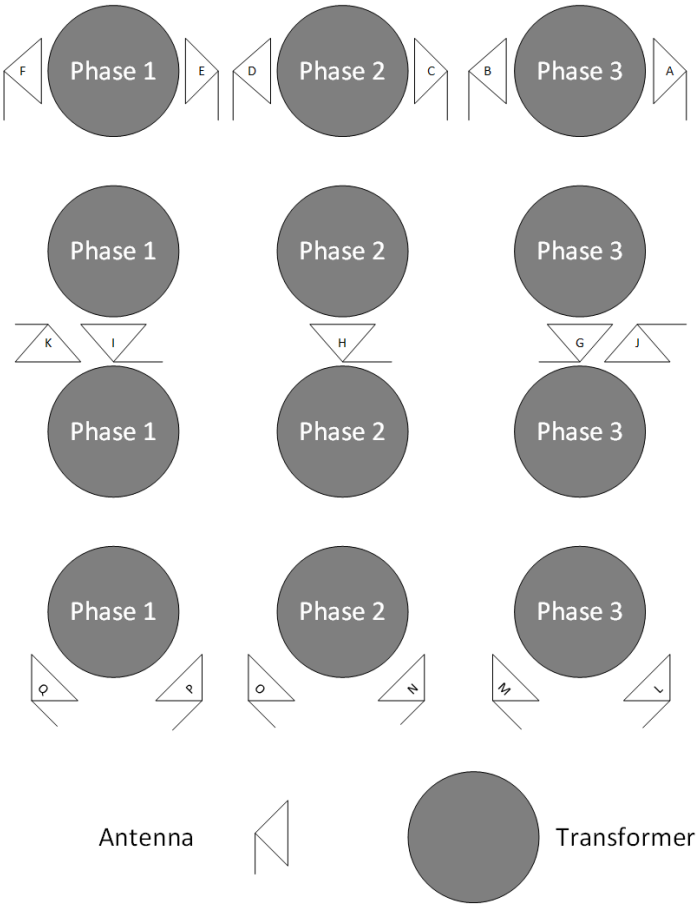

Figure 7.20: Tested positions of the antenna

The different positions were given names from A to Q according to the Fig. 7.20. For instance, in the Fig. 7.21, the measurement of the position A is presented.

The shielded measurement setup was positioned in all the presented positions and every time a reading round of the temperature sensor value was initiating. An additional remark in this point is that the RFID reader used was different than the one used during the installation process (ThingMagic M6 here and ThingMagic M6e previously). This was due to the fact that the developed interface failed to operate with this specific RFID reader. Instead, a small java based interface developed by the EDF team was used in this case [131]. In Table 7.1, Table 7.2 and Table 7.3 [132] the results of the measurements for each position are presented.

Figure 7.21: Measurement of the RFID sensor tags from position A

Table 7.1: Phase 1

RFID sensor tags (3 last digits of the EPC code)	*Average temperature measured for each antenna position (°C)**					
	E	*F*	*I*	*K*	*P*	*Q*
8A1	-	-	-	-	-	-
8A2	-	-	-	-	-	-
8A3	*45.5*	*-2.1*	*43.4*	-	*2.4*	*40.2*
8A4	-	-	-	-	-	-
8A5	-	-	-	-	-	-
8A6	*26.9*	-	-	-	-	-
8A7	-	*45.2*	-	*47.4*	*47*	*48.1*

** For the phase 1 the dedicated positions of the antenna were the: E, F, I, K, P, Q*

The results of the measurements in the transformers of the hydroelectric power-plant of Grand'Maison

Table 7.2: Phase 2

RFID sensor tags (3 last digits of the EPC code)	*Average temperature measured for each antenna position (°C)**					
	C	*D*	*H*	*N*	*O*	-
0B1	*40.5*	-	*41.1*	*41.9*	-	-
0B2	*40.3*	*40.3*	*40.3*	*41.3*	*41.5*	-
0B3	-	-	*41.7*	*45*	-	-
0B4	*44.1*	-	*46.5*	*48.9*	-	-
0B5	-	-	-	-	-	-
0B6	-	-	-	-	-	-
0B7	*46*	*45.7*	-	*46.9*	-	-

**For the phase 2 the dedicated positions of the antenna were the: C, D, H, N, O*

Table 7.3: Phase 3

RFID sensor tags (3 last digits of the EPC code)	*Average temperature measured for each antenna position (°C)**							
	A	***A_H*	***A_V*	*B*	*G*	*J*	*L*	*M*
0A1	*41*	*42.5*	-	-	-	*41.8*	*41.9*	*18.3*
0A2	-	*44.4*	-	-	-	-	-	*44.3*
0A3	-	-	-	-	-	-	-	-
0A4	-	-	-	-	-	-	-	-
0A5	-	-	*48.9*	*49.8*	-	-	-	*50.8*
0A6	-	*28.9*	-	-	*25.4*	-	-	*38*
0A7	-	*50.6*	-	*47.9*	*48.8*	-	-	*50*

** For the phase 3 the dedicated positions of the antenna were the: A, B, G, J, L, M*
*** In the position A, a linear antenna with gain of 8 dBi was also tested, where AH when the antenna was held horizontally and AV when the antenna was held vertically*

were encouraging. The first conclusion was that the RFID sensor tags can operate under the effects of high magnetic and electric field. Furthermore, the positioning of the antenna of the RFID reader plays a major role in the readability of the RFID sensor tags. Indicatively, for the phase 3 the position M was the most prominent for the antenna to be installed in a permanent measurement setup. Also, some RFID sensor tags yield quite different results for different positions of the RFID antenna. This is due to the operation of the RFID chip, where if the received power is not quite enough, the reference voltages are not acquiring the proper value and wrong data are transmitted. In addition, a number of RFID sensor tags were not read and this is due to the tuning process of trimming. The trimming procedure was performed manually, allowing a

big margin of error at the resonance frequency of each RFID sensor tag. Also, another reason for not being able to read all the tags was the positioning of some of them where all the tested antenna positions might not be the most beneficial.

7.2.6 Visit in the hydroelectric power-plant of Super-Bissorte

During the visit in the hydroelectric power-plant of Super-Bissorte, the opportunity to explore another type generator presented. In this power-plant the generators were considerably larger than the previous examined sites. The stator and the rotor of the generator are presented in Fig. 7.22 and Fig. 7.23 respectively.

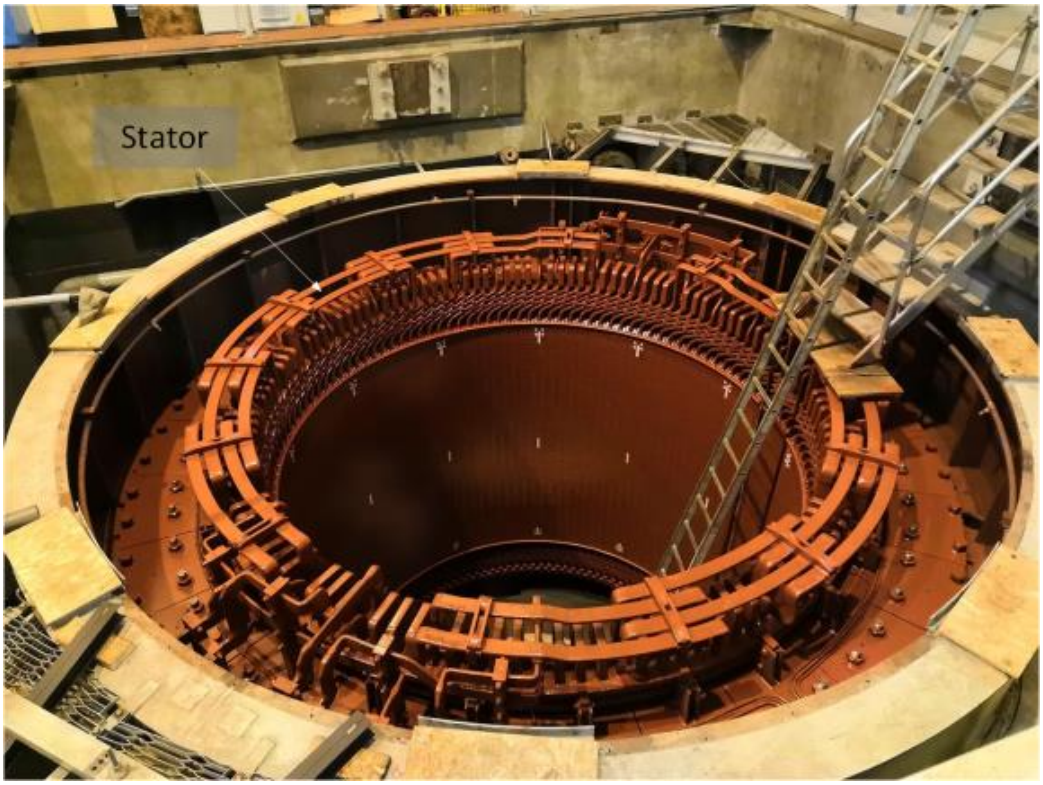

Figure 7.22: Stator of the generator at the hydroelectric power-plant of Super-Bissorte

Figure 7.23: Rotor of the generator and the interpolar connections at the hydroelectric power-plant of Super-Bissorte

In this occasion, the opportunity to test some RFID sensor tags presented. Two RFID sensor tags were attached on the interpolar connection to test their performance. The attached RFID sensor tags are presented in Fig. 7.24.

The equipment used during these measurements was the RFID reader Thingmagic M6e with a right-handed circular polarized antenna with gain 6 dBi. The developed interface presented earlier at §7.2.5 was used to acquire the temperature value of RFID sensor tag. The RFID sensor tags were tested regarding their maximum read range corresponding to the custom command of the RFID chip which acquires the value of the temperature sensor (without presenting errors).

Figure 7.24: Attached RFID sensor tags on the interpolar connection of the rotor at the hydroelectric power-plant of Super-Bissorte

The RFID sensor tags presented a read range of around 1 m during these measurements.

7.2.7 Visit in the hydroelectric power-plant of Aussois

The scheduled maintenance of a generator in the hydroelectric power-plant of Aussois allowed the possibility of the installation of the RFID sensor tags in a generator environment. The RFID sensor tags were initially installed on the interpolar connections of the rotor. For this installation, two interpolar connections were selected and two RFID sensor tags were installed on each one. In this case, three $\lambda/4$ rectangular RFID sensor tags and one rectangular $\lambda/2$ were used. The rotor and the interpolar connections with the installed RFID sensor tags are presented in Fig. 7.25 and Fig. 7.26(a) respectively.

Figure 7.25: Rotor of the generator at the hydroelectric power-plant of Aussois

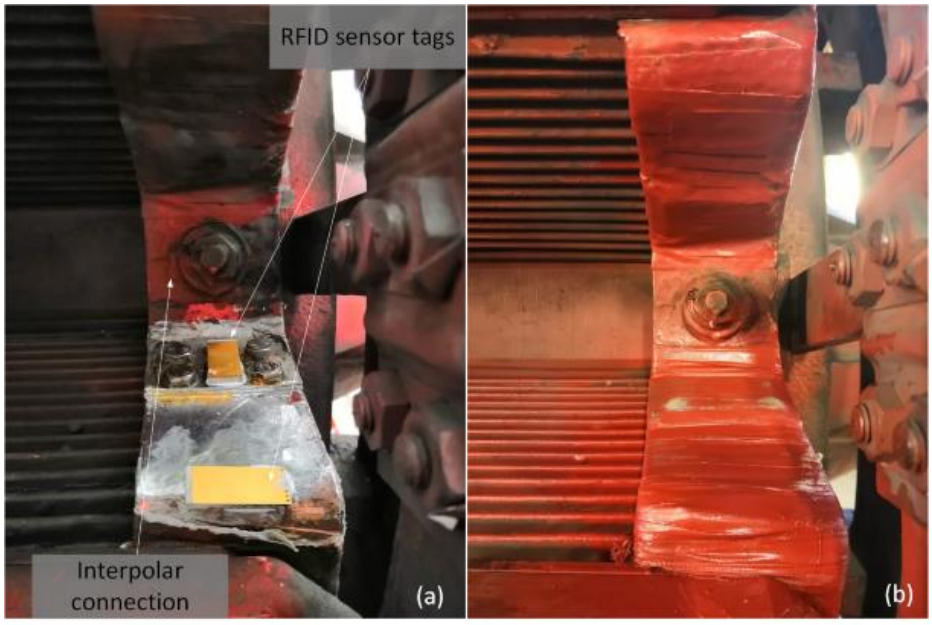

Figure 7.26: (a) Interpolar connection of the rotor with the installed RFID sensor tags at the hydroelectric power-plant of Aussois (b) Interpolar connection after the application of the protective tape

The RFID sensor tags were positioned vertically aiming to test if the polarization direction will have a major part regarding the readability of the RFID sensor tags. After the installation of the RFID sensor tags a protective tape was applied (see Fig. 7.26(b)). This kind of tape is generally applied in order to protect the interpolar connection from dust and rites.

After the installation of the RFID sensors, the installation of the antenna of the RFID reader followed. The type of the generator at the power-plant of Aussois has stator with many small holes which act as air ducts. A small antenna (presented in §4.3.2) was also installed in the interior of the generator and these air ducts were exploited to pass a thin RF cable to connect the antenna with the RFID reader. The stator with the air ducts visible and the installed antenna of the RFID reader are illustrated in Fig. 7.27.

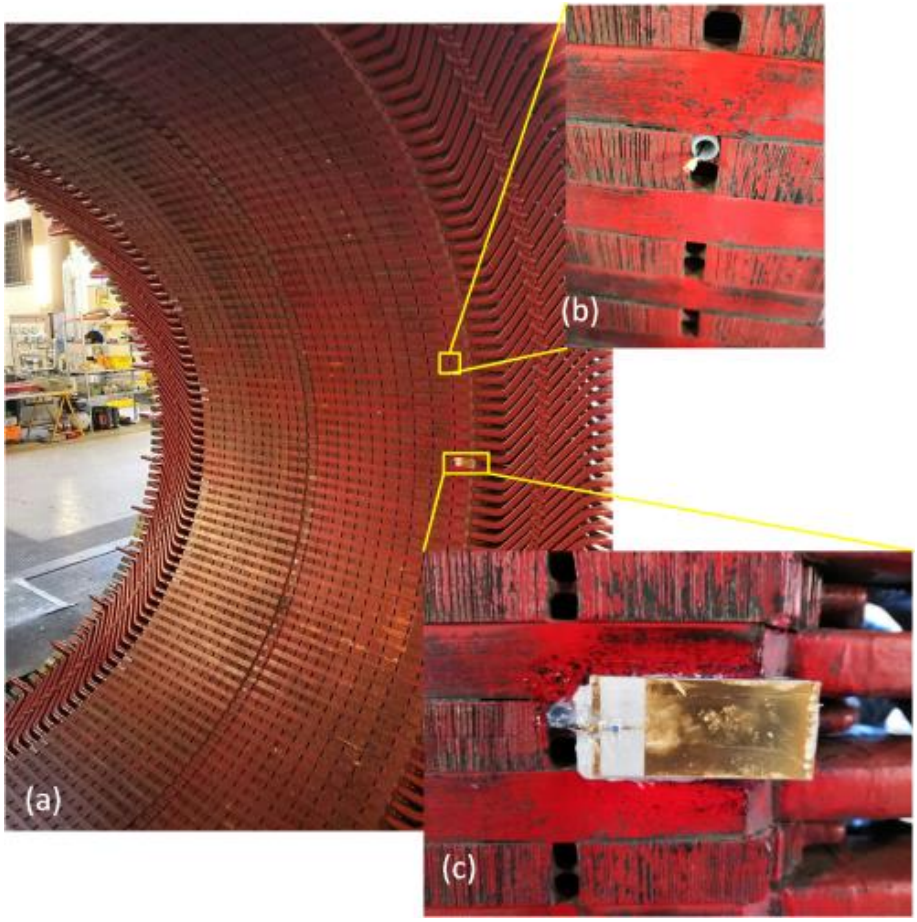

Figure 7.27: (a) The stator at the hydroelectric power-plant of Aussois (b) The air ducts with the RF cable (c) The installed antenna of the RFID reader

The antenna of the RFID reader was installed on the stator by using glue and it was overlapped by a

silicon layer to avoid any short-circuits. The RF cable passing through the air ducts ended up behind the stator (see Fig. 7.28). From there and through a small hole drilled at the generator chassis, the RF cable can be connect to an RFID reader. With such configuration a LOS scenario between RFID sensor tags and RFID reader antenna can be achieved.

Figure 7.28: RF cable ending behind the stator

One important issue that came up during this installation was the fact that the antenna of the RFID reader could not be very well aligned with the interpolar connections where the RFID sensor tags were installed. The antenna was positioned as close to the ending of the walls of the stator as possible and it would need approximately another 10 cm in order to be aligned with the RFID sensor tags. Installing the antenna further was prohibited due to security reasons, since it could result in a generator failure if it was installed out of the stator walls. This can be seen in Fig. 7.27(c) where the right side of the antenna is floating. Another issue from this installation is the available power which can be transmitted from the RFID reader setup.

According to ETSI regulation 33 dBm of ERP is allowed and by using the small fabricated antenna the available transmitted power would be less due to its limited gain (less than 1 dB).

Even though the installation at the hydroelectric power-plant of Aussois is completed, it has not been possible to perform measurements in the generator while it is operating yet. Due to a problem of the generator, it is expected to operate again probably around the end of the current year (2019). Thus any measurements with the installed system will be performed in the future.

7.3 Conclusion

In this chapter, the outcome as well as the tasks performed during visits at the industrial sites of various hydroelectric power-plants of EDF were presented. The visits included the exploration of different generator geometries and types, the possibility to conduct a variety of measurements and useful insights of the limitations which would arise during the work for the Innov'Hydro project.

One of the initial areas of focus was the impact of the multipath in the RFID communication. The multipath phenomena are extremely difficult to be predicted, especially in complex environments with numerous reflective surfaces. The nature of the multipath effects can result to destructive or constructive interferences, thus either boosting or downgrading the readability of the RFID tags. Some useful information regarding the multipath effects were extracted from measurements at an industrial site especially regarding the polarization mismatch. However, the multipath effects can be circumstantial, thus it was not possible to lead in a safe general conclusion.

Most of the visits were dedicated to acquire experience on the specific features of the different types of generators. The fact that there is a great diversity of different types of generators with different geometries of interpolar connections had an impact on the resonance characteristics of the designed RFID sensor tags. The strict specifications of the RFID sensor tags, especially concerning their size, resulted in designs with narrow band characteristics. Also, the ETSI frequency band poses additionally difficulties to the designed RFID sensor tags due to the limited bandwidth of operation. These two factors in combination with the diverse generator environments led to the need of tuning of the RFID sensor tags according to the specific environment of operation. This problem was addressed by trimming the RFID sensor tags in order to operate at the desired frequency band. Furthermore, the metallic surfaces where the RFID sensor tags were installed had different sizes, affecting the radiation characteristics of the RFID sensor tags and specifically of the directivity that they present.

In addition, an RFID sensing system was installed in the transformers of a power-plant and it was successfully tested being, according to the author's knowledge, the first industrial application of RFID sensing in the unhospitable environment of high voltage transformers.

Finally, an RFID sensing setup in the interior of a generator was proposed and implemented, where a small antenna would be installed on the stator structure of the generator aiming to read the RFID sensor tags. This setup is planned to be used for measurements in the near future.

CHAPTER 8
CONCLUSION

8.1 General conclusion

This thesis has been dedicated to UHF RFID sensing in harsh environmental conditions and in particular in the industrial environment of hydroelectric power-plants and in the interior of large scale generators. The main contributions to the scientific community of this thesis can be summarized as follows:

- The sensing functions by using the RFID technology is a relative new field, with high interest and high potential of research and improvement. The techniques which are used for sensing with RFID technology in the UHF band were not structurally classified and thus a classification scheme has been proposed. The UHF RFID sensing techniques are classified as internal and external, based on the manner which the sensing functions are taking place, on how the communication channel between RFID sensor tag and RFID reader evolves and how the useful sensing information are processed in the RFID reader. A variety of RFID sensing concepts were analyzed based on the principles of the proposed classification. The different RFID sensing systems were also compared based on several metrics of their performance.

- The environment of the indented operation of the RFID sensing system is posing a series of potential disturbing effects such as high values of magnetic and electric field, dense metallic environment as well as high rotational speed. These effects have been studied in practice in order to identify their impact on the RFID communication and the RFID sensor tags overall. In general, it has been shown that the electric and magnetic field due to their low frequency are not a disruptive factors of the UHF RFID operation. This interaction has been studied also in the environment of a high voltage transformer. In addition, the time delay of the communication between RFID reader and RFID sensor tag has been explored in detailed analysis of the time constraints of the RFID communication. This analysis includes the calculations and measurements of the potentials delays of the RFID communication and sets a threshold to the maximum rotational speed which can be supported by the RFID technology.

- A variety of novel RFID sensor tag antennas were notably introduced. These RFID sensor tags antennas were conforming to a set of specifications, specially selected for the intended application in

the large scale generators. The design process of the RFID sensor tag antennas was accompanied by measurements of the selected RFID chip in order to better match RFID tag antenna and RFID chip. The RFID sensor tags were evaluated for their performed maximum read range value, succeeding to cover the specification requirements. In addition, one of the proposed RFID sensor tag antenna designs (rectangular $\lambda/4$) presented an interesting property, where by exploiting the metallic environment was able to operate in different regulated RFID bands (ETSI and FCC) just by being flipped over a metallic surface. The operation of the RFID sensor tag antenna was modeled by an equivalent circuit, aiming to describe the property of the design RFID sensor tag antenna in more depth.

- Moreover, a novel structure of twin RFID sensor tag was additionally introduced. The twin RFID sensor tag antenna was consisting from two sub-antennas, inspired by some of the previous presented RFID sensor tag antenna designs. This twin RFID sensor tag included two RFID chips, with each one responsible of sensing a different temperature range. The main application of this twin RFID sensor tag was the possibility to offer better quality temperature sensing in comparison to similar sized RFID sensor tags with one RFID chip. In addition, two novel antenna designs were developed to serve as the antennas of the RFID reader in a space constrained environment.

- Besides the principal RFID sensor tag designs, which were conforming to the specifications, some other techniques and concepts of RFID sensing were developed and tested. The utilization of a self-tuning circuit of an RFID chip was tested, regarding its potential to perform temperature sensing functions by utilizing a temperature sensitive substrate. This operation was explored in more depth, initially by performing electromagnetic simulations and applying the anticipated phenomena of the temperature in the numerical model of the RFID sensor tag antenna. Measurements of the impedance of a fabricated prototype of the proposed RFID sensor tag antenna and of the RFID chip followed, in a temperature varying environment aiming to confirm the simulated behavior. The proposed concept was validated by a test application in temperature controlled environment by showcasing the performance of the self-tuning RFID sensor tag. In addition, a variety of chipless RFID sensor tags were developed, intended to sense various physical parameters, such as temperature, humidity and rotational motion. The basic operating principles of the chipless RFID sensors were regarding the exploitation of their substrate materials, which were acting as transducers. This operation was resulting in the variation of their resonance characteristics according to the variation of the desired physical

parameter. This was the case of the chipless RFID sensor tags dedicated to measuring temperature and humidity. For the rotational motion chipless RFID sensor, the polarization mismatch between the antenna of the RFID reader and the chipless sensor was utilized to measure the rotational speed. Furthermore, an RFID reader architecture based on SDR device was proposed and its validity was tested by reading the presented chipless RFID sensor tags.

- Moreover, the study of various real industrial sites of hydroelectric power-plants with "an RFID technology point of view" was presented. These visitations were supported by measurements, offering insights on the limitations and the advantages of the RFID technology in such industrial sites. In addition, the first (according to author's knowledge), RFID temperature measurement system operating in the transformers of a power-plant was presented, where promising results were obtained. Furthermore, an installation in a large scale generator was performed, by utilizing specifically designed antennas of the RFID reader. An original setup configuration was used by utilizing the air ducts of the generator's stator and a series of RFID sensor tags were installed on the generator's rotor. For this installation the measurement results are pending.

8.2 Future research lines

- The impact of the dense metallic environment at the resonance characteristics of the RFID sensor tags needs to be addressed with a more efficient way than the tuning by trimming part of the RFID sensor tag antenna which was selected in this thesis. The strict specifications on the characteristics of the RFID sensor tags result in limited options regarding the RFID sensor tag antenna. Hence, the main focus point to solve this problem could be a self-tuning method, similar to the one presented in the §6.2. In fact, very recently an RFID chip (Axzon / RFMicron RFM405 Xerxes I) with an integrated temperature sensor, a self-tuning circuit and ports for connecting external sensors has been introduced. Thus one solution could be the transition to a new, enhanced RFID chip by continuing using the same RFID sensor tag antennas. This argument can be supported also from the fact that the used RFID chip (SL900A) has been characterized as obsolete and it is difficult to be found anymore in a packaged form.

- The designed RFID sensor tag antennas can be improved to demonstrate better characteristics and offer even better performance regarding their bandwidth and read range. This can be achieved either

with improvements on the design of the RFID sensor tag antenna or by choosing different substrate materials. In any case, there is always the margin of amelioration of the performance. The same applies for the presented antennas of the RFID reader which were designed and fabricated to operate in the interior of the generator and namely on the stator walls. In addition, different type of RF connector can potentially be used with these antennas (a UMCC connector was used), since this kind of connector is quite fragile and it presents a high risk of failure in the harsh environment of the generator.

- The twin RFID sensor concept has the potential to be exploited not only to offer higher quality temperature measurements or multi-sensor operation, but also for more applications. For instance, if in the place of the one of the two RFID chips, another circuit is implemented with a variable impedance can lead to a type of self-tuning operation for the other RFID chip of the twin RFID sensor tag. This or more potential extra functionalities of the twin RFID sensor tag are yet to be discovered and tested on their validity.

- The 3 dB 90° hybrid coupler concept presented in §6.3.5 can be further explored in order to offer exploitable results and to be better understood its practical application. Also this concept it would be beneficial to be tested in integrated design were the impedance values and several other characteristics of the components could be better controlled and determined.

8.3 List of publications

Peer-reviewed international journals

1. H. El Matbouly, S. Tedjini, **K. Zannas** and Y. Duroc, "Chipless Sensing System Compliant with the Standard Radio Frequency Regulations," in IEEE Journal of Radio Frequency Identification, vol. 3, no. 2, pp. 83-90, June 2019. doi: 10.1109/JRFID.2019.2909092

2. **K. Zannas**, H. El Matbouly, Y. Duroc and S. Tedjini, "Self-Tuning RFID Tag: A New Approach for Temperature Sensing," in IEEE Transactions on Microwave Theory and Techniques, vol. 66, no. 12, pp. 5885-5893, Dec. 2018. doi: 10.1109/TMTT.2018.2878568

3. H. El Matbouly, **K. Zannas**, Y. Duroc and S. Tedjini, "Analysis and Assessments of Time Delay Constrains for Passive RFID Tag-Sensor Communication Link: Application for Rotation Speed Sens-

ing," in IEEE Sensors Journal, vol. 17, no. 7, pp. 2174-2181, 1 April1, 2017. doi: 10.1109 /JSEN.2017.2662058

4. H. El Matbouly, S. Tedjini, **K. Zannas**, and Y. Duroc, "Compact Multi Bit Slotted C-Scatterer for Threshold Sensitive Chipless Wireless Temperature Sensor, " Technologies, vol. 6, no. 3, p. 59, Jun. 2018.

Book chapter

5. **K. Zannas**, H. El Matbouly, Y. Duroc and S. Tedjini, "From Identification to Sensing: Augmented RFID tags", Wireless Power Transmission for Sustainable Electronics, Wiley, (submitted-publication pending)

International conferences with reviewed committee and proceedings

6. **K. Zannas**, H. E. Matbouly, Y. Duroc and S. Tedjini, "Flipping a Coin, Heads or Tails. Flipping an RFID Tag on Metal, ETSI or FCC Bands," 2019 IEEE MTT-S International Microwave Symposium (IMS), Boston, MA, USA, 2019, pp. 283-285.

7. H. El Matbouly, S. Tedjini, **K. Zannas** and Y. Duroc, "Chipless RFID Threshold Temperature Sensor Compliant with UHF and ISM Radio Frequency," 2018 2nd URSI Atlantic Radio Science Meeting (AT-RASC), Meloneras, 2018, pp. 1-4. doi: 10.23919/URSI-AT-RASC.2018.8471585

8. **K. Zannas**, H. E. Matbouly, Y. Duroc and S. Tedjini, "On the Cooperative Exploitation of Antenna Sensitivity and Auto-Tuning Capability of UHF RFID Chip. Application to Temperature Sensing," 2018 IEEE/MTT-S International Microwave Symposium - IMS, Philadelphia, PA, 2018, pp. 374-377. doi: 10.1109 /MWSYM.2018.8439619

9. H. E. Matbouly, **K. Zannas**, Y. Duroc and S. Tedjini, "Chipless Wireless Temperature Sensor Based on C-like Scatterer for Standard RFID Reader," 2017 XXXIInd General Assembly and Scientific Symposium of the International Union of Radio Science (URSI GASS), Montreal, QC, 2017, pp. 1-3. doi: 10.23919 /URSIGASS.2017.8105026

10. **K. Zannas**, H. E. Matbouly, Y. Duroc and S. Tedjini, "Antenna design for compact RFID sensors dedicated to metallic environments," 2017 XXXIInd General Assembly and Scientific Symposium of

the International Union of Radio Science (URSI GASS), Montreal, QC, 2017, pp. 1-3. doi: 10.23919 /URSIGASS.2017.8105333

11. H. E. Matbouly, **K. Zannas** and Y. Duroc, ”Design of passive chipless wireless motion sensor using dual polarization effect,” 2017 11th European Conference on Antennas and Propagation (EUCAP), Paris, 2017, pp. 3908-3911. doi: 10.23919/EuCAP.2017.7928695

National conference articles

12. **K. Zannas**, H. El Matbouly, Y. Duroc and S. Tedjini, ”Nouveau Concept pour la Réalisation d’un Capteur de Température RFID UHF Passif Exploitant la Fonction d’Auto-Tuning des Puces,” 21èmes Journées Nationales Micro-Ondes, Caen, France, 2019

13. H. El Matbouly, **K. Zannas**, Y. Duroc and S. Tedjini, ”Capteur RFID sans Puce pour la Mesure de Seuil de Température en Environnement Réel, ” 21èmes Journées Nationales Micro-Ondes, Caen, France, 2019

Appendices

APPENDIX A
AMS SL900A RFID CHIP

In this section, the main characteristics of the RFID chip SL900A will be presented and generally a discussion regarding its operation. In Table 1 the main characteristics of the SL900A RFID chip are presented.

Table A.1: SL900A RFID chip main characteristics

Parameter	*Comments*	*Value*	*Units*
Antenna pad impedance	*Measured at 915 MHz, QFN package for PCB assembly*	*123-j×303*	Ω
Antenna pad sensitivity	*Measured at 915 MHz, QFN package for PCB assembly for passive operation*	-6.9	*dBm*
Antenna pad sensitivity	*Measured at 900 MHz, battery assisted operation*	-15	*dBm*
Operating ambient temperature range		$-40\ to\ 125$	$°C$
Carrier frequency		$860\ to\ 960$	*MHz*
Default temperature range	*Reconfigurable (calibration required)*	$-29.3\ to\ 58$	$°C$
EEPROM memory size	*Re-writable*	9	*Kbits*

One first important observation from Table A.1 is that the antenna pad impedance (i.e., the input impedance) is defined as a complex impedance for a specific frequency. Usually, in the datasheets of RFID chips this impedance is defined with an equivalent RC circuit. From the equivalent RC circuit then it is quite easy to find the impedance value for random frequency value. Hence, the assumption that there will be an equivalent RC circuit of this RFID chip was made and the values of the RC circuit which result in the defined input impedance value were extracted. The values found for the RC equivalent circuit were $R = 857\ \Omega$ and $C = 0.49\ pF$. From these values, the diagram of Fig. A.1 was plotted.

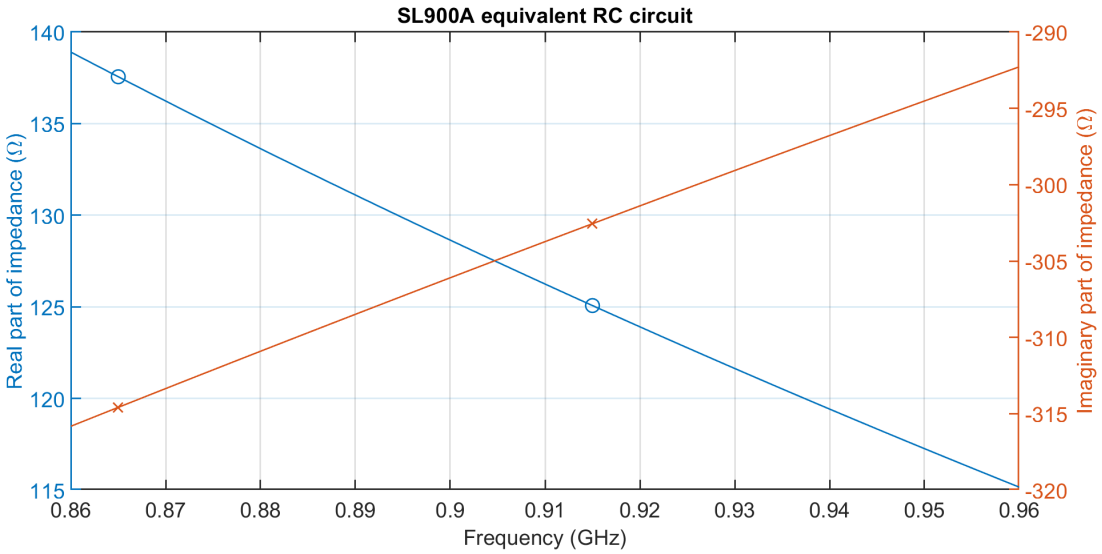

Figure A.1: Impedance of the SL900A RFID chip from the equivalent RC circuit

From Fig.A.1 it can be seen that the value of the complex impedance at 915 MHz agrees with the impedance value given in the datasheet ($123 - j \times 303\Omega$). For the 866 MHz value the complex input impedance is $138 - j \times 315\Omega$. These two values during RFID tag antennas simulations yielded very similar results and thus the originally defined value of impedance was used until the time where the measurements of §3.3 were performed and the acquired impedance values were used. Also, it is important to mention the fact (was also stated in §3.3) that the earlier versions of the SL900A RFID chip datasheets defined the input impedance value as $31 - j \times 320\Omega$ and it was redefined in later versions of the datasheet. Another interesting point was the value of the antenna pad sensitivity (i.e., activation power). For passive operation it is defined as $-6.9\ dBm$ but during the measurements of the realized prototypes, this value could not be confirmed. A value that was offering better agreement between measured and simulated results was a value around $-4.8\ dBm$. Lacking additional information there is high uncertainty regarding the actual value of activation power in passive operation.

In Fig. A.2 the block diagram of the SL900A chip can be viewed.

One of the unique characteristics of the SL900A RFID chip which led to its selection were the integrated temperature sensor and the external sensor front-end. The output of either the integrated temperature sensor or the external sensor front-end are send to a 10-bit ADC through a multiplexer. The output of the ADC is then communicating with the processing digital control unit and through the cool-Log command set can be transmitted to an RFID reader appropriately programmed.

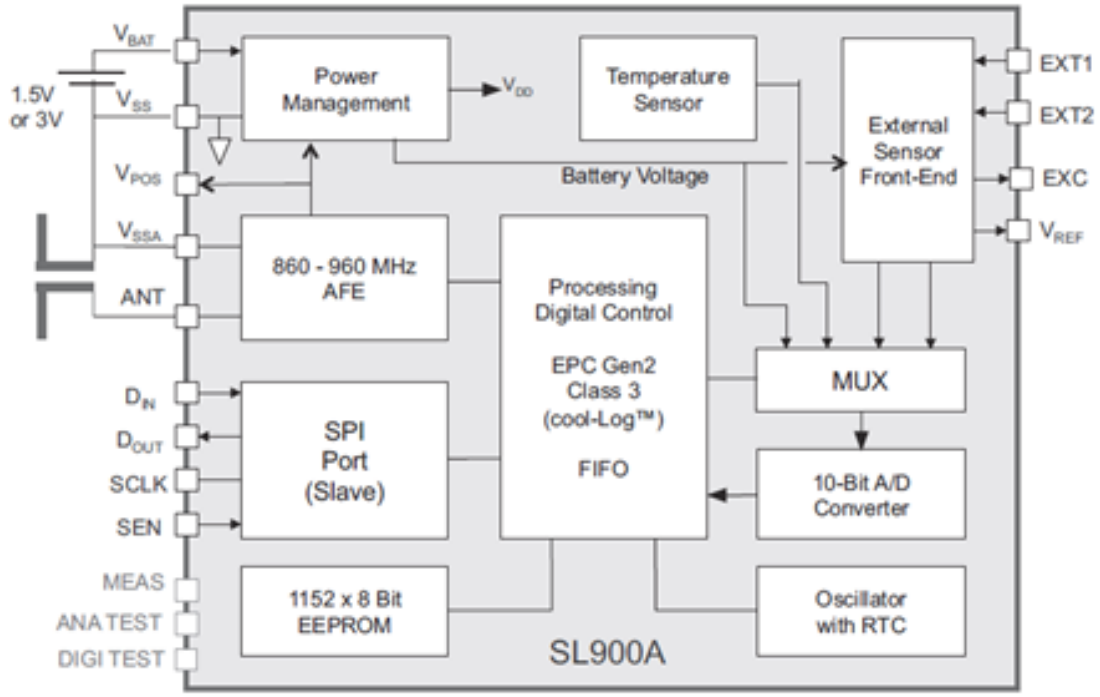

Figure A.2: Block diagram of the SL900A RFID chip [31]

The cool-Log command set, is a series of custom commands based on the EPC Gen2 Class 3 protocol and they were introduced to the SL900A RFID chip from the manufacturer. With these custom commands, several values corresponding to the extra functionalities of the RFID chip can be exchanged with an appropriate RFID reader. For instance, the value of the ADC converter with the output of integrated temperature sensor can be received after a specific cool-Log command is transmitted to the SL900A RFID chip.

APPENDIX B
AMS FEMTO AS3993 RFID READER

The Femto AS3993 is a low cost, EPC Gen2 class 3 compliant RFID reader appropriate for development and application demonstrations, see Fig. B.1.

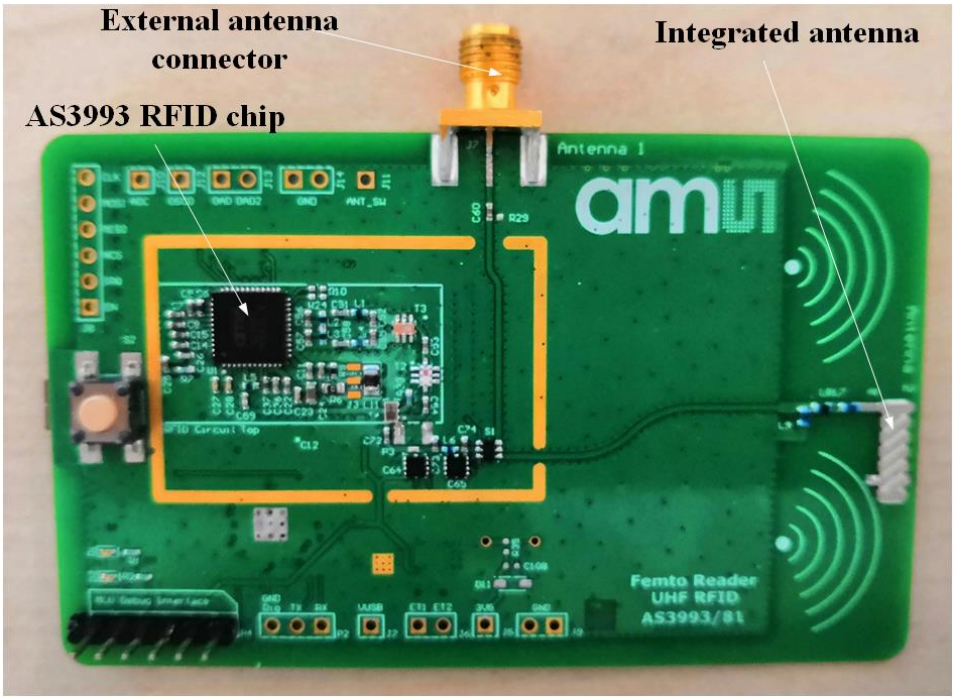

Figure B.1: Femto AS3993 RFID reader

The Femto RFID reader has an integrated antenna as well as a port for connecting an external antenna. The main characteristics of the Femto reader are presented in Table B.1.

Table B.1: Femto AS3993 RFID reader main characteristics

Parameter	*Comments*	*Value*	*Units*
Maximum Tx output power	*Adjustable internal power amplifier*	*20*	*dBm*
Highest Rx sensitivity	*Adjustable sensitivity*	*-83*	*dBm*
Frequency of operation	*Adaptable to different frequency schemes*	*860-940*	*MHz*

Some very useful extra characteristics of the Femto RFID reader and its graphical user interface (GUI) are:

- Support for SL900A RFID chip (cool-Log command set)
- Diagnostic features such as: Received Signal Strength Indicator (RSSI) and measurement of the reflected power
- Possibility to adjust parameters of the Gen2 protocol (e.g. anti-collision slots, Tari value)
- SPI connectivity

The Femto RFID reader's extra characteristics were quite important for the project, since it could cover the requirements of testing realized prototypes with SL900A RFID chip. With its interface functionality and through the custom commands of the cool-Log set, the characteristics of the integrated temperature sensor of the SL900A RFID chip could be set according to the required configuration and the value of temperature could be extracted. The Femto RFID reader has been discontinued and there is no active web link for the datasheet.

REFERENCES

[1] M. Bolić, D. Simplot-Ryl, and I. Stojmenović, Eds., *RFID Systems*. John Wiley & Sons, Ltd, Jul. 2010. DOI: 10.1002/9780470665251.

[2] A. Lozano-Nieto, *RFID Design Fundamentals and Applications*. CRC Press, Dec. 2017. DOI: 10.1201/b10265.

[3] K. Finkenzeller, *RFID Handbook:Fundamental Operating Principles*. John Wiley & Sons, Ltd, Jun. 2010. DOI: 10.1002/9780470665121.

[4] P. Nikitin, K. Rao, and S. Lazar, "An Overview of Near Field UHF RFID", in *2007 IEEE International Conference on RFID*, IEEE, 2007. DOI: 10.1109/{RFID}.2007.346165.

[5] R. Want, "An Introduction to RFID Technology", *IEEE Pervasive Computing*, vol. 5, no. 1, pp. 25–33, Jan. 2006. DOI: 10.1109/mprv.2006.2.

[6] R. Want, "RFID Explained: A Primer on Radio Frequency Identification Technologies", *Synthesis Lectures on Mobile and Pervasive Computing*, vol. 1, no. 1, pp. 1–94, Jan. 2006. DOI: 10.2200/s00040ed1v01y200602mpc001.

[7] D. M. Dobkin, *The RF in RFID*. Elsevier, 2008. DOI: 10.1016/b978-0-7506-8209-1.x5001-3.

[8] J. Xi and H. Zhu, "UHF RFID Impedance Matching: T-match-dipole Tag Design on the Highway", in *2015 IEEE International Conference on RFID (RFID)*, IEEE, Apr. 2015. DOI: 10.1109/{RFID}.2015.7113077.

[9] E. Perret, *Radio Frequency Identification and Sensors*. John Wiley & Sons, Inc., Dec. 2014. DOI: 10.1002/9781119054016.

[10] S. Tedjini, N. Karmakar, E. Perret, A. Vena, R. Koswatta, and R. E-Azim, "Hold the Chips: Chipless Technology, an Alternative Technique for RFID", *IEEE Microwave Magazine*, vol. 14, no. 5, pp. 56–65, Jul. 2013. DOI: 10.1109/mmm.2013.2259393.

[11] E. P. Arnaud Vena and S. Tedjini, *Chipless RFID based on RF Encoding Particle*. Elsevier, 2016, p. iv. DOI: 10.1016/b978-1-78548-107-9.50007-0.

[12] R. Alencar, N. Barbot, M. Garbati, and E. Perret, "Practical Comparison of Decoding Methods for Chipless RFID System in Real Environment", in *2019 IEEE International Conference on RFID Technology and Applications (RFID-TA) (IEEE RFID-TA 2019)*, Pisa, Italy, Sep. 2019.

[13] L. D. Xu, W. He, and S. Li, "Internet of things in industries: A survey", *IEEE Transactions on Industrial Informatics*, vol. 10, no. 4, pp. 2233–2243, Nov. 2014. DOI: 10.1109/tii.2014.2300753.

[14] A. Gupta and R. K. Jha, "A survey of 5g network: Architecture and emerging technologies", *IEEE Access*, vol. 3, pp. 1206–1232, 2015. DOI: 10.1109/access.2015.2461602.

[15] A. Ijaz, L. Zhang, M. Grau, A. Mohamed, S. Vural, A. U. Quddus, M. A. Imran, C. H. Foh, and R. Tafazolli, "Enabling massive IoT in 5g and beyond systems: PHY radio frame design considerations", *IEEE Access*, vol. 4, pp. 3322–3339, 2016. DOI: 10.1109/access.2016.2584178.

[16] R. Want, "Enabling ubiquitous sensing with RFID", *IEEE Computer*, vol. 37, no. 4, pp. 84–86, Apr. 2004. DOI: 10.1109/mc.2004.1297315.

[17] Statista. (2016). RFID market size - global forecast through 2020, [Online]. Available: http://www.statista.com/statistics/299966/size-of-the-global-{RFID}-market/ (visited on 07/18/2019).

[18] (2019). Atlas RFID Store, Avery Denison UHF RFID tag AD229, [Online]. Available: https://www.atlas{RFID}store.com/avery-dennison-ad-229r6-uhf-{RFID}-wet-inlay-monza-r6/ (visited on 06/25/2019).

[19] (2019). Atlas RFID Store, Omni-Id Active RFID tag, [Online]. Available: https://www.atlas-{RFID}store.com/omni-id/ (visited on 06/25/2019).

[20] (2011). NXP, RFID White Papers, [Online]. Available: https://www.{NXP}.com/docs/en/white-paper/Carbon-Footprint-White-Paper.pdf (visited on 06/25/2019).

[21] H. Liu, M. Bolic, A. Nayak, and I. Stojmenovic, "Taxonomy and challenges of the integration of RFID and wireless sensor networks", *IEEE Network*, vol. 22, no. 6, pp. 26–35, Nov. 2008. DOI: 10.1109/mnet.2008.4694171. [Online]. Available: https://doi.org/10.1109/mnet.2008.4694171.

[22] J. Mitsugi, T. Inaba, B. Pátkai, L. Theodorou, J. Sung, T. López, D. Kim, D. Mcfarlane, H. Hada, Y. Kawakita, K. Osaka, and O. Nakamura, "Architecture development for sensor integration in the epcglobal network", Jan. 2007.

[23] C. Occhiuzzi, S. Caizzone, and G. Marrocco, "Passive UHF RFID antennas for sensing applications: Principles, methods, and classifications", *IEEE Antennas and Propagation Magazine*, vol. 55, no. 6, pp. 14–34, Dec. 2013. DOI: 10.1109/map.2013.6781700.

[24] J. Grosinger, L. Gortschacher, and W. Bosch, "Sensor add-on for batteryless UHF RFID tags enabling a low cost IoT infrastructure", in *2016 IEEE MTT-S International Microwave Symposium (IMS)*, IEEE, May 2016. DOI: 10.1109/mwsym.2016.7540331.

[25] J. F. Salmeron, F. Molina-Lopez, A. Rivadeneyra, A. V. Quintero, L. F. Capitan-Vallvey, N. F. de Rooij, J. B. Ozaez, D. Briand, and A. J. Palma, "Design and development of sensing RFID tags on flexible foil compatible with EPC gen 2", *IEEE Sensors Journal*, vol. 14, no. 12, pp. 4361–4371, Dec. 2014. DOI: 10.1109/jsen.2014.2335417.

[26] R. Colella, L. Tarricone, and L. Catarinucci, "SPARTACUS: Self-powered augmented RFID tag for autonomous computing and ubiquitous sensing", *IEEE Transactions on Antennas and Propagation*, vol. 63, no. 5, pp. 2272–2281, May 2015. DOI: 10.1109/tap.2015.2407908.

[27] J. Virtanen, L. Ukkonen, T. Bjorninen, L. Sydanheimo, and A. Z. Elsherbeni, "Temperature sensor tag for passive UHF RFID systems", in *2011 IEEE Sensors Applications Symposium*, IEEE, Feb. 2011. DOI: 10.1109/sas.2011.5739788.

[28] M. M. Islam, V. Viikari, J. Nikunen, and M. Reinikainen, "UHF RFID sensors based on frequency modulation", in *2016 IEEE SENSORS*, IEEE, Oct. 2016. DOI: 10.1109/icsens.2016.7808807.

[29] F. Bibi, C. Guillaume, N. Gontard, and B. Sorli, "A review: RFID technology having sensing aptitudes for food industry and their contribution to tracking and monitoring of food products", *Trends in Food Science & Technology*, vol. 62, pp. 91–103, Apr. 2017. DOI: 10.1016/j.tifs.2017.01.013.

[30] S. Tedjini, G. Andia-Vera, M. Zurita, R. Freire, and Y. Duroc, "Augmented RFID tags", in *2016 IEEE Topical Conference on Wireless Sensors and Sensor Networks (WiSNet)*, IEEE, Jan. 2016. DOI: 10.1109/wisnet.2016.7444324.

[31] (2019). AMS, SL900A EPC sensor tag, [Online]. Available: https://ams.com/sl900a (visited on 06/25/2019).

[32] (2019). Farsens, ANDY 100, [Online]. Available: http://www.farsens.com/en/products/andy100/ (visited on 06/25/2019).

[33] (2019). Farsens, ROCKY 100, [Online]. Available: http://www.farsens.com/en/products/rocky100/ (visited on 06/25/2019).

[34] (2019). AXZON(former RFMICRON), RFM405 xerxes-I, [Online]. Available: https://axzon.com/xerxes-i/ (visited on 06/25/2019).

[35] (2019). AXZON (former RFMICRON), RFM3300-D Magnus®-S3, [Online]. Available: https://axzon.com/rfm3300-d-magnus-s3-m3d-passive-sensor-ic (visited on 06/25/2019).

[36] (2019). EM Microelectronics, EM4325, [Online]. Available: https://www.emmicro-electronic.com/product/epc-and-uhf-ics/em4325 (visited on 06/25/2019).

[37] (2019). Impinj, Monza X-8K Dura datasheet, [Online]. Available: https://support.impinj.com/hc/en-us/articles/202756868-Monza-X-8K-Dura-Datasheet (visited on 06/25/2019).

[38] A. Sample, D. Yeager, P. Powledge, A. Mamishev, and J. Smith, "Design of an RFID-based battery-free programmable sensing platform", *IEEE Transactions on Instrumentation and Measurement*, vol. 57, no. 11, pp. 2608–2615, Nov. 2008. DOI: 10.1109/tim.2008.925019.

[39] K. Zannas, H. E. Matbouly, Y. Duroc, and S. Tedjini, "Self-tuning RFID tag: A new approach for temperature sensing", *IEEE Transactions on Microwave Theory and Techniques*, vol. 66, no. 12, pp. 5885–5893, Dec. 2018. DOI: 10.1109/tmtt.2018.2878568.

[40] S. Caizzone, E. DiGiampaolo, and G. Marrocco, "Constrained pole-zero synthesis of phase-oriented RFID sensor antennas", *IEEE Transactions on Antennas and Propagation*, vol. 64, no. 2, pp. 496–503, Feb. 2016. DOI: 10.1109/tap.2015.2511788.

[41] (2016). Etsi en-302-208-v3.1.0, european telecommunications standards institute, Radio frequency identification equipment operating in the band 865 mhz to 868 mhz with power levels up to 2 W and in the band 915 mhz to 921 mhz with power levels up to 4 W; harmonized standard covering the essential requirements of article 3.2 of the directive 2014/53/eu, [Online]. Available: http://www.etsi.org (visited on 06/25/2019).

[42] S. Rima, A. Georgiadis, A. Collado, R. Goncalves, and N. Carvalho, "Passive UHF RFID enabled temperature sensor tag on cork substrate", in *2014 IEEE RFID Technology and Applications Conference (RFID-TA)*, IEEE, Sep. 2014. DOI: 10.1109/{RFID}-ta.2014.6934205.

[43] T. Björninen and F. Yang, "Signal strength readout and miniaturised antenna for metal-mountable UHF RFID threshold temperature sensor tag", *Electronics Letters*, vol. 51, no. 22, pp. 1734–1736, Oct. 2015. DOI: 10.1049/el.2015.2661.

[44] R. Bhattacharyya, C. Floerkemeier, S. Sarma, and D. Deavours, "RFID tag antenna based temperature sensing in the frequency domain", in *2011 IEEE International Conference on RFID*, IEEE, Apr. 2011. DOI: 10.1109/{RFID}.2011.5764639.

[45] R. Krigslund, P. Popovski, and G. F. Pedersen, "Orientation sensing using multiple passive RFID tags", *IEEE Antennas and Wireless Propagation Letters*, vol. 11, pp. 176–179, 2012. DOI: 10.1109/lawp.2012.2185918.

[46] A. Vena, B. Sorli, A. Foucaran, and Y. Belaizi, "A RFID-enabled sensor platform for pervasive monitoring", in *2014 9th International Symposium on Reconfigurable and Communication-Centric Systems-on-Chip (ReCoSoC)*, IEEE, May 2014. DOI: 10.1109/recosoc.2014.6861358.

[47] S. Manzari, S. Caizzone, C. Rubini, and G. Marrocco, "Feasibility of wireless temperature sensing by passive UHF-RFID tags in ground satellite test beds", in *2014 IEEE International Conference on Wireless for Space and Extreme Environments (WiSEE)*, IEEE, Oct. 2014. DOI: 10.1109/wisee.2014.6973074.

[48] M. Tentzeris and S. Nikolaou, "RFID-enabled ultrasensitive wireless sensors utilizing inkjet-printed antennas and carbon nanotubes for gas detection applications", in *2009 IEEE International Conference on Microwaves, Communications, Antennas and Electronics Systems*, IEEE, Nov. 2009. DOI: 10.1109/comcas.2009.5385940.

[49] A. A. Babar, S. Manzari, L. Sydanheimo, A. Z. Elsherbeni, and L. Ukkonen, "Passive UHF RFID tag for heat sensing applications", *IEEE Transactions on Antennas and Propagation*, vol. 60, no. 9, pp. 4056–4064, Sep. 2012. DOI: 10.1109/tap.2012.2207045.

[50] S. D. Nguyen, C. M. Dang, T. T. Pham, S. Tedjini, E. F. Blanc, and N. N. Le, "Approach for quality detection of food by RFID-based wireless sensor tag", *Electronics Letters*, vol. 49, no. 25, pp. 1588–1589, Dec. 2013. DOI: 10.1049/el.2013.3328.

[51] (2019). AXZON, (former RFMicron) , RFM3240 Long-range wireless temperature sensor, [Online]. Available: https://axzon.com/rfm3240-long-range-wireless-temperature-sensor/ (visited on 06/25/2019).

[52] (2019). Farsens, Cyclon-14BA, [Online]. Available: http://www.farsens.com/en/products/cyclon-14ba/ (visited on 06/25/2019).

[53] H. E. Matbouly, K. Zannas, Y. Duroc, and S. Tedjini, "Analysis and assessments of time delay constrains for passive RFID tag-sensor communication link: Application for rotation speed sensing", *IEEE Sensors Journal*, vol. 17, no. 7, pp. 2174–2181, Apr. 2017. DOI: 10.1109/jsen.2017.2662058.

[54] C. A. Balanis, *Antenna Theory: Analysis and Design, 3rd Edition*. Wiley-Interscience, 2005, pp. 184–202, ISBN: 047166782X.

[55] *Matlab Antenna toolbox, licence number 6322491*, The MathWorks, Natick, MA, USA, 2019a.

[56] W. L. Stutzman and G. A. Thiele, *Antenna Theory and Design*. Wiley, 2012, ISBN: 0470576642.

[57] *The Handbook of Antenna Design, Vol. 1 (Electromagnetic Waves, Nos. 15 & 16)*. The Institution of Engineering and Technology, 1982, ISBN: 0906048826.

[58] W. C. Gibson, *The Method of Moments in Electromagnetics*. Chapman and Hall/CRC, 2007, ISBN: 1420061453.

[59] N. Yarkony and N. Blaunstein, "PREDICTION OF PROPAGATION CHARACTERISTICS IN INDOOR RADIO COMMUNICATION ENVIRONMENTS", *Progress In Electromagnetics Research*, vol. 59, pp. 151–174, 2006. DOI: 10.2528/pier05090801.

[60] W. D. Rummler, "Time- and frequency-domain representation of multipath fading on line-of-sight microwave paths", *The Bell System Technical Journal*, vol. 59, no. 5, pp. 763–796, 1980. DOI: 10.1002/j.1538-7305.1980.tb03032.x.

[61] W. Wiesbeck, C. Sturm, W. Soergel, M. Porebska, and G. Adamiuk, "Influence of antenna performance and propagation channel on pulsed uwb signals", in *2007 International Conference on Electromagnetics in Advanced Applications*, Sep. 2007, pp. 915–922. DOI: 10.1109/ICEAA.2007.4387454.

[62] A. Taflove and K. Umashankar, "Review of FD-TD numerical modeling of electromagnetic wave scattering and radar cross section", *Proceedings of the IEEE*, vol. 77, no. 5, pp. 682–699, May 1989. DOI: 10.1109/5.32059. [Online]. Available: https://doi.org/10.1109/5.32059.

[63] X. Q. Sheng and W. Song, "Finite-element method", in *Essentials of Computational Electromagnetics*, John Wiley & Sons, Ltd, Apr. 2012, pp. 153–206. DOI: 10.1002/9780470829646.ch3.

[64] (2016). CST microwave studio, [Online]. Available: https://www.cst.com/products/cstmws (visited on 07/22/2019).

[65] (2016). ANSYS HFSS, [Online]. Available: https://www.ansys.com/products---/electronics/ansys-hfss/ (visited on 07/22/2019).

[66] P. V. Nikitin and K. V. S. Rao, "Theory and measurement of backscattering from RFID tags", *IEEE Antennas and Propagation Magazine*, vol. 48, no. 6, pp. 212–218, Dec. 2006. DOI: 10.1109/MAP.2006.323323.

[67] I. Farris, L. Militano, A. Iera, and S. C. Spinella, "Assessing the performance of a novel tag-based reader-to-reader communication paradigm under noisy channel conditions", *IEEE Transactions on Wireless Communications*, vol. 15, no. 7, pp. 4813–4825, Jul. 2016. DOI: 10.1109/TWC.2016.2546882.

[68] C. Duan, L. Yang, and Y. Liu, "Accurate spatial calibration of RFID antennas via spinning tags", in *2016 IEEE 36th International Conference on Distributed Computing Systems (ICDCS)*, Jun. 2016, pp. 519–528. DOI: 10.1109/ICDCS.2016.32.

[69] H. N. Khan, J. Grosinger, B. Auinger, D. Amschl, P. Priller, U. Muehlmann, and W. Bosch, "Measurement based indoor simo RFID simulator for tag positioning", in *2015 International EURASIP Workshop on RFID Technology (EURFID)*, Oct. 2015, pp. 112–119. DOI: 10.1109/EU{RFID}.2015.7332395.

[70] A. Buffi, P. Nepa, and F. Lombardini, "A phase-based technique for localization of uhf-RFID tags moving on a conveyor belt: Performance analysis and test-case measurements", *IEEE Sensors Journal*, vol. 15, no. 1, pp. 387–396, Jan. 2015. DOI: 10.1109/JSEN.2014.2344713.

[71] P. V. Nikitin, R. Martinez, S. Ramamurthy, H. Leland, G. Spiess, and K. V. S. Rao, "Phase based spatial identification of uhf RFID tags", in *2010 IEEE International Conference on RFID (IEEE RFID 2010)*, Apr. 2010, pp. 102–109. DOI: 10.1109/{RFID}.2010.5467253.

[72] C. Norstrom, A. Wall, and Wang Yi, "Timed automata as task models for event-driven systems", in *Proceedings Sixth International Conference on Real-Time Computing Systems and Applications. RTCSA'99 (Cat. No.PR00306)*, Dec. 1999, pp. 182–189. DOI: 10.1109/RTCSA.1999.811218.

[73] J. Fraden, *Handbook of Modern Sensors: Physics, Designs, and Applications*. Springer, 2010.

[74] H. E. Matbouly, F. Domingue, V. Palmisano, L. Boon-Brett, M. Post, C. Rivkin, R. Burgess, and W. Buttner, "Assessment of commercial micro-machined hydrogen sensors performance metrics for safety sensing applications", *International Journal of Hydrogen Energy*, vol. 39, no. 9, pp. 4664–4673, Mar. 2014. DOI: 10.1016/j.ijhydene.2014.01.037.

[75] B. Wang, M.-K. Law, A. Bermak, and H. C. Luong, "A passive RFID tag embedded temperature sensor with improved process spreads immunity for a for a -30 to 60°C sensing range", *IEEE Transactions on Circuits and Systems I: Regular Papers*, vol. 61, no. 2, pp. 337–346, Feb. 2014. DOI: 10.1109/tcsi.2013.2278388.

[76] L. Vojtech, A. M. F. Lopez, M. Neruda, and Z. Lokaj, "Embedded system with RFID technology and inductive proximity sensor", in *2013 36th International Conference on Telecommunications and Signal Processing (TSP)*, Jul. 2013, pp. 213–217. DOI: 10.1109/TSP.2013.6613922.

[77] J. Yin, J. Yi, M. K. Law, Y. Ling, M. C. Lee, K. P. Ng, B. Gao, H. C. Luong, A. Bermak, M. Chan, W.-H. Ki, C.-Y. Tsui, and M. Yuen, "A system-on-chip EPC gen-2 passive UHF RFID tag with embedded temperature sensor", *IEEE Journal of Solid-State Circuits*, Nov. 2010. DOI: 10.1109/jssc.2010.2072631.

[78] A. Tetelin, C. Pellet, A. Achen, and M. Toepper, "Capacitive humidity sensors based on oxidized photobcb polymer films: Enhanced sensitivity and response time", in *SENSORS, 2005 IEEE*, Oct. 2005, 4 pp.–. DOI: 10.1109/ICSENS.2005.1597761.

[79] G. S. Deep, J. S. R. Neto, A. M. N. Lima, R. C. S. Freire, and P. C. Lobo, "Thermoresistive radiation sensor response time employing electrical heating", *IEEE Transactions on Instrumentation and Measurement*, vol. 45, no. 1, pp. 332–335, Feb. 1996. DOI: 10.1109/19.481364.

[80] A. Vergara, K. D. Benkstein, and S. Semancik, "Thermally-assisted transient analysis for reducing the response time of microhotplate gas sensors", in *SENSORS, 2013 IEEE*, Nov. 2013, pp. 1–4. DOI: 10.1109/ICSENS.2013.6688156.

[81] F. Wen, G. Zhang, and D. Ben, "Estimation of multipath parameters in wireless communications using multi-way compressive sensing", *Journal of Systems Engineering and Electronics*, vol. 26, no. 5, pp. 908–915, Oct. 2015. DOI: 10.1109/JSEE.2015.00098.

[82] P. V. Nikitin and K. V. S. Rao, "Effect of gen2 protocol parameters on RFID tag performance", in *2009 IEEE International Conference on RFID*, Apr. 2009, pp. 117–122. DOI: 10.1109/{RFID}.2009.4911178.

[83] E. Cerciello, G. Massei, and L. Paura, "Optimization of tag anti-collision algorithm for epc gen2 RFID", in *2014 Euro Med Telco Conference (EMTC)*, Nov. 2014, pp. 1–6. DOI: 10.1109/EMTC.2014.6996631.

[84] K. Liu, Y. Feng, and R. Ding, "A fast and stable anti-collision algorithm for the epcglobal uhf class 1 generation 2 standard", in *Proceedings 2013 International Conference on Mechatronic Sciences, Electric Engineering and Computer (MEC)*, Dec. 2013, pp. 367–371. DOI: 10.1109/MEC.2013.6885100.

[85] W. Chen, "A new RFID anti-collision algorithm for the epcglobal uhf class-1 generation-2 standard", in *2012 9th International Conference on Ubiquitous Intelligence and Computing and 9th International Conference on Autonomic and Trusted Computing*, Sep. 2012, pp. 811–815. DOI: 10.1109/UIC-ATC.2012.73.

[86] (2005). EPC radio-frequency identity protocols class-1 generation-2 UHF RFID protocol for communications at 860mhz—960mhz, Version 1.0.9, [Online]. Available: http://www.gs1.org. (visited on 07/22/2019).

[87] H. Solar, A. Beriain, I. Zalbide, E. d Éntremont, and R. Berenguer, "A robust, -40 to 150°C wireless rotor temperature monitoring system based on a fully passive UHF RFID sensor tag", in *2014 IEEE MTT-S International Microwave Symposium (IMS2014)*, IEEE, Jun. 2014. DOI: 10.1109/mwsym.2014.6848480.

[88] L. Ukkonen, L. Sydanheirno, and M. Kivikoski, "A novel tag design using inverted-f antenna for radio frequency identification of metallic objects", in *2004 IEEE/Sarnoff Symposium on Advances in Wired and Wireless Communications*, IEEE. DOI: 10.1109/sarnof.2004.1302848.

[89] L. Ukkonen, L. Sydanheimo, and M. Kivikoski, "Effects of metallic plate size on the performance of microstrip patch-type tag antennas for passive RFID", *IEEE Antennas and Wireless Propagation Letters*, vol. 4, pp. 410–413, 2005. DOI: 10.1109/lawp.2005.860212.

[90] A. Sharma, A. T. Hoang, F. Nekoogar, F. U. Dowla, and M. S. Reynolds, "An electrically small, 16.7 m range, ISO18000-6c UHF RFID tag for industrial radiation sources", *IEEE Journal of Radio Frequency Identification*, vol. 2, no. 2, pp. 49–54, Jun. 2018. DOI: 10.1109/jrfid.2018.2850316. [Online]. Available: https://doi.org/10.1109/jrfid.2018.2850316.

[91] R. A. Ramirez, E. A. Rojas-Nastrucci, and T. M. Weller, "UHF RFID tags for on-/off-metal applications fabricated using additive manufacturing", *IEEE Antennas and Wireless Propagation Letters*, vol. 16, pp. 1635–1638, 2017. DOI: 10.1109/lawp.2017.2658599.

[92] K. Zannas, H. E. Matbouly, Y. Duroc, and S. Tedjini, "Antenna design for compact RFID sensors dedicated to metallic environments", in *2017 XXXIInd General Assembly and Scientific Symposium of the International Union of Radio Science (URSI GASS)*, IEEE, Aug. 2017. DOI: 10.23919/ursigass.2017.8105333.

[93] J. Grosinger, W. Pachler, and W. Bosch, "Tag size matters: Miniaturized RFID tags to connect smart objects to the internet", *IEEE Microwave Magazine*, vol. 19, no. 6, pp. 101–111, Sep. 2018. DOI: 10.1109/mmm.2018.2844029.

[94] D. M. Pozar, *Microwave Engineering*. Wiley, 1997, ISBN: 0471170968.

[95] K. Rao, P. Nikitin, and S. Lam, "Impedance matching concepts in RFID transponder design", in *Fourth IEEE Workshop on Automatic Identification Advanced Technologies (AutoID 05)*, IEEE. DOI: 10.1109/autoid.2005.35.

[96] J. Siden and H.-E. Nilsson, "An electrically small elliptic PIFA for RFID in harsh metallic environments", in *2013 IEEE International Conference on Microwaves, Communications, Antennas and Electronic Systems (COMCAS 2013)*, IEEE, Oct. 2013. DOI: 10.1109/comcas.2013.6685309.

[97] (2019). Rogers corporation, "RT/ Duroid 6010/6006 laminates, [Online]. Available: https://www.rogerscorp.com/acs/products/36/RT-duroid-6006-6010-Laminates.aspx (visited on 06/25/2019).

[98] (2019). Rogers corporation, general information of dielectric constant for rt/duroid® 6010.2lm & ro3010 high frequency circuit materials, [Online]. Available: https://www.rogerscorp.

com/documents/2379/acs/General-Information-of-Dielectric-Constant-for-RT-duroid-6010-2LM-RO3010-High-Frequency-Circuit-Materials.pdf (visited on 06/25/2019).

[99] (2019). Damaskos ,model 08 thin dielectric sheet tester system, [Online]. Available: http://www.damaskosinc.com/cavitiy.htm (visited on 06/25/2019).

[100] T. Weiland, "On the unique numerical solution of maxwellian eigenvalue problems in three dimensions", Deutsches Elektronen-Synchrotron (DESY), 1984.

[101] M. Hamid and R. Hamid, "Equivalent circuit of dipole antenna of arbitrary length", *IEEE Transactions on Antennas and Propagation*, vol. 45, no. 11, pp. 1695–1696, 1997. DOI: 10.1109/8.650083.

[102] (2019). Coilcraft," 0805HP high Q ceramic chip inductors, [Online]. Available: https://www.coilcraft.com/0805hp.cfm (visited on 06/25/2019).

[103] (2019). Rogers corporation, RO4003C laminates, [Online]. Available: https://www.rogerscorp.com/acs/products/54/RO4003C-Laminates. (visited on 07/16/2019).

[104] (2019). Keysight technologies, N9918A fieldfox handheld microwave analyzer, 26.5 GHz, [Online]. Available: https://www.keysight.com/en/pdx-x201927-pn-N9918A/fieldfox-handheld-microwave-analyzer-265-ghz?cc=US&lc=eng (visited on 07/16/2019).

[105] (2019). JP Selecta, Plactronic model 6155100, [Online]. Available: http://www.grupo-selecta.com/en/catalogo/productos/111/Rectangular\%20hotplates (visited on 07/16/2019).

[106] (2019). PR electronics, Universal transmitter, [Online]. Available: https://www.prelectronics.com/ (visited on 07/16/2019).

[107] J. Grosinger and J. D. Griffin, "A bend transducer for backscatter RFID sensors", in *Proceedings of the 2012 IEEE International Symposium on Antennas and Propagation*, IEEE, Jul. 2012. DOI: 10.1109/aps.2012.6349258.

[108] A. Rennane, F. Benhamoud, A. Abdelnour, N. Fonseca, D. Kaddour, R. Touhami, and S. Tedjini, "Passive UHF RFID bending and absolute force strain gauge based sensors", in *2017 Mediterranean Microwave Symposium (MMS)*, IEEE, Nov. 2017. DOI: 10.1109/mms.2017.8497164.

[109] (2019). Micro measurements, cea-06-125un-350, [Online]. Available: https://www.micro-measurements.com/pca/detail/5c49d0aaeaf7657493741978 (visited on 07/16/2019).

[110] (2019). Keysight technologies, U1253B handheld digital multimeter, 4, 1/2 digit, oled display, [Online]. Available: https://www.keysight.com/en/pdx-2878706-pn-U1253B/handheld-digital-multimeter-4-digit-oled-display?cc=US\&lc=eng (visited on 07/16/2019).

[111] (2019). National instruments, how is temperature affecting your strain measurement accuracy?, [Online]. Available: http://www.ni.com/fr-fr/innovations/white-papers/06/how-is-temperature-affecting-your-strain-measurement-accuracy-.html (visited on 07/16/2019).

[112] (2019). Impinj, Monza R6, [Online]. Available: https://support.impinj.com/hc/en-us/articles/202765328-Monza-R6-Product-Brief-Datasheet (visited on 07/26/2019).

[113] (2019). NXP, SL3S1205-15 UCODE 8/8m, [Online]. Available: https://www.{NXP}.com/docs/en/data-sheet/SL3S1205-15-DS.pdf (visited on 07/26/2019).

[114] S. Srinivas, J. Kuhn, R. A. Oliver, J. D. Hyde, and C. J. Diorio, *Self tuning RFID tags*, May 24, 2016.

[115] (2019). Axzon (former RFmicron), Magnus S product family, [Online]. Available: http://rfmicron.com/magnus-family/ (visited on 07/16/2019).

[116] (2019). Axzon, sensors, [Online]. Available: https://axzon.com/sensors/ (visited on 07/16/2019).

[117] M. C. Caccami and G. Marrocco, "Electromagnetic modeling of self-tuning RFID sensor antennas in linear and nonlinear regimes", *IEEE Transactions on Antennas and Propagation*, vol. 66, no. 6, pp. 2779–2787, Jun. 2018. DOI: 10.1109/tap.2018.2820322.

[118] M. C. Caccami and G. Marrocco, "Electromagnetic characterisation of self-tuning UHF RFID tags for sensing application", in *2016 IEEE International Symposium on Antennas and Propagation (APSURSI)*, IEEE, Jun. 2016. DOI: 10.1109/aps.2016.7696344.

[119] L. Liu, Y. Weng, S. W. Cheung, T. I. Yuk, and L. J. Foged, "Modeling of cable for measurements of small monopole antennas", in *2011 Loughborough Antennas & Propagation Conference*, IEEE, Nov. 2011. DOI: 10.1109/lapc.2011.6114153.

[120] M. M. Islam, K. Rasilainen, S. Karki, and V. Viikari, "Designing a passive retrodirective wireless sensor", *IEEE Antennas and Wireless Propagation Letters*, pp. 1–1, 2017. DOI: 10.1109/lawp.2017.2671411.

[121] H. El Matbouly, S. Tedjini, K. Zannas, and Y. Duroc, "Chipless RFID threshold temperature sensor compliant with uhf and ism radio frequency", in *2018 2nd URSI Atlantic Radio Science Meeting (AT-RASC)*, May 2018, pp. 1–4. DOI: 10.23919/URSI-AT-RASC.2018.8471585.

[122] C. M. Butler, "Investigation of a scatterer coupled to an aperture in a conducting screen", *IEE Proceedings H - Microwaves, Optics and Antennas*, vol. 127, no. 3, pp. 161–169, Jun. 1980. DOI: 10.1049/ip-h-1.1980.0035.

[123] S. Genovesi, F. Costa, M. Borgese, F. A. Dicandia, A. Monorchio, and G. Manara, "Chipless RFID sensor for rotation monitoring", in *2017 IEEE International Conference on RFID Technology Application (RFID-TA)*, Sep. 2017, pp. 233–236. DOI: 10.1109/{RFID}-TA.2017.8098885.

[124] C. Feng, W. Zhang, L. Li, L. Han, X. Chen, and R. Ma, "Angle-based chipless RFID tag with high capacity and insensitivity to polarization", *IEEE Transactions on Antennas and Propagation*, vol. 63, no. 4, pp. 1789–1797, Apr. 2015. DOI: 10.1109/TAP.2015.2393851.

[125] R. G. Machado and A. M. Wyglinski, "Software-defined radio: Bridging the analog–digital divide", *Proceedings of the IEEE*, vol. 103, no. 3, pp. 409–423, Mar. 2015. DOI: 10.1109/JPROC.2015.2399173.

[126] J. Hao, T. Huang, Z. D. Chen, H. Zhao, and J. Li, "A GNU radio based fmcw radar with a simple frequency correction technique for accurate indoor localization applications", in *2018 IEEE MTT-S International Wireless Symposium (IWS)*, May 2018, pp. 1–4. DOI: 10.1109/IEEE-IWS.2018.8400973.

[127] (2019). Jadak, ThingMagic M6e UHF RAIN RFID, [Online]. Available: https://www.jadaktech.com/products/{RFID}/embedded-uhf-{RFID}-readers/mercury6e-m6e (visited on 07/18/2019).

[128] A. G. Boujemaa, "Développement d'une application windows pour la commande et a communication d'un tag RFID dans un environnement electromagnétique severe", Universite de Tunis El Manar, 2018-09-29.

[129] (2019). Jadak, ThingMagic Mercury6 fixed mount UHF RAIN RFIDjadak, [Online]. Available: https://www.jadaktech.com/products/{RFID}/fixed-mount-{RFID}-readers/mercury6-fixed-mount/ (visited on 07/18/2019).

[130] (2019). XT power, XT-16000QC3 powerbank modern DC / USB battery with 15600mah - up to 24V, [Online]. Available: https://www.xtpower.de/XT-16000QC3-PowerBank-modern-DC-/-USB-battery-with-15600mAh-up-to-24V (visited on 07/18/2019).

[131] A. Petit, *Software Java SL900A with the library Mercury API 1.31.2.40 for reading the temperature*, 2019.

[132] A.Petit, "CRI mesure des températures des sondes RFID du t712 de grand maison du 18/04/2019", EDF, 2018-04-19.

RÉSUMÉ

Développement de capteurs RFID passifs dédiés au monitoring des génératrices dans les centrales électriques.

Dans le contexte de l'Internet des Objets et l'Industrie 4.0, de nouvelles technologies sont attendues pour apporter des solutions à plusieurs problèmes industriels. La technologie RFID, et son évolution vers les capteurs, est très prometteuse et pourrait potentiellement trouver des applications en environnement industriel. Le travail développé dans cette thèse s'est réalisé dans le cadre du projet Innov'Hydro, en partenariat avec plusieurs acteurs académiques et industriels. Ce projet visait principalement à explorer de nouvelles solutions de capteurs destinés aux environnements sévères des centrales hydroélectriques, en particulier l'intérieur des génératrices. En effet, les générateurs encombrants des centrales sont susceptibles de tomber en panne en raison de l'oxydation de pièces internes à cause des courants électriques forts. Une solution pour éviter de telles pannes consiste à surveiller la température et/ou la déformation à l'intérieur des générateurs et en particulier les parties vulnérables. Afin de surveiller ces pièces, la taille réduite, la grande précision et le fonctionnement passif sont des facteurs critiques de toute solution de détection. Toutes ces caractéristiques peuvent être satisfaites par la technologie RFID UHF et la transformation récente des tags en tag-capteur RFID. Ainsi l'utilisation de nouvelles configurations et concepts de tag-capteurs, la mesure de la température et du stress dans un environnement réel de centrale hydroélectrique sont explorés en profondeur. Des résultats prometteurs sont obtenus grâce à un ensemble de mesures et de tests à la fois en laboratoire et en environnement réel.

ABSTRACT

Development of Passive RFID Sensors Dedicated to the Monitoring of Power Plant Generators.

In the context of the Internet of Things and the industrial revolution 4.0, new technologies are expected to offer solutions in several industrial related problems. The RFID technology and its evolution to a sensing solution is very promising and could potentially find application in the industrial environment. The work of this thesis was carried out in the context of Innov'Hydro project with the participation of several academic and industrial partners. The main goal of the Innov'Hydro project was to explore new sensing solutions for the harsh industrial environment of hydroelectric power-plants and especially in the interior of the generators. The bulky generators of the power-plants are susceptible to break downs due to the oxidation of high current conducting parts. One solution to avoid such break downs is to monitor the temperature and/or the deformation in the interior of the generators and especially of the vulnerable parts. In order to monitor these parts, the small size, the high accuracy and a potential passive operation of the sensors are critical attributes of the sensing solution. All these attributes can be found in the UHF RFID technology and the recently introduced concept of sensor-tags. Therefore, by utilizing novel RFID sensor-tag designs and RFID configurations, the possibility of temperature and stress sensing in the real environment of the hydroelectric power-plants is explored in depth. A series of measurements and tests are conducted in both laboratory and real industrial environment with promising results.